Ghent University
Faculty of Sciences
Department of Solid State Sciences
Krijgslaan 281/S1, 9000 Ghent, Belgium

Thin Film Synthesis of VO_2 and VN by Gas-Solid Reactions and Atomic Layer Deposition

Geert Rampelberg

Promotor: Prof. Dr. Christophe Detavernier

Members of the Jury:

Prof. Dr. Jan Ryckebusch (UGent, chair)
Prof. Dr. Diederik Depla (UGent)
Dr. Hilde Poelman (UGent)
Prof. Dr. Stefan De Gendt (KULeuven, IMEC)
Dr. Naoufal Bahlawane (Luxemburg Institute of Science and Technology)
Prof. Dr. Steven George (University of Colorado Boulder, USA)

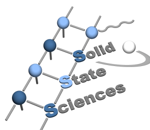

Thesis submitted for the degree of
Doctor in Sciences: Physics
March 2016

Preface

This PhD thesis describes the synthesis of VO_2 and VN thin films by gas-solid reactions and atomic layer deposition. One of the driving forces for this research is the semiconductor-metal transition in VO_2, which may for instance be applied in Mott-transistors, and which was investigated as well at IMEC during the past years. However, many more applications could benefit from the material synthesis methods presented in this work. The experimental work has been carried out in the Department of Solid State Sciences at Ghent University, in the CoCooN research group of professor Christophe Detavernier, and was started in March 2010.
This thesis is mainly based on the results which have been presented in 5 papers, published in peer-reviewed journals. These are included in the appendix. For both VO_2 and VN, a chapter is presented which includes a literature review and a summary of the experimental work. I hope that I succeeded in presenting my work in a comprehensive way, and that this research will be useful for future investigation of these fascinating material systems.

Geert Rampelberg
Ghent, January 2016

Table of contents

Preface i

Nederlandstalige samenvatting vii

English summary xi

1 Introduction 1
- 1.1 Vanadium oxides . . . 1
- 1.2 The semiconductor-metal transition in VO_2 . . . 3
  - 1.2.1 Introduction . . . 3
  - 1.2.2 Mechanism behind the transition . . . 5
  - 1.2.3 Parameters influencing the SMT characteristics . . . 7
  - 1.2.4 Applications . . . 11
  - 1.2.5 Alternative SMT/MIT material systems . . . 18
- 1.3 Vanadium nitrides . . . 20
- 1.4 Copper diffusion barriers . . . 22
- 1.5 Goals and outline of this thesis . . . 23

2 Experimental 31
- 2.1 Thin film deposition techniques . . . 31
  - 2.1.1 Magnetron sputtering . . . 32
  - 2.1.2 Atomic layer deposition . . . 33
- 2.2 Characterization of thin film thickness, density and composition . 36
  - 2.2.1 X-ray reflectivity . . . 36
  - 2.2.2 X-ray fluorescence . . . 37
  - 2.2.3 Rutherford backscattering spectroscopy . . . 38
  - 2.2.4 The vanadium molar density . . . 39
  - 2.2.5 X-ray photoelectron spectroscopy . . . 39
- 2.3 Gas-solid reactions . . . 40
  - 2.3.1 Thermodynamics and phase diagrams . . . 40
  - 2.3.2 Kinetics . . . 44
  - 2.3.3 Oxygen partial pressure control . . . 48
- 2.4 In-situ X-Ray diffraction during annealing . . . 56
  - 2.4.1 XRD systems . . . 57

2.4.2 In-situ reaction chambers: experimental and commercial systems . . . 59
2.4.3 In-situ XRD at UGent . . . 59
2.5 Characterization of the semiconductor-metal transition . . . 61
2.5.1 Temperature-dependent XRD . . . 61
2.5.2 Temperature-dependent sheet resistance measurements . . 62
2.5.3 Temperature-dependent spectroscopic ellipsometry . . . 63

3 Synthesis and characterization of VO_2 thin films 69
3.1 Literature on thin film VO_2 synthesis . . . 69
3.1.1 Reactive sputtering . . . 70
3.1.2 Oxidation of V and reduction of V_2O_5 . . . 71
3.1.3 Chemical vapor deposition . . . 71
3.1.4 Atomic layer deposition . . . 72
3.2 Synthesis of VO_2 thin films by oxidation of vanadium and reduction of V_2O_5 . . . 76
3.2.1 Magnetron sputtering of vanadium thin films . . . 76
3.2.2 Oxidation of vanadium thin films in varying oxygen partial pressure . . . 77
3.2.3 Reduction of V_2O_5 thin films in H_2 . . . 80
3.2.4 Stabilization of the VO_2 phase in a H_2-O_2 gas mixture . . 81
3.2.5 Semiconductor-metal transition . . . 82
3.2.6 Summary . . . 85
3.3 Atomic layer deposition of VO_2 thin films and nanoparticles . . . 86
3.3.1 ALD growth characteristics . . . 87
3.3.2 Film properties and stability . . . 88
3.3.3 Conformality . . . 92
3.3.4 Crystalline phase formation . . . 95
3.3.5 Morphology of crystalline VO_2 films and nanoparticles . . 100
3.3.6 Semiconductor-metal transition . . . 102
3.3.7 Summary . . . 103
3.4 Conclusions . . . 104

4 Synthesis and characterization of VN thin films 111
4.1 Literature on thin film VN synthesis . . . 111
4.1.1 Reactive sputtering . . . 111
4.1.2 Nitridation of V and V_2O_5 . . . 112
4.1.3 Chemical vapor deposition . . . 113
4.1.4 Atomic layer deposition . . . 114
4.2 High-temperature nitridation of vanadium . . . 116
4.3 Low-temperature atomic layer deposition of VN . . . 120
4.3.1 ALD growth Characteristics . . . 120
4.3.2 Film properties and influence of post-deposition annealing 121
4.3.3 VN thin films as copper diffusion barrier . . . 124
4.3.4 Oxidation resistance of VN thin films . . . 126

4.4 Conclusions 128

5 Conclusions and suggestions for future work 133
5.1 Summary and conclusions 133
5.2 Suggestions for future work 136

List of abbreviations 141

List of figures 145

List of tables 147

List of publications and conference contributions 149

Appendix: Papers I-V 153

Paper I: *In-situ* X-ray diffraction study of the controlled oxidation and reduction in the V-O system for the synthesis of VO_2 and V_2O_3 thin films 155

Paper I - supplementary information: *In-situ* X-ray diffraction study of the controlled oxidation and reduction in the V-O system for the synthesis of VO_2 and V_2O_3 thin films 175

Paper II: Semiconductor-metal transition in thin VO_2 films grown by ozone based atomic layer deposition 183

Paper III: Crystallization and semiconductor-metal switching behavior of thin VO_2 layers grown by atomic layer deposition 191

Paper IV: Vanadium oxide thin films and nanoparticles prepared by atomic layer deposition and controlled post-deposition annealing 211

Paper V: Low temperature plasma-enhanced atomic layer deposition of thin vanadium nitride layers for copper diffusion barriers 231

Dankwoord 241

Nederlandstalige samenvatting –Summary in Dutch–

Introductie en situering van het onderzoek

Vanadium is een transitiemetaal dat gekenmerkt wordt door een groot aantal oxide fasen. Naast de hoofdreeks, bestaande uit de enkelvoudige valenties +2, +3, +4 en +5, zijnde respectievelijk VO, V_2O_3, VO_2 en V_2O_5, zijn tal van intermediaire fasen gekend met gemengde valenties. Dit zijn de Magnéli (V_nO_{2n-1}) en de Wadsley (V_nO_{2n+1}) reeksen, waarin fasen als V_4O_7 en V_6O_{13} terug te vinden zijn. Vanadium oxides kennen vele toepassingen, zoals in katalyse en energie-opslag. Eén van de meest fascinerende eigenschappen, die gedeeld wordt door vele vanadium oxide fasen, is de halfgeleider-metaal transitie (ook wel metaal-isolator transitie genoemd). Typerend is een zeer sterke stijging van de elektrische geleidbaarheid wanneer deze materialen opgewarmd worden tot boven hun transitietemperatuur. Ongetwijfeld het meest bestudeerde materiaal in deze reeks is vanadium dioxide (VO_2), met een scherpe transitie bij 68 °C en een verandering in resistiviteit tot 5 grootte-ordes. Simultaan is er een sterke daling van de optische transmissie, voornamelijk in het infrarode golflengtegebied, en een structurele verandering van monoklien VO_2(M1) naar tetragonaal VO_2(R). Omwille van deze eigenschappen wordt VO_2 intensief bestudeerd voor o.a. toepassing als intelligente coating voor glas, waarbij stralingswarmte (infrarood licht) geblokkeerd wordt bij hoge temperaturen, of als materiaal voor geheugens, transistoren en selectoren in micro-elektronische chips. In hoofdstuk 1 wordt deze halfgeleider-metaal transitie, alsook de potentiële toepassingen, uitgebreid besproken.

Naast vanadium oxides bestaan er ook enkele vanadium nitride fasen, waarvan VN de meest stabiele en meest voorkomende is. Net als vele andere transitiemetaalnitrides kan VN voornamelijk toegepast worden als slijtvaste coating, of als diffusiebarrière in micro-elektronische chips. Maar ook het gebruik voor supercondensatoren en batterijen werd recent gerapporteerd.

Gezien de vele oxidatietoestanden, is de synthese van VO_2 en VN niet evident, en de meeste gerapporteerde processen (PVD, CVD, PLD) zijn slechts succesvol binnen een nauw procesvenster. Dit doctoraatsonderzoek richt zich op de synthese van VO_2 en VN dunne filmen. Er wordt gefocust op twee-stapsprocessen, bestaande uit een depositie op lage temperatuur en een uitgloeibehandeling, wat

eenvoudigere optimalisatie van procescondities en een breder procesvenster toelaat. In een eerste methode worden dunne vanadiumlagen gesputterd en vervolgens gecontroleerd geoxideerd of genitrideerd. Voor de tweede methode wordt gebruik gemaakt van atomaire laag depositie (ALD). Dit is een techniek gebaseerd op het cyclisch blootstellen van een substraat aan twee verschillende gassen. De chemisorptiereacties die bij zulke processen betrokken zijn, vertonen een zelf-limiterend gedrag, zodat per cyclus slechts één monolaag materiaal gegroeid wordt. De sterkste troeven van ALD zijn de controle van laagdikte op atomaire resolutie, de uniformiteit over grote substraatoppervlakken, en de conformaliteit op en in 3-dimensionale (nano)structuren. Naast de synthese van VO_2 dunne filmen wordt ook aandacht besteed aan de karakterisatie van de halfgeleider-metaal transitie. De experimentele methoden worden toegelicht in hoofdstuk 2, terwijl de experimentele resultaten uitgebreid aan bod komen in hoofdstuk 3 (VO_2) en hoofdstuk 4 (VN).

Ontwikkeling van experimentele methoden

In-situ XRD systeem voor de studie van kristallisatie en gas - vaste stof reacties: Gezien het belang van uitgloeibehandelingen om de eigenschappen van de gedeponeerde dunne filmen te optimaliseren, is er nood aan een efficiënte methode om de invloed van o.a. temperatuur en partieeldrukken op de kristallijne fasevorming te bestuderen. Binnen het kader van dit onderzoek werd apparatuur ontwikkeld om de reacties van een vaste stof met gassen te bestuderen, meer bepaald oxidatie, reductie of nitridatie. De techniek betreft in-situ X-stralen diffractie (XRD), waarbij de verschillende kristallijne fasen kunnen gemonitord worden als functie van temperatuur en bijvoorbeeld partieeldruk zuurstof. Een beschrijving van deze in-situ XRD methode, evenals de gebruikte methodes voor controle van zuurstofpartieeldrukken, is terug te vinden in hoofdstuk 2.

Karakterisatie van de halfgeleider-metaal transitie: De halfgeleider-metaal transitie in VO_2 wordt gekarakteriseerd door sterke veranderingen in elektrische, optische en structurele eigenschappen. Om deze transitie te karakteriseren werd gebruik gemaakt van drie complementaire technieken: resistiviteitsmetingen, spectroscopische ellipsometrie en XRD werden uitgevoerd tijdens thermische cycli rond de transitietemperatuur. Merk op dat resistiviteitsmetingen een continue laag vereisen, terwijl ellipsometrie en XRD eveneens gebruikt kunnen worden voor geïsoleerde VO_2 nanodeeltjes. Deze technieken worden in detail beschreven in hoofdstuk 2.

Synthese en karakterisatie van VO_2

Wegens het grote aantal vanadium oxide fasen is de synthese van zuivere VO_2 dunne filmen niet evident. Weinige van de gerapporteerde technieken zijn een-

voudig toepasbaar zonder een drastische optimalisatie van procescondities. Vaak moeten verschillende procesparameters simultaan bijgeregeld worden om de depositie van fasezuiver VO_2 te garanderen. Bij reactief sputteren bijvoorbeeld moeten sputtervermogen, zuurstofpartieeldruk en temperatuur nauw afgesteld worden om kristallijn VO_2 te groeien. Bij chemische damp depositie (CVD) is een precieze controle van gasstromen, partieeldrukken en depositietemperatuur vereist. Hoofdstuk 3 omvat een literatuuroverzicht over dunne film depositie van VO_2.

Oxidatie- en reductiereacties in het V-O systeem: Gesputterde vanadiumlagen werden geoxideerd onder een brede waaier van temperaturen en zuurstofpartieeldrukken. Met behulp van in-situ XRD werd de oxidatie nauwlettend opgevolgd. Bij alle zuurstofpartieeldrukken in het bereik van 20 Pa tot 20000 Pa werd kristallijn VO_2 waargenomen. Weliswaar bleek enkel bij de laagste partieeldruk van 20 Pa de VO_2 fase stabiel, terwijl bij hogere zuurstofconcentraties verdere oxidatie optrad naar V_6O_{13} en V_2O_5. Maximaal 3 ordes verandering in resistiviteit werden waargenomen voor films geoxideerd bij 20 Pa O_2. Bij oxidatie in lucht werden enkel gelijkaardige grootte-ordes waargenomen door een nauwkeurige optimalisatie van de oxidatietijd. Deze tijd correspondeerde met de observatie van een maximale kristallijne fractie VO_2 en kon algemeen in verband gebracht worden met de zuurstofpartieeldruk en de temperatuur. Verbeterde elektrische transities, tot 4 grootte-ordes, werden bekomen door oxidatie in een gasmengsel van 5000 Pa H_2 met 20 tot 200 Pa O_2. Vermoedelijk leidt de competitie tussen reductie en oxidatie tot een hogere zuiverheid van de VO_2 fase in de bulk, aan de korrelgrenzen of beiden. Ook de reductie van V_2O_5 werd bestudeerd. In inert gas treedt nauwelijks reductie op, terwijl in waterstof een continue reductie doorheen o.a. de fasen V_6O_{13} en VO_2 optreedt, tot uiteindelijk V_2O_3 gevormd wordt. Het gasmengsel met waterstof en zuurstof leidde daarentegen tot de stabilisatie van de VO_2 fase, en een nog grotere elektrische transitie van bijna 5 grootte-ordes. Ook in de V_2O_3 lagen werd een halfgeleider-metaal transitie waargenomen: de resistiviteit veranderde met 3 grootte-ordes rond -110 °C.

Atomaire laag depositie van vanadium oxides: Voor de atomaire laag depositie van vanadium oxides werd gebruik gemaakt van tetrakis(ethylmethylamino)-vanadium als metaal-organische precursor (TEMAV), en H_2O, O_3 of O_2-plasma als reactant. Deposities werden voornamelijk uitgevoerd bij een temperatuur van 150 °C. De gesatureerde groeitempo's voor de drie reactanten bedroegen respectievelijk 0.8, 0.7 en 1.5 Å per cyclus. Zowel H_2O als O_3 resulteerden in depositie van amorf VO_2, maar de densiteit van de lagen bleek sterk afhankelijk van het reactant. Voor H_2O gebaseerde ALD processen was de densiteit aanzienlijk hoger dan voor O_3 gebaseerde ALD. Bij gebruik van O_2 plasma als reactant werden kristallijne V_2O_5 lagen gegroeid. Om tot kristallijn VO_2 te komen bleek een extra thermische nabehandeling dus noodzakelijk. In inerte atmosfeer werden echter geen kristallijne fasen gevormd. Een minimale partieeldruk zuurstof van de orde van 1 Pa leidde daarentegen wel tot kristallisatie van VO_2. Bij hogere zuurstofdrukken

werden nog andere vanadiumoxide fasen opgemerkt. Concreet, afhankelijk van het reactant tijdens ALD en de partieeldruk zuurstof en temperatuur tijdens de nabehandeling konden in totaal 4 verschillende kristallijne fasen bekomen worden: VO_2(R) (H_2O en O_3 proces), VO_2(B) (O_3 en O_2-plasma proces), V_6O_{13} (O_3 en O_2-plasma proces) en V_2O_5 (alle ALD processen). Bovendien bleek het gasmengsel van 5000 Pa H_2 met 20 Pa O_2 ook voor de ALD lagen succesvol voor stabilisatie van VO_2. De halfgeleider-metaal transitie werd ook voor deze lagen gedetecteerd met een drietal grootte-ordes elektrische transitie, gelijkaardig of groter dan voor VO_2 lagen van dezelfde dikte gevormd door oxidatie van gesputterd vanadium. Lagen dunner dan 10 nm agglomereerden echter, met de vorming van nanodeeltjes als gevolg. Voor deze nanodeeltjes werd m.b.v. ellipsometrie nog steeds een (optische) transitie waargenomen, met een significante verbreding van het hysteresisgedrag (tot 50 °C).

Synthese en karakterisatie van VN

Hoge-temperatuursnitridatie van vanadium: VN werd gevormd tijdens de reactie van gesputterd vanadium met een stikstofatmosfeer. Door de gevoeligheid van vanadium voor oxidatie bleken zeer hoge temperaturen ($\approx$ 1000 °C) en zeer hoge opwarmtempo's ($\approx$ 5 °C/s) noodzakelijk om zuiver, zuurstofvrij VN te bekomen. De minimale resistiviteit bedroeg 80 $\mu\Omega \cdot cm$, vergelijkbaar met gerapporteerde waarden.

Atomaire laag depositie van vanadium nitride: De groei van VN via ALD werd bekomen door combinatie van de TEMAV precursor met NH_3 plasma, wat leidde tot een gesatureerd groeitempo van 0.7 Å per cyclus bij 150 °C. Vanaf ongeveer 400 ALD cycli werd kristallijn VN gedetecteerd, met een resistiviteit van 200 $\mu\Omega \cdot cm$. Thermische nabehandeling in N_2 of in een $H_2{-}N_2$ gasmengsel leidde tot een verdere daling van de resistiveit tot $90\mu\Omega \cdot cm$. Depositie van elektrisch geleidende coatings op polymeerfolie was eveneens succesvol. Dunne VN lagen werden verder nog geëvalueerd als diffusiebarrière tussen Cu en Si. De diffusie van Cu in Si kon uitgesteld worden tot een temperatuur van ongeveer 700 °C, in vergelijking met 230 °C zonder barrière.

Conclusie

Nieuwe methoden werden ontwikkeld om dunne lagen VO_2 en VN te synthetiseren. Deze twee-stapsprocessen omvatten een lage-temperatuursdepositie en een uitgloeibehandeling, en laten een eenvoudige optimalisatie toe van procesparameters.

English summary

Introduction and research objectives

Vanadium is a transition-metal which is characterized by a large number of oxide phases. Apart from the main series of single-valence states +2, +3, +4 and +5, corresponding to VO, V_2O_3, VO_2 and V_2O_5, several intermediate phases of mixed valences exist. These are known as the Magnéli (V_nO_{2n-1}) and Wadsley (V_nO_{2n+1}) series, in which phases such as V_4O_7 and V_6O_{13} can be found. Vanadium oxides are known for many applications, such as catalysts and energy storage. One of the most fascinating features, shared by many vanadium oxide phases, is the semiconductor-metal transition (also known as metal-insulator transition). Characteristic is a sharp and strong increase of the electrical conductivity when the transition temperature is crossed. The most studied material in this series is vanadium dioxide (VO_2), which has a very sharp transition at 68 °C and a change in resistivity up to 5 orders of magnitude. Simultaneously, a strong reduction of the optical transmittance is observed, mainly in the infrared wavelength region, and a structural transition from monoclinic VO_2(M1) to tetragonal VO_2(R). Because of these features, VO_2 is being intensively investigated for applications such as intelligent thermochromic coatings on glass, for blocking radiation heat (infrared light) at high temperatures, or as a material for memories, transistor and selectors in microelectronic chips. A detailed description of this semiconductor-metal transition, as well as some potential applications, is given in chapter 1.

Vanadium forms as well a few vanadium nitride phases. VN is the most stable one and is most often observed by researchers. Like other transition-metal nitrides, VN may be applied for instance as wear-resistant coating, or as diffusion barrier in microelectronic chips. During the last decade, VN is as well reported for its potential use in supercapacitors or batteries.

Due to the large range of oxidation states, the synthesis of VO_2 and VN thin films is not straightforward. Most reported deposition processes (PVD, CVD, PLD) are only successful in a narrow process window. This research focuses on the synthesis of VO_2 and VN thin films. The focus lies on two-step processes which include a low-temperature deposition and a thermal annealing step. This allows for easier optimization and a broader process window. A first method is the controlled oxidation or nitridation of metallic vanadium films prepared by magnetron sputtering. The second method involves atomic layer deposition (ALD). This technique is based on the cyclic exposure of a substrate to two different

gases. The chemisorption reactions involved in these processes are characterized by a self-limiting behavior, such that every cycle only one monolayer of material is deposited. The main advantages are the atomic scale resolution of thickness control, uniformity on large area substrates and excellent conformality on and into 3-dimensional (nano)structures. For VO_2, an additional thermal treatment will be required to obtain the crystalline phase which shows the semiconductor-metal transition. Apart from the synthesis of VO_2 thin films, this semiconductor-metal transition will also be investigated. The experimental methods will be explained in chapter 2, while the experimental results will be discussed in chapter 3 (VO_2) and chapter 4 (VN).

Development of experimental methods

In-situ XRD system for the study of crystallization and gas-solid reactions: Due to the importance of thermal annealing to optimize the properties of the deposited thin films, there is a need for an efficient method to study the influence of parameters such as temperature and partial pressures on the crystalline phase formation. For the purpose of this research, an apparatus was developed for studying gas-solid reactions, i.e. oxidation, reduction and nitridation. The technique is in-situ X-ray diffraction (XRD), which allows for monitoring the crystalline phases as a function of temperature and, for instance, oxygen partial pressure. Although a similar system was already present in the research group, prior to the start of this research, a new system was required to allow for the high-temperature oxidation reactions. A description of this in-situ XRD method, as well as the methods to control the oxygen partial pressure, is given in chapter 2.

Characterization of the semiconductor-metal transition: The semiconductor-metal transition in VO_2 is characterized by drastic changes in electrical, optical and structural properties. Three complementary techniques have been used to monitor these features: sheet resistance measurements, spectroscopic ellipsometry and XRD have been performed during thermal cycling around the transition temperature. Note that the sheet resistance measurements require continuous films, whereas ellipsometry and XRD can as well be used for isolated nanoparticles. These techniques are discussed in chapter 2.

Synthesis and characterization of VO_2

Due to the large number of vanadium oxide phases, the synthesis of single-phase VO_2 thin films is a challenging task. Most of the synthesis methods require a dedicated optimization of process conditions. Often, many process parameters cannot be changed independently without altering the composition of the deposited vanadium oxide film. For instance, during reactive sputtering, the sputter power, oxygen partial pressure and temperature should be precisely controlled to ensure

the deposition of high-quality crystalline VO_2. During chemical vapor deposition (CVD), a precise control of gas flows, partial pressures and deposition temperature is required. In chapter 3 a literature overview is presented on the growth of VO_2 thin films.

Oxidation- and reduction reactions in the V-O system: Sputtered vanadium layers were oxidized under a broad range of temperatures and oxygen partial pressures. By means of in-situ XRD, the oxidation reactions were monitored. At all oxygen partial pressures in the range from 20 to 20000 Pa, crystalline VO_2 was observed. However, only at the lowest oxygen partial pressure of 20 Pa, VO_2 remained stable, whereas at higher values, a subsequent oxidation towards V_6O_{13} and V_2O_5 was observed. Maximum 3 orders of magnitude switching of the resistance was obtained for the films annealed at 20 Pa O_2. For oxidation in air, such high values were almost reached by careful control of the oxidation time. This oxidation time corresponded with the observation of a maximum fraction of crystalline VO_2, and could in general be related to the oxygen partial pressure and temperature. The resistance switching ratio could be improved to more than 4 orders of magnitude by using a mixture of 5000 Pa H_2 and 20 to 200 Pa O_2. It is believed that the competition of reduction by hydrogen and oxidation by oxygen results in a strongly improved purity of the VO_2 phase in the bulk, at the grain boundaries, or both. In addition to the oxidation of V, the reduction of V_2O_5 was investigated. In inert gas, barely any reduction was observed, whereas in H_2 the continues reduction through phases as V_6O_{13} and VO_2 was observed, until finally V_2O_3 was obtained. In contrast, VO_2 was successfully achieved by making use of the H_2-O_2 gas mixture, and nearly 5 orders of magnitude electrical switching ratio was observed, close to the values reported for bulk VO_2. The V_2O_3 layers were as well characterized by a semiconductor-metal transition: the resistivity changed by 3 orders of magnitude near -110 °C.

Atomic layer deposition of vanadium oxides: For the atomic layer deposition of vanadium oxides, the tetrakis(ethylmethylamino)vanadium precursor (TEMAV) was used in combination with H_2O, O_3 or O_2 plasma as reactant. The depositions were mainly carried out at 150 °C. Saturated growth rates of respectively 0.8, 0.7 and 1.5 Å per cycles were achieved. Both the H_2O and O_3 processes resulted in amorphous VO_2 layers, but the density of the films depended strongly on the reactant. Processes using H_2O resulted in a much higher density compared to films grown using O_3 as reactant. On the other hand, crystalline V_2O_5 films were grown using O_2 plasma. In order to obtain crystalline VO_2, post-deposition annealing was required. Although the films were expected to contain sufficient oxygen, annealing in inert gas did not result in a reliable crystallization process. Only when small amounts of oxygen were added to the inert gas flow, at a typical oxygen partial pressure of 1 Pa, crystalline VO_2 was successfully obtained at temperatures around 400 to 450 °C. At higher oxygen partial pressures, many other vanadium oxide phases were observed. Four different pure phases could be obtained, de-

pending on the reactant used during deposition, and the temperature and oxygen partial pressure used during post-deposition annealing: VO_2(R) (H_2O and O_3 process), VO_2(B) (O_3 and O_2-plasma process), V_6O_{13} (O_3 and O_2-plasma process) and V_2O_5 (all ALD processes). In addition, the gas mixture of 5000 Pa H_2 and 20 Pa O_2 proved as well successful for stabilization of VO_2. The semiconductor-metal transition was detected in the VO_2 films with maximum resistance switching ratios of more than 3 orders of magnitude. Films thinner than 10 nm agglomerated and resulted in the formation of isolated nanoparticles. Characterization of these nanoparticles by ellipsometry showed an optical transition with broadened hysteresis widths up to 50 °C.

Synthesis and characterization of VN

High-temperature nitridation of vanadium: VN was formed during reaction of sputtered V films with N_2 gas. By the extreme sensitivity of vanadium for oxidation, very high temperatures ($\approx$ 1000 °C) and fast temperature increase ($\approx$ 5 °C/s) were indispensable to obtain pure, oxygen-free VN films. A minimum resistivity of 80 $\mu\Omega \cdot cm$ was obtained, in correspondence with reported values.

Atomic layer deposition of vanadium nitride: The growth of VN thin films by ALD was achieved by combining the TEMAV precursor with NH_3 plasma. At 150 °C a saturated growth rate of 0.7 Å per cycle was observed. Starting from 400 ALD cycles, crystalline VN appeared with a resistivity of 200 $\mu\Omega \cdot cm$. This value was further reduced down to 90 $\mu\Omega \cdot cm$ by post-deposition annealing in N_2 or in a H_2-N_2 gas mixture. Deposition of electrically conductive coatings on polymer foils proved as well successful. Furthermore, thin VN films were evaluated as diffusion barrier for Cu on Si. The diffusion of Cu into Si was prevented up to high temperatures around 700 °C, compared to only 230 °C when no barrier was present.

Conclusions

New methods were developed for the synthesis of VO_2 and VN thin films. These two-step processes, which include a low-temperature deposition and a thermal annealing step, allow for easy optimization of the process parameters.

1 Introduction

The subject of this thesis is the synthesis and characterization of thin film vanadium oxides and vanadium nitrides, more specifically VO_2 and VN. Within this introductory chapter, sections 1.1 and 1.3 will give an overview of the vanadium oxide and nitride phases, together with their reported (potential) applications. Very specific for VO_2 is its characteristic semiconductor-metal transition, which will be discussed in detail in section 1.2. Finally, the goals and outline of this thesis will be explained in section 1.5.

1.1 Vanadium oxides

The vanadium-oxygen phase diagram: Figure 1.1 shows the vanadium-oxygen phase diagram as it was established by Wriedt.[1] Vanadium has five different valence states, i.e. 0, +2, +3, +4 and +5, which result in the phases V, VO, V_2O_3, VO_2 and V_2O_5. Apart from these single-valence phases, mixed valence states are known as the Magnéli and Wadsley series, which can be written as V_nO_{2n-1} ($n = 4 - 9$) and V_nO_{2n+1} ($n = 3, 4, 6$) respectively.[1–3] In chapter 2, section 2.3.1, alternative phase diagrams will be presented, which allow to understand the favorable conditions of oxygen partial pressures and temperatures to synthesize various VO_x phases. In chapter 3 a literature overview will be presented on synthesis methods for thin film vanadium oxides, with a focus on VO_2 thin films.

V_2O_5 research at the department of solid state sciences: The department of solid-state sciences at Ghent University has been a leading group on the synthesis and characterization of V_2O_5. Starting from the late 1960s, high-purity single-

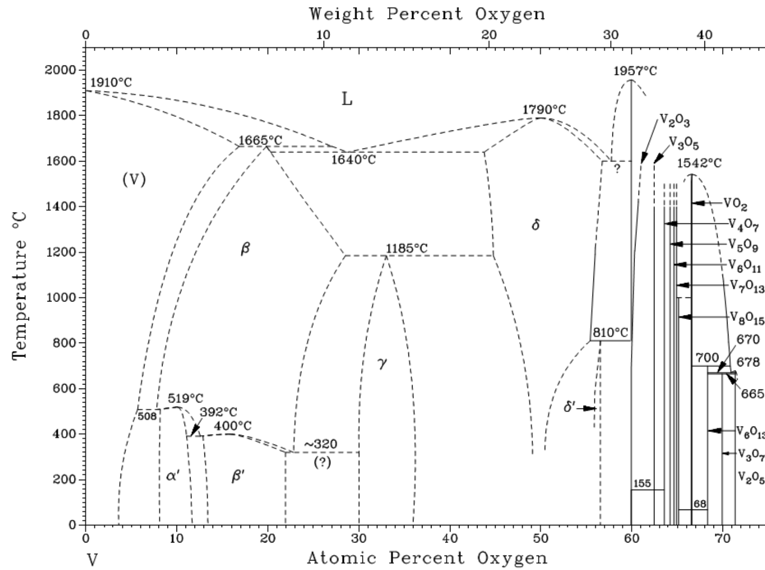

Figure 1.1. *The vanadium-oxygen phase diagram as constructed by Wriedt.* [1]

crystal growth of V_2O_5 was successfully achieved by Jo Haemers,[4] which was the start for years of thorough investigation of the electronic, optical, structural, and surface properties.[5;6] Later on, V_2O_5 thin films were grown and characterized, with catalysis as the main application.[7–11]

Properties and applications of vanadium oxides: Vanadium oxides are used for a wide variety of applications. A list of the most frequently investigated applications is given here:

- Catalysts: mainly V_2O_5 has been studied widely as a catalyst. Reports have been published on its use for dehydrogenation of propane, oxidation of *o*-xylene, and it is used for the production of sulfuric acid.[3;12–14]

- Energy storage: monoclinic VO_2(B), as well as the layered vanadium oxides V_2O_5, V_6O_{13}, V_4O_9 and V_3O_7 have been intensively investigated for their use as cathode materials for Li-ion batteries.[3;15–20] Furthermore, V_2O_5 is involved in the fabrication of hybrid electrodes for supercapacitors and sodium-bases pseudocapacitors.[3] Also redox and redox flow batteries are based on the variety of oxidation states in vanadium oxides and are considered as energy storage systems for photovoltaics and wind energy.[21;22]

- One of the most remarkable features, shared by many vanadium oxide phases, is the **semiconductor-metal transition (SMT)**, also referred to as metal-insulator transition (MIT). Changes of many orders of magnitude in electrical conductivity and optical properties have been observed in VO, V_2O_3,

VO_2 and many other vanadium oxides, when the transition temperature is crossed.[23;24] Reported (potential) applications include optical and electrical switches, RF-microwave switches, tunable plasmonic and metamaterial systems, and smart windows.[24;25] In section 1.2 this semiconductor-metal transition will be discussed in detail, including a theoretical description, material systems and applications.

1.2 The semiconductor-metal transition in VO_2

1.2.1 Introduction

Since Morin reported on the metal-insulator transitions (MIT) in some lower oxides of vanadium and titanium, a huge scientific investigation of these metal oxide phases was initiated.[23] Certainly VO_2 attracted a lot of interest, since the transition temperature is close to room temperature. When heating VO_2 across a temperature of 68 °C, the conductivity increases very abruptly with five orders of magnitude for bulk material, as illustrated in figure 1.2.[26] Due to the small band gap of the insulating phase, as will be discussed in section 1.2.2, the term semiconductor-metal transition (SMT) will be used in this work, instead of metal-insulator transition.

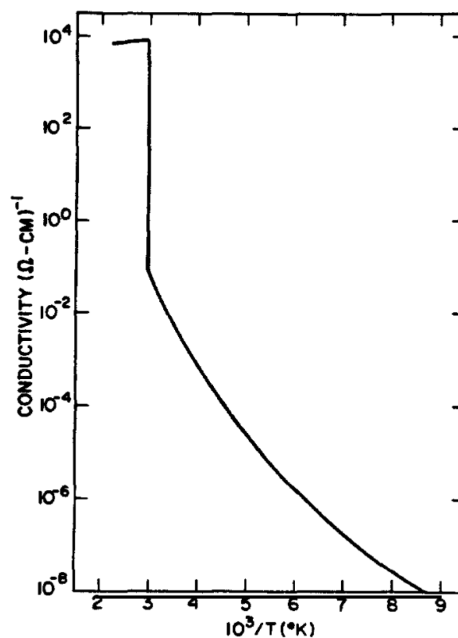

Figure 1.2. *Variation of the electrical conductance in single crystal VO_2 as a function of temperature.*[26]

Both terms are commonly used in literature. This electronic transition also manifests itself as a drastic reduction of the optical transmission, which is mainly observed in the infrared region of the spectrum.[27–29] An example is shown in figure 1.3 for a thin film of 80 nm, during thermal cycling around the transition temperature.

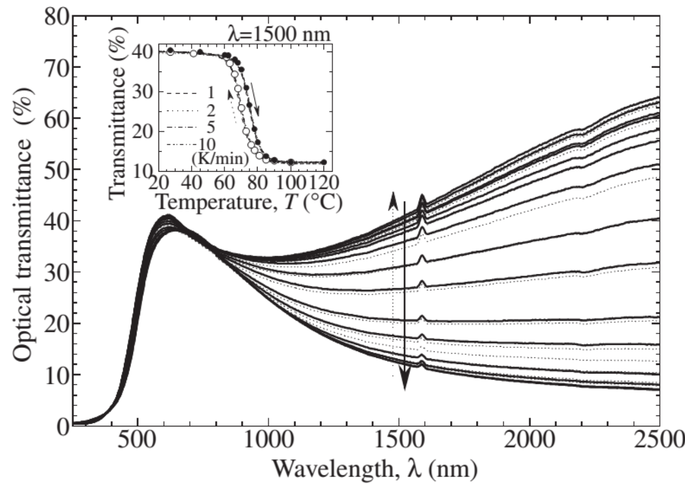

Figure 1.3. *The optical transmittance of a VO_2 thin film of 80 nm during thermal cycling between 25 and 120 °C.*[28]

Simultaneous with this electronic transition, a change in crystal structure is observed.[30;31] The low-temperature structure is monoclinic (space group P21/c, $a = 5.75290$, $b = 4.52630$, $c = 5.38250$, $\beta = 122.60$), and is referred to as the VO_2(M1) phase, while above the transition temperature the lattice transforms to a body-centered tetragonal rutile structure (space group P42/mnm (136), $a = 4.55400$, $c = 2.85570$), denoted as VO_2(R).[32] Both structures are shown in figure 1.4. In the monoclinic structure, V atoms form a zigzag structure along the c-axis with alternating short and long V-V bonds of 2.619 and 3.164 Å. Above the transition temperature, the symmetry increases to a rutile structure with disappearance of the zigzag V chains, while the V-V bond length along the c-axis obtains a constant value of 2.815 Å. It should be noted that other VO_2 polymorphs exist, which are not involved in this transition, i.e. monoclinic VO_2(B) and tetragonal VO_2(A).

Although temperature is mainly considered as the parameter which triggers the transition, electrical, optical and pressure-induced switching (or combinations) are achieved as well.[24] The timescale of the transition is extremely fast, down to 75 fs, as was experimentally verified by optical pump-probe methods.[33] In the next sections, a detailed description of the mechanism behind the transition, the parameters influencing the transition characteristics, some applications, as well as some alternative material systems will be discussed.

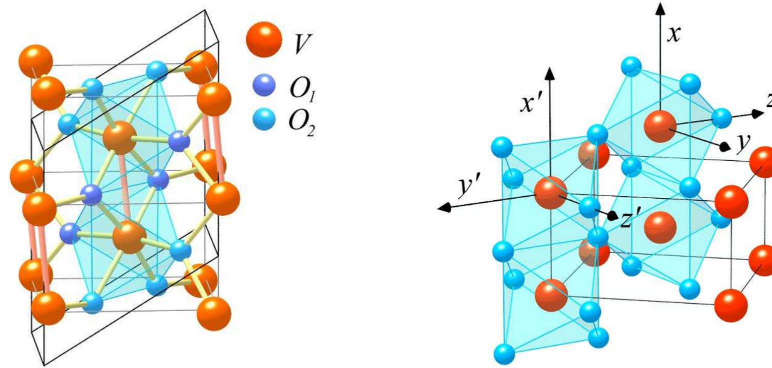

Figure 1.4. The VO_2 crystal structures involved during the SMT: (left) low-temperature monoclinic VO_2(M1), (right) high-temperature tetragonal VO_2(R).[31]

1.2.2 Mechanism behind the transition

Within the classical theory for the description of metals and insulators, electrons are supposed to be noninteracting or only weakly interacting with each other. The distinction between metals and insulators is based on the electronic bands, which are a consequence of the periodic lattice structure, and their filling with electrons. At zero temperature, insulators have a completely filled highest band, while for metals this highest band is partially filled, which allows electrons to move through metals. This basic distinction between metals and insulators was established shortly after the introduction of quantum mechanics. Semiconductors are insulator-like materials, characterized by a small band gap between the highest filled band (valence band) and lowest empty band (conduction band). Thermal excitation of electrons from the valence band to the conduction band contributes to a certain degree of conductivity.

However, de Boer and Verwey reported that many transition-metal oxides show an insulating behavior, although their partially filled d-electron band would suggest them to behave like metals.[34] Wigner and Mott explained these observations by the introduction of electron-electron interactions.[35;36] Metals which behave like insulators due to correlated electrons are nowadays often referred to as Mott (or Mott-Hubbard) insulators, and the transition from metal to insulator is called a Mott (or Mott-Hubbard) metal-insulator transition. More precisely, Coulomb interaction between the electrons prevent them to move from one unit cell to another. A critical carrier density exists, described by the formula $n_c^{1/3} a_H \approx 0.2 - 0.25$, with a_H the Bohr radius of the material.[37;38] When the carrier density increases to a value higher than n_c, a transition from insulator to metal occurs. This is called the Mott-criterion.

Although the semiconductor-metal transition in VO_2 could initially be explained by the correlated electron theory of Mott, the fact that during the electronic transition a change in crystal structure is observed, allowed Peierls to introduce an

alternative mechanism based on electron-phonon interaction.[39] A structural deformation modifies the periodic ionic potential and consequently results in a band structure change. The band structures of both the low-temperature semiconducting and high-temperature metallic phase were described by Goodenough,[30] and are presented in figure 1.5. In the high-temperature metallic state, the $d_{||}$ and $\pi^\star$ band are partially filled. The $d_{||}$ orbitals are aligned along the rutile c-axis. During cooling down across the transition temperature, the dimerization of the V atoms, which creates the zigzag V chains, causes the $d_{||}$ band to split up into a filled, bonding $d_{||}$ band and an empty, anti-bonding $d_{||}^\star$ band. At the same time, the $\pi^\star$ band shifts upwards away from the Fermi level. In this way, a classical band insulator (or semiconductor) appears. The band gap has a value of approximately 0.7 eV.[30;40]

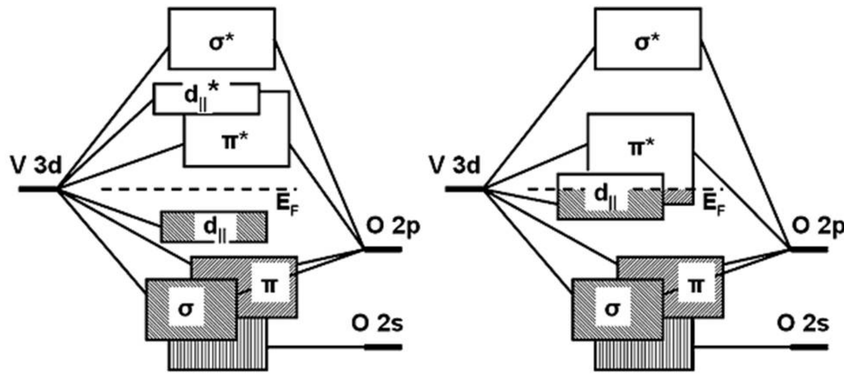

Figure 1.5. *The band structure of VO_2: (left) low-temperature semiconducting phase, (right) high-temperature metallic phase.*[30;41]

The exact origin of the transition has been a subject of debate for several decades. Is the structural change causing the SMT in VO_2, or is it a consequence of a carrier-induced transition? In other words, is the SMT a Peierls-type or a Mott-type transition? Wentzcovich et al. concluded from local density approximation calculations of the monoclinic M1 structure that the semiconducting phase should be treated as a band insulator and not as a Mott insulator.[42] However, the transition is more complicated due to the existence of an intermediate semiconducting monoclinic structure (M2), which is of the Mott type.[43] Within this M2 phase, only one V chain forms a zigzag structure, whereas in the M1 phase both V chains do. Cavalleri et al. applied ultra-fast spectroscopy to study the time-domain hierarchy between the structural and electronic effects.[33] Formation of the metallic phase was obtained by photo-doping into the valence band of the semiconducting phase. The delay of the semiconductor-metal transition with respect to the photo-doping was explained to be associated by the phonons connecting the two structures, and was believed to be indicative of a band-like character of VO_2 in its semiconducting phase. On the other hand, Kim et al. found evidence

for a monoclinic and correlated metal intermediate phase in between the SMT and the structural phase transition by using femtosecond pump-probe measurements.[44] These authors interpreted these results as a possible evidence for the Mott mechanism. More recently, experimental photo-emission spectroscopy, supported by DFT calculations pointed out that below the transition temperature, VO_2 cannot be considered as a pure Mott insulator, but as a many-body Peierls insulator. Both electron correlations and the Peierls effect need to be taken into account for describing the SMT.[45;46] Thorough reviews on metal-insulator transitions have been published by e.g. Mott and Imada.[37;47]

1.2.3 Parameters influencing the SMT characteristics

In bulk, single crystal pure VO_2, the first-order semiconductor-metal transition is characterized by a very sharp transition with a clearly defined transition temperature near 68 °C, a small hysteresis of only a few °C and a 5 order of magnitude change in resistivity. These characteristics are however seldom observed in thin films. Several parameters cause a shift of the transition temperature, a widening of the hysteresis and a suppressed magnitude and sharpness of the transition. These parameters include stoichiometry, doping, pressure, stress and grain size. In the following paragraphs, these parameters and their effect on the transition characteristics are discussed.

Stoichiometry: The synthesis of stoichiometric VO_2 is a challenging task for material scientists, certainly in the case of thin films. Griffiths and Eastwood studied the influence of oxygen-nonstoichiometry on the SMT characteristics of VO_2 thin films.[48] Slightly oxygen-rich or oxygen-deficient films showed a reduction of the transition temperature and a drastic suppression of the electrical switching magnitude.

Doping: Doping is a well-known technique to alter the transition temperature. By replacing V with elements like W, Mo or Nb, the transition temperature can be decreased by several tens of degrees.[49;50] W is the most studied doping element, and a temperature effect of approximately -24 °C/at.%W has been found, as shown in figure 1.6.[51] Also co-doping with W and Ti has been studied.[52] In general, however, doping is limited to only a few percent, since the magnitude of the transition is drastically suppressed. Wei et al. showed that hydrogen can stabilize the metallic phase below the normal transition temperature as well.[53]

External pressure and stress: The effect of uniaxial stress and hydrostatic pressure on the transition temperature was determined by Ladd and Paul on VO_2 single crystals.[26] Stress along the a- or b-axes broadened the transition, but did not show a significant effect on the transition temperature. In contrast, the shape of the resistivity versus temperature curve was not altered by stress applied along the c-axis, while a temperature coefficient for the transition temperature (T_c) of

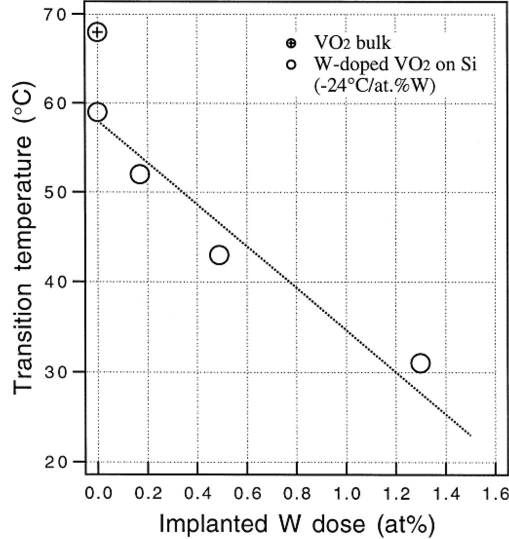

Figure 1.6. *Effect of W-doping on the transition temperature of VO_2.*[51]

$dT_c/dS = -12\,°C/GPa$ was measured up to 0.05 GPa of stress (S). In the semiconducting phase, just below T_c, the resistance (R) decreased at a rate of $(dlnR/dS) = -0.4$/GPa. Hydrostatic pressures (P) up to 0.8 GPa increased the transition temperature with $(dT_c/dP) = 0.6\,°C/GPa$, while for pressures up to 0.03 GPa, the room temperature resistance decreased linearly with a coefficient of $(dlnR/dP) = -0.15$/GPa.

Several researchers investigated the influence of stress in thin films of VO_2. For instance, Muraoka and Hiroi studied the stress-induced influence of a rutile TiO_2 substrate on the SMT in epitaxially grown thin films of VO_2, as shown in figure 1.7.[54] The lattice parameters of the rutile TiO_2 structure differ slightly from those of the VO_2(R) phase, such that during epitaxial growth stress is present at the interface. VO_2 films grown on TiO_2 (001) show a reduction of the transition temperature with $\approx 40\,°C$, due to compressive stress on the c-axis of VO_2. On TiO_2 (110) crystals, tensile stress on the VO_2 c-axis causes an increase of T_{SMT} with almost $20\,°C$.

Remark that the transition itself also causes stress in a VO_2 crystal. During the transition from low to high temperature the rutile c-axis is compressed by approximately 1%, while the a- and b-axis expand by approximately 0.6% and 0.1% respectively.[55;56] In polycrystalline VO_2 thin films, an overall shrinkage of approximately 0.3% takes place during transition from VO_2(M1) to VO_2(R). This might have a drastic impact on the potential use of the phase transition in this material. It has been observed that in single crystals the stress generated during the SMT leads to fracture after only a few cycles.[49;57] In contrast, thin films are known to survive during repeated cycling. Guzman et al. reported on the stable electrical

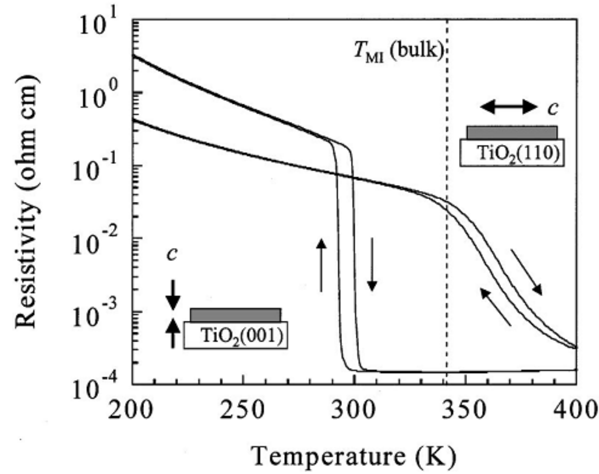

Figure 1.7. *The effect of uniaxial stress along the c-axis on the semiconductor-metal transition of VO_2 for epitaxial thin films of $\approx$ 10 nm grown on rutile TiO_2 (001) and (110) substrates. The vertical dotted line indicates the transition temperature for bulk VO_2.* [54]

switching in 200 nm thin of over 10^8 cycles without degradation of the electrical properties. [58]

On the other hand, the shrinkage of the VO_2 crystal may cause such a high levels of stress on the substrate that substrate bending can be achieved. Wafer curvature measurements have been measured by Dumortier for VO_2 films of 170 nm deposited on Si wafers. [59] This effect is also used for the application of VO_2 for micromechanical devices (see section 1.2.4).

Grain size: The question also rises what happens with the characteristics of the SMT when scaling the material size down to the nanometer scale. Here it is important to make a differentiation between nanometer thin films and isolated nanoparticles. The main feature of the SMT which is influenced by the grain size is the hysteresis: while for bulk VO_2 the hysteresis width is around 2 °C, in thin films and isolated nanoparticles it increases to values of the order of 10 and 60 °C respectively. [60–63] Figure 1.8 shows an example of the increased hysteresis width in VO_2 nanoparticles. [61]

Donev et al. explained the increased hysteresis width in nanoparticles by heterogeneous nucleation. [64] In practice, this means that the phase transition starts at defects. As the driving force to trigger the transition increases, for example by increasing the extent of undercooling or overheating, more defects become active. Assuming a certain defect density, it is straightforward that smaller crystallites have less defects, and initiation of the phase transition is postponed. This explains why in bulk VO_2 the hysteresis is very small, and in nanoparticles the hysteresis width increases, as in the trend observed by Lopez et al. (figure 1.8). On the other

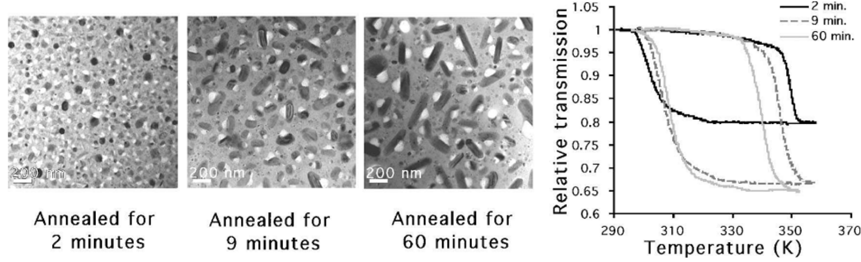

Figure 1.8. *(Left) Transmission electron micrographs (TEM) of VO_2 precipitates in SiO_2. (Right) Their transmission at a wavelength $\lambda = 1.5$ μm as a function of temperature, indicating the increased hysteresis width when nanoparticle size decreases.*[61]

hand, Suh et al. observed that for increased nanoparticle sizes the hysteresis got broader.[65] This was explained by the higher purity, and consequently lower defect concentration, of the larger particles due to longer annealing. As such, the mechanism of heterogeneous nucleation still holds.

Remark that defects are not necessarily only present within the VO_2 crystallites itself. Also defects at grain boundaries, for instance in thin films, or at the interface with the substrate, might act as nucleation spots for the phase transition. Therefore, although thin films can be considered as collections of nanoparticles, their hysteresis width is usually less pronounced compared to isolated nanoparticles. Most reports show hysteresis values of the order of 10 °C in VO_2 thin films.

Apart from the effect of particle size on hysteresis, other SMT characteristics can be influenced as well. Brassard et al. observed that thinner films are characterized by smaller grain sizes, smaller amplitudes of the electrical transition and less sharp transitions.[66] It was stated that the reduced grain size leads to an increasing density of grain boundaries, which tend to lower the resistivity of the semiconducting state, through the presence of defect levels in the gap, while decreasing the conductivity of the metallic state, by grain boundary scattering of electrons.

General shape of the SMT curve: It is important to be aware of the fact that nonuniformity complicates the shape of the hysteresis loop. Klimov et al. constructed a mathematical model which accounts for particle size distributions and nonuniform oxygen nonstoichiometries within VO_2 thin films.[60] It was assumed that each individual domain is homogeneous and is characterized by a hysteresis loop which is sharp and has well-defined transition temperatures during cooling and heating. Summation of all the elementary hysteresis loops results in the major hysteresis loop, which can show multiple transition branches in case of grain size distributions with several maxima, or can be asymmetric, for instance due to an oxygen concentration gradient. These features are illustrated in figure 1.9.

To summarize, the SMT in VO_2 can be modified using various approaches: the

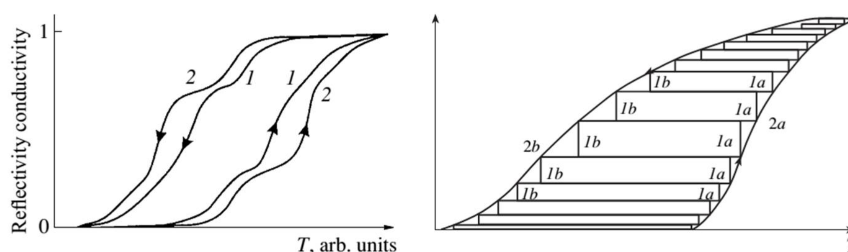

Figure 1.9. *Hysteresis loops for VO_2 thin films with complex particle size distribution (left) or nonuniform oxygen nonstoichiometries (right).*[60]

transition temperature is mostly affected by oxygen nonstoichiometry, by doping with elements like W, or by stress. The **hysteresis** can be broadened by reducing the VO_2 particle size. However, very wide hysteresis widths have only been observed in isolated nanoparticles. The **magnitude of the transition** is mainly determined by the purity and the grain size (in case of thin films). Oxygen nonstoichiometry or doping cause a drastic suppression of the transition. Finally, the **sharpness of the transition** is determined by the degree of uniformity of all these parameters.

1.2.4 Applications

In the following sections, some applications will be highlighted which make use of the SMT in VO_2. Thermochromic coatings for smart windows and electronic devices are two of the most studied application fields, and will therefore be discussed in detail.

1.2.4.1 Smart windows

Until a decade ago, thermochromic VO_2 as a coating material for smart windows had been one of the most promising applications of the SMT in VO_2. In this context, smart windows are used to control the transmittance of solar radiation as a function of temperature.[57;67–69] The principle is illustrated in figure 1.10. Below the transition temperature, most solar radiation is transmitted through the window, since VO_2 is in its semiconducting state. When heated above the transition temperature, the metallic phase will reflect a large fraction of the solar radiation. As illustrated in figure 1.3, the high transmittance of the visible spectrum is maintained, whereas the infrared light will be blocked drastically. This concept is an attractive alternative to air-conditioning systems in buildings. The typical VO_2 film thickness for this kind of application is in most reported studies around 100 nm. A critical aspect is the reduction of the transition temperature down to approximately 25 °C. This is for instance achieved by doping with W, as explained in the previous section. However, another issue is the yellowish color of VO_2 coatings,

which is not attractive for commercial applications. Alternative strategies are being developed, including VO_2-based porous structures and Mg- or F-doped VO_2 nanoparticles.[25]

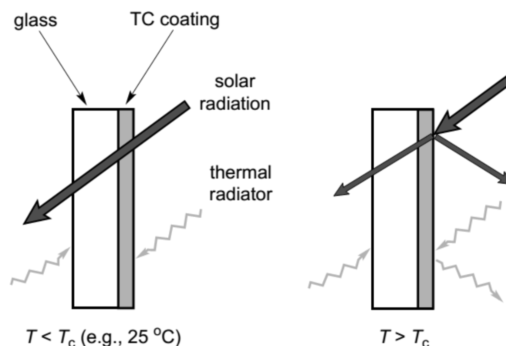

Figure 1.10. *Operation principle of VO_2 based thermochromic coatings for smart solar-control windows.*[57]

1.2.4.2 Electronic devices

The semiconductor-metal transition in VO_2, which occurs at a sub-picosecond timescale, gained significant interest for microelectronic applications, such as memories, transistors and selectors. Of course, a few minimal requirements should be met to allow for introduction of VO_2 for these kinds of applications. Some of these requirements are listed here:

- Triggering by electric field: The transition should be triggered by applying a voltage, instead of being triggered thermally. However, as will get clear in the following paragraphs, applying a voltage will in many cases indirectly cause thermal triggering by Joule-heating.

- Operating temperature: The device should have a stable operation in a certain temperature range, which is typically 0 to 70 °C for commercial electronics and -40 to 85 °C for industrial devices. For volatile memories (VM), transistors and switches, this means that the transition temperature of both the heating and cooling branch should preferably be increased to values well above 70 or 85 °C, or alternatively well below 0 or -40 °C. As was explained in section 1.2.3, this might be achieved by doping or stress, although this could negatively influence the other SMT characteristics.

- Bistable state: For nonvolatile memories (NVM), a bistable state is required. This means that at all temperatures within the operating temperature range, both states should be accessible by applying suitable voltages. This means that the hysteresis window should completely overlap the above mentioned

temperature ranges, which is so far not yet proven to be feasible. As explained in section 1.2.3, the maximum reported hysteresis width is approximately 60 °C.

- Retention time: The amount of time that a memory cell can retain its state is called the retention time. For nonvolatile memories this period of time should be at least 10 years. Radu et al. concluded from extrapolation of experimental data that the relaxation time of the SMT in thin VO_2 films, at the transition temperature of 68 °C, can easily exceed a period of 10 years.[70]
- Switch time: The time to switch between the semiconducting and metallic state should be very short for transistors, switches and volatile memories. Although the intrinsic switching mechanism of the SMT occurs at the sub-picosecond timescale, various device parameters will lead to increased switching times.

Meeting these requirements is a challenging task for material scientists and microelectronic engineers. Although alternative SMT materials (see section 1.2.5) might be more attractive for some of these requirements, VO_2 is at least an interesting case study material, allowing to investigate the basic understanding of the application of the SMT in microelectronic devices. In the following paragraphs, a few proposed device concepts will be discussed.

Two-terminal devices: During the past 15 years, several two-terminal electronic device concepts, based on the SMT in VO_2, have been proposed and investigated.[24;71–74] In many of those publications it is stated that the electrical field is the direct cause of the SMT. However, recently Radu et al. performed a detailed study on the switching mechanism in a two-terminal nano-scale device, and found evidence that the transition proceeds through Joule-heating instead of direct triggering by the applied electric field.[71] The device, shown in figure 1.11(a,b), consists of a VO_2 thin film of 50 nm thickness, and two electrodes with separation down to 100 nm. The limited spacing between the electrodes of only 100 nm, which is on the order of the VO_2 grain size, eliminates the possible formation of filaments,

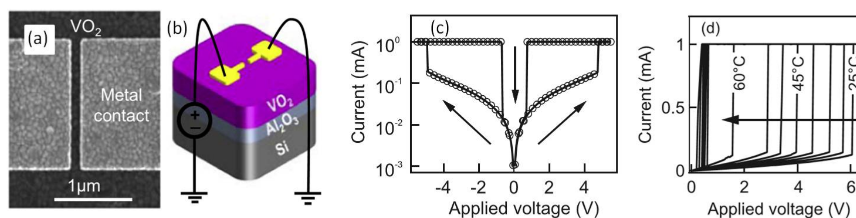

Figure 1.11. Two-terminal device based on the SMT in VO_2: (a) SEM image of the VO_2 film and electrodes, (b) 3D schematic representation of the device, (c) current-voltage characteristics showing the SMT at a threshold voltage of approximately 4.5 V (current compliance: 1 mA), and (d) temperature dependency of the threshold voltage during SMT.[71]

as has been reported by Verbruggen for micron-scale inter-electrode spacing.[75] By applying a voltage over the device, the current increases significantly once a certain voltage is crossed (figure 1.11(c)). At this threshold voltage, the SMT is triggered and the VO_2 switches from a high-resistive state (HRS) to a low-resistive state (LRS). The maximum current is limited by a compliance of 1 mA in this example. When the voltage is decreased again, the opposite switch occurs, from LRS to HRS, but at a significantly lower voltage. This phenomenon is explained by Joule-heating: at low voltages a low current flows through the high-resistive, semiconducting VO_2 film, and the dissipated power ($P_{HRS} = U^2/R_{HRS}$) is low. At the threshold voltage the dissipated power is sufficient to heat the VO_2 film above its transition temperature, causing the resistance to decrease and the current to increase. In this LRS the power ($P_{LRS} = U^2/R_{LRS}$) is much higher, such that upon decrease of the voltage, a significantly lower voltage is required to bring the device back into the HRS. Figure 1.11(d) shows how the threshold voltage is reduced by increase of the operating temperature, since at higher temperatures less Joule-heating is required for the switch.
The switching from the HRS to the LRS state can thus easily be obtained by a voltage pulse. The opposite transition can however not be triggered externally, such that cooling by the surroundings is required. Radu et al. reported switching times from HRS to LRS down to 20 ns, and 100 to 200 ns from LRS to HRS, for a device with 100 nm electrode separation and 2 μm width. Endurance testing up to 2×10^{10} cycles showed to be successful without degradation of the device, and approximately constant resistance values of the HRS and LRS with a ratio $R_{HRS}/R_{LRS} \approx 100$.

This kind of two-terminal device has potential use as switch or selector. An interesting example, proposed by Lee et al., is a VO_2 switch for Resistive Random Access Memory (RRAM) based on a NiO memory element.[74] This type of nonvolatile memory requires a switch for correct readout of each individual cell, without being disturbed by the state of the neighboring cells. The concept is illustrated in figure 1.12. As visualized in figure 1.12(b), the readout of a NiO cell in the HRS can be incorrect if it is surrounded by cells in the LRS. To circumvent this issue, each NiO memory element has a VO_2 switch. By this approach, the memory cell can only be accessed when the switch is "ON", while neighboring cells cannot influence the readout operation, since their respective switches are switched "OFF". In figure 1.12(e,f), the current-voltage characteristics are shown for both the VO_2 switch and NiO memory cell separately. The graphs show that the VO_2 switch is turned "ON" or "OFF" at the respective voltages of approximately 0.7 and 0.2 V, whereas the NiO memory element is switched from HRS to LRS at 1.3 V and from LRS to HRS at 0.5 V. The current-voltage characteristic of the combined stack is shown in figure 1.12(g). By applying a voltage corresponding to V_{SET} or V_{RESET}, the LRS or HRS state can be written to the cell, while a voltage in range (b) allows for readout of the cells state. During accessing of one cell, the voltage over all other cells should be limited to range (a), such that the VO_2 switch is "OFF" for those cells.

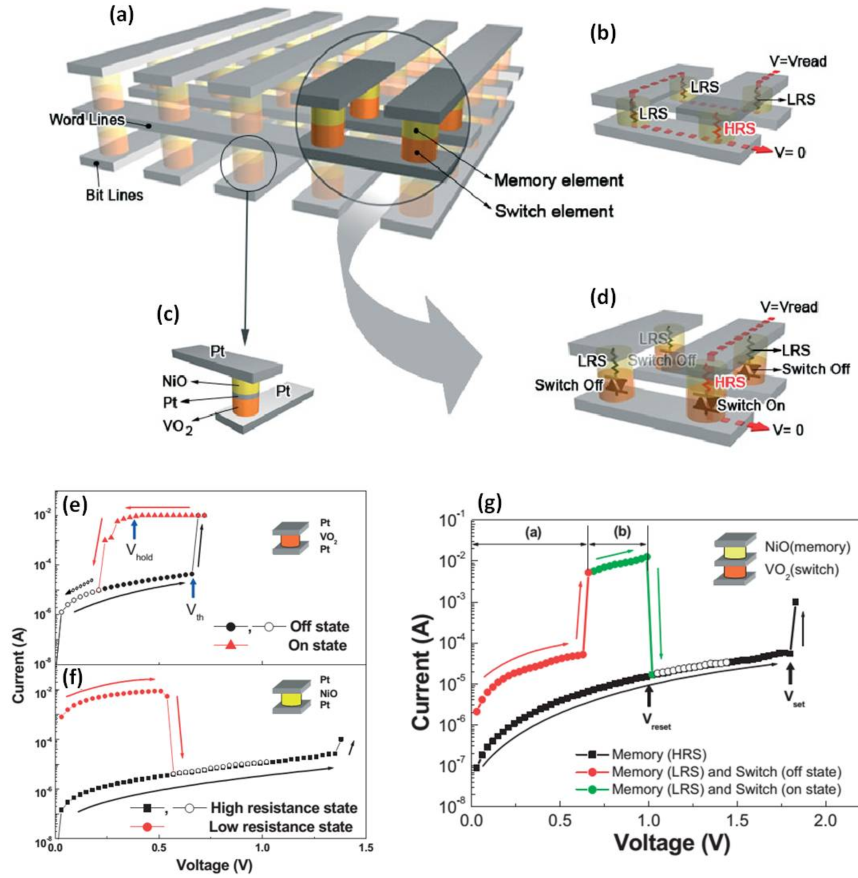

Figure 1.12. *Non-volatile memory based on NiO memory cells combined with VO_2 switches: (a-d) schematic representation of the memory device and its operation principle, (e-f) current-voltage measurements of individual VO_2 and NiO cells, indicating their respective threshold voltage to switch between "ON" and "OFF" or HRS and LRS and vice versa, (g) current-voltage characteristic of the combined stack of a VO_2 and NiO cell, illustrating the function of the VO_2 switch.*[74]

Three-terminal devices: A three-terminal field-effect transistor (FET) operates by altering the resistance of a gate channel, which connects the source and drain contacts, by applying a voltage on the gate electrode. In this way, a low resistance of the channel results in the "ON" state, whereas the high resistance corresponds to the "OFF" state. VO_2 has been considered as a good candidate for replacing the doped Si gate material into currently used FET devices.[72;73;76;77] An example of such a VO_2 based FET, often referred to as Mott-FET, is illustrated in figure 1.13.[73] A schematic drawing is shown in the inset of the left panel. A WSi gate contact was covered with a layer of SiO_2. Two Au/Cr electrodes served as source

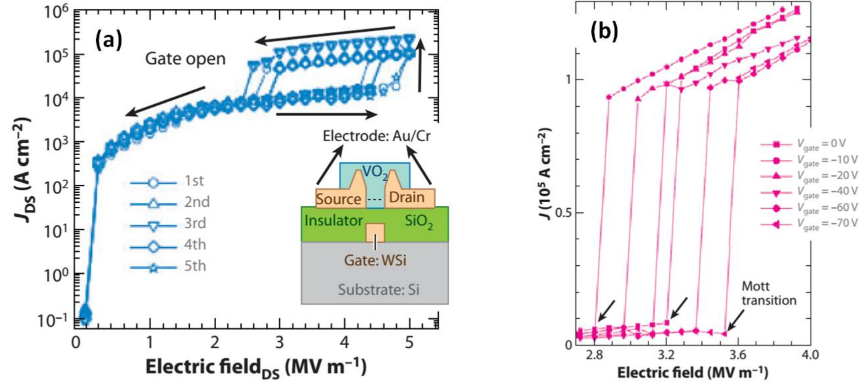

Figure 1.13. *Illustration of a VO_2 based three-terminal device proposed by Kim et al.*[73]

and drain contacts, and a 90 nm VO_2 film was deposited in between source and drain. The graph in the left panel shows, for an open gate, how during increase of the electric field over the source and drain, the current is characterized by a sudden increase around 4 to 5 MV/m, while upon decreasing the electric field, it drops quickly near 2.5 to 3 MV/m. This observation can be considered as similar to the semiconductor-metal transition in two-terminal devices, as explained in the previous paragraph. The right panel of figure 1.13 shows how in case of a negative voltage of -10 V on the gate electrode, the threshold electric field decreases for triggering the SMT, and is explained by the injection of holes. This illustrates how the field-effect can be exploited for fabrication of VO_2 based transistors. However, further increase of the negative gate voltage leads again to an increase of the SMT switching voltage, which was explained by a reduced conductivity of the channel due to a too high hole carrier density.

Another device is shown in figure 1.14.[76] Here, it was observed how applying

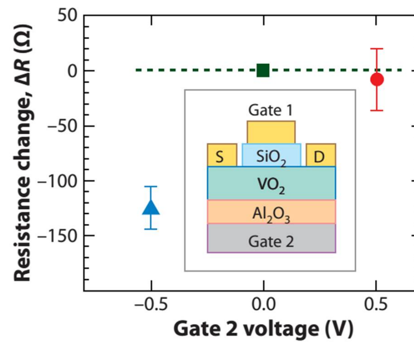

Figure 1.14. *Illustration of a VO_2 based three-terminal device proposed by Ruzmetov et al.*[76]

a negative voltage on the bottom gate decreased the resistance of the VO_2 channel with respect to the open gate value, while a positive voltage on the bottom gate did not have any effect.

Although these examples give some indication of possible VO_2 based FET devices, the success is rather limited, since the fabrication of high-quality thin VO_2 films in combination with low-leakage gate electrodes is essential. Recently, Martens et al. were able to construct VO_2 field effect transistor structures with VO_2 thicknesses between 3 and 10 nm, and a high-k HfO_2 gate oxide. A direct field-induced SMT was however not observed.[79] In an alternative approach, ionic liquids have been applied to prove bulk-like SMT switching by electric fields.[80] However, in another report it was shown that these ionic liquids cause formation of oxygen vacancies in the VO_2 films by electrochemical effects, ultimately leading to reduction towards metallic lower vanadium oxide phases.[81] So far, a well-functioning Mott-FET using VO_2 has not been achieved yet.

Recently, Shukla et al. presented a novel approach for using VO_2 in three-terminal FET devices. These authors connected a VO_2 element in series with the source of a conventional MOSFET, and called it a hyper-FET.[78] The device concept, as well as the operation principle, compared with the MOSFET, is illustrated in figure 1.15. For a certain source-drain voltage, the conventional MOSFET

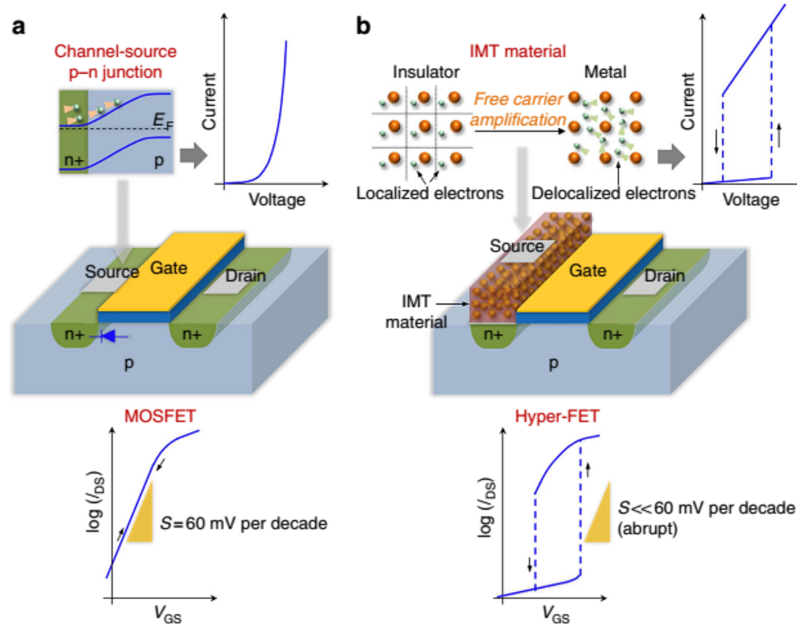

Figure 1.15. *Comparison of the architecture, and operation principle of a conventional MOSFET (a) with a novel VO_2 based hyper-FET (b).*[78]

shows an exponential increase of the current through the channel as a function of the applied gate voltage. In contrast, a VO_2 element on top of the source enables to maintain low currents through the channel, until the gate voltage reaches a certain threshold voltage, at which the current increases very steeply. The main advantage that is claimed, is the low OFF-state leakage current, relevant for low-power circuit applications. However, optimization of this kind of device would be challenging, and the additional VO_2 element might cause the footprint of the transistor to increase significantly with respect to the conventional MOSFET.

1.2.4.3 Other applications

The semiconductor-metal transition in VO_2 has many more potential applications, in a variety of different fields. The list below gives a brief, non-exhaustive overview of applications and devices which are based on the SMT in VO_2. These and many more are reported in review papers and books.[24;25;41]

- Nakano et al. reported on an **infrared-sensitive electrochromic device** based on VO_2, which enables switching the transmittance of infrared light through the device, without cutting of the view in visible light.[29]
- Briggs et al. developed a compact silicon **photonic waveguide modulator** based on the phase transition in VO_2.[82]
- Jostmeier et al. developed optically imprinted reconfigurable **photonic elements** in a VO_2 nanocomposite.[63]
- Shukla et al. were able to develop a device for inducing **synchronized charge oscillations** using a negative feedback mechanism in combination with the SMT in VO_2.[83]
- Kats et al. created a temperature-controlled **tunable absorber** based on the SMT in a VO_2 thin film.[84]
- **Microactuators** based on the structural phase transition in VO_2 have been developed by Cao et al. and Liu et al.[55;56]

1.2.5 Alternative SMT/MIT material systems

Vanadium oxide Magnéli phases: Apart from VO_2, many other vanadium oxides show SMT/MIT characteristics. These include VO, V_2O_3 and most of the Magnéli phases.[23;38;67;85–87] Figure 1.16 shows the resistivity versus temperature curves for the Magnéli phases, including VO_2 and V_2O_3. There is only one phase with a higher transition temperature than VO_2, i.e. V_3O_5, which shows a resistivity drop of 2 orders of magnitude near 155 °C. V_7O_{13} is the only Magnéli phase which does not show a transition and is metallic at all temperatures. V_2O_3 has the highest resistance switching of 7 orders of magnitude near -108 °C. This is similar to VO (not shown), which has a transition temperature around -147 °C.[23]

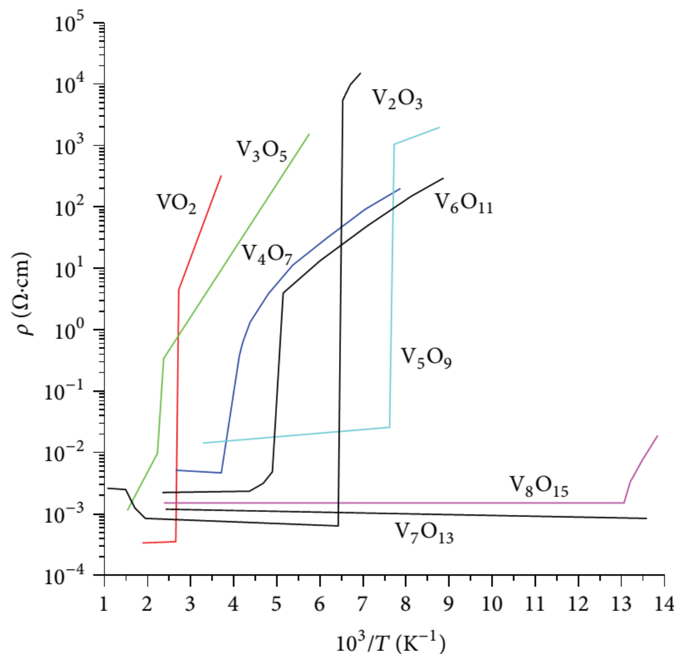

Figure 1.16. *Electrical resistivity across the SMT in the vanadium oxide Magnéli phases.*[38]

Remark that a SMT has been reported for V_2O_5 as well,[88] which is typically known as a semiconductor with a bandgap of 2.2 eV. This transition, which was observed at 280 °C, is however attributed to the loss of oxygen and a reduction to mixtures of lower oxides and can thus not be considered as a true, reversible SMT.[38]

Other examples: There exist many other transition-metal oxides which are characterized by a SMT/MIT. Figure 1.17 includes some of the most studied materials, such as Ti_2O_3, Ti_3O_5, NbO_2 and Fe_3O_4. Note that, although some titanium oxide phases show interestingly high transition temperatures, these phases are highly unstable and difficult to synthesize due to preferential oxidation towards TiO_2.[23;24;37;47] Another class of SMT materials includes the rare-earth nickelates. Examples are $PrNiO_3$, $NdNiO_3$ and $SmNiO_3$, as illustrated in figure 1.17.[24;37;47] More recently, some metal-sulfides gained interest for their SMT characteristics. FeS for example shows a transition at the high temperature of 147 °C and thin films of this material have been prepared and characterized by Fu.[89] Hollander et al. fabricated an electronic device based on TaS_2, which shows a temperature induced transition near -90 °C.[90]

The SMT materials mentioned here are only a small fraction of those which have been reported.[37;47] The magnitude of transition differs significantly from one

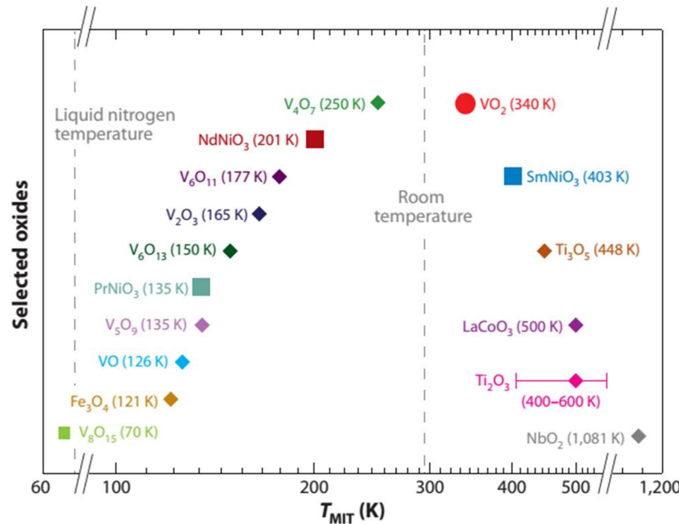

Figure 1.17. *Overview of the transition temperature of some transition metal oxides and rare-earth nickelates.*[24]

material to another. An interesting remark is that the transitions in these materials are driven by different mechanisms. The transition in V_2O_3 is pure Mott-Hubbard, whereas the SMT in $K_{0.3}MoO_3$ is an example of a pure Peierls mechanism. Other mechanisms include the Anderson and Wigner or Verwey transitions, but these are outside the scope of this work.[37] Both from theoretical and practical view, VO_2 is however one of the most intriguing SMT materials, due to its dual nature and near-room temperature transition with high resistive switching ratio.

1.3 Vanadium nitrides

The vanadium-nitrogen phase diagram: Compared to vanadium oxides, the vanadium-nitrogen system is less complicated. Only three vanadium nitride phases are known: β-V_2N, δ-$V_{32}N_{26}$ and δ-VN.[91] In chapter 4 it will be shown that δ-VN is the most frequently obtained phase, and some reported methods for thin film deposition of VN will be briefly discussed.

Properties and applications of vanadium nitride: In general, refractory metal nitrides such as TiN, TaN_x, NbN and ZrN are characterized by a high melting point (>2000 °C), excellent high temperature stability, hardness and corrosion resistance. Therefore these are often used for wear-resistant coatings and cutting tools. Many transition metal nitrides exhibit superconducting properties, NbN having the highest transition temperature of $\approx$ 18 K. In microelectronics, TiN and TaN have been investigated for use as diffusion barriers in Ohmic contacts, low barrier

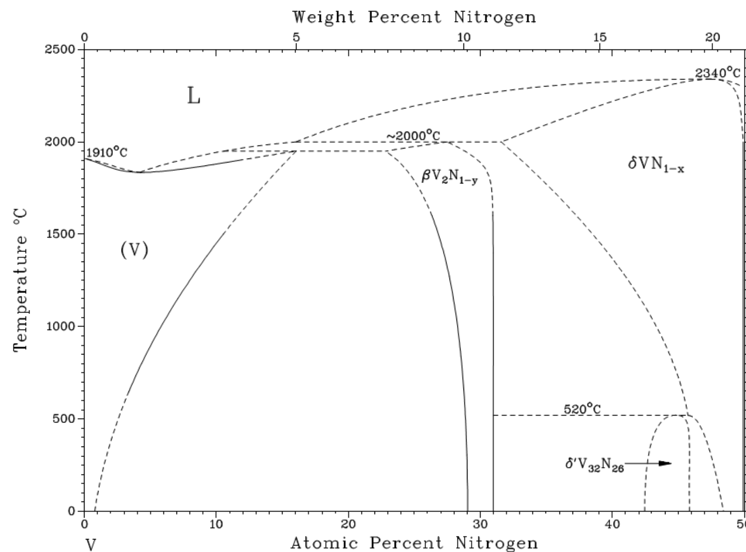

Figure 1.18. *The vanadium-nitrogen phase diagram.* [91]

Schottky diodes and gate electrodes in MOS transistors. [92]

More specific, VN shows similar properties to most transition metal nitrides, but some other exceptional features make VN attractive for other applications as well. A summary of some (potential) applications is listed here:

- Copper diffusion barriers: VN, as well as other transition metal nitrides have been investigated as barrier layers to prevent copper diffusion into silicon chips. This is required since the replacement of aluminum by copper for interconnects in microelectronic devices. [93;94] In the next section, this topic is discussed in more detail. In chapter 4, thin layers of VN deposited by plasma-enhanced ALD will be evaluated for this purpose.

- Wear resistant coatings: VN is characterized by a high hardness, which allows to use it as wear-resistant coating material. For this purpose, coatings are applied by methods with high deposition rates, such as magnetron sputtering and chemical vapor deposition. [95;96]

- High-temperature self-lubricant coatings: dry sliding of wear-resistant coatings causes high mechanical and thermal loads. In the case of VN, formation of Magnéli phases occurs at temperatures above 700 °C due to oxidation. Melting of these phases results in a remarkable drop of the friction coefficient, consequently leading to a self-lubricant coating effect. [97;98]

- Superconductors: VN is a superconducting material below a critical temperature of approximately 9 K. [99]

- Supercapacitors: more recently, nanocrystalline VN has shown excellent characteristics for supercapacitor fabrication. While the high electrical conductivity of VN is desired for the supercapacitor operation, the numerous vanadium oxides at the surface result in very high specific capacitance.[100;101]

- Anode material for Li-ion batteries: VN thin films, prepared by reactive magnetron sputtering, have been evaluated as anode material for Li-ion batteries. A high reversible capacity of 800 mAh/g for 50 cycles was observed in a galvanostatic cycling test.[102]

- Catalysts: VN has been synthesized and evaluated for several catalyst reactions, including n-Butane dehydrogenation and decomposition of ammonia at temperatures above 400 °C.[103–105]

1.4 Copper diffusion barriers

Since 1997, aluminum has been replaced by copper for interconnects in microprocessors.[93] Copper allowed for making chips faster, smaller and less expensive. One drawback was the need for a barrier metal which completely surrounds the copper wires, since copper easily diffuses into silicon, degrading the properties of the components. Figure 1.19 shows a cross-section of the hierarchical scaling of a microprocessor unit (MPU). According to the International Technology Roadmap

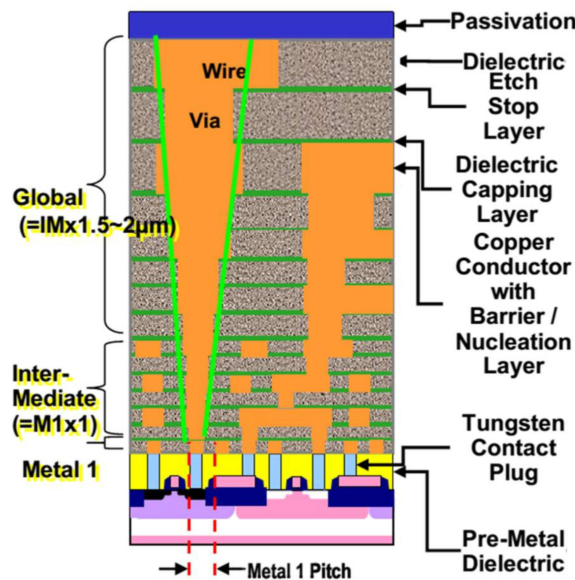

Figure 1.19. Cross-section of the hierarchical scaling of a microprocessor unit (MPU).[106]

for Semiconductors (ITRS), the metal pitch, i.e. the minimal center-to-center distance between two copper wires, should reduce from 64 nm in 2015 down to 32 nm in 2021.[106] Meanwhile, the barrier layer thickness should reduce from 1.9 nm in 2015 to 1.0 nm in 2021.

Metal-nitrides are known as excellent barriers for preventing copper diffusion into silicon. TaN_x and TiN have been investigated most intensively for this purpose. Also for the case of VN, reports have been published on its use as copper diffusion barrier, however, only for reactively sputtered thin films.[107;108] VN barrier layers of 10 nm have shown high temperature stability up to 600 °C for 1 hour of annealing. The task of developing suitable low-resistive barrier layers which effectively block copper diffusion for layer thicknesses below 2 nm is one of the major challenges in semiconductor manufacturing. In addition, the processing temperature for copper interconnects in the back end of line (BEOL) is limited to approximately 400 to 500 °C, and the barrier layers should be conformal at these dimensions, particularly in the presence of 2 nm surface roughness likely present from patterning line edge roughness and low-k interlevel dielectric (ILD) porosity.

1.5 Goals and outline of this thesis

The subject of this thesis is the synthesis of thin films of VO_2 and VN, two materials with high technological value, as explained in the previous sections. Many techniques have already been reported for their synthesis, including reactive sputtering and chemical vapor deposition. In this work, we will focus on two different approaches. The first one is the synthesis by gas-solid reactions of oxygen or nitrogen with sputtered V thin films, which allows for fast and cheap deposition, but is limited to planar substrates. The second method concerns low temperature growth by atomic layer deposition, a technique suited for covering 3-dimensional objects conformally with nanometer thin films at the highest available precision. After synthesis, the thin films are characterized, with a strong focus on the semiconductor-metal transition in VO_2.

In the case of VO_2, a critical aspect is achieving the V^{4+} valence. As will be discussed in chapter 3, many methods rely on single-step synthesis of this material, which requires many different parameters to be accurately controlled simultaneously, making it difficult to achieve similar results in different deposition systems. In contrast, the two-step approaches that will be studied in this work, are characterized by a more straightforward optimization of process conditions, since deposition and post-deposition annealing parameters are separated from each other. The depositions include magnetron sputtering of metallic V and atomic layer deposition of VO_2. Crystalline VO_2 will be achieved by post-deposition annealing at well-controlled conditions for oxygen partial pressure and temperature. The study of crystalline phase formation will be performed by means of a dedicated in-situ X-ray diffraction (XRD) system, which was developed in the course of this thesis. The semiconductor-metal transition in the synthesized VO_2 thin films will

be investigated by three complementary techniques, which allow to reveal both the structural, electronic and optical changes. These techniques are temperature-dependent XRD, sheet resistance measurements and spectroscopic ellipsometry. Depending on the potential application, different thicknesses are required, ranging from several tens or hundreds of nanometers for thermochromic coatings for smart windows, down to only around 10 nanometer for devices in microelectronics. It will be investigated which deposition techniques are suitable for achieving these requirements, and what are the lower thickness limits of those techniques.

As already stated in the previous sections, tuning of the phase transition properties may be critical for some applications, e.g. lowering the transition temperature down to approximately 25 °C for smart windows, or increasing the transition temperature to values well above 85 °C for microelectronic devices. Some experimental work, based on doping VO_2 with elements as W, Al and Ti will be discussed briefly. On the other hand, modification of the hysteresis width, which may be achieved by the synthesis of nanoparticles, will be investigated as well. A hysteresis width that covers a range from below 0 °C to above 85 °C might be suitable for bistable operation in microelectronic devices such as non-volatile memories.

Where applicable, results on V_2O_3 thin film synthesis and the observation of the semiconductor-metal transition in these films, will be briefly discussed as well.

At first sight, synthesis of VN thin films requires less optimization, since it is the most favored vanadium nitride phase. However, since V is extremely prone to oxidation, the synthesis of oxygen-free VN films is challenging. The same methods as for the deposition of VO_2 thin films will be studied, i.e. high-temperature nitridation of sputtered V films, and low-temperature atomic layer deposition. Specifically for the application of VN thin films as copper diffusion barriers, processes are favored with a maximum process temperature of 400 to 500 °C, which allow for ultrathin conformal film growth, even below 2 nm. In addition, a low resistivity of these films will be required, and it will be investigated if the lowest reported values between 40 and 80 $\mu\Omega \cdot \mathrm{cm}$ can be obtained using the two methods developed during this research. Although a detailed investigation of the potential use of VN thin films as copper diffusion barriers is outside the scope of this work, as a proof of concept, in-situ XRD will be used for a first evaluation.

References

[1] H. A. Wriedt, *Bulletin of Alloy Phase Diagrams* **10**(3), 271–277 (1989).

[2] Y.-B. Kang, *J. Eur. Ceram. Soc.* **32**(12), 3187–3198 (2012).

[3] N. Bahlawane and D. Lenoble, *Chem. Vapor Depos.* **20**(7-8-9), 299–311 (2014).

[4] J. Haemers, *Bull. Soc. Chim. Belges* **79**(7-8), 473–477 (1970).

[5] J. Haemers, E. Baetens, and J. Vennik, *Phys. Stat. Sol. (a)* **20**(1), 381–386 (1973).

[6] L. Fiermans, P. Clauws, W. Lambrecht, L. Vandenbroucke, and J. Vennik, *Phys. Stat. Sol. (a)* **59**(2), 485–504 (1980).

[7] H. Poelman, H. Tomaszewski, D. Poelman, L. Fiermans, R. De Gryse, M.-F. Reyniers, and G. B. Marin, *Surf. Interface Anal.* **34**(1), 724727 (2002).

[8] G. Silversmit, D. Depla, H. Poelman, G. B. Marin, and R. De Gryse, *J. Electron Spectrosc.* **135**(2-3), 167–175 (2004).

[9] M. Olea, I. Sack, V. Balcaen, G. Marin, H. Poelman, K. Eufinger, D. Poelman, R. De Gryse, J. Paul, B. Sels, and et al., *Appl. Catal. A - Gen.* **318**, 37–44 (2007).

[10] H. Poelman, K. Eufinger, D. Depla, D. Poelman, R. De Gryse, B. Sels, and G. Marin, *Appl. Catal. A - Gen.* **325**(2), 213–219 (2007).

[11] H. Poelman, B. Sels, M. Olea, K. Eufinger, J. Paul, B. Moens, I. Sack, V. Balcaen, F. Bertinchamps, and E. Gaigneaux, *J. Catal.* **245**(1), 156–172 (2007).

[12] J. Keränen, A. Auroux, and L. Niinistö, *Appl. Catal. A* **228**, 213–225 (2002).

[13] A. Gervasini, P. Carniti, J. Keränen, L. Niinistö, and A. Auroux, *Catal. Today* **96**(4), 187–194 (2004).

[14] www.wikipedia.org.

[15] M. S. Whittingham, *Chem. Rev.* **104**(10), 4271–4302 (2004).

[16] S. Beke, *Thin Solid Films* **519**(6), 1761–1771 (2011).

[17] J. C. Badot, S. Ribes, E. B. Yousfi, V. Vivier, J. P. Pereira-Ramos, N. Baffier, and D. Lincot, *Electrochem. Solid St.* **3**(10), 485–488 (2000).

[18] M. M. Rahman, J.-Z. Wang, N. H. Idris, Z. Chen, and H. Liu, *Electrochim. Acta* **56**(2), 693–699 (2010).

[19] N. Ganganagappa and A. Siddaramanna, *Mater. Charact.* **68**, 58–62 (2012).

[20] K. Geryl, *Atomic layer deposition of vanadium oxides for lithium-ion batteries*, Master's thesis, Ghent University, (2014).

[21] M. Skyllas-Kazacos, M. Rychick, and R. Robins, (1988), US Patent 4,786,567.

[22] C. Fabjan, J. Garche, B. Harrer, L. Jrissen, C. Kolbeck, F. Philippi, G. Tomazic, and F. Wagner, *Electrochim. Acta* **47**(5), 825–831 (2001).

[23] F. J. Morin, *Phys. Rev. Lett.* **3**(1), 34–36 (1959).

[24] Z. Yang, C. Ko, and S. Ramanathan, *Ann. Rev. Mater. Res.* **41**(1), 337–367 (2011).

[25] M. Soltani and A. B. Kaye, *Properties and Applications of Thermochromic*

Vanadium Dioxide Smart Coatings, 461–490, Elsevier Inc. (2015).
[26] L. A. Ladd and W. Paul, *Solid State Commun.* **7**, 425–428 (1969).
[27] Y. Shigesato, M. Enomoto, and H. Odaka, *Jp. J. Appl. Phys.* **39**(10R), 6016 (2000).
[28] H. Kakiuchida, P. Jin, S. Nakao, and M. Tazawa, *Jpn. J. Appl. Phys.* **46**(5), L113 (2007).
[29] M. Nakano, K. Shibuya, N. Ogawa, T. Hatano, M. Kawasaki, Y. Iwasa, and Y. Tokura, *Appl. Phys. Lett.* **103**(15), 153503 (2013).
[30] J. B. Goodenough, *J. Solid State Chem.* **3**, 490–500 (1971).
[31] V. Eyert, *Ann. Phys.* **514**, 650–704 (2004).
[32] K. D. Rogers, *Powder Diffr.* **8**, 240 (1993).
[33] A. Cavalleri, T. Dekorsy, H. H. W. Chong, J. C. Kieffer, and R. W. Schoenlein, *Phys. Rev. B* **70**(16), 161102 (2004).
[34] J. H. de Boer and E. J. W. Verwey, *P. Phys. Soc.* **49**(4S), 59 (1937).
[35] E. Wigner, *T. Farad. Soc.* **34**, 678–685 (1938).
[36] N. F. Mott, *P. Phys. Soc.* **62**(7), 416 (1949).
[37] N. F. Mott, *Metal-Insulator Transitions*, Taylor and Francis, (1990).
[38] A. L. Pergament, G. B. Stefanovich, N. A. Kuldin, and A. A. Velichko, *ISRN Condens. Matter Phys.* **2013**, 1–6 (2013).
[39] R. E. Peierls, *Quantum theory of solids*, Clarendon Press, (1964).
[40] S. Shin, S. Suga, M. Taniguchi, M. Fujisawa, H. Kanzaki, A. Fujimori, H. Daimon, Y. Ueda, K. Kosuge, and S. Kachi, *Phys. Rev. B* **41**(8), 4993 (1990).
[41] S. Ramanathan, *Thin Film Metal-Oxides*, Springer US, (2010).
[42] R. M. Wentzcovitch, W. W. Schulz, and P. B. Allen, *Phys. Rev. Lett.* **72**(21), 3389 (1994).
[43] T. Rice, H. Launois, and J. Pouget, *Phys. Rev. Lett.* **73**(22), 3042 (1994).
[44] H.-T. Kim, Y. W. Lee, B.-J. Kim, B.-G. Chae, S. J. Yun, K.-Y. Kang, K.-J. Han, K.-J. Yee, and Y.-S. Lim, *Phys. Rev. Lett.* **97**(26), 266401 (2006).
[45] J. M. Tomczak, F. Aryasetiawan, and S. Biermann, *Phys. Rev. B* **78**(11) (2008).
[46] V. Eyert, *Phys. Rev. Lett.* **107**(1), 016401 (2011).
[47] M. Imada, A. Fujimori, and Y. Tokura, *Rev. Mod. Phys.* **70**(4), 1039 (1998).
[48] C. H. Griffiths and H. K. Eastwood, *J. Appl. Phys.* **45**(5), 2201–2206 (1974).
[49] C. B. Greenberg, *Thin Solid Films* **110**(1), 73–82 (1983).
[50] J. C. Rakotoniaina, R. Mokrani-Tamellin, J. R. Gavarri, G. Vacquier, A. Casalot, and G. Calvarin, *J. Solid State Chem.* **103**, 81–94 (1993).
[51] P. Jin, S. Nakao, and S. Tanemura, *Thin Solid Films* **324**, 151–158 (1998).
[52] M. Soltani, M. Chaker, E. Haddad, R. V. Kruzelecky, and J. Margot, *Appl. Phys. Lett.* **85**(11), 1958–1960 (2004).
[53] J. Wei, H. Ji, W. Guo, A. H. Nevidomskyy, and D. Natelson, *Nat. Nanotechnol.* **7**(6), 357–362 (2012).
[54] Y. Muraoka and Z. Hiroi, *Appl. Phys. Lett.* **80**(4), 583 (2002).
[55] J. Cao, W. Fan, Q. Zhou, E. Sheu, A. Liu, C. Barrett, and J. Wu, *J. Appl. Phys.* **108**(8), 083538 (2010).

[56] K. Liu, C. Cheng, Z. Cheng, K. Wang, R. Ramesh, and J. Wu, *Nano Lett.* **12**(12), 63026308 (2012).
[57] I. P. Parkin and T. D. Manning, *J. Chem. Educ.* **83**(3), 393 (2006).
[58] G. Guzman, F. Beteille, R. Morineau, and J. Livage, *J. Mater. Chem.* **6**(3), 505–506 (1996).
[59] J. Dumortier, *Groei en karakterisatie van gedoteerde vanadium dioxide lagen voor de nano-elektronica*, Master's thesis, Ghent University, (2012).
[60] V. A. Klimov, I. O. Timofeeva, S. D. Khanin, E. B. Shadrin, A. V. Ilinskii, and F. Silva-Andrade, *Tech. Phys.* **47**(9), 1134–1139 (2002).
[61] R. Lopez, L. A. Boatner, T. E. Haynes, L. C. Feldman, and R. F. Haglund, *J. Appl. Phys.* **92**(7), 4031 (2002).
[62] J. Wei, Z. Wang, W. Chen, and D. H. Cobden, *Nat. Nanotechnol.* **4**(7), 420–424 (2009).
[63] T. Jostmeier, J. Zimmer, H. Karl, H. J. Krenner, and M. Betz, *Appl. Phys. Lett.* **105**(7), 071107 (2014).
[64] E. U. Donev, *Metal-semiconductor transition in nanoscale VO_2 thin films, subwavelength holes and nanoparticles*, PhD thesis, Vanderbilt University, (2008).
[65] J. Y. Suh, R. Lopez, L. C. Feldman, and R. F. Haglund Jr, *J. Appl. Phys.* **96**(2), 1209–1213 (2004).
[66] D. Brassard, S. Fourmaux, M. Jean-Jacques, J. C. Kieffer, and M. A. El Khakani, *Appl. Phys. Lett.* **87**(5), 051910 (2005).
[67] S. M. Babulanam, T. S. Eriksson, G. A. Niklasson, and C. G. Granqvist, *Sol. Energ. Mater.* **16**, 347–363 (1987).
[68] C. G. Granqvist, *Thin Solid Films* **193**(194), 730–741 (1990).
[69] T. D. Manning, I. P. Parkin, R. J. H. Clark, D. Sheel, M. E. Pemble, and D. Vernadou, *J. Mater. Chem.* **12**(10), 2936–2939 (2002).
[70] I. P. Radu, K. Martens, S. Mertens, C. Adelmann, X. Shi, H. Tielens, M. Schaekers, G. Pourtois, S. Van Elshocht, S. De Gendt, M. Heyns, and J. A. Kittl, *ECS Trans.* , 233–243 (2011).
[71] I. P. Radu, B. Govoreanu, S. Mertens, X. Shi, M. Cantoro, M. Schaekers, M. Jurczak, S. De Gendt, A. Stesmans, J. A. Kittl, M. Heyns, and K. Martens, *Nanotechnology* **26**(16), 165202 (2015).
[72] G. Stefanovich, A. Pergament, and D. Stefanovich, *J. Phys. Condens. Matter* **12**(41), 8837 (2000).
[73] H.-T. Kim, B.-G. Chae, D.-H. Youn, S.-L. Maeng, G. Kim, K.-Y. Kang, and Y.-S. Lim, *New J. Phys.* **6**, 52 (2004).
[74] M.-J. Lee, Y. Park, D.-S. Suh, E.-H. Lee, S. Seo, D.-C. Kim, R. Jung, B.-S. Kang, S.-E. Ahn, C. B. Lee, D. H. Seo, Y.-K. Cha, I.-K. Yoo, J.-S. Kim, and B. H. Park, *Adv. Mater.* **19**(22), 3919–3923 (2007).
[75] J. Verbruggen, *Tailored functional oxides for nanoelectronics*, Master's thesis, Ghent University, (2011).
[76] D. Ruzmetov, G. Gopalakrishnan, C. Ko, V. Narayanamurti, and S. Ramanathan, *J. Appl. Phys.* **107**(11), 114516 (2010).
[77] S. Sengupta, K. Wang, K. Liu, A. K. Bhat, S. Dhara, J. Wu, and M. M.

Deshmukh, *Appl. Phys. Lett.* **99**(6), 062114 (2011).
[78] N. Shukla, A. V. Thathachary, A. Agrawal, H. Paik, A. Aziz, D. G. Schlom, S. K. Gupta, R. Engel-Herbert, and S. Datta, *Nat. Commun.* **6**, 7812 (2015).
[79] K. Martens, J. W. Jeong, N. Aetukuri, C. Rettner, N. Shukla, E. Freeman, D. N. Esfahani, F. M. Peeters, T. Topuria, P. M. Rice, A. Volodin, B. Douhard, W. Vandervorst, M. G. Samant, S. Datta, and S. S. P. Parkin, *Phys. Rev. Lett.* **115**(19), 196401 (2015).
[80] M. Nakano, K. Shibuya, D. Okuyama, T. Hatano, S. Ono, M. Kawasaki, Y. Iwasa, and Y. Tokura, *Nature* **487**(7408), 459–462 (2012).
[81] J. Jeong, N. Aetukuri, T. Graf, T. D. Schladt, M. G. Samant, and S. S. Parkin, *Science* **339**(6126), 1402–1405 (2013).
[82] R. M. Briggs, I. M. Pryce, and H. A. Atwater, *Opt. Express* **18**(11), 11192 (2010).
[83] N. Shukla, A. Parihar, E. Freeman, H. Paik, G. Stone, V. Narayanan, H. Wen, Z. Cai, V. Gopalan, R. Engel-Herbert, and et al., *Sci. Rep.* **4** (2014).
[84] M. A. Kats, D. Sharma, J. Lin, P. Genevet, R. Blanchard, Z. Yang, M. M. Qazilbash, D. N. Basov, S. Ramanathan, and F. Capasso, *Appl. Phys. Lett.* **101**(22), 221101 (2012).
[85] W. Brückner, E. Wieser, W. Moldenhauer, and W. Reichelt, *Phys. Status Solidi A* **44**(1), K95–K98 (1977).
[86] U. Schwingenschlögl and V. Eyert, *Ann. Phys.* **13**(9), 475–510 (2004).
[87] A. Perucchi, L. Baldassarre, P. Postorino, and S. Lupi, *J. Phys. Condens. Matter* **21**(32), 323202 (2009).
[88] M. Kang, I. Kim, S. W. Kim, J.-W. Ryu, and H. Y. Park, *Appl. Phys. Lett.* **98**(13), 131907 (2011).
[89] G. Fu, *Metal-semiconductor transition materials. FeS and VO_2 thin films by RF reactive sputtering*, PhD thesis, (2007).
[90] M. J. Hollander, Y. Liu, W.-J. Lu, L.-J. Li, Y.-P. Sun, J. A. Robinson, and S. Datta, *Nano Lett.* **15**(3), 1861–1866 (2015).
[91] O. N. Carlson, J. F. Smith, and R. H. Nafziger, *Metall. Mater. Trans. A* **17**(10), 1647–1656 (1986).
[92] M. Wittmer, *J. Vac. Sci. Technol. A* **3**(4), 1797–1803 (1985).
[93] http://www-03.ibm.com/ibm/history/ibm100/us/en/icons/copperchip/, Accessed: 2015-11-15.
[94] H. Kim, *J. Vac. Sci. Technol. B* **21**(6), 2231 (2003).
[95] X. Chu, S. A. Barnett, M. S. Wong, and W. D. Sproul, *J. Vac. Sci. Technol. A* **14**(6), 3124–3129 (1996).
[96] I. P. Parkin and G. S. Elwin, *J. Mater. Chem.* **11**(12), 3120–3124 (2001).
[97] G. Gassner, P. H. Mayrhofer, K. Kutschej, C. Mitterer, and M. Kathrein, *Tribol. Lett.* **17**(4), 751–756 (2004).
[98] N. Fateh, G. Fontalvo, G. Gassner, and C. Mitterer, *Wear* **262**(9-10), 1152–1158 (2007).
[99] J. Zasadzinski, R. Vaglio, G. Rubino, K. E. Gray, and M. Russo, *Phys. Rev. B* **32**(5), 2929 (1985).
[100] D. Choi, G. E. Blomgren, and P. N. Kumta, *Adv. Mater.* **18**(9), 1178–1182

(2006).
[101] L. Zhang, C. M. B. Holt, E. J. Luber, B. C. Olsen, H. Wang, M. Danaie, X. Cui, X. Tan, V. W. Lui, W. P. Kalisvaart, and D. Mitlin, *J. Phys. Chem. C* **115**(49), 24381–24393 (2011).
[102] Q. Sun and Z.-W. Fu, *Electrochim. Acta* **54**(2), 403–409 (2008).
[103] H. Kwon, S. Choi, and L. T. Thompson, *J. Catal.* **184**(1), 236–246 (1999).
[104] W. J. McGill and F. Sebba, *J. Catal.* **2**(2), 104–108 (1963).
[105] S. T. Oyama, *J. Catal.* **133**(2), 358–369 (1992).
[106] www.itrs.net, Accessed: 2016-03-15.
[107] M. B. Takeyama, T. Itoi, K. Satoh, M. Sakagami, and A. Noya, *J. Vac. Sci. Technol. B* **22**(5), 2542 (2004).
[108] X.-P. Qu, M. Zhou, T. Chen, Q. Xie, G.-P. Ru, and B.-Z. Li, *Microelectronic Eng.* **83**(2), 236240 (2006).

2
Experimental

This chapter covers the experimental aspects of this research. First the thin film deposition techniques, i.e. magnetron sputtering and atomic layer deposition, are discussed in section 2.1. Some thin film characterization techniques are discussed in section 2.2. In section 2.3 some theoretical and practical aspects are explained concerning gas-solid reactions. Where applicable, reference will be made to the vanadium-oxygen system. Section 2.4 deals with in-situ X-ray diffraction, used for the study of gas-solid reactions and crystallization in vanadium oxide and vanadium nitride thin films. Finally three complementary techniques for the characterization of the semiconductor-metal transition in VO_2 are discussed in section 2.5, i.e. temperature-dependent X-ray diffraction, spectroscopic ellipsometry and sheet resistance measurements.

2.1 Thin film deposition techniques

For this research two approaches have been applied for the synthesis of VO_2 and VN thin films. First, metallic vanadium thin films were grown by magnetron sputtering, which were used to study oxidation and reduction reactions in the vanadium-oxygen system or nitridation towards VN. Second, atomic layer deposition (ALD) has been applied for the deposition of vanadium oxide and vanadium nitride layers.

2.1.1 Magnetron sputtering

Magnetron sputtering is a physical vapor deposition (PVD) technique.[1] It involves the bombardment ("sputtering") of a target material by argon ions, which causes atomic and ionic species to be ejected from this target. A substrate is placed opposite to the target, on which the sputtered species physisorb, and finally chemisorb, leading to the growth of a thin layer of the sputtered material.

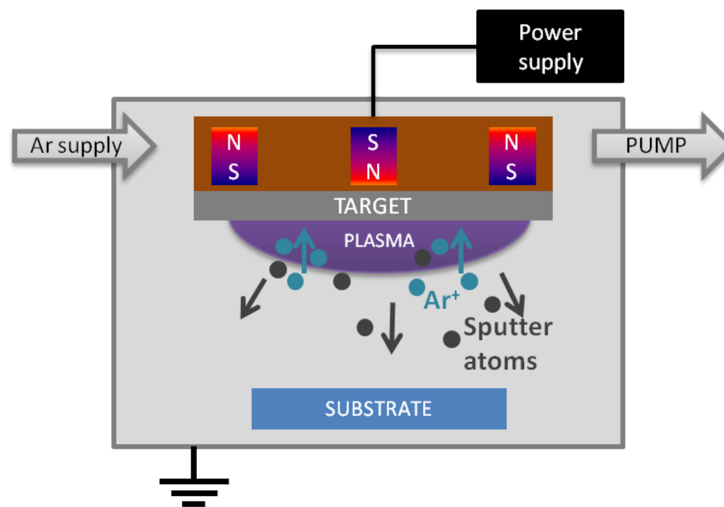

Figure 2.1. *Schematic presentation of the operation principle of magnetron sputtering.*

Figure 2.1 schematically shows how sputtering is performed. It is operated under vacuum conditions at a typical argon pressure of 5×10^{-1} Pa. By applying a high negative voltage on the target, a plasma will be generated by collisions between free electrons and argon atoms. Positively charged argon ions will be attracted and accelerated towards the target, leading to the sputtering process. The term "magnetron sputtering" refers to the use of a magnetic field at the target, which greatly improves the energy efficiency of the process as higher deposition rates can be achieved for a lower energy input. Typical deposition rates are on the order of tens or even hundreds of nanometers per minute, depending on power, target material, surface area of target and substrate,... Sputtering is a "line-of-sight" deposition technique and cannot deposit a coating "around the corner". For this reason sputtering is mainly applicable to flat substrates although for instance in microelectronics it is as well applied for deposition in trench structures with limited aspect ratios. However, the more novel approach of high-power impulse magnetron sputtering (HIPIMS) allows to deposit in trench structures, although the conformality is less good as compared to other techniques such as atomic layer deposition (see section 2.1.2). Apart from microelectronics, several other application domains benefit from this technique, such as coatings in the glass industry, wear-resistant coatings, metallization,...[2]

Magnetron sputtering is most suited for the deposition of pure metals. Metal nitrides or metal oxides can as well be deposited by introducing nitrogen or oxygen gas respectively together with the argon gas. This is referred to as reactive sputtering.[1] The chemical composition of the growing thin film will largely be influenced by the partial pressure of the reactive gas. Alternatively a metal oxide or metal nitride target can be used to sputter metal oxide or metal nitride thin films. In many cases a combination of both methods is applied. Deposition rates of metal oxides or nitrides are drastically lower compared to the sputtering of pure metals.

For the vanadium-oxygen system, pure V and V_2O_5 can be easily deposited. Many reports are available in literature on the synthesis of VO_2 or other vanadium oxides by reactive sputtering, but severe optimization of process conditions such as oxygen partial pressure and substrate temperature is required. In chapter 3, section 3.1, a thorough literature review will be presented.

For this work, VO_2 is synthesized by sputtering of V and subsequent oxidation in a controlled environment. The theoretical and experimental aspects related to such oxidation processes are presented in section 2.3 of this chapter, whereas the results are discussed in section 3.2 of chapter 3.

2.1.2 Atomic layer deposition

Atomic layer deposition (ALD) is a cyclic gas-phase technique for the deposition of thin films.[3–6] The main principles of ALD were already formulated in the 1950's by the Soviet researcher Aleskovskii, leading to a first publication in 1963.[7] At

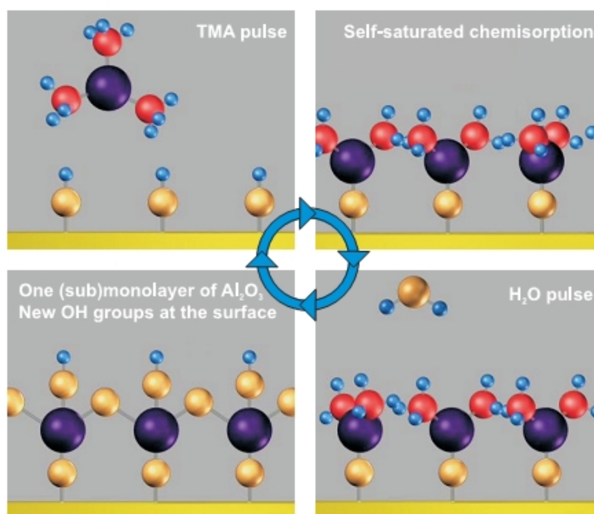

Figure 2.2. *Principle of ALD explained for the first cycle of Al_2O_3 growth from TMA and H_2O. Aluminum atoms are shown in purple, oxygen in yellow, hydrogen in blue and carbon in red.*[3]

that time, the term “molecular layering” (ML) was used. In the 1970’s the Finnish researcher Suntola independently invented the technique using the term “atomic layer epitaxy” (ALE), and he further developed it for the deposition of ZnS and Al_2O_3 layers for thin film electroluminescent displays in the 1980’s.[8]

Similar to chemical vapor deposition (CVD) it is based on the chemisorption of precursors on a substrate surface. The difference with CVD is related to the self-limiting nature of the surface chemisorption reactions. Only one monolayer of precursor molecules will chemisorb, such that a cyclic exposure to at least two precursors is required to enable film growth.

Figure 2.2 illustrates the principle of ALD of Al_2O_3 from trimethylaluminum (TMA) and water vapor. The deposition starts with the exposure of the OH-terminated substrate to TMA molecules. The methyl (CH_3) ligands react with the OH groups at the surface, such that the Al atom bounds to the oxygen atom and methane (CH_4) is released as a reaction product. When all OH groups have reacted with TMA molecules, the reaction stops, leaving one monolayer of chemisorbed TMA molecules and a surface terminated by CH_3 groups. TMA molecules that are not consumed in the surface reactions are evacuated or purged with inert gas. In the next step the surface is exposed to water vapor. Now the CH_3 surface groups react with the H_2O, forming Al-O bounds and releasing CH_4, while the surface is terminated again with OH groups. Once all CH_3 surface groups are replaced with OH groups, the reaction stops. At this point, the first ALD cycle has been completed, resulting in a first monolayer of Al_2O_3. Since the surface is again terminated by OH groups, a subsequent exposure to TMA can be applied to start the next cycle.

Due to the layer-by-layer growth, ALD has some unique advantages over other deposition methods:

- Subnanometer control of film thickness: every cycle the same increase in layer thickness is obtained, typically on the order of 0.1-2 Å/cycle, mainly depending on the precursor chemistry. Large precursor molecules typically result in lower growth rates due to steric hindrance of the ligands. Also the density of reactive adsorption species on the surface has a major impact on the growth rate, which often varies with temperature and might change during the initial stages of film growth.[4] Thus, although the ALD community often refers to monolayer-per-monolayer growth, in most cases submonolayers of the material are deposited each cycle.

- Excellent conformality on 3D structures: everywhere the gas can reach the surface, material will be deposited, such that ALD is suited for the conformal growth of thin films on 3-dimensional (nano)structures. Even the internal surface of porous materials can be coated, ideal for instance for tuning pore size distributions, or for the deposition of catalytic active material on high surface area porous substrates.[3]

- Excellent uniformity: the thickness of the deposited films is highly uniform on large area substrates.

- Stoichiometry: ALD involves ligand exchange between two precursors. Therefore, precursor chemistry will dictate the stoichiometry of the deposited film.
- Low deposition temperatures: compared to CVD, much lower temperatures are required for ALD growth. Typical deposition temperatures are in the range from room temperature up to 400 °C.
- Small effect of temperature on growth characteristics: this facilitates reactor design, compared to CVD systems, while batch-to-batch variation is much smaller.

These unique benefits of ALD made it a key enabling technology for further miniaturization in microelectronics. ALD has been applied for 3D DRAM capacitors, high-k gate oxides in transistors and more recently for spacer-defined double patterning (SDDP).[9–11]

The main disadvantage of ALD is the low deposition rate. Whereas for CVD growth rates of hundreds of nanometers per minute can be achieved, the growth rate of ALD is low due to the cyclic nature of the process. Since in between two precursor exposures the reactor needs to be pumped or purged, cycle times of seconds or even minutes are not an exception. For this reason ALD only found its way to a limited number of applications, such as microelectronics and some niche products, where the benefits of high-quality coatings and excellent process control greatly exceed the disadvantage of limited coating speed. For other applications, involving large area substrates, this bottleneck has been overcome by the commercial introduction of spatial ALD, which enables growth rates of 1 nm/s or even higher.[12] This has led to the breakthrough of ALD in solar industry and for the coating of large area flexible substrates.[13–15]

Another limitation of ALD is the fact that many materials are only deposited as amorphous layers.[6] Several parameters influence the crystallinity of the film, such as deposition temperature, reactants, impurities, substrate and film thickness, but often the range of process conditions is too limited to enable growth of crystalline material. Specifically for this research, it will be clear that the vanadium oxide thin films grown by ALD are amorphous, and post-deposition annealing will be required to obtain the desired crystalline phase.

The ALD method discussed so far is referred to as thermal ALD, since in most cases sufficient thermal energy is needed to allow for film growth. The required energy can as well be provided by the activation of reactant species in a plasma. Plasma-enhanced ALD (PE-ALD) has several advantages over thermal ALD, including reduced deposition temperatures, a larger range of suitable precursors, higher purity of the deposited films, certainly in the case of metal nitrides, and sometimes the possibility of growing crystalline films.[16–18] Since more precursors can be used in plasma-enhanced ALD, the library of available coating materials is larger. Furthermore, cheaper precursors can be accessed to reduce process cost.

Figure 2.3 shows a schematic overview of one of the ALD reactors used during this research. It is a high-vacuum, pump-type reactor, coupled to a PVD chamber. The combination of ALD and magnetron sputtering without exposing the sample

to ambient air in between both depositions is an important feature for the study of VN layers as copper diffusion barrier (chapter 4).

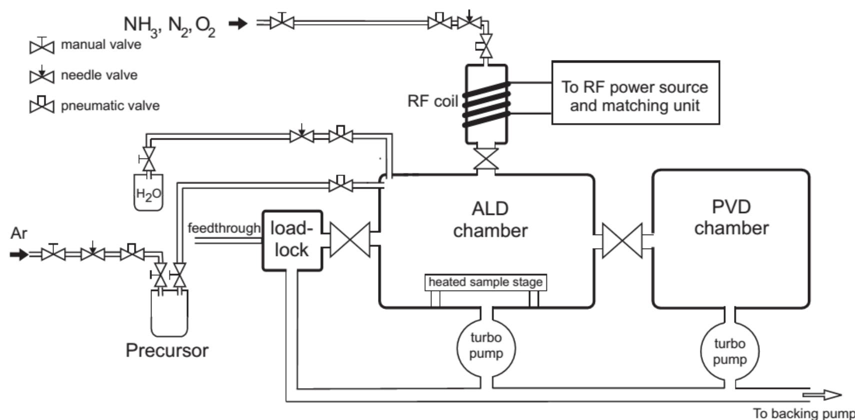

Figure 2.3. *Schematic drawing of the ALD reactor used during this research.*

2.2 Characterization of thin film thickness, density and composition

In this work, two techniques have been used frequently for the determination of film thickness and density, i.e. X-ray reflectivity (XRR) and X-ray fluorescence (XRF). Rutherford backscattering spectroscopy (RBS) has been used for calibration of XRF measurements. In the following subsections, each of these techniques will be described briefly, followed by an explanation of the determination of the vanadium molar density, which is an important parameter in describing the film properties. Furthermore, X-ray photoelectron spectroscopy (XPS) was used to determine the composition and vanadium valence of the deposited films. This technique is treated in a last subsection.

2.2.1 X-ray reflectivity

X-ray reflectivity is a non-destructive technique which measures the intensity of the specular reflection of an X-ray beam on a planar substrate as a function of the incident angleto determine film thickness, roughness and density. In this work it will only be used for the quantification of film thickness. The typical measurable range is limited from a few nanometers to a few hundreds of nanometers. A few spectra are shown in figure 2.4 for thin films of different materials on a Si substrate. The width of the fringes is characteristic for the film thickness, and increases with decreasing film thickness. Below a certain critical angle, total reflection occurs, which is characteristic for the density of the film. For high-density films (e.g. Ta

in the figure) the critical angle shifts to higher values. When the density of the film approaches the density of the substrate, or when the roughness increases to several nanometers, the height of the fringes disappears, limiting the applicability of XRR. Due to the relatively small difference between ALD grown vanadium oxides and the substrate, determination of the density will be rather difficult, and other approaches are required for determining other parameters than film thickness. These are explained in the following sections.

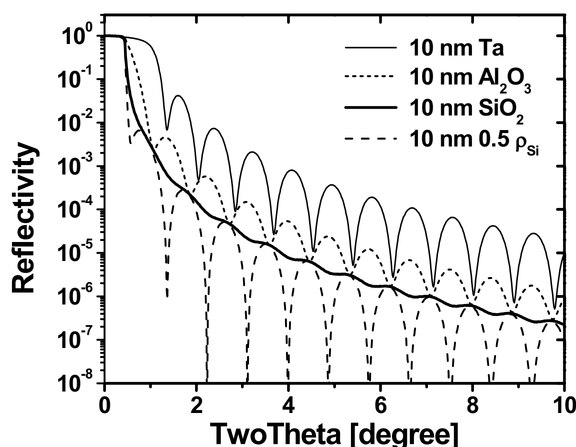

Figure 2.4. *Examples of XRR spectra for different materials with film thickness of 10 nm.*

2.2.2 X-ray fluorescence

X-ray fluorescence is used to characterize the chemical composition of thin films. During irradiation of a sample with X-rays, electrons are ejected from their shells if the corresponding binding energy is lower than the X-ray photon energy. As a consequence, vacancies are created within the respective shells. This is illustrated in figure 2.5(a). These vacancies allow for electrons in higher shells to be fall back to these lower shells, causing emission of fluorescent X-rays, as shown in figure 2.5(b). The energy of the emitted X-rays are related to the difference in binding energy difference of the two shells involved, which is characteristic for the chemical element.

As long as the film thickness is limited to a few tens of nanometers, the intensity of fluorescent X-rays corresponding to a certain atom is linearly dependent on the amount of atoms per unit of area. For higher film thicknesses, self-absorption needs to be taken into account, complicating the quantification. In this work, XRF has been used to quantify the amount of deposited V atoms per unit of area for the ALD-deposited vanadium oxide layers. However, a calibration was required to correlate the measured XRF peak intensities to a quantitative value of the V areal

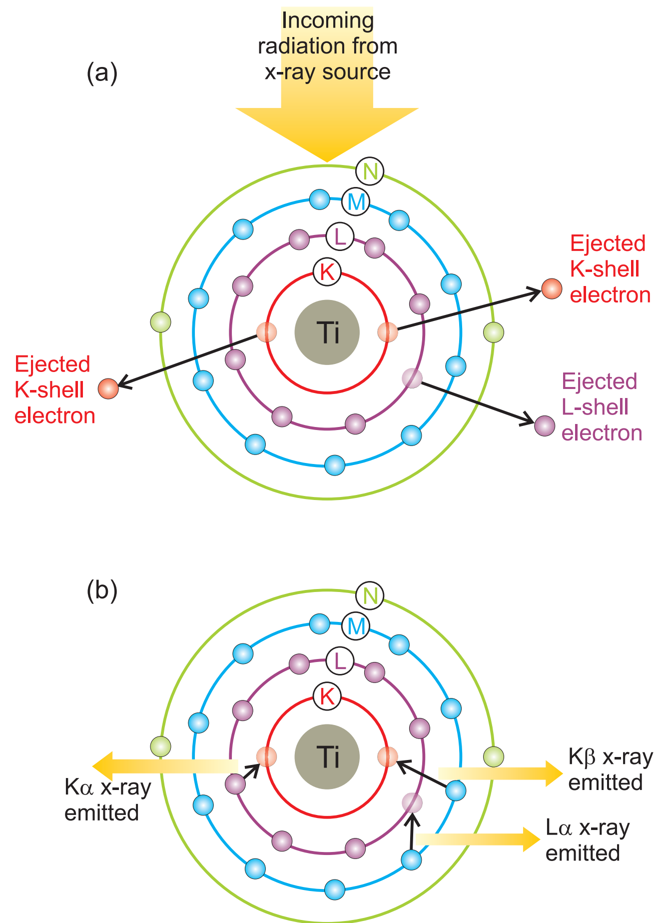

Figure 2.5. *Description of the X-ray fluorescence method.*

density. For this purpose, a reference samples was prepared and quantified by an RBS measurement.

2.2.3 Rutherford backscattering spectroscopy

Similar as XRF, Rutherford backscattering spectroscopy is technique used to measure the elemental composition of thin films. During an RBS measurement, the sample is bombarded with highly energetic He^{++} nuclei. Interaction of these nuclei with the sample material causes scattering. The backscattered ions show an energy distribution which depends on the elements present in the film, as well as their distribution. RBS measurement of and ALD-deposited vanadium oxide reference sample was performed at KULeuven, yielding a value for the V areal density

in atoms/cm^2, which was then used for calibration of the XRF measurements.

2.2.4 The vanadium molar density

By dividing the vanadium areal density, derived from XRF and RBS, by the thickness, dervived from XRR, the vanadium molar density is obtained, expressed in mole/cm^3. This parameter may give valuable information on the vanadium oxide composition, as illustrated in table 2.1, which gives a summary on some properties of crystalline vanadium and vanadium oxide phases, including the V molar density. An important remark is that crystalline materials have in general a higher density compared to amorphous films, for the same elemental composition. Certainly in the case of ALD films, this is often observed. The V molar density as listed in the table should thus be considered as upper limits. If, for instance, a V molar density of 0.052 has been determined by the combination of XRF and XRR measurements, the composition can be attributed to VO_2(M1/R) or lower vanadium oxide phases, but not to VO_2(B), V_2O_5 or one of the Magnéli phases.

Phase	Structure	Molar weight (g/mole)	Density (g/cm^3)	V molar density (mole/cm^3)
V	body-centered cubic	50.94	6.097	0.120
V_2O_3	rhombohedral	149.88	5.016	0.067
VO_2(R)	tetragonal	82.94	4.651	0.056
VO_2(M1)	monoclinic	82.94	4.666	0.056
VO_2(B)	monoclinic	82.94	4.000	0.048
V_6O_{13}	base-centered monoclinic	513.64	3.905	0.046
V_4O_9	tetragonal	347.76	3.301	0.038
V_3O_7	base-centered tetragonal	264.82	3.614	0.041
V_2O_5	orthorhombic	181.88	3.364	0.037

Table 2.1. *Properties of some crystalline vanadium and vanadium oxide phases, relevant for this work.*

2.2.5 X-ray photoelectron spectroscopy

X-ray photoelectron spectroscopy uses monochromatic X-rays to cause emission of electrons from the atoms present in the thin film. The difference in energy between the X-rays and the detected photoelectron are a direct measure for the binding energy of that certain electron. These binding energies are characteristic or each element, and depend slightly on the chemical state of that element within the film. Therefore, XPS is suitable to deliver information on the oxidation state in vanadium oxides. The X-rays can easily penetrate over a depth of hundreds of nanometers or several micrometers within the film. However, the photoelectrons have a typical mean free path of only a few or a few tens of Ångströms, which is the reason for the limited information depth of XPS of only a few nanometers. For this work, the analysis of XPS spectra will be based on the work of Silversmith et al., who performed a dedicated study of the determination of valence states of

V in different vanadium oxide phases.[19] All experiments were performed using a monochromatic Al Kα X-ray source.

2.3 Gas-solid reactions

An understanding of gas-solid reactions is fundamental and essential for the study and synthesis of metal oxides (and nitrides). By oxidation of a metal in an oxygen containing gas, a certain metal oxide will form, depending on the set of conditions such as temperature and oxygen partial pressure. Opposite is the reduction of a metal oxide to a metal or a metal oxide with a lower oxygen content. While thermodynamics will determine which phases can be formed under certain conditions, kinetics will determine the rate at which such gas-solid reactions will proceed. The first two sections will briefly highlight the fundamentals of thermodynamics and kinetics and refer to the V-O system where applicable. In the third section, some methods to control the oxygen partial pressure will be discussed. Practical limitations will be considered to motivate the methods selected in this work.

2.3.1 Thermodynamics and phase diagrams

As stated above, thermodynamics form an important topic in the study of gas-solid reactions, since these determine which metal oxide phase is stable for a given set of conditions. Phase diagrams serve as a graphical representation of the values of thermodynamic variables at the equilibrium between two different phases. In what follows it will be explained how from the Gibbs energy change of a reaction the chemical equilibrium conditions can be derived, and how this can be used to develop phase diagrams.

Gibbs energy: In chapter 3, section 3.2, the synthesis of VO_2 by gas-solid reactions in the V-O system will be studied. One of the investigated reactions is the oxidation of V towards VO_2 by thermal annealing in O_2 gas, which is described by the chemical formula

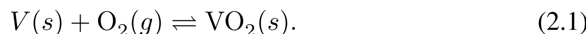

$$V(s) + \mathrm{O}_2(g) \rightleftharpoons \mathrm{VO}_2(s). \tag{2.1}$$

In what follows, it will be explained how the temperature and oxygen partial pressure will determine whether the oxidation reaction will proceed or not. Therefore, some thermodynamic calculations have to be made.

The Gibbs energy of a system is described in terms of its enthalpy H, entropy S and temperature T:

$$G = H - TS. \tag{2.2}$$

Given a constant temperature and pressure, a system tends to reach an equilibrium state that minimizes G. This means that a chemical reaction can only proceed if the Gibbs energy change of the reaction is negative, i.e.

$$\Delta_r G = \Delta_r H - T\Delta_r S < 0. \tag{2.3}$$

Under standard pressure conditions (0.1 MPa), the Gibbs energy change of the reaction can be calculated from the following set of equations:

$$\Delta_r G^0 = \Delta_r H^0 - T\Delta_r S^0 \quad (2.4)$$

$$\Delta_r H^0 = \sum \Delta_f H^0_{products} - \sum \Delta_f H^0_{reactants} \quad (2.5)$$

$$\Delta_r S^0 = \sum S^0_{products} - \sum S^0_{reactants} \quad (2.6)$$

$$\Delta_f H^0_i = \Delta_f H^0_i(25\,^\circ\mathrm{C}) + \int_{25\,^\circ\mathrm{C}}^{T} C^0_{P,i}\,dT \quad (2.7)$$

$$S^0_i = S^0_i(25\,^\circ\mathrm{C}) + \int_{25\,^\circ\mathrm{C}}^{T} \frac{C^0_{P,i}}{T}\,dT \quad (2.8)$$

$\Delta_f H^0_i(25\,^\circ\mathrm{C})$ and $S^0_i(25\,^\circ\mathrm{C})$ are the formation enthalpy and absolute entropy of the individual substances of the chemical reaction at standard conditions (0.1 MPa and 25 °C) and are tabulated in several text books and online databases, such as the NIST webbook of chemistry.[20] The standard heat capacity $C^0_{P,i}$ of each substance is a function of temperature, and is often approximated as a power series of the temperature, such as in the Shomate equation:[20]

$$C^0_P(T) = a + bT + cT^2 + dT^3 + e/T^2. \quad (2.9)$$

The coefficients of this approximation are as well tabulated for many substances. When all the enthalpy, entropy and heat capacity parameters are known for a certain temperature range, $\Delta_r G^0$ can be calculated for every temperature within that range.

As an example, let us consider the oxidation reaction of V in O_2 gas for the formation of VO_2, as was presented in reaction 2.1. At a temperature of 500 °C, the standard Gibbs energy change is -576 kJ/mol. Since $\Delta_r G^0 < 0$, the reaction will proceed spontaneously. However, if we consider the oxidation reaction from VO_2 towards V_2O_5, i.e.

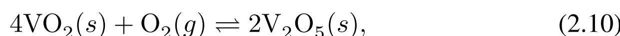

$$4\mathrm{VO_2}(s) + \mathrm{O_2}(g) \rightleftharpoons 2\mathrm{V_2O_5}(s), \quad (2.10)$$

we would find as well a negative value for the standard Gibbs energy change of this reaction: -115 kJ/mol at the temperature of 500 °C. Thus, under standard O_2 pressure conditions, the oxidation of V would result in V_2O_5 instead of VO_2. Remark that although V_2O_5 is known to have a low vapor pressure, it is only treated as a solid phase in this discussion.

Chemical equilibrium: In order to obtain VO_2 as a thermodynamic stable phase, deviation from standard conditions will be required. The Gibbs energy change is related to the standard Gibbs energy change by the reaction quotient Q:

$$\Delta_r G = \Delta_r G^0 + RT\ln Q, \quad (2.11)$$

with R the universal gas constant. In the case of gas-solid reactions, the reaction quotient is defined by the partial pressures of the reactant and product gases and their respective reaction coefficients (c_i):

$$Q = \frac{\prod p_{products,i}^{c_i}}{\prod p_{reactants,i}^{c_i}}. \tag{2.12}$$

For the oxidation reactions 2.1 and 2.10, we thus get

$$\Delta_r G = \Delta_r G^0 - RT \ln p_{O_2}. \tag{2.13}$$

Here p_{O_2} is the oxygen partial pressure. Chemical equilibrium is achieved when $\Delta_r G = 0$, or

$$\Delta_r G^0 = RT \ln p_{O_2}. \tag{2.14}$$

At the temperature of 500 °C we find an equilibrium oxygen partial pressure of 1.7×10^{-3} Pa for the reaction 2.10. This corresponds to the maximum allowable oxygen partial pressure to prevent VO_2 to be oxidized towards V_2O_5, at this temperature.

Phase diagrams: In the introductory chapter, figure 1.1 showed a phase diagram of the vanadium-oxygen system in terms of composition and temperature. As an alternative, phase diagrams can be constructed by plotting the equilibrium standard

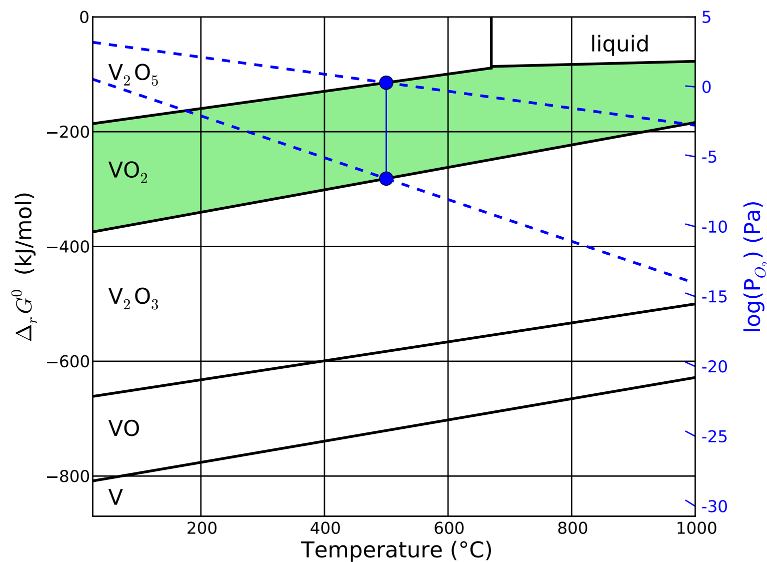

__Figure 2.6.__ Ellingham diagram of the principle vanadium oxide phases, including indications for the allowable oxygen partial pressure range for VO_2 phase stabilization at 500 °C.

Gibbs energy change of the oxidation-reduction reactions between the metal-oxide phases as a function of temperature. This is referred to as an Ellingham diagram.[22] Figure 2.6 shows the Ellingham diagram for the principle vanadium-oxide phases, i.e. V, VO, V_2O_3, VO_2 and V_2O_5. The black lines represent the equilibrium conditions between the respective vanadium-oxide phases, while the green region indicates the conditions to thermodynamically stabilize the VO_2 phase. Ellingham diagrams are very useful to estimate the required oxygen partial pressures as a function of temperature. Each partial pressure is represented by a straight line which starts at the origin, according to equation 2.14. In the figure, the oxygen partial pressures are indicated on the right axis. As an example, the temperature of 500 °C is selected as reaction temperature. The two blue dotted lines cross the phase equilibrium lines between V_2O_5, VO_2 and V_2O_3 at the temperature of 500 °C, and correspond to respectively 10^{-3} and 10^{-14} Pa. This is the thermodynamically stable range of oxygen partial pressures to form VO_2 at 500 °C. Remark that in this example the Magnéli and Wadsley phases are not yet considered. The actual allowed oxygen partial pressure range will thus be even narrower.

Phase diagrams can as well be constructed as a function of temperature and oxygen partial pressure. Figure 2.7 shows a calculated phase diagram of the V-O system along with reported experimental data, including the Magnéli and Wadsley phases.[21] This phase diagram illustrates that the V-O system is much more complicated than represented in figure 2.6, in which only the principle vanadium-oxide phases were included. Considering again the temperature of 500 °C, an even more restricted region of oxygen partial pressures is allowed to stabilize the VO_2 phase, from approximately 10^{-4} to 10^{-9} Pa.

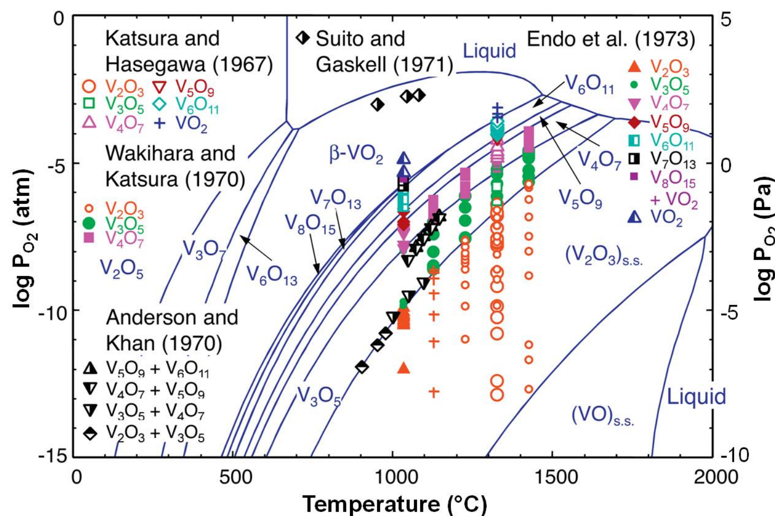

Figure 2.7. *A calculated phase diagram of the V-O system as a function of temperature and oxygen partial pressure along with reported experimental data.*[21]

These extremely low values of the oxygen partial pressure lead to some practical issues for the oxidation process. First of all, one should be aware that even a very thin film of vanadium will consume a certain amount of oxygen which is in general not present in the gas phase at such oxygen partial pressures. Let us consider the example of an 80 nm V thin film with an area of 1 squared centimeter (corresponding to the typical sample specifications used in this work). It was calculated that approximately 1×10^{-6} mole of oxygen will be consumed. Considering a reactor volume of 5 liter (corresponding with the experimental conditions in this work) and an oxygen partial pressure of 10^{-4} Pa, i.e. the upper limit for thermodynamic phase stability as explained above, only 2×10^{-10} mole of oxygen is available, which is orders of magnitude below the required value of 1×10^{-6} mole. Although a continuous supply of oxygen to the reactor could encounter this problem, it would be extremely challenging to find a balance between oxygen feeding and oxygen consumption without exceeding the value of 10^{-4} Pa of oxygen. As explained in section 2.3.3, this issue is often circumvented by the use of buffered gas mixtures such as H_2/H_2O or CO/CO_2, which cause stabilization of the oxygen partial to certain values depending on the ratio of the two gases involved and the temperature, even if oxygen is being consumed during the reaction.

Second, and as will be explained in section 2.3.3 the minimal oxygen partial pressure which can be controlled during in-situ XRD is on the order of 1 Pa. At such oxygen partial pressures, temperatures above 600 °C would be required to thermodynamically stabilize VO_2. However, as will be shown in chapter 3 most experiments will be carried out at higher oxygen partial pressures and/or lower temperatures, such that the experimental conditions during this research fall within the region where V_2O_5 is assumed to be the thermodynamically favored phase and VO_2 is in principle not expected to be stable. Fortunately, the rate at which oxidation and reduction occurs is determined by kinetics and quite often this is observed as the limiting step, as explained in the next section.

2.3.2 Kinetics

Although thermodynamics predict which metal-oxide phase is stable under certain conditions of temperature and oxygen partial pressure, it should be clear that there is another factor into play which limits metals to oxidize spontaneously. Without this limiting factor, pure metals, apart from some noble metals which do not tend to oxidize, would not exist under standard conditions. Specifically for the case of V, this would mean that only V_2O_5 would be present, as can be derived from figures 2.6 and 2.7. This limiting factor is the kinetics of the process. In the case of oxidation of metals, kinetics describe how the oxidation rate is influenced by parameters as temperature and oxygen partial pressure.

Deal-Grove model: When a metal is oxidized at elevated temperatures, a metal-oxide layer is formed at the surface. Quite often, the thickness of this metal-oxide layer increases in a linear-parabolic way. An appropriate model which describes

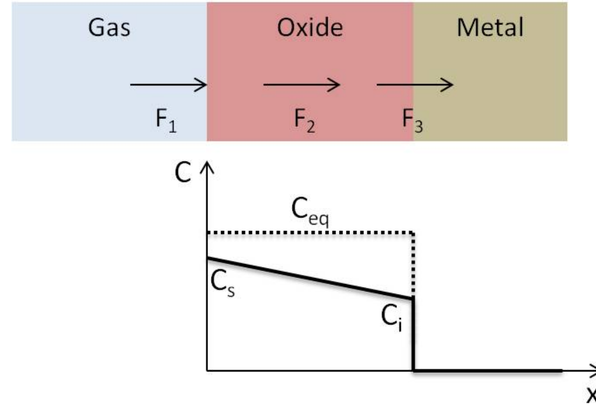

Figure 2.8. *Schematic illustration of the model of Deal and Grove applied for the oxidation of metals.*

this phenomenon was developed by Deal and Grove in the 1960's for the oxidation of silicon.[23] The model, as visualized in figure 2.8, is based on the inwards flux of oxygen and takes into account the three following steps in the oxidation process:

- Oxygen is transported from the gas phase to the surface of the metal-oxide layer, where it reacts or is absorbed. The flux of oxygen is given by

  $$F_1 = h(C_{eq} - C_s), \tag{2.15}$$

  where h is a gas-phase transport coefficient, C_s the oxygen concentration at the metal-oxide surface, and C_{eq} is the equilibrium concentration of oxygen in the metal-oxide phase. The equilibrium concentration is often assumed to be related to the oxygen partial pressure by Henry's law, i.e.

  $$C_{eq} = KP_{O_2}, \tag{2.16}$$

  although this is not necessarily the case.

- Oxygen diffuses through the metal-oxide layer from the surface towards the interface between the metal and the metal-oxide. The flux of oxygen is assumed to be given by Fick's law:

  $$F_2 = -D(dC/dx). \tag{2.17}$$

  D is the effective diffusion coefficient and dC/dx is the concentration gradient of oxygen in the metal-oxide layer. In steady-state, the flux F_2 is constant throughout the oxide layer, consequently leading to a linear gradient of the oxygen concentration. Therefore, the flux F_2 can be written as

  $$F_2 = D(C_s - C_i)/x, \tag{2.18}$$

where C_i is the oxygen concentration at the interface between the metal and the metal-oxide and x the thickness of the metal-oxide layer.

- Finally, the flux related to the oxidation reaction at the interface between the metal and the metal-oxide is given by

$$F_3 = kC_i, \tag{2.19}$$

with k the reaction rate coefficient of the oxidation reaction.

In steady-state the fluxes are equal, i.e. $F_1 = F_2$ and $F_2 = F_3$, and solving for C_i and C_s leads to the relations

$$\frac{C_i}{C_{eq}} = \frac{1}{1 + k/h + kx/D} \tag{2.20}$$

and

$$\frac{C_s}{C_{eq}} = \frac{1 + kx/D}{1 + k/h + kx/D}. \tag{2.21}$$

In case the diffusivity is small compared to the rate coefficients at the surface and interface, $C_i \rightarrow 0$ and $C_s \rightarrow C_{eq}$. This condition is referred to as diffusion controlled. With C_i and C_s eliminated, the flux is given by

$$F = F_1 = F_2 = F_3 = \frac{kC_{eq}}{1 + k/h + kx/D}. \tag{2.22}$$

The growth rate of the metal-oxide layer can be expressed by the differential equation

$$\frac{dx}{dt} = \frac{F}{N_{ox}} = \frac{kC_{eq}/N_{ox}}{1 + k/h + kx/D}, \tag{2.23}$$

with N_{ox} the number of oxygen molecules incorporated in a volume unit of the metal-oxide phase. Assuming the oxide thickness $x = 0$ at time $t = 0$, the solution of the differential equation can be written as

$$x = \frac{A}{2}\left(\sqrt{1 + \frac{t}{A^2/4B}} - 1\right), \tag{2.24}$$

which relates the oxide thickness to the oxidation time, with

$$A = 2D(1/h + 1/k), \tag{2.25}$$

$$B = 2DC_{eq}/N_{ox}. \tag{2.26}$$

Two interesting cases can be derived when considering short and long oxidation times. For short oxidation times, i.e. $t \ll A^2/4B$, the growth can be approximated as linear:

$$x \cong \frac{B}{A}t, \tag{2.27}$$

with

$$\frac{B}{A} = \frac{hk}{h+k}\frac{C_{eq}}{N_{ox}} \tag{2.28}$$

the linear rate constant. In the case of long oxidation times, i.e. $t \gg A^2/4B$, a parabolic growth is observed:

$$x \cong \sqrt{Bt}. \tag{2.29}$$

The coefficient B is referred to as the parabolic rate constant.

Influence of oxygen partial pressure and temperature on the oxidation rate: The role of the oxygen partial pressure on the oxidation rate is incorporated by the assumption of formula 2.16. Thus, in the initial linear growth stage, the growth rate depends linearly on the oxygen partial pressure (formula 2.27), while for the parabolic growth stage, the growth rate depends on the square root of the oxygen partial pressure (2.29). In fact, under these assumptions we can state that the oxide thickness increases linearly or parabolically with respect to the product of time and oxygen partial pressure. In case of very low values of the oxygen partial pressure, as for instance illustrated at the end of the previous section, the flow C_{eq}, and consequently F_1 will be so low that the time required for oxidation of a V film will get extremely large.

The influence of temperature on the oxidation rate is incorporated in the diffusion and reaction coefficients, as described by Boltzmann statistics:

$$D = D_0 \exp(-E_{a,D}/k_bT) \tag{2.30}$$
$$h = h_0 \exp(-E_{a,h}/k_bT) \tag{2.31}$$
$$k = k_0 \exp(-E_{a,k}/k_bT) \tag{2.32}$$

Here, D_0, h_0 and k_0 are prefactors, $E_{a,i}$ are the respective activation energies, k_b is the Boltzmann constant and T the temperature. Thus, by increasing the temperature, the reaction rate increases exponentially. The activation energy is characteristic for the process and can be experimentally determined from the slope of an Arrhenius plot, which plots the logarithm of the reaction rate as a function of inverse temperature.

Oxidation kinetics of vanadium: Early studies on kinetics of the thermal oxidation of vanadium were performed by means of vacuum microbalances, indicating the mass gain of a vanadium foil due to oxygen uptake.[24–29] From these experiments it was concluded that VO_2 grows at a linear-parabolic rate, related to a diffusion-limited process. Salomonsen et al. studied the kinetics of vanadium thin films, however only in pure oxygen at atmospheric pressure and in a limited temperature region from 310 °C to 370 °C.[30] He did not observe crystalline vanadium oxide phases by XRD, but RBS revealed a layered structures with V_2O_5 on top of V_6O_{13}. From Kirkendall marker experiments he furthermore concluded that oxygen is the diffusing species, which is in fact one of the assumptions made in the model of Deal and Grove.

2.3.3 Oxygen partial pressure control

As discussed in section 2.3.1, the oxygen partial pressure plays a crucial role for controlling the stoichiometry of metal oxides. Referring to the V-O phase diagram (figure 2.7), the maximum allowable oxygen partial pressure to stabilize VO_2 is around 1000 Pa at temperatures above 1000 °C. However, for thin films the temperatures during processing often needs to be restricted to prevent morphological degradation. Also some substrates, such as glass, do not withstand high temperatures. When a temperature of e.g. 500 °C is being used, the oxygen partial pressure should in principle be restricted to levels in the range 10^{-9} to 10^{-4} Pa to maintain VO_2 as a thermodynamic stable phase. There exist several methods to control the oxygen partial pressure, and the most common are discussed in the following list:

1. **Vacuum systems:** in a vacuum system the total gas pressure is reduced by many orders of magnitude with respect to atmosphere. One uses the term high vacuum (HV) when the base pressure is between 10^{-2} and 10^{-7} Pa or ultra-high vacuum (UHV) if the base pressure is below 10^{-7} Pa. By introducing oxygen gas and monitoring the total pressure in the vacuum chamber, the oxygen partial pressure can be easily adjusted. As stated above, at an oxygen partial pressure of 10^{-4} Pa, which falls within the HV range, VO_2 can be stabilized from thermodynamical grounds.

2. **Oxygen dilution in inert gas flow:** instead of using a HV or UHV system, adding a low fraction of oxygen to an inert gas also enables oxygen partial pressure control. Although this might look straightforward, from a practical point of view this method is limited to a relatively high range of oxygen partial pressures. First of all, inert gas as delivered in gas cylinders typically has a remaining impurity level of 1 to 10 ppm. When using inert gas at atmospheric pressure, i.e. 10^5 Pa, one is in fact unintentionally operating at an oxygen partial pressure around 10^{-1} to 1 Pa (assuming the impurities are oxygen). To reach lower oxygen partial pressures, additional purifiers such as titanium getters would be required.[31] But even in such cases, small leaks in the reactor itself, as well as in the gas tubings between the purifier and the reactor, will cause the oxygen partial pressure to increase again. In addition, prior to the introduction of the controlled gas mixture into the reactor, the reactor should be evacuated or purged sufficiently. Outgassing of the reactor walls and parts inside the reactor will cause as well an increased background pressure of oxygen and water vapor. Without the use of a HV or UHV system, it is rather impractical to reach oxygen partial pressures below 10^{-1} Pa using this method.

3. **Gas buffer:** An often applied method for precisely controlling the oxygen partial pressure is the dynamic equilibrium in a gas mixture, also referred to as a gas buffer. Common mixtures are H_2/H_2O and CO/CO_2. As being clear from the following chemical reactions, O_2 will be consumed or produced in

these gas mixtures:

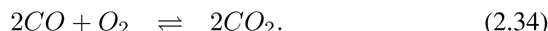

$$2H_2 + O_2 \rightleftharpoons 2H_2O \quad (2.33)$$
$$2CO + O_2 \rightleftharpoons 2CO_2. \quad (2.34)$$

If furthermore dynamic equilibrium exists in the gas phase, the oxygen partial pressure will be fixed to a specific value, which depends on the introduced ratio of the reactant gases and the temperature. The additional advantage of this approach is that as long as the partial pressure of H_2 or CO is sufficient, O_2 impurities in the gas or originating from leaks in the reactor and gas tubings will be consumed in the gas phase reactions, limiting their contribution to the oxygen partial pressure.

For our setup (in detail described in section 2.4), method 1 was not applicable. The use of a HV compatible pump, e.g. a turbomolecular pump, would be required to allow for HV, which was rather impractical due to increased complexity of the system. Furthermore it would be impractical since exposing a HV system to ambient air, when loading a new sample, requires a long time to pump down the system to HV again. In addition, the heating system does not allow for reliable temperature control under vacuum conditions.

Method 3, i.e. the gas buffer, has many reasons why not being the preferred way of controlling the oxygen partial pressure, as listed below:

- Safety: CO is a toxic gas and is thus not advised to be used. H_2 is flammable when its volume percent is in the range between 4 and 75 % in air, or between 4 and 94 % in O_2 at 10^5 Pa. The explosion limits lie in between 18 and 59 %. Dilution in inert gas is required to circumvent these safety issues. At elevated temperatures, the safety limits drop drastically.[32]

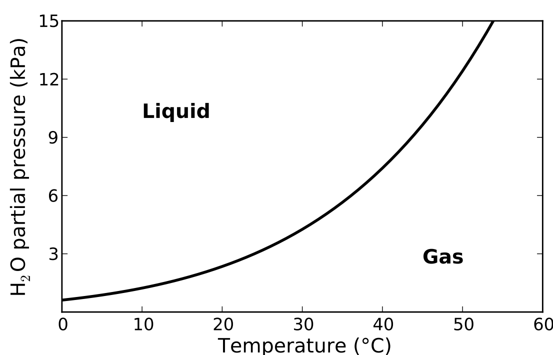

Figure 2.9. *Dewpoint line of water as a function of temperature. When the water vapor pressure exceeds the dewpoint, the water vapor will condense. Below the dewpoint, water will be in the gas phase.*

- Condensation of water vapor: when using a mixture of H_2 with H_2O, the possibility might exist that water vapor condenses at cold reactor spots. Water will condense when its vapor pressure is higher than the saturated water vapor pressure of the temperature at the coldest spot in the reactor, leading to a deviation from the selected gas mixture. Figure 2.9 shows the dewpoint line of water. It indicates the boundary conditions for water to be in the gas or liquid phase as a function of temperature and vapor pressure. For instance, at a temperature of 20 °C water will be in the gas phase as long as the vapor pressure is below 2300 Pa. If the vapor pressure would increase above 2300 Pa, condensation will occur, and the vapor pressure will settle to 2300 Pa. In our case, the reactor wall is not heated, while also cooling water ($\approx$ 15 °C) is used for active cooling of the heater block. Therefore, only water vapor pressures below $\approx$ 1700 Pa are allowed from a practical point of view.

- Oxidation by gas species other than O_2: in the foregoing discussion of gas dynamic equilibrium it has been assumed that only O_2 is responsible for the oxidation process. However, it is not unlikely that other species such as CO_2 and H_2O can also serve as sources for oxygen and thus have a direct contribution to the oxidation process. It is for instance well known that oxidation of silicon can proceed in H_2O vapor, referred to as wet oxidation.[23] In this specific case the oxidation rate is even higher compared to dry oxidation in oxygen. The smaller molecule size of H_2O compared to O_2 may play a significant role. In contrast to silicon, wet oxidation of vanadium has not been reported, but it cannot be excluded that water vapor might have an influence on the oxidation behavior.

- Incorporation of impurities: when using mixtures of CO and CO_2, contamination of the film with carbon might occur. In some cases, such as for materials as Ca or Ba, annealing in CO_2 can even result in the formation of carbonates. Although vanadium carbonates might not necessarily occur during oxidation in CO/CO_2 mixtures, carbon impurities might become incorporated.

- Kinetics of gas dynamic equilibrium: one of the most critical aspects when applying the gas dynamic equilibrium is the time required for achieving the equilibrium state. When two gases are mixed for the purpose of being used as buffer gas, they need to react with each other in a short timeframe to ensure reliable control of the oxygen partial pressure. In practice, in the absence of catalysts a H_2/H_2O mixture typically requires temperatures above 800 °C to equilibrate in less than one minute. CO/CO_2 mixtures require even higher temperatures.[33] Since for this work annealing experiments will be carried out in temperature ranges around 500 °C, it may not be assumed at all that the gas dynamic equilibrium will hold. Moreover, the system operates with a cold reactor wall, while the sample heater has only a small

area. Working with a buffered gas mixture does not seem to be appropriate in such a non-isothermal system.

Based on these arguments the conclusion can be drawn that the method of choice for our experimental setup is the dilution of oxygen in an inert gas flow, although it puts some drastic restrictions on the lower values of the oxygen partial pressure. The main limitation is the base pressure of approximately 1 Pa of the in-situ chamber during evacuation. This means oxygen partial pressures below 1 Pa cannot be guaranteed. Three systems for oxygen dilution in inert gas have been used: a variable leak valve in combination with an oxygen sensor, an oxygen pump, and mass flow controllers. In what follows a short description of these systems is given:

- **Variable leak valve:** This is a mechanical device typically used in HV or UHV applications to precisely regulate a certain flow or pressure of a gas in a vacuum reactor. By adjusting the distance between an optically flat sapphire and a captured metal gasket, as shown in figure 2.10, a variable leak can be introduced from an external gas supply towards the vacuum. The leak can be controlled to a minimum flow rate of 10^{-8} sccm (standard cubic centimeter per minute). When diluting oxygen in a flow of inert gas, the oxygen partial pressure is given by the ratio of the leak flow of oxygen to the total gas flow. For instance, at a flow of 1000 sccm of inert gas and a total pressure of 10^{5} Pa in the reactor, the minimum adjustable oxygen partial pressure value would be approximately 10^{-6} Pa. This is far below the practical limit of 1 Pa of the reactor.

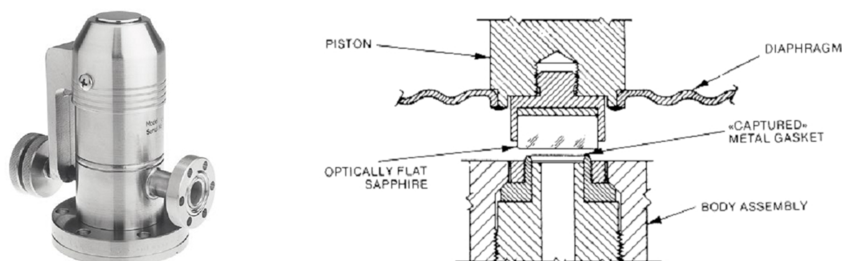

Figure 2.10. *Left: picture of a variable leak valve. Right: cross section drawing of a variable leak valve.*

Although the flow of oxygen can be regulated very precisely, it is far from straightforward. Adjustment of the knob does not result in a linear increase of the leak rate. Furthermore the leak rate is also a function of the pressures before and behind the leak valve. To exactly regulate the oxygen partial pressure, an oxygen sensor is required for feedback, as described next. For a manually operated leak valve, as was used for this research, the user has to manipulate the position of the knob to ensure the desired oxygen partial

pressure. An alternative would have been a motorized leak valve, which is also commercially offered. In combination with an oxygen sensor, a feedback loop with PID regulation of the motor drive should enable a stable control of the oxygen partial pressure.

Figure 2.11 shows how for dilution of a mixture of 10% O_2 + 90% N_2 (from a gas bottle) in a He flow of 1 slm (standard liter per minute) the oxygen partial pressure could be adjusted in the range between 0.5 and 1000 Pa by regulation of the variable leak valve.

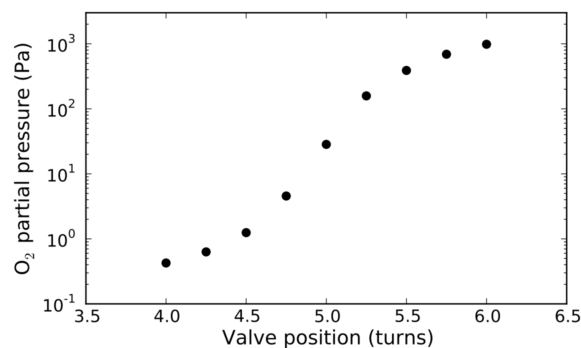

Figure 2.11. *Variation of the oxygen partial pressure as a function of the variable leak valve position, i.e. the number of turns of the knob, illustrating the degree of control that could be obtained.*

- **Oxygen sensor:** The oxygen sensor used in this work is a potentiometric-type gas sensor based on a solid electrolyte. A picture and schematic illustration are shown in figure 2.12. Two Pt electrodes are separated by a

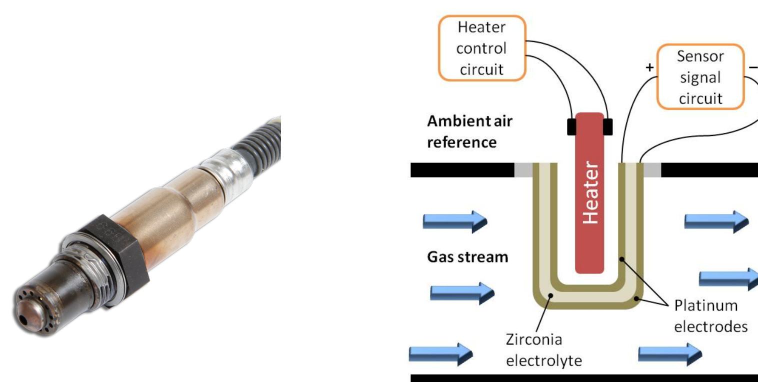

Figure 2.12. *Picture (left) and schematic illustration (right) of the solid electrolyte oxygen sensor.*

stabilized ZrO_2 oxygen ion conductor. When the sensor is at high temperature and a difference in oxygen partial pressure is present between both sides of this sensing element, an open-circuit voltage can be measured, given by the Nernst equation:

$$E = \frac{RT}{4F} ln \left(\frac{p_{O_2}}{p_{O_2}^{ref}} \right) \tag{2.35}$$

R is the universal gas constant, T the temperature, F the Faraday constant (i.e. 9.65×10^4 C/mol), p_{O_2} the oxygen partial pressure at the sensing side of the sensor and $p_{O_2}^{ref}$ the reference oxygen partial pressure. If the reference partial pressure is kept constant, the voltage at constant temperature, which is regulated by an internal heater, is directly related to p_{O_2} at the sensing electrode.

A Cambridge Sensotec Rapidox 2100 zirconia oxygen sensor was installed, which allows for measurement of oxygen partial pressures in the range from 10^{-20} ppm (parts per million) to 100%. The reference electrode is in contact with air, while the sensor head is placed at the gas outlet line. Figure 2.13 shows a schematic overview of the gas panel configuration, including the variable leak valve and oxygen sensor. Using a 6-way switching valve, the gas from the mixing panel can be directed first to the in-situ chamber and then to the sensor, or directly to the sensor. In this way, both the gas directed towards the in-situ chamber, and the exhaust of the in-situ chamber can be monitored.

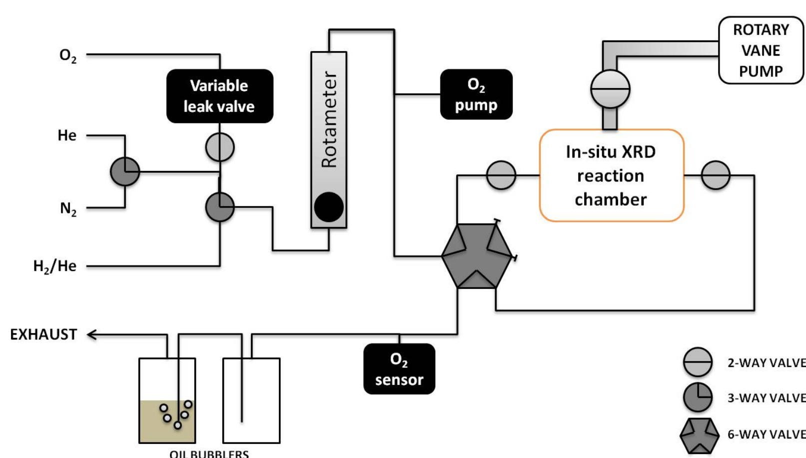

Figure 2.13. *Drawing of the first gas panel configuration of the in-situ XRD system, including the variable leak valve, oxygen pump and oxygen sensor.*

- **Oxygen pump:** The oxygen sensor makes use of a zirconia solid electrolyte which can act as an oxygen ion conductor at high temperatures. By applying

a voltage over the sensor electrodes, the sensor can operate as an oxygen pump.[34] This type of operation is used for adding well-controlled amounts of oxygen into the inert gas flow which is directed to the in-situ chamber. A spare oxygen sensor was used for this purpose. At the air side of the cell, oxygen molecules are adsorbed onto the Pt electrode and are captured in the oxygen ion vacancies in the solid electrolyte upon acquiring electrons from the external circuit by the reaction

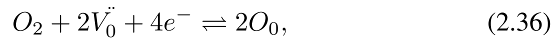

$$O_2 + 2V_0^{\cdot\cdot} + 4e^- \rightleftharpoons 2O_0, \tag{2.36}$$

where $V_0^{\cdot\cdot}$ represents a doubly ionized oxygen vacancy and O_0 a lattice oxygen atom. Due to the externally applied voltage, oxygen ions diffuse towards the other side of the cell and are oxidized back to oxygen molecules by the reverse of reaction 2.36. Thus, the transfer of one oxygen molecule from the air side of the pump to the inert gas flow requires four electrons. More precisely, a linear relation between the flux of oxygen molecules J_{O_2}, and the electric current I can be written as

$$J_{O_2} = \frac{I}{4F}(mol/s). \tag{2.37}$$

For instance, a current of 1 mA will imply an O_2 flux of approximately 2.6×10^{-9} mol/s. At an inert gas flow of 1000 sccm the resulting oxygen fraction is 3.5 parts per million by volume. At atmospheric pressure this corresponds to an O_2 partial pressure of 0.35 Pa. Rather than applying a constant voltage over the oxygen pump, a constant current source is used to accurately control the desired oxygen feed. This allows for a stable and accurate control of the oxygen partial pressure without any further need for an oxygen sensor. The internal heater, used for heating the ZrO_2 solid electrolyte, was connected to a DC power supply, using a voltage of 12 or 16 V for N_2 or He as inert gas respectively. The higher voltage was required for

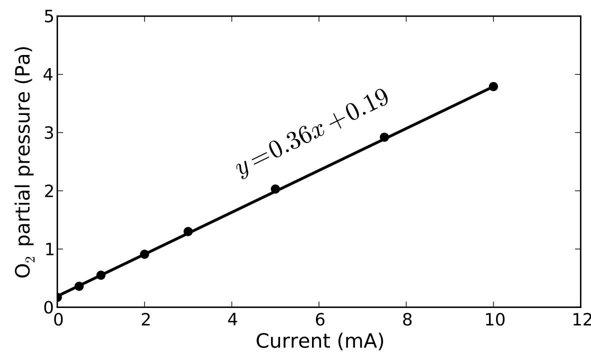

Figure 2.14. *Calibration measurement of the oxygen pump: oxygen partial pressure as a function of electrical current through the oxygen pump for a He flow of 1000 sccm.*

He since this gas has a higher thermal conductivity, resulting in an increased cooling of the pump. The location of the oxygen pump on the gas panel is shown in figure 2.13.

To ensure the relation between current and oxygen partial pressure, a calibration experiment was performed for validation. In this experiment a fixed He flow of 1000 sccm was set using the rotameter, while varying the current through the oxygen pump. The oxygen partial pressure was read out from the oxygen sensor. Figure 2.14 confirms the expected linear relation between the applied current and the oxygen partial pressure. From the slope it is concluded that per mA of electric current the oxygen partial pressure increases with 0.36 Pa, closely corresponding to the calculated value.

In addition to the current through the cell, the applied voltage over the cell was monitored. Above 5 mA it was observed that the voltage slightly increased over time. This is believed to be caused by depletion of oxygen at the air side of the pump, since air can only slowly penetrate through the insulation of the electrical wires towards the reference electrode. Up to 4 mA this was not observed, even for many hours of operation.

To conclude, the use of the zirconia oxygen pump in combination with a constant current supply and inert gas flow enables precise and reliable control of the oxygen partial pressure. Since the minimal adjustable flow range of the rotameter is approximately 100 sccm, and the maximum current through the pump is 4 mA, only oxygen partial pressures up to approximately 15 Pa can be obtained using this set of equipment.

- **Mass flow controllers:** Alternatively, mass flow controllers (MFC) were installed to allow for gas mixing. A mass flow controller is a closed-loop device that sets, measures, and controls the flow of a particular gas (or liquid). By combining mass flow controllers, gases can be mixed very accurately. Typically a mass flow controller is calibrated for a specific gas and is

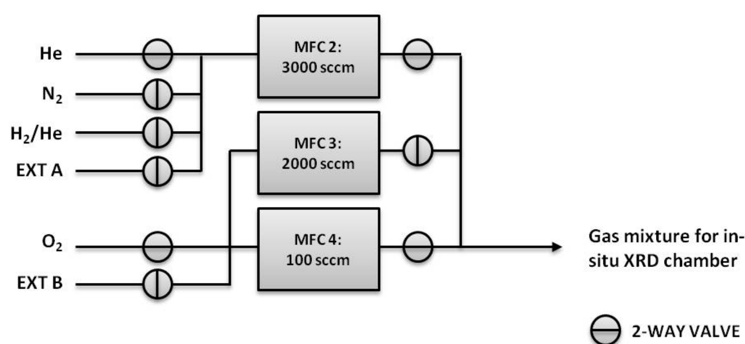

Figure 2.15. *Configuration of the mass flow controllers of the second gas mixing panel at the in-situ XRD system.*

designed for a certain flow range. Operation is most accurate in between 10 and 90 % of its full range. When using a MFC with another gas, a correction factor should be used to account for the difference in thermal conductivity, which affects the measurement of the flow. Figure 2.15 shows the construction of the gas mixing panel. Inert and reducing gases share the same MFC with a full range of 3000 sccm, while oxidizing gases are passed to two mass flow controllers with full ranges of 100 and 2000 sccm. This allows to control the oxygen partial pressure in a wide range from pure oxygen down to approximately 0.4%, i.e. 400 Pa. Lower oxygen partial pressures are obtained by connecting a gas bottle with oxygen diluted in inert gas (position "EXT B" in figure 2.15).

2.4 In-situ X-Ray diffraction during annealing

In situ is a Latin phrase that translates literally to *on site* or *in position*. It means *locally*, *on site*, *on the premises* or *in place* to describe an event where it takes place, and is used in many different contexts.[35] In this work, *in-situ* refers to the action of gathering physical or chemical information of a material while it is being synthesized or while it is subject to a certain process. Examples are the measurement of the thickness of a thin film during its growth from the gas phase, determination of the crystal structure during a thermal process and measurement of the optical and electronic properties as a function of temperature.

The use of in-situ characterization techniques offers several advantages. In thin film synthesis, the influence of deposition parameters on the growth behavior can be investigated in a fast way. Conventional methods rely on performing a series of depositions, only varying one parameter (e.g. temperature, pressure, exposure time) every deposition, and measuring the thin film properties after the deposition. This involves much experimental effort and requires a lot of samples, gases and chemicals. By performing in-situ characterization, the influence of all these parameters can be evaluated in a few experiments or in the best case in only one single experiment. The same holds for investigation of the parameters of thermal processing. Often a series of identical samples is processed at various temperatures or annealing times, after which all samples are measured one by one. Again this is a time-consuming job which can be drastically shortened by using in-situ characterization. In addition, meta-stable or transient phases are often not detected by the conventional methods. In-situ characterization also enables fast study of kinetics such as diffusion and nucleation kinetics in solid-state or gas-solid reactions.[36;37]

X-ray diffraction (XRD) is a technique enabling the determination of crystal structures by diffraction of X-rays on a crystal lattice. In most cases such measurements are performed at ambient conditions, i.e. at room temperature and atmospheric pressure. During in-situ XRD the effect of non-standard conditions on the crystal structure is investigated. A straightforward example is the determination of thermal expansion coefficients, as the temperature affects the lattice spac-

ings in the crystal. Many dedicated experimental systems have been developed for enabling the controlled variation of temperature, pressure, stress and humidity during XRD measurements. During the last decades such systems have also emerged commercially.

For the research covered in this thesis, a few topics have been investigated by in-situ XRD. The first one is the study of gas-solid reactions for the synthesis of VO_2 by oxidation and reduction reactions in the V-O system (chapter 3, section 3.2) and the synthesis of VN by nitridation of vanadium (chapter 4, section 4.2). A second topic covers the crystallization of amorphous vanadium oxide thin films grown by ALD (chapter 3, section 3.3). A third topic is the study of structural changes during the semiconductor-metal transition in VO_2 thin films (chapter 3, sections 3.2 and 3.3). Finally in-situ XRD is used to study the effectiveness of VN thin films as copper diffusion barriers (chapter 4, section 4.3).

Two important parts are required for an in-situ XRD setup: the XRD system including X-ray source, detector and goniometer, and a dedicated in-situ system for variation of the experimental conditions. In the following sections these are discussed in more detail.

2.4.1 XRD systems

The basic requirements for performing XRD measurements are an X-ray source and detector and a goniometer. This holds as well for in-situ XRD experiments. However, the purpose of in-situ XRD is to gather diffraction patterns while changing experimental conditions. If a large parameter space needs to be investigated and a high parameter resolution is desired, fast data collection becomes important. This is the reason why initially most in-situ XRD results were collected at

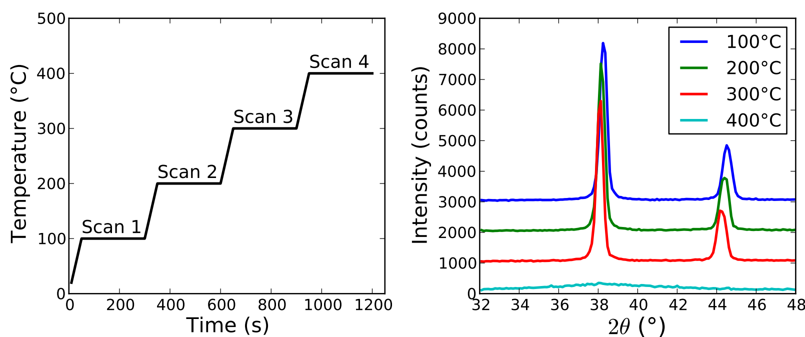

Figure 2.16. *Stepwise in-situ XRD: the temperature has a stepwise profile (left) and scanning XRD measurements are performed during the isothermal periods. The result is a limited series of XRD scans at well-defined temperatures (right). The data correspond to a measurement of a thin film of 50 nm Au on Si, indicating the eutectic temperature between 300 and 400 °C.*

synchrotron facilities, where the high photon flux enables drastically shorter measurement times compared to laboratory XRD systems.

In the simplest configuration a point detector is used, which requires source or sample stage and detector to move over the desired ranges to perform a scan of the diffraction pattern. Under laboratory conditions each measurement can easily take several minutes, or even hours in the case of very thin films. For temperature-dependent XRD for instance, the sample temperature can be increased stepwise, and XRD scans are taken during isothermal periods, as shown in figure 2.16. Due to the long data collection time for each measurement, the number of temperature steps should be limited to allow for a reasonable time to finish one in-situ XRD experiment. In such a way it is difficult to extract the precise temperatures at which reactions are occurring, while on the other hand phases or crystal structures which only appear in small temperature regions can be easily overlooked. Furthermore, if reactions are occurring within an isothermal region, data will be difficult to interpret. In fact, it may even not be appropriate to use the term in-situ in such cases.

To mitigate these limitations, the use of a linear (or area) detector is highly recommended. Linear detectors can operate in *snapshot mode*, meaning that both X-ray source, sample and detector are kept at fixed position during measurement. Each channel of the detector corresponds to a certain 2θ value, depending on source and detector position and the geometry of the detector. An important remark is that this approach is only suitable for diffraction measurements on powders or polycrystalline materials. Since the acquisition time is on the order of seconds or even shorter, it allows for measuring during temperature ramp profiles, as shown in figure 2.17, resulting in true in-situ XRD experiments with a fine temperature resolution.

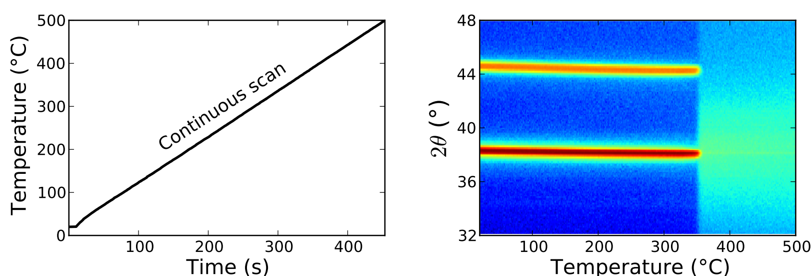

Figure 2.17. *Continuous in-situ XRD: the temperature is increased at a constant rate (left), while XRD snapshots are collected every few seconds. The result is a large dataset, typically visualized in a 2D colorplot (right) with temperature on the x-axis, 2θ values on the y-axis and counts indicated using a color scale. The data correspond to a measurement of a thin film of 50 nm Au on Si, indicating the eutectic temperature near 360 °C.*

2.4.2 In-situ reaction chambers: experimental and commercial systems

During several decades many research groups have developed experimental reaction chambers for the purpose of in-situ XRD. Apart from experimental in-situ chambers, a few companies such as Anton Paar and Edmund Bühler offer commercial reaction chambers for in-situ XRD. These include temperature stages from -193 °C up to 2700 °C, high-pressure cells up to 100 bar, chambers with controlled humidity, tensile stages,...[38;39]

2.4.3 In-situ XRD at UGent

A short history: During the last decade a lot of know-how was gathered in the field of in-situ XRD in the CoCooN research group. Before 2006 all experiments were performed at the National Synchrotron Light Source (NSLS) in the Brookhaven National Laboratory at New York, USA. A research group at IBM Research had built a system capable of heating small wafer samples up to a temperature of 1200 °C at maximum heating rates of 35 °C/s while performing phase identification via XRD.[40;41] The high photon flux at the beam line combined with a linear CCD detector, covering a 14° range in 2θ, enabled collection of XRD snapshots at acquisition times as short as 17 ms.

In 2006, Werner Knaepen built a first dedicated in-situ XRD setup in the CoCooN lab with the purpose of studying solid-state reactions.[41] A Bruker D8 Discover was used as the XRD system, containing a copper source which emits Cu$K\alpha$ radiation at a wavelength of 0.154 nm and a maximum power of 1.6 kW. Cu$K\beta$ radiation was stripped by a Göbel mirror, which as well transformed the divergent X-ray beam into a parallel beam. The spot size on the sample was around $5 \times 20\,\text{mm}^2$. A 1450 channel, linear Våntec-1 detector was used to perform in-situ XRD measurements in a similar *snapshot mode* as at the synchrotron setup. The maximum 2θ range was 21°at a distance of 100 mm from the center of the goniometer, leading to an angular resolution of 0.014°, while the minimum acquisition time was 100 ms. A home-built annealing chamber was placed in the center of the goniometer. The graphite heating element allowed for a maximum temperature of 1100 °C and heating rates up to approximately 10 °C/s, in inert and reducing gases. Simultaneous with in-situ XRD, sheet resistance measurements could be performed using 4 probes.

Annealing chamber for oxidizing conditions: With the objective of also being able to perform annealing experiments in oxidizing environments, as required for the topic of this thesis, a new experimental in-situ XRD chamber was developed within this work. A schematic illustration is shown in figure 2.18. The new setup allowed for maximum temperatures up to 1100 °C and maximum heating rates of 5 °C/s. High-temperature annealing in both inert, reducing and oxidizing atmospheres are thus possible for samples with maximum dimensions of 50×30 mm^2. An improved window design allowed for X-ray transmission while retaining pure

gas conditions in the annealing chamber. Prior to introducing the desired gas mixture, the chamber is typically pumped down to a low vacuum of 1 Pa by means of a rotary vane pump. Introduction of gas mixtures with controlled oxygen partial pressure was already discussed in section 2.3. During the experiments, the total pressure was kept slightly above atmospheric pressure, i.e. 10^5 Pa.

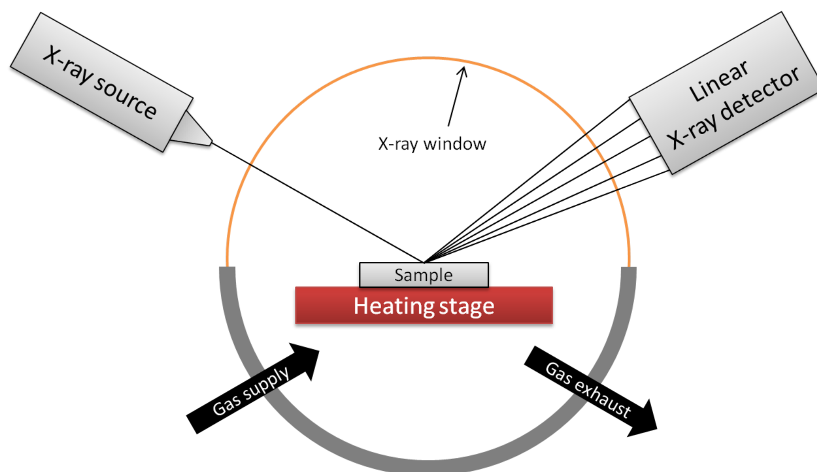

Figure 2.18. *Schematic illustration of the in-situ XRD annealing chamber.*

Temperature calibration: One of the most critical parameters during in-situ XRD experiments is the temperature. A K-type thermocouple is used for temperature measurement in between the heaters and the sample. The exact sample temperature deviates slightly from the measured value, and therefore a calibration is required. For this purpose, the eutectic systems Au-Si, Al-Si and Ag-Si have been used. Above their respective eutectic temperatures (363, 577 and 835 °C) Au, Al and Ag form liquid mixtures with Si, while below these temperatures, these metals are observed in their pure and crystalline form. By monitoring the XRD patterns as a function of temperature, the eutectic transition, observed as a disappearance of the diffraction peaks of Au, Al and Ag, enables to link the measured temperature to the real sample temperature. Two additional calibration points are added, one at room temperature and one by an extrapolation to 1200 °C. Through these 5 points, an interpolation is made to calibrate all temperatures in the range from room temperature up to 1200 °C. Several calibrations are used, since the heating rate and type of gas have an additional influence on the difference in measured and real sample temperature.

Example: As an example of the research performed within this thesis, figure 2.19 shows the oxidation of 80 nm sputtered vanadium towards different vanadium oxide phases, during temperature increase of 0.25 °C/s. Depending on the oxygen

partial pressure, different phases are formed, including V_2O_5, V_3O_7, V_6O_{13} and VO_2. These results will be discussed in detail in chapter 3, section 3.2.

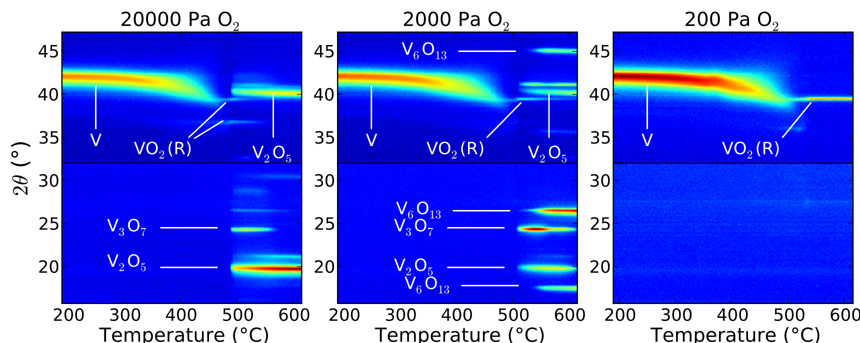

Figure 2.19. *Example of in-situ XRD for the study of the oxidation of a vanadium film of 80 nm upon thermal annealing in various oxygen partial pressures, at a temperature increase of 0.25 °C/s.*

2.5 Characterization of the semiconductor-metal transition

As explained in the introductory chapter (section 1.2), the semiconductor-metal transition in VO_2 is characterized by both a structural and an electronic transition. Three complementary techniques were developed in the lab for the study of this transition. These are explained in the next sections.

2.5.1 Temperature-dependent XRD

The in-situ XRD technique, as explained in the previous section, allows for the distinction between the low-temperature monoclinic VO_2(M1) phase and the high-temperature tetragonal (rutile) VO_2(R) phase. In the same setup as used for the annealing processes for oxidation of V and crystallization of amorphous VO_2, thermal cycles were applied on these crystalline films, between room temperature and 110 °C. Figure 2.20(a) shows such a measurement on a VO_2 film of 170 nm. The two strong peaks clearly shift in peak position between temperatures of 60 °C and 70 °C during heating and between 60 °C and 50 °C during cooling. Figures 2.20(b) and (c) represent the fitted peak positions related to these two peaks, as a function of temperature. The shift and a hysteresis of approximately 10 °C are very clear. Typical measurements were performed at a heating and cooling rate of 0.1 °C/s, while the collection time was 10 s. The temperature resolution is thus 1 °C. For thinner films, certainly the ALD films of less than 10 nm, the peak intensity was however too low for a high quality fit.

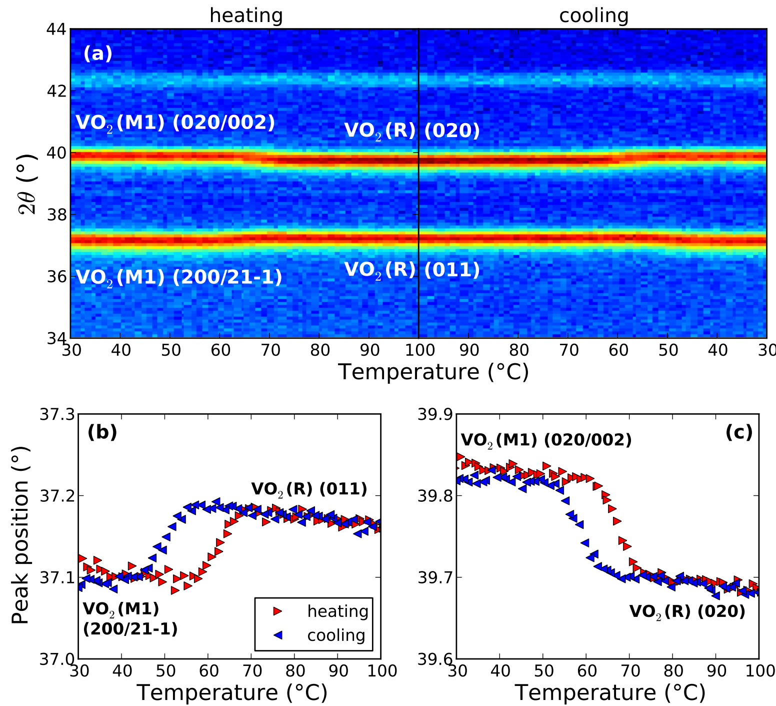

Figure 2.20. *Temperature-dependent XRD measurement during thermal cycling of a 170 nm VO_2 thin film at fixed heating and cooling rates of 0.1 °C/s: (a) in-situ XRD scan during heating (left panel) and cooling (right panel), (b-c) fitted diffraction peak positions as a function of temperature.*

2.5.2 Temperature-dependent sheet resistance measurements

Similar to the temperature-dependent XRD measurements, sheet resistance was measured on the VO_2 thin films during thermal cycling between room temperature and 110 °C. Similar heating and cooling rates were used. Four spring probes in a square configuration with an interprobe distance of a few mm were clamped on the sample. A HP-2601A source-measure unit was used to set a fixed current through two of the probes of 1×10^{-5} A with a voltage threshold of 10 V, while measuring the voltage over the two other probes. The fast acquisition time allowed for a finer temperature resolution compared to XRD. Sheet resistance is expressed in Ω/square and is obtained by dividing the measured voltage by the applied current, and multiplying this value by a correction factor which depends on the probe configuration. A correction factor of 10.5 was determined by the measurement of a calibration sample.

Figure 2.21 shows the example of such a temperature dependent sheet resistance measurement on a 170 nm VO_2 film. Note that a minimal condition for a suc-

cessful sheet resistance measurement is the need for a continuous film. In cases where agglomeration of the film occurs, and separate nanoparticles are created, sheet resistance measurements are not possible, and one should rely on other techniques to visualize the transition, such as XRD or ellipsometry (explained in the next section). Measurement of electrical properties in nanoparticles may be possible by e.g. conductive atomic force microscopy (CAFM) in case the nanoparticles are synthesized on a conductive substrate. For this research however, only changes in the optical properties of nanoparticles were monitored, by spectroscopic ellipsometry, as discussed in the next section.

Apart from VO_2, V_2O_3 thin films have as well been prepared in this work. This material shows a semiconductor-metal transition near -108 °C. A cryogenic system allowed for sheet resistance measurements down to approximately -160 °C by liquid nitrogen cooling. Results will be presented in chapter 3, section 3.2.

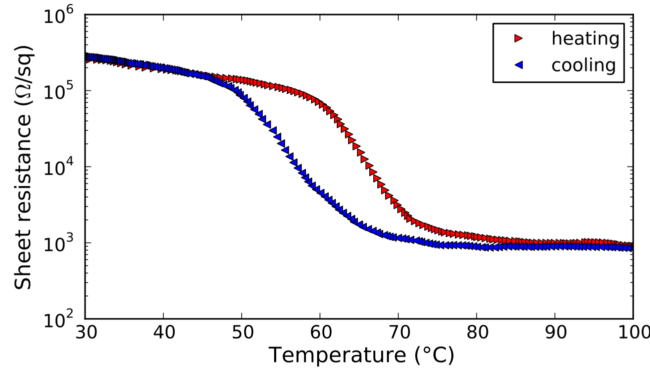

Figure 2.21. *Temperature-dependent sheet resistance measurement during thermal cycling of a 170 nm VO_2 thin film at fixed heating and cooling rates of 0.1 $°C/s$.*

2.5.3 Temperature-dependent spectroscopic ellipsometry

Ellipsometry is an optical characterization technique for studying the properties of thin films, including optical constants, thickness, roughness,... It is based on the interaction of polarized light with a material and its surface and interfaces, as illustrated in figure 2.22.[35;42] More precisely, when a polarized beam is reflected from the sample, the change in polarization state is characterized by the ellipsometric parameters Ψ and Δ:

$$tan(\Psi) \cdot e^{i\Delta} = \rho = \frac{r_p}{r_s}. \tag{2.38}$$

Here, ρ is defined as the ratio of the reflectivity for p-polarized light to the reflectivity for s-polarized light. $tan(\Psi)$ represent the magnitude of the reflectivity ratio, Δ the phase.

Although single-wavelength systems exist, most information is obtained from spectroscopic ellipsometry (SE), in which a broad band light source is used.[43] The

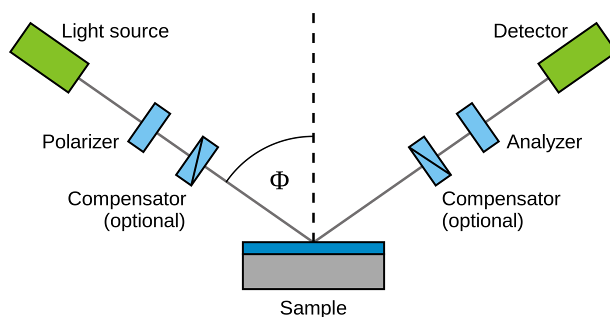

Figure 2.22. *Schematic setup of an ellipsometry measurement.*

data that is generated needs to be analyzed by an appropriate model which takes into account the optical constants, layer thicknesses and sequences of layers. Although optical models for VO_2 thin films have been reported,[44] these did not seem to match with the data of the ALD films prepared during this work. The use of in-situ ellipsometry during the ALD growth of vanadium oxide thin films was therefore not successful. Nevertheless, even without an appropriate model, ellipsometry enables the characterization of phase transitions, including the semiconductor-metal transition in VO_2.[45;46] Due to the sensitivity of this technique, and the fast data collection time on the order of a few seconds, ellipsometry is used in this work to monitor the transition in both thin films and nanoparticles of VO_2. The characterization is however limited to the determination of the transition temperature and hysteresis width. Figure 2.23 shows a typical measurement during a thermal cycle between room temperature and 110 °C. The ellipsometric parameter Ψ is plotted as a function of temperature. Here, only the value of Ψ at a wavelength of 500 nm is considered, since it was observed that the transition temperature does not vary

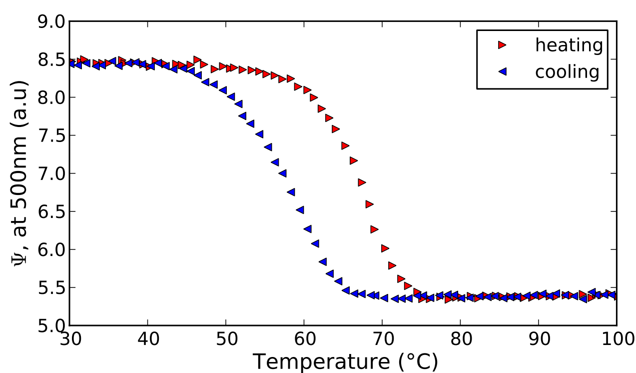

Figure 2.23. *Temperature-dependent ellipsometry measurement during thermal cycling of a 170 nm VO_2 thin film at fixed heating and cooling rates of 0.1 °C/s.*

significantly with the wavelength.

References

[1] D. Depla and S. Mahieu, *Reactive sputter deposition*, Springer series in materials science. Springer, (2008).
[2] P. J. Kelly and R. D. Arnell, *Vacuum* **56**(3), 159–172 (2000).
[3] C. Detavernier, J. Dendooven, S. P. Sree, K. F. Ludwig, and J. A. Martens, *Chem. Soc. Rev.* **40**(11), 5242–5253 (2011).
[4] R. L. Puurunen, *J. Appl. Phys.* **97**(12), 121301 (2005).
[5] S. M. George, *Chem. Rev.* **110**(1), 111–131 (2010).
[6] V. Miikkulainen, M. Leskelä, M. Ritala, and R. L. Puurunen, *J. Appl. Phys.* **113**(2), 021301 (2013).
[7] A. A. Malygin, *J. Ind. Eng. Chem.* **12**(1), 1–11 (2006).
[8] T. Suntola and J. Antson, (1977), US Patent 4,058,430.
[9] M. Gutsche, H. Seidl, T. Hecht, S. Kudelka, and U. Schroeder, *Future Fab. Int.* **14**, 1009 (2003).
[10] I. J. Raaijmakers, *ECS Trans.* **41**(2), 3–17 (2011).
[11] A. J. M. Mackus, A. A. Bol, and W. M. M. Kessels, *Nanoscale* **6**(19), 10941–10960 (2014).
[12] P. Poodt, D. C. Cameron, E. Dickey, S. M. George, V. Kuznetsov, G. N. Parsons, F. Roozeboom, G. Sundaram, and A. Vermeer, *J. Vac. Sci. Technol. A* **30**(1), 010802 (2012).
[13] www.levitech.nl, Accessed: 2015-11-06.
[14] www.solaytec.com, Accessed: 2015-11-06.
[15] www.beneq.com, Accessed: 2015-11-06.
[16] E. W. Kessels and M. Putkonen, *MRS Bulletin* **36**(11), 907–913 (2011).
[17] H. B. Profijt, S. E. Potts, M. C. M. Van de Sanden, and W. M. M. Kessels, *J. Vac. Sci. Technol. A* **29**(5), 050801 (2011).
[18] J. Musschoot, *Advantages and challenges of plasma enhanced atomic layer deposition*, PhD thesis, Ghent University, (2011).
[19] G. Silversmit, D. Depla, H. Poelman, G. B. Marin, and R. De Gryse, *J. Electron Spectrosc.* **135**(2-3), 167–175 (2004).
[20] http://webbook.nist.gov/chemistry/, Accessed: 2015-11-20.
[21] Y.-B. Kang, *J. Eur. Ceram. Soc.* **32**(12), 3187–3198 (2012).
[22] H. J. T. Ellingham, *J. Soc. Chem. Ind.* **63**, 125 (1944).
[23] B. E. Deal and A. S. Grove, *J. Appl. Phys.* **36**(12), 3770 (1965).
[24] E. A. Gulbransen and K. F. Andrew, *J. Electrochem. Soc.* **97**(11), 396–404 (1950).
[25] W. R. Price and J. Stringer, *J. Less-Common Met.* **8**, 165–185 (1965).
[26] W. R. Price, S. J. Kennett, and J. Stringer, *J. Less-Common Met.* **12**, 318–325 (1967).
[27] A. Mukherjee and S. P. Wach, *J. Less-Common Met.* **92**, 289–300 (1983).
[28] A. Mukherjee, *J. Less-Common Met.* **107**, 89–97 (1985).
[29] A. Mukherjee and S. P. Wach, *J. Less-Common Met.* **132**, 107–113 (1987).
[30] G. Salomonsen, N. Norman, O. Lonsjo, and T. G. Finstad, *J. Less-Common Met.* **158**, 251–265 (1990).

[31] K. Naito, T. Tsuji, T. Matsui, and K. Une, *J. Nucl. Sci. Technol.* **11**(1), 22–28 (1974).

[32] J. Dwyer Jr, J. G. Hansel, and T. Philips, *Temperature influence on the flammability limits of heat treating atmospheres*, ASM International (2003).

[33] A. Bolind, *Control of oxygen partial pressure of the cover gas in a molten lead-bismuth eutectic system*, PhD thesis, University of Illinois at Urbana-Champaign, (2006).

[34] K. Naito, T. Tsuji, and Y. Asakura, *J. Nucl. Sci. Technol.* **12**(5), 314–319 (1975).

[35] www.wikipedia.org.

[36] W. Knaepen, C. Detavernier, R. Van Meirhaeghe, J. Jordan Sweet, and C. Lavoie, *Thin Solid Films* **516**(15), 4946–4952 (2008).

[37] W. Knaepen, S. Gaudet, C. Detavernier, R. L. Van Meirhaeghe, J. J. Sweet, and C. Lavoie, *J. Appl. Phys.* **105**(8), 083532 (2009).

[38] www.anton-paar.com, Accessed: 2015-11-07.

[39] www.edmund-buehler.de, Accessed: 2015-11-07.

[40] D. Deduytsche, *An in-situ study of the stability of thin film Ni-silicide layers*, PhD thesis, Ghent University, (2006).

[41] W. Knaepen, *Characterization of solid state reactions and crystallization in thin films using in situ X-ray diffraction*, PhD thesis, Ghent University, (2010).

[42] www.jawoollam.com, Accessed: 2015-11-07.

[43] K. Vedam, *Thin solid films* **313**, 1–9 (1998).

[44] H. Kakiuchida, P. Jin, S. Nakao, and M. Tazawa, *Jpn. J. Appl. Phys.* **46**(5), L113 (2007).

[45] A. Dejneka, I. Aulika, V. Trepakov, J. Krepelka, L. Jastrabik, Z. Hubicka, and A. Lynnyk, *Opt. Express* **17**(16), 14322 (2009).

[46] M. Nagashima and H. Wada, *Thin Solid Films* **312**(1), 61–65 (1998).

3

Synthesis and characterization of VO_2 thin films

In this chapter the synthesis and characterization of VO_2 thin films is discussed. First, section 3.1 gives a non-exhaustive literature overview of existing approaches to deposit vanadium dioxide (and other vanadium oxide) thin films. A few techniques will be discussed in detail, including reactive sputtering, oxidation of V and reduction of V_2O_5 films, CVD and ALD. In section 3.2 the results are discussed on the oxidation of V and the reduction of V_2O_5 as obtained during this thesis. Section 3.3 summarizes the experimental work on ALD of VO_2. In the appendix, four papers are included that were published on these topics.

3.1 Literature on thin film VO_2 synthesis

Many techniques are available for the synthesis of vanadium oxide thin films. However, the complexity of the V-O phase diagram raises difficulties in obtaining pure vanadium oxide phases of desired stoichiometry. In the next sections, a literature overview is presented on vanadium oxide thin film deposition by sputtering, oxidation of V and reduction of V_2O_5 films, CVD and ALD, since these techniques are widely applicable for industrial processes such as in microelectronics and coatings on glass, requiring large area uniform coatings. Other techniques such as sol-gel, pulsed laser deposition (PLD) and molecular beam epitaxy (MBE) have as well been reported,[1–7] but these will not be treated.

3.1.1 Reactive sputtering

Sputtering is a type of physical vapor deposition (PVD), and has been described in detail in chapter 2, section 2.1.1. Metallic vanadium can easily be sputtered with argon in DC (direct current) mode. The synthesis of other vanadium oxide thin films is established using DC or RF (radiofrequent) reactive sputtering in oxygen-argon mixtures, from both metallic V targets and vanadium oxide targets.[8] Films of various stoichiometries have been deposited, such as V_2O_5, VO_2 and V_2O_3.[9–12;12–15] A short summary of some relevant publications on VO_2 sputter depositions is listed below:

- Duchene et al. applied both DC and RF magnetron sputtering on a vanadium target in argon-oxygen mixtures around 3×10^{-1} Pa total pressure.[10] Metallic films were grown for O_2/Ar ratios below 5%. Above 6% the deposition rate decreased significantly and low-resistive semiconducting materials were deposited, assigned to V_3O_5 and V_4O_7. At 10% O_2, amorphous VO_2 was deposited which did not show a semiconductor-metal transition. Substrate heating was required for achieving crystalline phase formation during film growth, with an optimum substrate temperature between 400 °C and 450 °C, resulting in VO_2 layers that exhibited 3 orders of magnitude resistance switching at a film thickness of 120 nm.

- Griffiths and Eastwood did a thorough study on the impact of both oxygen partial pressure and substrate temperature on the stoichiometry of vanadium oxide thin films prepared by RF reactive sputtering in argon-oxygen mixtures from a vanadium target.[11] A minimum in the unit-cell volume could be linked to the stoichiometry closest to VO_2, which as well corresponded to a maximum in the resistivity ratio across the semiconductor-metal transition.

- Brassard et al. studied the effect of grain size on the semiconductor-metal transition in VO_2 thin films prepared by reactive RF sputtering in argon-oxygen (10%) around 3×10^{-1} Pa and 500 °C.[13] The grain size decreased drastically when the film thickness was reduced, resulting in suppression of the resistance switching ratio from 3.2 orders of magnitude (350 nm) down to 2 orders of magnitude (50 nm).

- Shigesato et al. studied the deposition of VO_2 by reactive RF magnetron sputtering from V, V_2O_3 and V_2O_5 targets.[12] In the case of reactive sputtering using a V-metal target, VO_2 films could be obtained only under the very narrow deposition conditions of the transition region where the deposition rate decreases drastically with increasing oxygen gas flow rate. In the case of a V_2O_3 target, VO_2 films were obtained by the introduction of oxygen gas [O_2/(Ar+O_2)=1-1.5%], whereas hydrogen gas [H_2/(Ar+H_2)=2.5-10%] was required in the case of a V_2O_5 target.

In general, V and V_2O_5 can be easily sputter deposited without much optimization. In contrast, sputter deposition of VO_2 requires a precise control of the oxygen

partial pressure during sputtering. Substrate heating around 400 °C to 500 °C is required to obtain crystalline thin films. The complexity of process conditions is one of the reasons why during this thesis metallic vanadium layers have been sputtered, while VO_2 is synthesized by post-deposition annealing, as discussed in section 3.2 and paper I.

3.1.2 Oxidation of V and reduction of V_2O_5

Literature on the synthesis of VO_2 by gas-solid reactions in the V-O system is mainly limited to oxidation of V in pure O_2 at atmospheric pressure or in air, and reduction of V_2O_5 in H_2 gas. Most papers have been published during the past 5 years. The following list summarizes the most relevant publications:

- Salomonsen et al. studied the kinetics of V oxidation at 370 °C in dry O_2 gas at atmospheric pressure.[16] V films of 100 nm were prepared by e-beam evaporation. During oxidation, two layers of vanadium oxides were observed by RBS: a V_2O_5 layer at the surface and a V_6O_{13} layer in between the V_2O_5 and the V film. The layers gradually shifted downwards during the oxidation process.

- Xu et al. studied the oxidation of DC magnetron sputtered V films of 100 nm thickness in ambient air.[17] A temperature range from 420 to 510 °C was investigated. A relation was established between the optimal oxidation time and the inverse of the temperature. For instance, at 480 °C, 295 s were required for converting V into VO_2, whereas longer oxidation times would result in V_2O_5 formation. Under these optimized annealing times, between 2 and 3 orders of magnitude change in sheet resistance was observed.

- Liang et al. as well studied oxidation of DC magnetron sputtered V films.[18] The V film thickness was varied from 70 to 120 nm. Oxidation was carried out at 450 °C for 180 s in pure O_2 at atmospheric pressure. XPS showed the presence of different V valences (+3/+4/+5). The ratio between the different fractions varied depending on the film thickness. In all cases the major fraction was related to V^{4+}. Although an electrical transition was observed, it was limited to less than one order of magnitude switching ratio.

- Kim et al. investigated the reduction of ALD grown V_2O_5 films towards VO_2.[19] The reduction process was carried out in 2% H_2 at 350 °C for 6 hours. XPS showed a shift in binding energy of the $V2p_{3/2}$ level, attributed to the transformation from a V^{5+} to a V^{4+} valence, i.e. reduction from V_2O_5 towards VO_2. The semiconductor-metal transition was however not characterized.

3.1.3 Chemical vapor deposition

Chemical vapor deposition (CVD) is a gas-phase deposition technique, in which the substrate is exposed to one or more volatile precursors. These react or decom-

pose at the substrate surface, resulting in growth of a thin film. Due to the high deposition rates and wide range of available processes it is a very popular coating technique. Compared to sputtering (and other PVD techniques), CVD has the ability of coating 3-dimensional objects, although less conformal with respect to ALD. CVD however requires high substrate temperatures and the uniformity of the coating is very sensitive to temperature variations and gas distribution in the reaction chamber.

Deposition of V_2O_3, VO_2 and V_2O_5 by CVD is well established. Table 3.1 gives a non-exhaustive list of reported CVD processes. Many precursors are available, including chlorides, acetylacetonates and isopropoxide. A more thorough literature overview of vanadium oxide CVD processes has been recently reported by Bahlawane and Lenoble.[20]

Precursor	Reactant(s)	Temperature (°C)	VO_x phases	References
VCl_4	H_2O	400-550	V_2O_5, VO_2, V_6O_{13}	21
$VOCl_3$	H_2O	350-600	V_2O_5	22
Vanadyl-	-	530	VO_2	23
tri(isopropoxide)	air	400	V_2O_5	23
Vanadyl-	-	300-700	VO_2	24
tri(isobutoxide)	O_2	600	VO_2	24
$VO(acac)_2$	O_2	370-520	VO_2(M1), VO_2(B), VO_2(A)	25;26
	methanol + H_2O	500-600	V_2O_3, VO_2, V_2O_5	27
	ethanol	500-600	V_2O_3, VO_2, V_2O_5	27
$V(acac)_3$	methanol + H_2O	500-600	V_2O_3, VO_2 + other phases	27
	ethanol	500-600	V_2O_3, VO_2 + other phases	27
$V(acac)_4$	-	420	V_2O_3	28
	O_2	400	VO_2	28
	O_2	340	V_2O_5	28

Table 3.1. *Literature overview of CVD processes for vanadium oxides.*

3.1.4 Atomic layer deposition

Atomic layer deposition of vanadium oxides was first studied for catalytic applications and for Li-ion batteries. In these cases V_2O_5 was the phase of interest.[29–37] V_2O_5 is easily obtained with the vanadyl-tri(isopropoxide) precursor.[29;30;35–37] Furthermore, post-deposition annealing of other vanadium oxide phases in air are expected to result in V_2O_5. Some ALD processes for VO_2 have as well been reported prior to the research of this thesis, but the results may be questionable, as discussed below. ALD of vanadium oxides with vanadium valences lower than +4, such as V_2O_3, have not been reported yet. The following ALD processes have been reported:

- Most depositions of vanadium oxides by ALD have been performed with vanadyl-tri(isopropoxide) ($VO(O(C_3H_7))_3$, $VO(O^iPr)_3$, denoted as VTIP) as metal-organic vanadium precursor, which results in V_2O_5 thin films (see table 3.2).[29;30;35–37] Reported deposition temperatures are in the range from 50 °C to 200 °C. Depending on the reactant, the growth rate varies from 0.1

to 0.7 Å per cycle (Figure 3.1). H_2O and H_2O plasma result in amorphous layers, and crystallization during post-deposition annealing occurs typically at temperatures above 400 °C. O_2 plasma and O_3 result in growth of crystalline V_2O_5 (Figure 3.2).

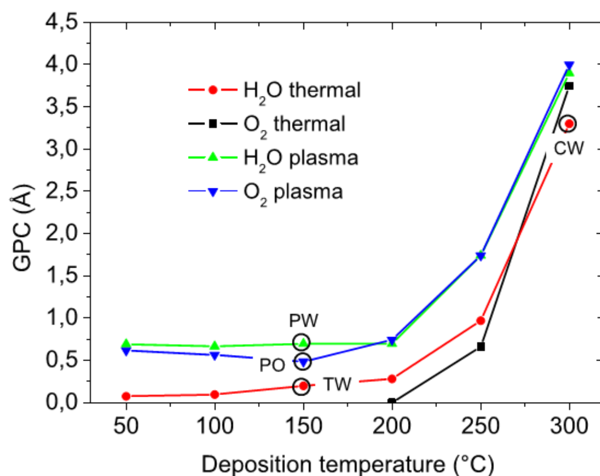

Figure 3.1. *Growth rate of vanadium oxide from VTIP precursor as a function of deposition temperature and reactant, as published by Musschoot et al.*[36] *(PW: plasma process with* H_2O*; PO: plasma process with* O_2*; TW: thermal process with* H_2O*, CW: CVD growth during thermal process with* H_2O*)*

- Østreng et al. deposited crystalline V_2O_5 from $VO(thd)_2$ and O_3 at 215 °C.[38] A non-linear growth was observed due to surface roughening of the crystalline film during deposition. The apparent growth rate increased from 0.1 to 0.4 Å per cycle.

- Dagur et al. deposited VO_2 from $VO(acac)_2$ and O_2 in the temperature range from 400 °C to 475 °C, which showed good resistance switching behavior up to 4 orders of magnitude.[39] Although it is stated to behave as an ALD process, no ALD characteristics were shown. The growth rate of 2.4 Å per cycle is high for ALD. Furthermore, the same temperature ranges are typically applied to perform CVD with this precursor. The constant growth per cycle could perhaps be explained by a limited precursor delivery to the reactor, which is not unlikely for a solid precursor like this one. Apart from this publication, no other results have been published using this precursor for ALD of vanadium oxides.

- The use of $VOCl_3$ with H_2O has been reported by Povey et al.[40] VO_2 was obtained at a temperature of 490 °C, but not as a pure phase. The observation of a mixture with higher oxide phases was reported. Details on the ALD characteristics were not shown.

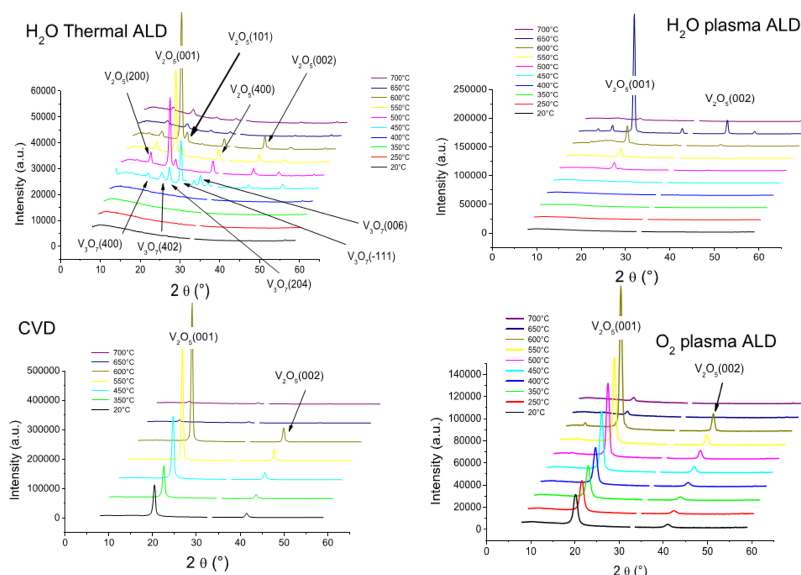

Figure 3.2. *Crystallization behavior of vanadium oxide films deposited from VTIP precursor for various reactants, as a function of post-ALD annealing temperature in O_2, as published by Musschoot et al.*[36]

- A more exotic ALD process was reported by Willinger et al., who used vanadyl tri-n-propoxide ($VO(O^nPr)_3$) and acetic acid at 200 °C.[41] From electron energy loss spectrometry (EELS) it was concluded that VO_2 was deposited. Again, no details on the growth characteristics are available.

In short, only processes for V_2O_5 have been well described in literature, whereas ALD of VO_2 has been reported but without explicit evidence of real ALD behavior. One of the assumptions that could be made, is that during an ideal ALD process which occurs via ligand exchange, the oxidation state of the metal atom is preserved. Therefore, the use of vanadium precursors with a V^{4+} valence would be advised for the growth of VO_2. Since the VTIP and $VOCl_3$ precursors have a V^{5+} valence, V_2O_5 is the expected vanadium oxide phase being grown. If these precursors would be used for deposition of VO_2, an additional reducing agent would be required during growth, transforming the V^{5+} into V^{4+}. Alternatively, the chemistry may result in V_2O_5 deposition, while vacuum conditions during the growth might cause in-situ reduction towards VO_2, certainly when the deposition temperature is rather high. In contrast, $VO(acac)_2$ has a V^{4+} valence, such that it is more plausible to deposit VO_2. However, the performance and ease of integration of an ALD process depends on some other parameters. Precursors for ALD should preferably show the following characteristics: (i) a high vapor pressure, which is often achieved for liquid precursors, but not for solids; (ii) a high reactivity, which enables fast saturation of the process; (iii) non-corrosive (and non-corrosive reac-

Table 3.2. *Literature overview of ALD processes for vanadium oxides. The papers published during this work are added as well.*

Precursor	**Reactant**	**Temperature ($^\circ$C)**	**Growth rate (Å/cycle)**	**VO_x phases**	**Crystallization temperature ($^\circ$C)**	**References**
$VO(O^iPr)_3$	H_2O	50-200	0.2	V_2O_5, V_3O_7	400-500	[29;30;35–37]
	H_2O plasma	50-200	0.7	V_2O_5	450-500	[36;37]
	O_2 plasma	50-200	0.7	V_2O_5	as deposited	[36;37]
	O_3	170-185	0.22-0.27	V_2O_5	as deposited	[42]
$VO(thd)_2$	O_3	215	0.1-0.4	V_2O_5	as deposited	[38]
$VO(O^nPr)_3$	CH_3COOH	200	0.4	VO_2	not reported	[41]
	H_2O	170-190	1.0	mixture	not reported	[43]
$VO(acac)_2$	O_2	400-475	2.4	VO_2(M1)	as deposited	[39]
$VOCl_3$	H_2O	490	not reported	VO_2(M1) + higher oxides	as deposited	[40]
TEMAV	O_3	100-175	0.3-2.9	VO_2(M1) / VO_2(B) / V_6O_{13} / V_2O_5	≈ 400	[44–48]
	H_2O	100-175	0.45-0.8	VO_2(M1) / V_2O_5	≈ 450	[46;48–50]
	O_2 plasma	100-175	1.5	V_2O_5 / VO_2(B) / V_6O_{13}	as deposited / ≈ 400 / ≈ 550	[44;48]

tion products). The first characteristic is not matched by the $VO(acac)_2$ precursor, while $VOCl_3$ does not meet the last one, since corrosive HCl is produced during reaction with H_2O.

ALD of VO_2 might thus be a tough task with the established precursors. A two-step synthesis process, involving ALD of V_2O_5 and a subsequent post-deposition reduction, could offer a solution. However, the question could rise which thermal budget, i.e. total amount of thermal energy (proportional to the temperature and duration of the process) would be required, and how this would affect the thin film morphology. Fortunately, during the past years, new metal-organic precursors have been developed which may be used for ALD of vanadium oxides (and nitrides). These include tetrakis(ethylmethylamino)vanadium [$V(N(C_2H_5)(CH_3))_4$, TEMAV], tetrakis(dimethylamino)vanadium [$V(N(CH_3)_2)_4$, TDMAV], tetrakis(diethylamino)vanadium [$V(N(C_2H_5)_2)_4$, TDEAV].[51–53] In this work, TEMAV is used for this purpose, which was developed by Air Liquide Electronics. The results are published in section 3.3 and papers II, III and IV.

Table 3.2 gives an overview of the reported ALD processes and their characteristics, where available. The data from this work, using the TEMAV precursor, are included as well.

3.2 Synthesis of VO_2 thin films by oxidation of vanadium and reduction of V_2O_5

This section summarizes the experimental work on the synthesis of vanadium oxide thin films by oxidation and reduction in the V-O system. The main objective was the formation of single-phase, crystalline VO_2(M1/R), starting from V or V_2O_5 which are easily deposited. V was deposited by magnetron sputtering, while V_2O_5 was obtained by high-temperature oxidation of these V layers in air, as discussed in section 3.2.2. For completeness, other observed phases such as V_6O_{13} and V_2O_3 will be highlighted as well in the next sections. The results are discussed in more detail in paper I.

3.2.1 Magnetron sputtering of vanadium thin films

Vanadium thin films were prepared on Si wafers, covered with SiO_2 or Al_2O_3 layers, by DC magnetron sputtering in Ar gas from a 3 inch vanadium target. Prior to the deposition, the PVD system was evacuated to a base pressure below 10^{-4} Pa. Ar was introduced at a pressure of 5×10^{-1} Pa and a power of 300 W was applied to the target. The samples were mounted on a rotating drum with diameter of 320 mm and a rotation speed of 10 rotations per minute. The distance between target and substrate was 105 mm. Under these conditions, a deposition rate of 4 nm per minute was achieved.

3.2.2 Oxidation of vanadium thin films in varying oxygen partial pressure

One route for the synthesis of VO_2 thin films was the controlled oxidation of metallic vanadium. For this purpose, vanadium layers of 20, 40 and 80 nm were oxidized under a wide range of oxygen partial pressures, at 20, 200, 2000 and 20000 Pa O_2. The oxygen partial pressure was regulated by means of mass flow controllers, as was discussed in chapter 2.

Ramp anneals: Temperature-programmed XRD with a heating rate of 0.25 °C/s was applied in a first set of experiments. It was concluded that during the initial stages of oxidation, which starts at temperatures between 300 °C and 400 °C, oxygen quickly dissolves in the vanadium layer, destroying the crystal structure and resulting in an undefined vanadium oxide layer. This initial step is followed by oxidation towards VO_2 at temperatures between 450 °C and 500 °C. The oxygen partial pressure is however determining the phase stability. Whereas at 20000 and 2000 Pa O_2 the VO_2 phase starts oxidizing towards the Wadsley phases V_6O_{13}, V_3O_7 and V_2O_5 at a temperature near 500 °C, VO_2 phase stability could be obtained at 200 and 20 Pa O_2. At these lowest O_2 partial pressures, V_2O_3 was observed as transient phase. Figure 3.3 shows the in-situ XRD measurements performed at 20000 and 20 Pa O_2.

It is concluded that VO_2 can in principle be obtained at all O_2 partial pressures in the range from 20 to 20000 Pa. However, the process window is very narrow, certainly at the high O_2 partial pressures where VO_2 is only observed as a transient phase. Therefore, it was chosen to perform a dedicated isothermal oxidation study over a wide range of oxygen partial pressures and temperatures.

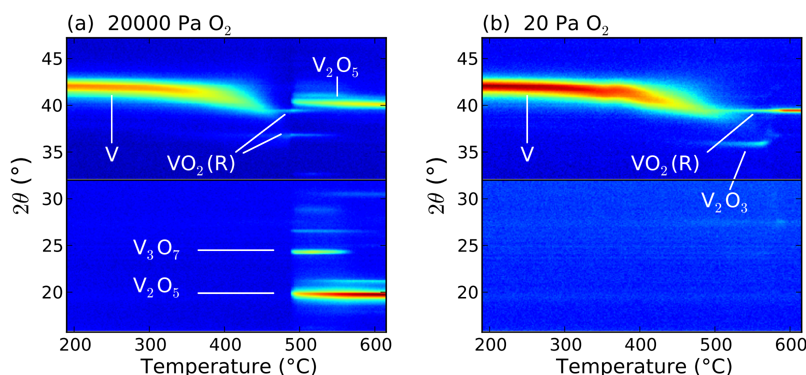

Figure 3.3. In-situ XRD measurements during thermal oxidation of 80 nm vanadium layers at a fixed heating rate of 0.25 °C/s in (a) 20000 Pa, and (b) 20 Pa O_2.

Isothermal anneals: Isothermal annealing experiments were performed in the wide temperature range from 430 °C to 615 °C and at varying oxygen partial pressures. Some relevant examples are shown in Figure 3.4. Stability of the VO_2 phase is observed only at 20 Pa O_2, in the temperature range from 480 °C to 570 °C. In contrast, the VO_2 layer further oxidizes at higher oxygen partial pressures. Single-phase V_6O_{13} is observed by oxidation at 200 Pa O_2 at 615 °C, whereas V_2O_5 is obtained by annealing in air starting at temperatures from 430 °C.

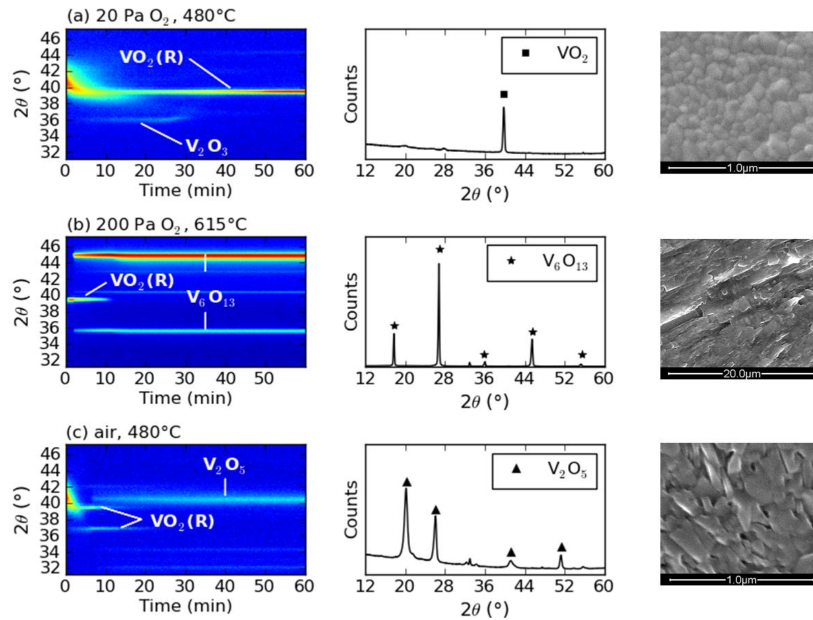

Figure 3.4. *Left column: in-situ XRD measurements during isothermal oxidation of 80 nm vanadium layers at various temperatures and oxygen partial pressures. Middle column: corresponding full XRD scans after oxidation. Right column: SEM images of the resulting thin films. (a,b,c) indicate conditions for stabilization of VO_2, V_6O_{13} and V_2O_5 respectively.*

Similar as observed during ramp annealing, the vanadium diffraction peak quickly disappears due to incorporation of oxygen in the film, followed by oxidation towards VO_2. From these observations it is concluded that a simple assumption of VO_2 growth on vanadium is not correct. Instead it is growing on an oxidized vanadium layer, such that a layered structure V/VO_2 cannot be manufactured via this route. This is in strong contrast with the oxidation of silicon, which is characterized by growth of a SiO_2 layer on top of silicon, with a sharp Si/SiO_2 interface (as discussed in chapter 2, section 2.3.2). Figure 3.5 schematically shows how the oxidation of V is believed to occur. In a first stage, the V thin film absorbs oxygen, with the formation of an undefined VO_x phase, with $x < 2$. The exact composition of this phase cannot be determined from the XRD measurements. However, in the case of oxidation at the lowest O_2 partial pressure of 20 Pa, a small

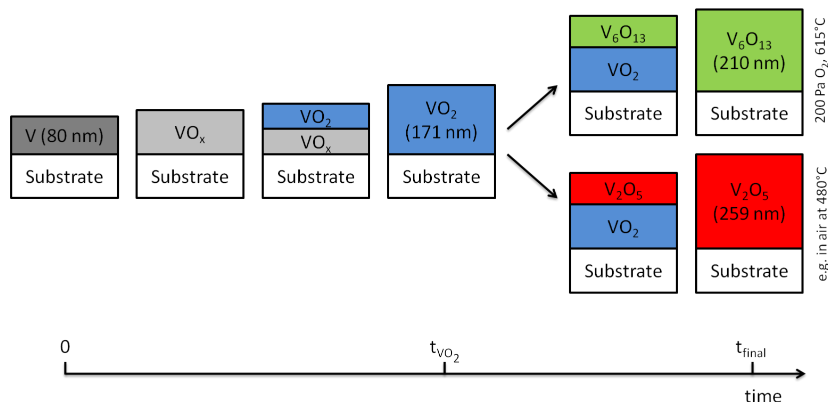

Figure 3.5. *Schematic representation of the oxidation of a V thin film.*

indication of crystalline V_2O_3 can be observed. In general, this undefined phase can even be a graded layer with a higher oxygen concentration at the top compared to the bottom. Once the V film has absorbed a sufficient amount of oxygen, VO_2 is formed at the surface, and this layer is growing with time. Depending on the O_2 partial pressure and temperature, the oxidation process stops when the complete film is transformed to VO_2, or oxidations continues towards the higher oxide phases V_6O_{13} or V_2O_5.

The in-situ XRD measurements were furthermore valuable to investigate the required oxidation time as a function of film thickness, temperature and oxygen partial pressure. For instance, to oxidize 80 nm vanadium towards VO_2 at 480 °C, approximately 3000 s and 400 s were required when annealing in 20 Pa O_2 and in

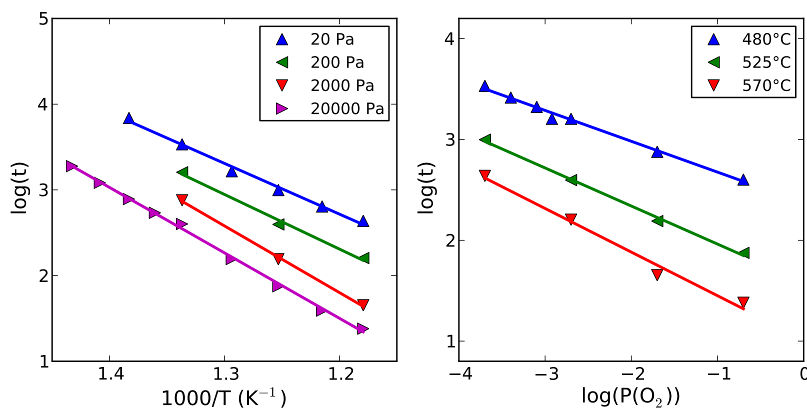

Figure 3.6. *Overview of the oxidation time to obtain a maximum VO_2 XRD peak intensity as a function of temperature and oxygen partial pressure for an 80 nm thick V film.*

air respectively (see figure 3.4(a,c)). Figure 3.6 shows the time required to reach a maximum VO_2 peak intensity in XRD as a function of temperature and oxygen partial pressure. In the case of a stable regime for VO_2, this corresponds to the point at which the complete V thin film is transformed to VO_2. In cases of higher oxygen partial pressures this corresponds to the point at which further oxidation towards V_6O_{13} or V_2O_5 is initiated. In Figure 3.5 this is indicated on the time bar as t_{VO_2}. The results show that the oxidation of a V thin film towards VO_2 is highly controllable by tuning the O_2 partial pressure and temperature. When these two parameters are fixed, the oxidation time can be derived from Figure 3.6.

Additional experiments on V films of 20 and 40 nm showed that the oxidation time is not linearly dependent on the film thickness: 200 s for 20 nm, 600 s for 40 nm and 3000 s for 80 nm V at 20 Pa O_2 and 480 °C. Oxidation processes often show a linear-parabolic growth, in which initially the oxidation rate is limited by oxygen uptake at the surface and oxidation reactions at the interface between the metal and the oxide layer, whereas for thicker oxide layers the rate is limited by diffusion of oxygen through the oxide layer. Such behavior has been described in detail by Deal and Grove for the case of thermal oxidation of silicon (see chapter 2, section 2.3.2).[54] Early publications on the oxidation of vanadium showed as well linear-parabolic growth.[55] The experimentally obtained oxidation times on 20, 40 and 80 nm V are a strong indication of such a linear-parabolic growth of VO_2.

It should however be noted that the deposited V film were polycrystalline. This means grain boundaries were present, such that oxidation not necessarily only takes place via diffusion through the growing oxide layer, but eventually also via grain boundaries. The microstructure of the sputtered V film would thus have an impact on the oxidation kinetics, but also on the microstructure and morphology of the oxidized film. Some parameters which influence the microstructure of the V film during deposition include deposition rate, pressure and substrate. A detailed study on the microstructure was not performed, but a difference in morphology between VO_2 films prepared on SiO_2 and Al_2O_3 has indeed been observed. VO_2 films on SiO_2 were in general characterized by a larger grain size compared to films prepared on Al_2O_3. Furthermore, for an initial V film of 20 nm, agglomeration has been observed during oxidation on the SiO_2 substrate, but not on Al_2O_3. Some supporting SEM images are available in the supplementary information of paper I.

3.2.3 Reduction of V_2O_5 thin films in H_2

The second route for VO_2 synthesis was the reduction of V_2O_5 thin films. Experiments carried out in inert gas did not result in sufficient reduction. In contrast, the use of H_2 (5000 Pa) as reducing agent resulted in a reduction process through V_6O_{13}, VO_2 and an undefined vanadium oxide phase (denoted as VO_x) towards V_2O_3 as final phase (Figure 3.7). The reduction process did not occur stepwise, but continuous, i.e. at all times a mixture of the phases V_2O_5, V_6O_{13}, VO_2 or VO_x was observed, until V_2O_3 appeared. Obtaining single-phase VO_2 by quenching is thus not feasible under H_2 ambient, in contrast to the oxidation of V.

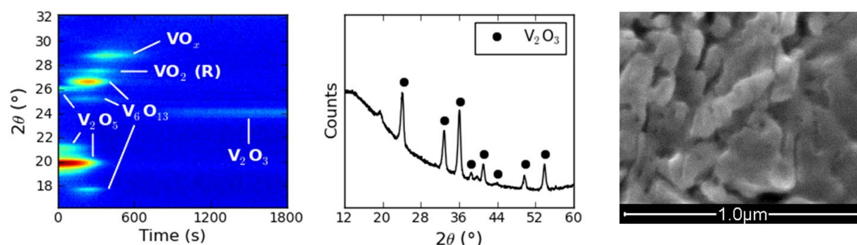

__Figure 3.7.__ Left: in-situ XRD measurement during isothermal reduction of a V_2O_5 layer of approximately 260 nm at 480 °C in 5000 Pa H_2. Middle: corresponding full XRD scan after reduction. Right: SEM image of the resulting film.

3.2.4 Stabilization of the VO_2 phase in a H_2-O_2 gas mixture

Since annealing of a V_2O_5 film in hydrogen results in V_2O_3 instead of VO_2 as stable phase, it was concluded that the oxygen partial pressure was too low. Therefore, oxygen was added in low concentration to the hydrogen gas. Oxygen and hydrogen will react with the formation of an equilibrium amount of water, determined by temperature and partial pressures:

$$2H_2 + O_2 \rightleftharpoons 2H_2O. \tag{3.1}$$

However, in chapter 2, section 2.3.3, it was explained that at the low temperatures (around 500 °C) involved during the experiments, the kinetics of this reaction are too slow to guarantee the reaction will equilibrate. It may thus be expected that the oxygen partial pressure does not vary much from the introduced partial pressure, which equals the ratio of gas flows of O_2 and H_2/He.

Oxygen was added to the hydrogen gas with oxygen partial pressures of 20 and 200 Pa O_2, since these values resulted in VO_2 formation in the case of oxidation of metallic vanadium. Applying this gas mixture on the V_2O_5 films at 480 °C resulted in a quick reduction and stabilization towards crystalline VO_2, as shown in figure 3.8 (top row).

The same gas mixture was applied to vanadium films at 480 °C, which as well resulted in VO_2 formation (figure 3.8, bottom row). Compared to the vanadium films oxidized in low oxygen partial pressures without hydrogen, oxidation however proceeded much slower, which is assigned to a competition between oxidation and reduction reactions. However, due to the increased phase stability, higher O_2 partial pressures are allowed for this balanced gas mixture, and in this way reasonable oxidation times could still be achieved.

Another interesting observation concerns the difference in microstructure and morphology of the VO_2 films prepared by oxidation in this H_2-O_2 mixture, compared to the V films oxidized in pure, low partial pressure O_2. Certainly in the case of films prepared on SiO_2, the use of the H_2-O_2 gas mixture leads to finer grains. Furthermore it prevented agglomeration of the 20 nm V film upon oxidation. Supporting SEM images can be found in the supplementary information of

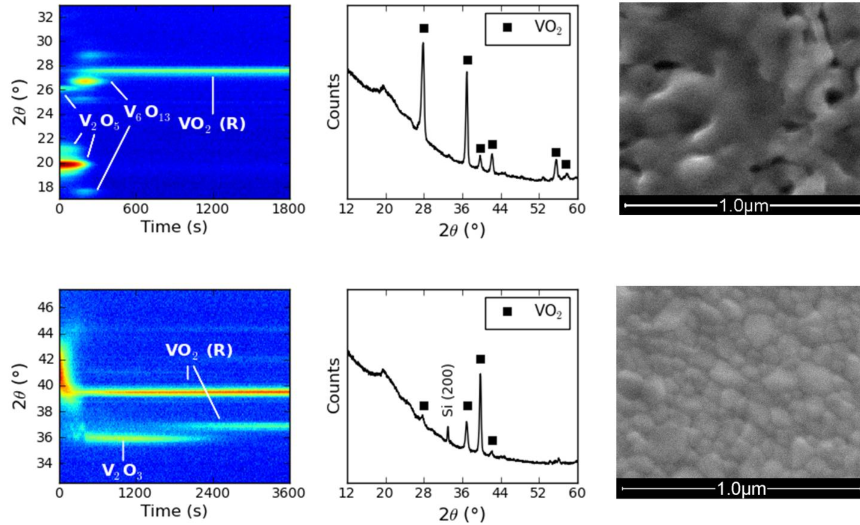

Figure 3.8. Left column: in-situ XRD measurements during isothermal annealing of a V_2O_5 layer (top row) and a V layer (bottom row) at 480 °C in a gas mixture of 5000 Pa H_2 and 200 Pa O_2. Middle column: corresponding full XRD scans after annealing. Right column: SEM images of the resulting films.

paper I.

3.2.5 Semiconductor-metal transition

Temperature-dependent sheet resistance measurements were carried out to monitor the semiconductor-metal transition in the VO_2 and V_2O_3 thin films that were obtained by controlled oxidation or reduction of sputtered films. Specifically in the case of VO_2, the influence of synthesis method and film thickness on the SMT characteristics was investigated, as discussed in the following sections.

3.2.5.1 Influence of VO_2 synthesis method

For the VO_2 films, the temperature-dependent sheet resistance measurements were carried out during thermal cycling between room temperature and 110 °C. Figure 3.9 shows the results for the various oxidation and reduction processes as described in the previous sections.

V films oxidized in air: Annealing V films in air results in a resistance switching ratio of 2 to 3 orders of magnitude (figure 3.9(a)). However, such switching ratios have only been achieved after careful optimization of the oxidation time. Shorter annealing times do not allow for full transformation of the V film into

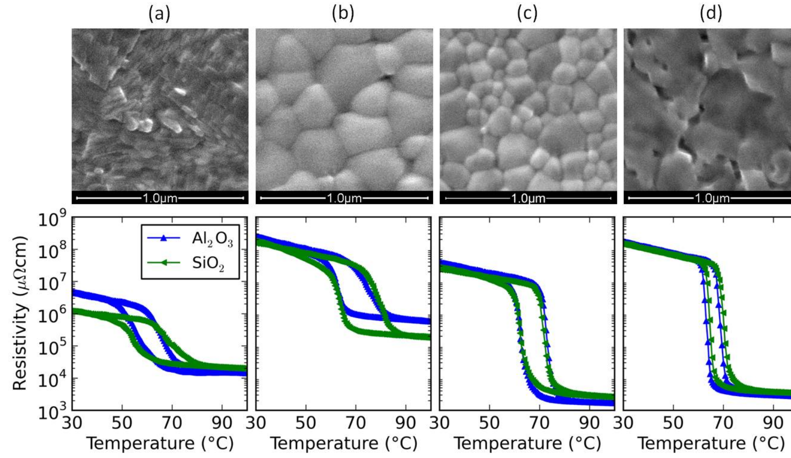

Figure 3.9. *Temperature-dependent resistivity measurements on VO_2 films on SiO_2 and Al_2O_3 substrates, prepared under different conditions: (a) oxidized V films in air for 2000 seconds at 430 °C, (b) oxidized V films in 20 Pa O_2 for 60 minutes at 480 °C, (c) oxidized V films in 5000 Pa H_2 + 200 Pa O_2 for 60 minutes at 480 °C, and (d) reduced V_2O_5 films V films in 5000 Pa H_2 + 200 Pa O_2 for 60 minutes at 480 °C. The top row shows SEM images of these films on the SiO_2 substrate.*

VO_2, whereas longer annealing times cause oxidation from VO_2 into V_2O_5. In both cases, the switching ratio is lower than for the optimized conditions.

V films oxidized in low partial pressure O_2: In case of annealing the V films in 20 Pa O_2 at 480 °C, switching ratios up to 3 orders of magnitude were observed as well (figure 3.9(b)). In this case, a minimal annealing time is required to achieve this ratio, corresponding to a maximum intensity of the VO_2 diffraction peak, while longer annealing does not affect the SMT characteristics anymore.

V films oxidized in a H_2-O_2 gas mixture: Oxidation of V film in the gas mixture of 5000 Pa H_2 with 200 Pa O_2 resulted in an improved switching ratio up to 4 orders of magnitude (figure 3.9(c)). A reduced defect density in the VO_2 bulk and/or at the grain boundaries is believed to be the cause of this improvement. Griffiths et al. showed how the oxygen partial pressure during reactive sputtering of VO_2 films influenced the SMT characteristics.[11] Only the purest VO_2 films showed high switching ratios, while oxygen vacancies or interstitials caused a drastic suppression of the resistance switch. On the other hand, Brassard et al. related the suppression of the sheet resistance switch to the presence of grain boundaries.[13] In the metallic phase, electrons are scattered at the grain boundaries, leading to an increase of the sheet resistance compared to the values observed in single crystals. In the semiconductive state, defects at the grain boundaries create additional paths for leakage currents, decreasing the sheet resistance. The combination of these

two effects causes a significant suppression of the sheet resistance switching ratio across the transition.

V_2O_5 films reduced in a H_2-O_2 gas mixture: Finally, the V_2O_5 films reduced under the H_2-O_2 mixture showed a remarkable resistance switching ratio of nearly 5 orders of magnitude (figure 3.9(d)). Such a high switching ratio is close to the observations in bulk VO_2, and is rarely observed in thin films. The SEM image shows a film which looks more like a molten and re-solidified structure, suggesting that grain boundaries are not present at the same density as for the V films oxidized under the same conditions. As a first remark, it should be stated that the preparation of the V_2O_5 film already caused drastic degradation of the film morphology, as was clear from the SEM image in figure 3.4. An additional SEM image is available in the supplementary information of paper I. Starting from such a rough morphology of the V_2O_5 film, it is unavoidable to obtain a rough VO_2 film upon reduction. Another way of preparing V_2O_5 films, e.g. by reactive sputtering may result in much smoother films, but this was not investigated. As a second remark, such morphology might not be appropriate for use in all kinds of applications. For instance in microelectronic applications, such as the targeted Mott-FET, smooth surfaces with a roughness less than a few nanometer would be required. For smart thermochromic coatings on glass however, this synthesis approach might be feasible.

3.2.5.2 Downscaling of VO_2 film thickness

As is often reported in literature, scaling down the thickness of VO_2 thin films drastically suppresses the resistance switching ratio during the transition. Figure 3.10 presents some data on VO_2 films of varying thickness prepared by controlled oxidation of V in the H_2-O_2 gas mixture at 480 °C. In case of films synthesized

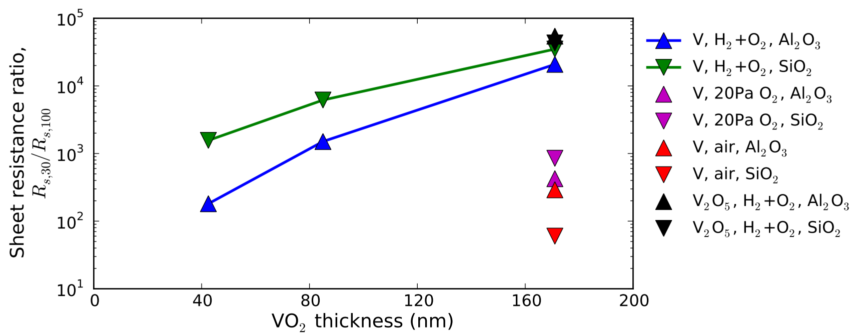

Figure 3.10. *Sheet resistance switching ratio as a function of VO_2 film thickness for films prepared by oxidation of V in a mixture of 5000 Pa H_2 and 200 Pa O_2 at 480 °C. For comparison, the switching ratios obtained for the other processes are shown as well for the thickest films (figure 3.9).*

on SiO_2 the resistance switching ratio $R_{s,30}/R_{s,100}$ decreases from 4 to 3 orders of magnitude when the VO_2 thickness is scaled down from 170 to 42 nm. Here $R_{s,30}$ and $R_{s,100}$ are the sheet resistance at 30 °C and 100 °C respectively. On the Al_2O_3 substrate the decrease is more pronounced, down to 2 orders of magnitude. This is believed to be related to the smaller grain size on Al_2O_3. Smaller grain sizes imply a higher density of grain boundaries which result in suppression of the SMT resistance curves.

3.2.5.3 Sheet resistance switching in V_2O_3 thin films

The V_2O_3 thin films prepared from the reduction of V_2O_5 did as well show a semiconductor-metal transition. Temperature dependent sheet resistance measurements between room temperature and -150 °C, as shown in figure 3.11, reveal a reversible transition near -100 °C with 3 orders of magnitude change in sheet resistance.

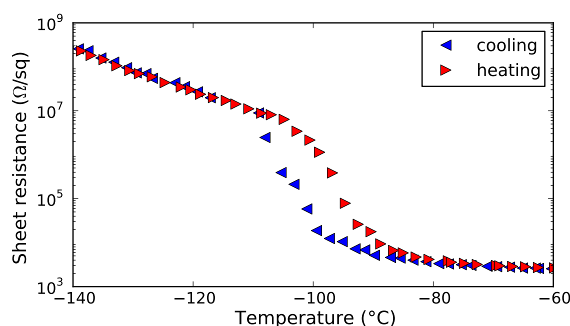

Figure 3.11. *Sheet resistance switching of a V_2O_3 film prepared by reduction of V_2O_5 in 5000 Pa H_2 at 480 °C.*

3.2.6 Summary

VO_2 thin films were synthesized by the controlled oxidation of sputtered vanadium layers and controlled reduction of V_2O_5 layers prepared by oxidation in air of sputtered vanadium layers. Oxidation of vanadium was studied in the temperature range from 430 °C to 615 °C over a wide range of oxygen partial pressures from 20 to 20000 Pa O_2. Although VO_2 was formed at all oxygen partial pressures, only at the lowest value of 20 Pa O_2 it was formed as a single phase, between 480 °C and 570 °C. Up to 3 orders of magnitude switch in sheet resistance were observed during the semiconductor-metal transition. The same switching behavior was observed for vanadium films annealed in air, but only for highly optimized annealing times. Improved switching behavior, with up to 4 orders of magnitude sheet resistance switching ratio, was obtained by oxidation of V in a balanced gas mixture of 5000 Pa H_2 and 200 Pa O_2.

Reduction of V_2O_5 layers in hydrogen resulted in a continuous reduction towards V_2O_3. This material showed 3 orders of magnitude switching ratio near -100 °C. The use of the balanced gas mixture however, stabilized the VO_2 phase. A resistance switching ratio of nearly 5 orders of magnitude was observed, close to the values reported for single-crystal VO_2, but with a poor morphology.

Figure 3.12 shows a schematic overview of the oxidation and reduction processes developed during this work. VO_2 was prepared from V or V_2O_5 layers, V_2O_5 and V_6O_{13} from V layers and V_2O_3 from V_2O_5 layers.

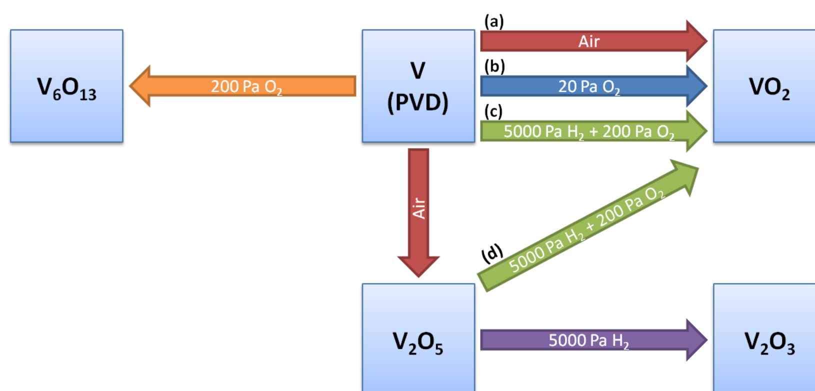

Figure 3.12. *Overview of the oxidation and reduction processes developed during this work. The gas ambient conditions for obtaining VO_2, V_2O_5, V_6O_{13} and V_2O_3 are indicated as well. (a)-(d) correspond to the results shown in figure 3.9.*

3.3 Atomic layer deposition of VO_2 thin films and nanoparticles

In this section, the synthesis of vanadium oxides by ALD using the TEMAV precursor is discussed. TEMAV has been combined with three reactants, i.e. H_2O, O_3 and O_2 plasma, resulting in vanadium oxide films with different characteristics. By post-deposition annealing in controlled oxygen partial pressures, different crystalline phases have been achieved, i.e. VO_2(M1/R), VO_2(B), V_6O_{13} and V_2O_5. The focus of the work is however the synthesis of the VO_2(M1/R) phase with the characteristic semiconductor-metal transition. Both films and nanoparticles have been prepared and characterized.

It should be noted that in the first published results films were only grown using O_3 as reactant (papers II and III). However, in what follows it will get clear that the results obtained using H_2O as reactant are as good or even better compared to the O_3 based ALD process. The reason of the initial choice of O_3 was that processes using H_2O resulted in non-uniform depositions, with deviations of 30% in thickness across a sample size of 50 mm. This non-uniformity was not observed

using O_3 as reactant. The issue of non-uniformity was caused by a cold spot on the reactor wall, and was solved by additional heating.

3.3.1 ALD growth characteristics

As stated earlier, tetrakis(ethylmethylamino)vanadium [$V(NC_2H_5CH_3)_4$], denoted as TEMAV, has been used during this work for growing vanadium oxide thin films by ALD. This precursor has a V^{4+} valence, which would be an ideal starting point for the growth of VO_2, if the ALD process takes place by ligand exhange, rather than oxidation. As a first test, the thermal stability of the TEMAV precursor was evaluated by exposing a substrate to TEMAV vapor pulses only. Starting from 175 °C, a vanadium containing film was deposited at a low deposition rate, which drastically increased at temperatures from 200 °C on (figure 3.13). The maximum temperature for pure ALD (i.e. ALD without CVD-like contributions due to precursor decomposition) is therefore below 175 °C. To avoid condensation of the precursor in the ALD reaction chamber, temperatures below 100 °C were avoided.

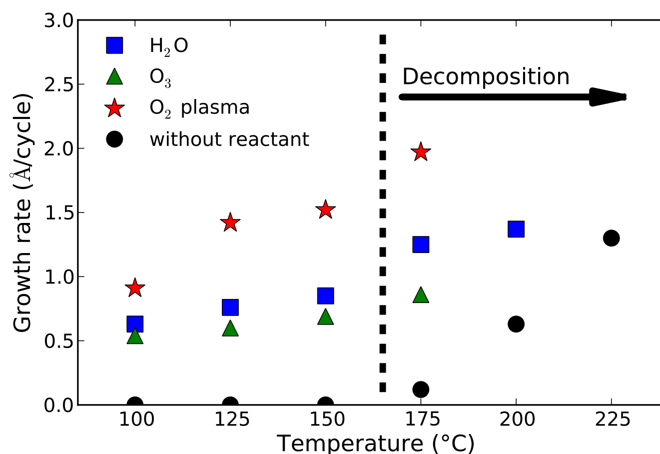

Figure 3.13. *Growth rate as a function of deposition temperature for different reactants.*

Three reactants were studied, i.e. H_2O, O_3 and O_2 plasma. Figure 3.13 shows the growth rate of vanadium oxides by the respective ALD processes, as a function of deposition temperature. These values were derived by XRR thickness measurements of films deposited using 100 ALD cycles for the various process conditions. Whereas the H_2O and O_3 based processes result in similar growth rates from approximately 0.6 to 0.8 Å/cycle, plasma-enhanced ALD has a significantly higher deposition rate near 1.5 Å/cycle. Remark that these growth rates are only a fraction of a monolayer of the crystalline VO_2 structures, which e.g. for VO_2(R) would vary from 2.86 to 4.55 Å depending on the orientation of the crystal structure. This can be explained by steric hindrance of the precursor molecules or by a low density

of reactive absoprtion species on the surface, as was already highlighted in section 2.1.2.

3.3.2 Film properties and stability

Density: The V molar density of the as grown films was determined by combining XRR thickness measurements and the V areal density measured by XRF. The results are presented in figure 3.14 for the three reactants and as a function of deposition temperature. The films deposited using H_2O show the highest density with values in between those of crystalline high density VO_2(M1) and lower density VO_2(B). This observation is a first indication that films grown using H_2O are VO_2. The O_3 based ALD results in lower densities. Finally, films grown by O_2 plasma have densities close to crystalline V_2O_5 or lower.

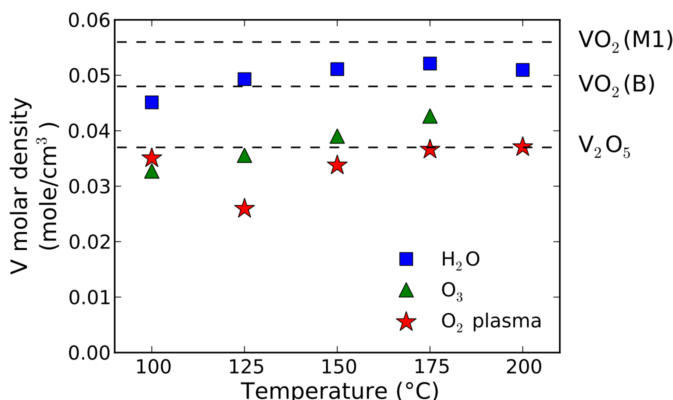

Figure 3.14. *V molar density of the as grown ALD films.*

V valence - VO_x phase: Determination of the vanadium oxide phase can be performed by means of XPS. Silversmit et al. described how the difference in binding energy between the O1s level and the $V2p_{3/2}$ level is a measure for the vanadium valence.[56] Figure 3.15 shows the XPS measurements carried out on several samples. The vertical lines indicate at which binding energy the $V2p_{3/2}$ level is expected for the case of a V^{4+} and V^{5+} valence. A first impression reveals that the H_2O and O_3 processes result in a V^{4+} valence, which corresponds to a film of VO_2. In contrast, the plasma-enhanced ALD process shows a V^{5+} valence, related to V_2O_5. The broader peaks in the case of the H_2O and O_3 processes, were however a possible indication of a mixed valence. When investigating the spectra in more detail, deconvolution revealed indeed a small contribution around 10 to 15% V^{5+} valence for the H_2O and O_3 processes. It is however important to remark that even in the case of deposition of pure VO_2, a small fraction of V^{5+} valence might be expected due to air exposure in between the deposition of the film and

the measurement by XPS, which would cause oxidation from VO_2 towards V_2O_5 at the surface. This is explained in detail in the following paragraph.

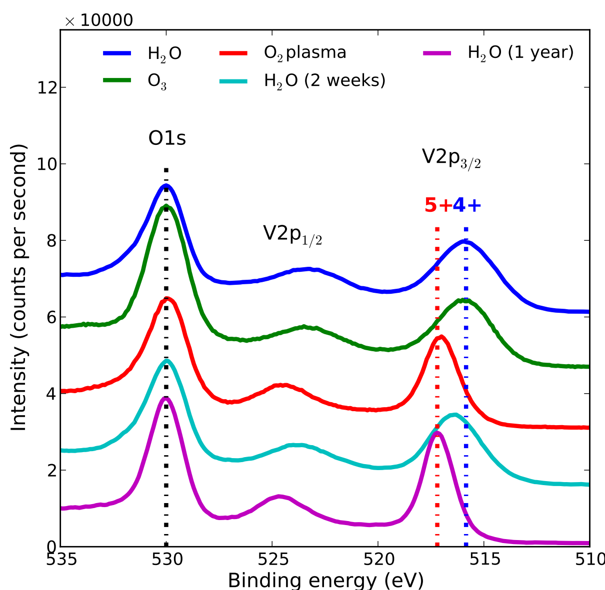

Figure 3.15. *XPS measurements on the ALD vanadium oxide films, shortly after deposition, and after various air exposure times.*

Aging: An important observation during this research was the aging of the ALD deposited VO_2 films, as illustrated in figure 3.16, in which the film thickness is plotted as a function of exposure time to ambient air. The parabolic increase in thickness is a typical observation related to oxidation, as already explained in chapter 2, section 2.3.2. Two additional XPS measurements confirm such oxidation (figure 3.15), as can be derived from the shift from a V^{4+} to a V^{5+} valence. Therefore, XPS measurements on VO_2 samples are only reliable if the exposure time to air in between the synthesis and the measurement is minimized. The mixed V valences with larger contributions of the V^{5+} valence compared to the V^{4+} valence for both H_2O and O_3 based ALD films, as reported by Blanquart et al. and Tangirala et al., are thus very doubtful.[46;50] On the other hand, the hard X-ray photoelectron spectroscopy (HAXPES) measurements performed by Premkumar et al. are more reliable due to the higher information depth on the order of 10 nm compared to only a few nm by conventional XPS,[49] since it would take several months to reach an increased V valence at such a depth. Premkumar et al. observed a pure V^{4+} valence in case of H_2O based ALD.

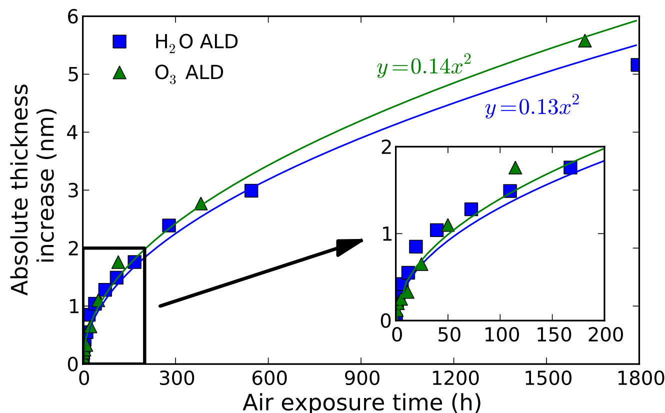

Figure 3.16. *Thickness increase upon air exposure for 10 nm VO_2 films grown by H_2O and O_3 based ALD.*

Crystallinity: XRD measurements (figure 3.17) revealed amorphous layers in the case of ALD using H_2O or O_3 as reactant. For the plasma-enhanced ALD process, both amorphous and crystalline material was observed. Crystalline V_2O_5 was obtained when the plasma exposure time was at least 5 s, the deposition temperature at least 150 °C, and a minimum of 100 ALD cycles were grown. In order to obtain crystalline VO_2, or other vanadium oxide phases, post-ALD annealing is required, as thoroughly discussed in section 3.3.4.

An excellent review on the growth of amorphous versus crystalline thin films by ALD has been published by Miikkulainen et al.[57] Since ALD often is performed at relatively low temperatures compared to CVD, less energy is available to allow for crystalline phase formation during deposition. There are however much more parameters influencing the ability of obtaining crystalline films. Contaminants such as carbon or nitrogen often hinder crystallization. Low impurity levels can be obtained by increasing the temperature of deposition, as long as one stays in the ALD-window. Too high temperature would lead to CVD-like growth and often results in higher impurity levels. Also the type of reactant plays a critical role. Whereas H_2O often operates via ligand exchange, O_2 plasma enables complete removal of undesired C and N species. O_3 is often more reactive than H_2O, but certainly less than O_2 plasma. Furthermore, highly energetic species, i.e. radicals and ions, created in the plasma, serve as an additional source of energy, which can be used to start nucleation. The choice of a suitable substrate may also allow for growth of crystalline material, certainly when the film that is being deposited has similar lattice parameters as the substrate. In some cases, it has been observed that in the initial stages of growth, amorphous material is being deposited, while crystalline film growth starts when film thickness is sufficient. Hausmann and Gordon proposed a model which described the growth of crystalline ZrO_2 by ALD. The model, as shown in figure 3.18, assumes that during each cycle nucleation events

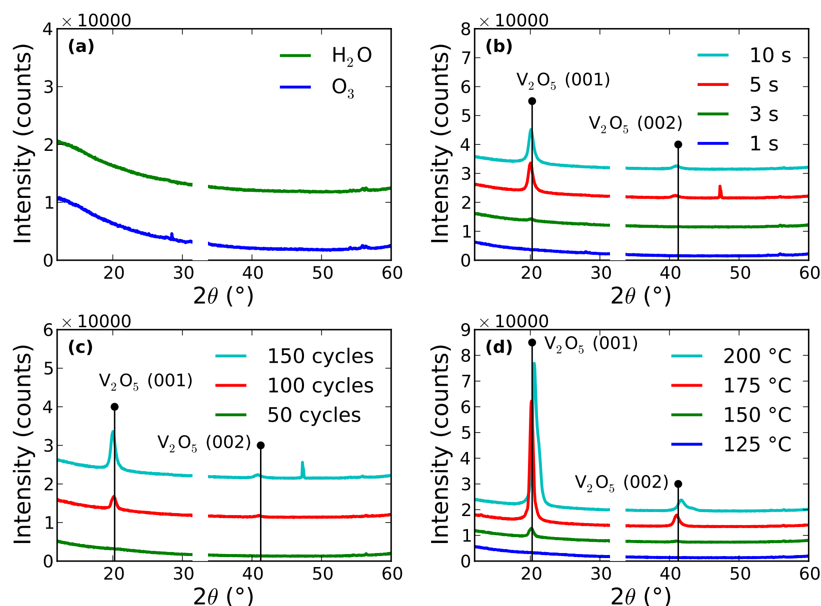

Figure 3.17. *XRD measurements on the as deposited ALD films. The different panels show amorphous films grown using H_2O or O_3 (a), as well as the influence of plasma exposure time (b), amount of ALD cycles (c) and deposition temperature (d) on the crystallinity of the PE-ALD films. For clarity the different spectra were shifted vertically and the Si(100) substrate peak near 33 ° was removed.*

can occur at the surface. Once a nucleus has formed, it will grow by the addition of material on top of it during the following cycles. Since new nuclei can form, and small nuclei can grown also in the direction parallel to with the growing film, the initial amorphous film growth will switch to fully crystalline deposition. Remark that other models exist for crystalline film growth by ALD, as summarized by Miikkulainen et al.

In this case of ALD of vanadium oxides from TEMAV precursor, only the use of O_2 plasma has shown to be suitable for crystalline film growth. And it has indeed been observed that increasing the temperature, dosing time and power lead to higher crystallinity. Also the film thickness is a critical parameter. If one looks to the XRD peak intensity as a function of the number of PE-ALD cycles, it is clear that the intensity is not linear with the amount of cycles. More precisely, some delay can be observed. This is in correspondence with the model of Hausmann and Gordon.

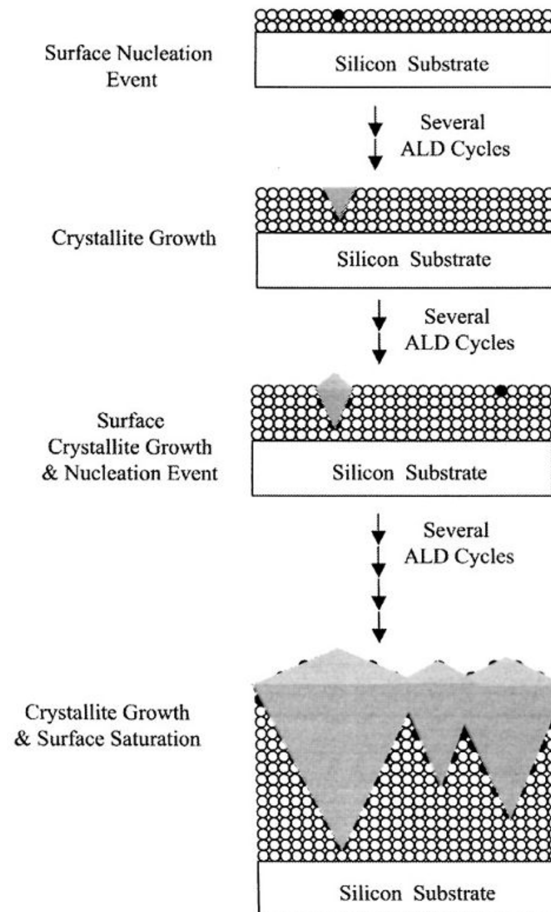

Figure 3.18. *Model for nucleation and crystal growth during ALD, as proposed by Hausmann and Gordon for the growth of ZrO_2.* [58]

3.3.3 Conformality

One of the excellent features of ALD is its capability of conformally coating 3-dimensional structures. Two types of 3D structures have been investigated during this work: macroscopic trenches using Si wafers, and Si micropillars.

Conformality in macroscopic trench structures: Similar to the experimental study on the conformality of ALD of Al_2O_3 from TMA and H_2O, reported by Dendooven,[59] macroscopic trench structures were used to verify the conformal growth of vanadium oxide. These structures were made by clamping 2 Si wafers onto each other, with a U-shaped piece of Al foil in between. The trench, and

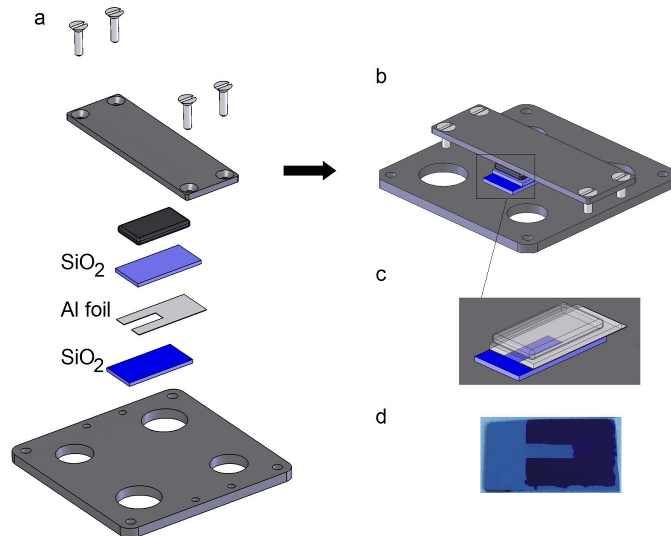

Figure 3.19. *(a,b) Schematic overview of the method used to construct macroscopic holes. (c) Detail of the created slot with rectangular cross section. (d) ALD film grown into a macroscopic hole (using SiO_2 substrates). The depth over which the film could grow into the test structure can be visually determined. (After Dendooven.[59])*

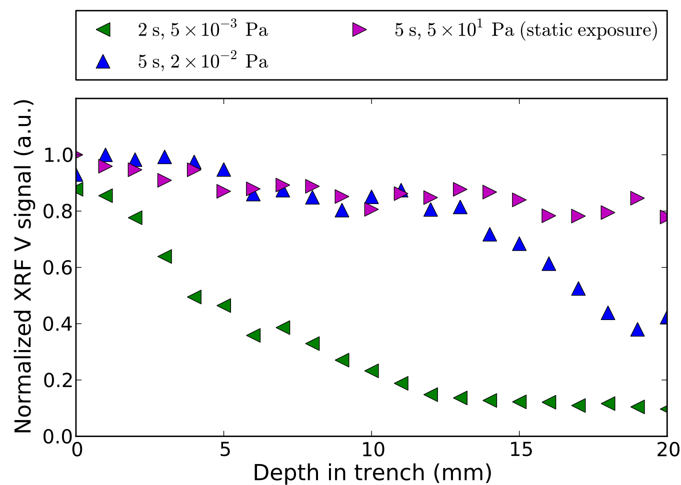

Figure 3.20. *Conformality measurements for O_3 based ALD processes in a macroscopic trench with a depth of 20 mm and a width of 0.5 mm, for various TEMAV exposures.*

a coated piece of Si wafer are illustrated in figure 3.19. The dark blue color is the uncoated Si (with 100 nm thermally grown SiO_2), the light blue color is the Si covered with an ALD film. The use of these macroscopic trenches allows for scanning the conformality by XRF. In figure 3.20, the V XRF signal, normalized to the value measured outside the trench, is shown as a function of depth in the trench. Three different conditions for TEMAV exposure have been applied: (i) 2 s at 5×10^{-3} Pa, (ii) 5 s at 2×10^{-2} Pa, and (iii) 5 s at 50 Pa. The high pressure for the latter one was achieved by a static pulse, i.e. by closing the valve to the pump during exposure. For all three cases, a static O_3 pulse of 5 s at 50 Pa was used as reactant. Clearly higher TEMAV exposures lead to an increased degree of conformality. Certainly the use of static precursor exposures yields an excellent conformality in this trench with aspect ratio 20, defined as half of the ratio of the depth (20 mm) to the height (0.5 mm).[59] An overall conformality of almost 80% was achieved down to the bottom of the trench.

Conformality on Si micropillars: In addition to these easy-to-fabricate macroscopic trenches, the conformality on Si micropillars was verified. These were

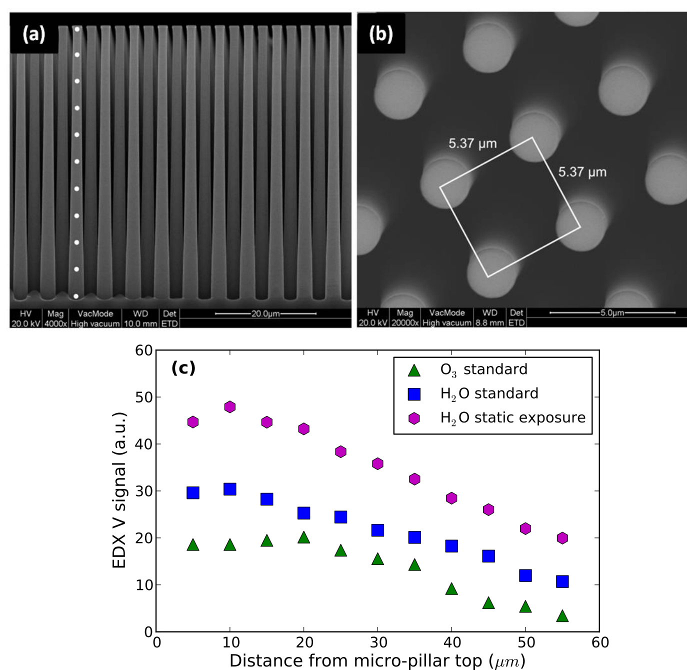

__Figure 3.21.__ (a,b) SEM images of the Si micropillars used for verification of the conformal growth of vanadium oxide by ALD. The white dots on the cross-section show the position of the EDX measurements. (c) EDX measurement of the conformality, showing the V signal as a function of the distance from the top of the micropillar.

fabricated at IMEC and are used as high surface area test structures for the development of solid-state Li-ion batteries.[60;61] Figure 3.21 shows SEM images of the micropillars, as well as the verification of the conformality of three ALD processes by energy-dispersive X-ray spectroscopy (EDX): (i) a regular O_3 based ALD process, (ii) a regular H_2O based ALD process, and (iii) a H_2O based ALD process with static TEMAV exposure. Although for all three processes the same amount of ALD cycles was used, the overall EDX V signal differs significantly. For the regular H_2O and O_3 processes, this may be explained by the lower growth rate and density of the O_3 grown films. The difference between the two H_2O processes is probably related to the fact that the regular process was not yet able of reaching saturated growth, not even at the top of the micropillars. Nevertheless, the overall shape of the curves looks similar for the three processes, and it seems that the micropillars were only conformally coated at the top 20 µm. However, it was questionable if the EDX mapping delivers a reliable measurement, since the conical shape of these micropillars could have an influence on the V signal. It is therefore difficult to draw quantitative conclusions concerning the conformality on these structures.

3.3.4 Crystalline phase formation

Crystallization of the VO_2(R) phase: Since the ALD processes result in amorphous VO_2 or crystalline V_2O_5 thin films, post-deposition treatment is required to transform these phases into crystalline VO_2(M1/R). Let us first consider the amorphous VO_2 films, which were deposited using the H_2O and O_3 based ALD processes. Compared to the synthesis of VO_2 thin films from sputtered V layers, as discussed in section 3.2, the ALD films are expected to contain sufficient oxygen. One would thus expect that annealing in inert gas would transform the amorphous films into crystalline VO_2. However, the in-situ XRD measurements performed in He atmosphere were rather irreproducible. Although it was observed that in many cases crystallization towards VO_2(R) occurred, the crystallization temperature, as well as the intensity of the diffraction peaks differed significantly from sample to sample. In some cases, crystallization did not occur at all. The irreproducibility originated from the very low background oxygen or water vapor pressure in the in-situ annealing chamber, which was difficult to measure and control. It was found that a minimal oxygen partial pressure is required to allow for reproducible crystallization of the films.

A reliable study of the crystallization behavior was enabled by the controlled mixing of oxygen in helium. The control of oxygen partial pressure was initially carried out by the combination of a leak valve for controlling the oxygen flow and an oxygen sensor for oxygen partial pressures above 10 Pa, while an oxygen pump was used for pressures up to 10 Pa. The results published in paper III are based on these systems. For the results in this chapter and paper IV, mass flow controllers have been used, since these allowed for control a much broader range of oxygen partial pressures in a more reliable way. All these methods for controlling the oxygen partial pressure have been discussed in detail in chapter 2.

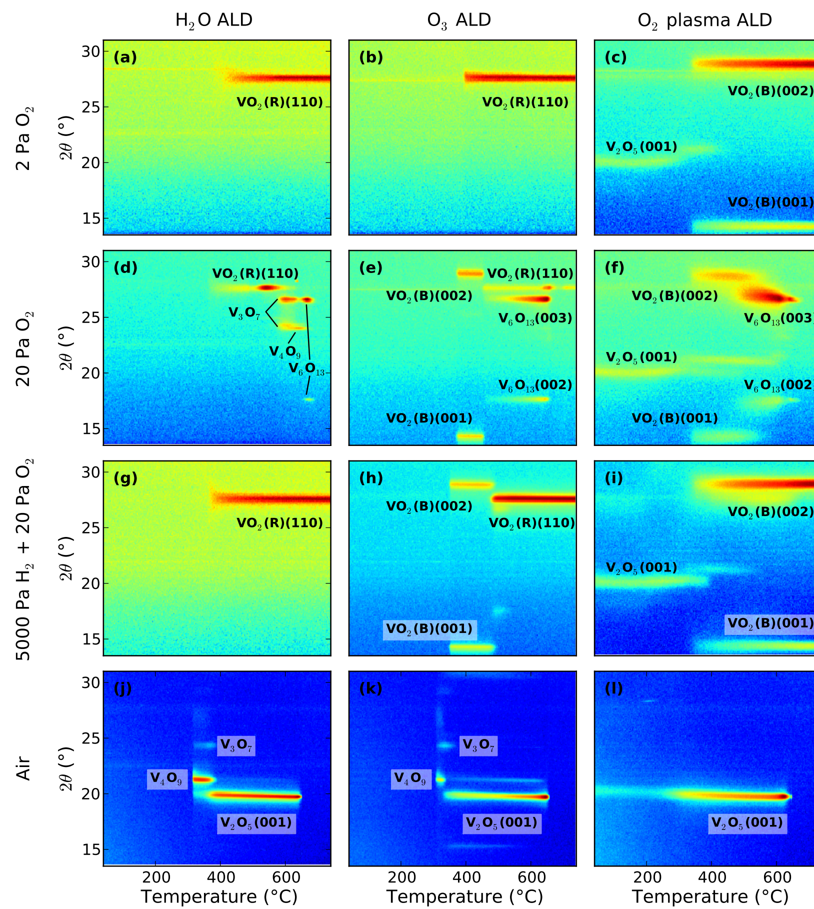

Figure 3.22. *In-situ XRD measurements during ramp annealing of 20 nm ALD vanadium oxide films in various ambients. Columns 1 to 3: H_2O, O_3 and O_2 plasma ALD processes. Rows 1 to 4: annealing in 2 Pa O_2, 20 Pa O_2, 5000 Pa H_2 + 20 Pa O_2 and air.*

From the sputtered V films it was concluded that an oxygen partial pressure of the order of 20 Pa is allowed as maximum value to prevent further oxidation towards V_6O_{13}, V_2O_5 or other Wadsley phases. Lower values were not tested, since the required oxidation time increased drastically. For the ALD films, however, lower oxygen partial pressures were evaluated as well, since sufficient oxygen is already present in the films. In order to achieve the lowest oxygen partial pressure on the order of 1 Pa, experiments were initially performed using the oxygen pump (described in detail in chapter 2, section 2.3.3). For the latest experiments, low flows of diluted O_2 were mixed with high flows of He by means of mass flow controllers. In addition, anneals were performed in a mixture of 5000 Pa H_2 with 20 Pa O_2, since from the gas-solid reactions described in section 3.2 this seemed to be the most reliable condition to transform any vanadium oxide phase into crystalline VO_2. Thus, it may be useful for VO_2 phase stabilization during both the crystallization of amorphous VO_2 ALD films and the controlled reduction of the crystalline V_2O_5 films, deposited by plasma enhanced ALD.

Figure 3.22 shows some of the most relevant in-situ XRD measurements. It is observed how annealing in 2 Pa O_2 results in crystallization of the amorphous VO_2 films towards the tetragonal VO_2(R) phase, whereas the crystalline V_2O_5 layers reduce towards monoclinic VO_2(B). This monoclinic phase is a metastable polymorph of the tetragonal phase, often observed during the reduction of V_2O_5.[62;63] In contrast to observations reported in literature of the transformation of VO_2(B) towards VO_2(R) near temperatures around 450 to 500 °C, the VO_2(B) films obtained by reduction of PE-ALD grown V_2O_5 are stable up to the maximum temperature during post-ALD annealing, i.e. 750 °C.

Similar results are obtained when a gas mixture of 20 Pa O_2 and 5000 Pa H_2 was used. As in the case of oxidation of sputtered V films or reduction of V_2O_5 films, the VO_2 phase is stabilized for both the H_2O, O_3 and O_2 plasma ALD processes. However, depending on the reactant used during ALD, VO_2(R) or VO_2(B) are observed as crystalline phases. For the H_2O ALD process, only VO_2(R) is observed, whereas in the case of the films grown by O_3, the VO_2(B) phase is present as transient phase, prior to transformation towards VO_2(R). This difference in initial crystallization between H_2O and O_3 based ALD films is believed to originate from the difference in density of the as deposited films, as was presented in figure 3.14. A plausible explanation is that the low-density films deposited by the O_3 based ALD process are more prone to oxidation at elevated temperatures, such that oxygen interstitials are easily incorporated in the lattice. These interstitials would allow for the formation of metastable, low-density VO_2(B), instead of forming the more stable, high-density VO_2(R) phase. Only when the temperature is further increased, the transformation towards VO_2(R) occurs. For the films deposited by O_2 plasma, reduction to VO_2(B) is observed as well, but transformation towards VO_2(R) does not occur.

Crystallization of other vanadium oxide phases: Many other vanadium oxide phases have been observed during post-deposition annealing of the ALD films at

elevated O_2 partial pressures, as shown in figure 3.22. First of all, annealing in air shows the crystallization of V_2O_5, the thermodynamical stable phase under these conditions. In case of the films grown by the H_2O and O_3 based ALD processes, V_4O_9 and V_3O_7 appeared as transient phases. V_6O_{13} was observed when annealing the ALD films in 20 Pa O_2. A thorough investigation of the influence of the oxygen partial pressure on the vanadium oxide phase formation is presented in figure 3.23, which summarizes the data from the in-situ XRD measurements performed on 20 nm amorphous VO_2 films grown by H_2O and O_3 based ALD. Experiments were performed at 2, 5, 10, 20, 50, 100, 200, 500, 1000, 2000, 5000, 10000 and 20000 Pa O_2. The horizontal dotted lines indicate these oxygen partial pressures.

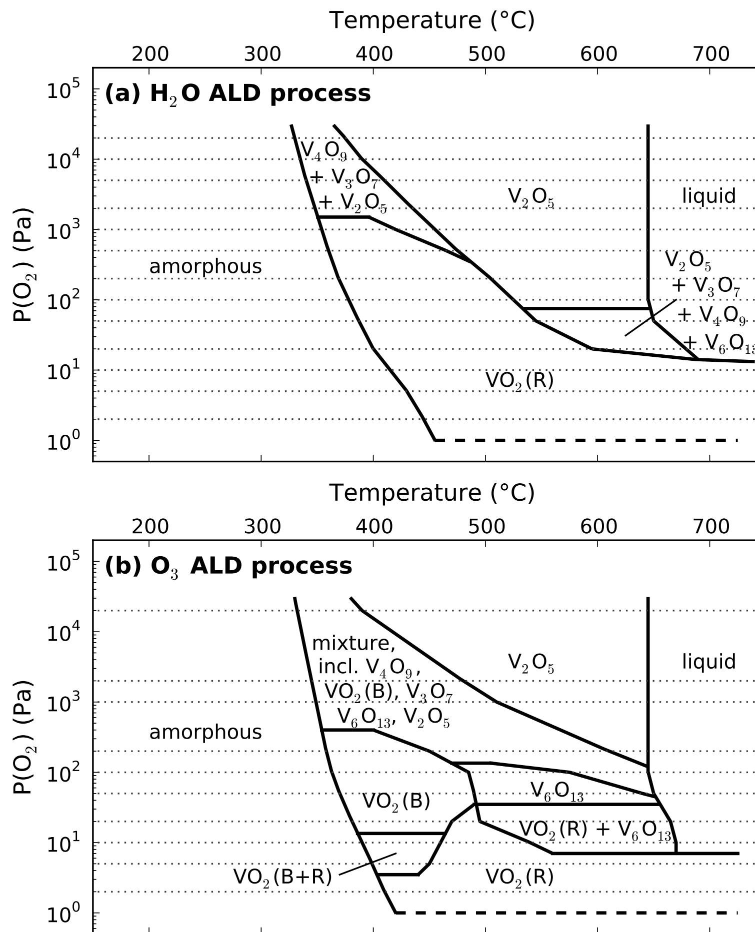

Figure 3.23. *Phase formation diagrams of vanadium oxide films of 20 nm grown by H_2O and O_3 based ALD during ramp annealing at 0.25 °C/s at various O_2 partial pressures.*

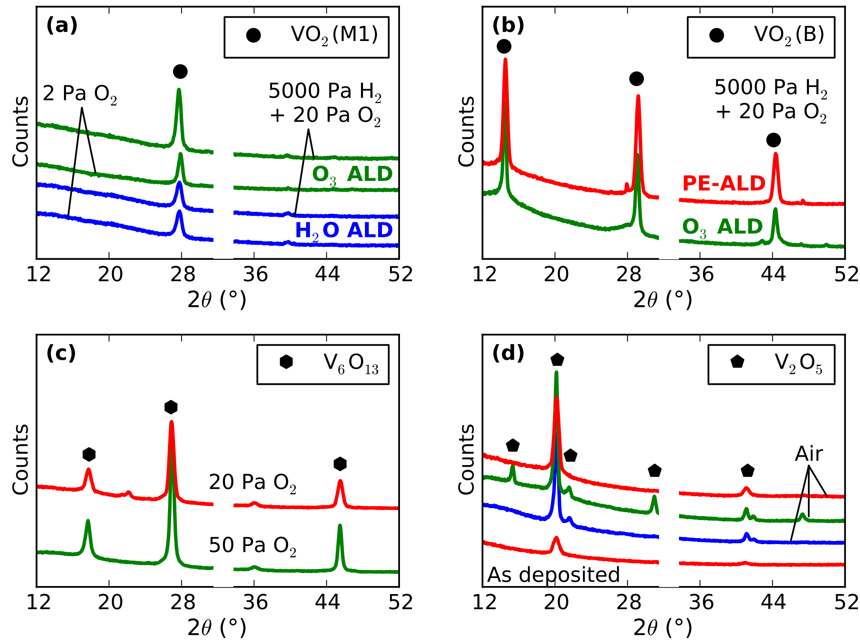

Figure 3.24. *Full scan XRD measurements of the crystalline vanadium oxide phases prepared by ALD and post-deposition annealing under various conditions (see table 3.3): (a) VO_2(M1/R), (b) VO_2(B), (c) V_6O_{13}, and (d) V_2O_5. The blue, green and red spectra correspond to the use of H_2O, O_3 and O_2 plasma as reactants. For clarity the different spectra were shifted vertically and the Si(100) substrate peak near 33 ° was removed.*

Vanadium oxide phase	ALD process	Annealing temperature	P(O_2)	P(H_2)
VO_2(M1/R)	H_2O	480 °C	2 Pa	-
	H_2O	480 °C	20 Pa	5000 Pa
	O_3	480 °C	2 Pa	-
	O_3	480 °C	20 Pa	5000 Pa
VO_2(B)	O_3	400 °C	20 Pa	-
	O_3	400 °C	20 Pa	5000 Pa
	O_2 plasma	480 °C	2 Pa	-
	O_2 plasma	480 °C	20 Pa	5000 Pa
V_6O_{13}	O_3	570 °C	50 Pa	-
	O_2 plasma	570 °C	20 Pa	-
V_2O_5	H_2O	400 °C	air	-
	O_3	400 °C	air	-
	O_2 plasma	as grown / 400 °C	air	-

Table 3.3. *Overview of synthesis parameters for vanadium oxide phases prepared by ALD and post-ALD annealing.*

The boundaries between the several phases (pure or mixed) are constructed by the appearance and disappearance of diffraction peaks during the anneals. It should be stated clearly that these phase formation diagrams cannot be considered as thermodynamic phase diagrams, since the crystallization and oxidation reactions are strongly affected by kinetics. This also means that the heating rate may have a significant impact on the phases formed during such experiments, as well as their respective temperatures of formation. The heating rate used for the experiments was 0.25 °C/s.

These phase formation diagrams illustrate how apart from VO_2(R), VO_2(B) and V_2O_5, the Wadsley phases, i.e. V_6O_{13}, V_4O_9 and V_3O_7, appear by annealing the amorphous VO_2 films deposited by H_2O and O_3 based ALD. The reactant used during deposition has a large impact on the phase formation. The lower density films grown by O_3 based ALD are characterized by a more complex phase formation diagram, compared to the ALD films grown using H_2O as reactant. For both ALD processes, the temperatures of initial crystallization and the possible subsequent oxidation towards higher oxide phases decrease with increasing oxygen partial pressures.

Only VO_2(R), VO_2(B), V_6O_{13} and V_2O_5 appear in single-phase regions in the phase formation diagrams. The optimal conditions for their preparation are summarized in table 3.3, while the full scan XRD measurements are shown in figure 3.24. On the other hand, V_4O_9 and V_3O_7 have only been observed as transient phases during the oxidation towards V_2O_5, and could not be obtained as pure phases.

3.3.5 Morphology of crystalline VO_2 films and nanoparticles

Although ALD is suited for the deposition of smooth films with very low roughness, the post-deposition annealing treatment results in a drastic surface roughening. This was observed for both the anneals carried out in 2 Pa O_2 and the mixture of 5000 Pa H_2 with 20 Pa O_2. While the crystallization temperature was found to be more or less independent on the film thickness, the agglomeration temperature changes significantly, as schematically shown in figure 3.25. In fact, surface roughening occurs for all film thicknesses, but as long as the film thickness is sufficient, a continuous film is maintained. A minimum film thickness of approximately 10 nm is required to allow for crystalline continuous layers.

Figure 3.26 shows AFM measurements on 10 nm and 2.5 nm films, annealed at 480 °C and 660 °C respectively. While the 10 nm film is converted to a crystalline layer with an RMS surface roughness of 1.6 nm, the 2.5 nm is transformed in a layer of non-connected crystalline nanoparticles with an approximate height of 25 nm and width around 50 to 100 nm.

Agglomeration in thin films is a typical phenomenon observed during thermal processing. The mechanism of agglomeration is believed to be the minimization of the total energy of the system. For very thin films, surface and interface energies become more significant with respect to the bulk energy, which is a driving force for agglomeration.[64] In addition, also the grain boundary energy needs to

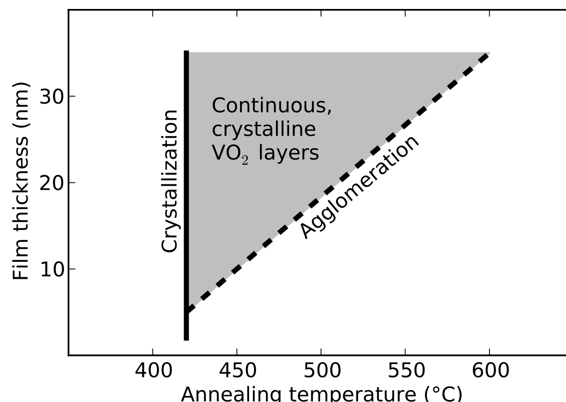

Figure 3.25. *Indicative process window as a function of film thickness and annealing temperature to obtain continuous crystalline VO_2 layers.*

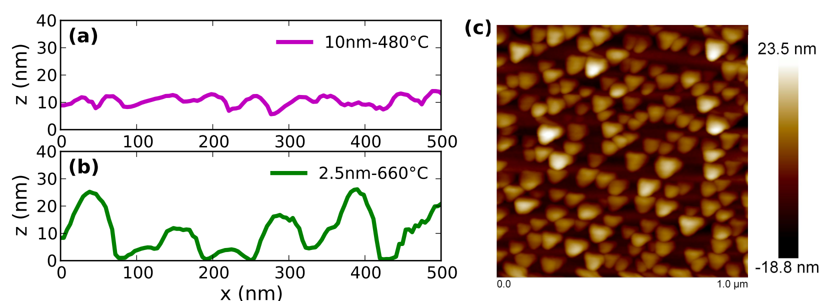

Figure 3.26. *(a) AFM line scans on a VO_2 thin film of 10 nm. (b-c) AFM line scan and 2D scan on VO_2 nanoparticles synthesized by annealing a 2.5 nm ALD film at 660 °C. Both films were annealed in the H_2-O_2 gas mixture.*

be taken into account, which means that texture and grain size can play an important role in the agglomeration behavior. During the synthesis of crystalline VO_2, agglomeration is a common issue for films with thickness below 50 nm.[13;65] The crystalline VO_2 films prepared in this work by ALD and post-deposition anneal are thus characterized by a much better scaling of thickness, down to 10 nm. Further downscaling would require additional conditions which favor smooth films, such as deposition on single-crystal Al_2O_3 or rutile TiO_2 substrates. Martens et al. showed how epitaxial growth of VO_2 on rutile TiO_2 resulted in atomically smooth films with a thickness down to 2 nm.[3] Whether this can also be achieved by ALD could be subject of further research. Apart from ALD on single-crystals, it would be worth investigating the agglomeration behavior on other types of substrates, including both amorphous and polycrystalline materials.

3.3.6 Semiconductor-metal transition

SMT in VO_2 thin films: The characteristic semiconductor-metal transition in VO_2 has been characterized by means of temperature dependent sheet resistance measurements in case of continuous films and temperature dependent ellipsometry for both continuous films and nanoparticles. Figure 3.27 shows a few sheet resistance measurements. More than 3 orders of magnitude change in resistivity across the transition were observed for films of 20 and 30 nm. The magnitude of transition drops to 2 orders for a film of 10 nm.

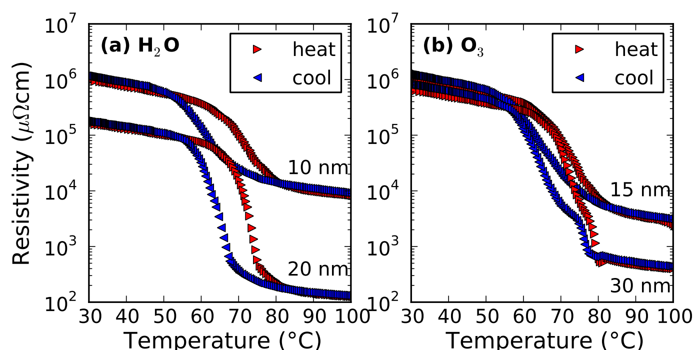

Figure 3.27. Measurements of the semiconductor-metal transition during thermal cycling between 30 °C and 110 °C: sheet resistance measurements on thin films grown by ALD using (a) H_2O, and (b) O_3 as reactant. The films were crystallized in the H_2-O_2 gas mixture at 480 °C.

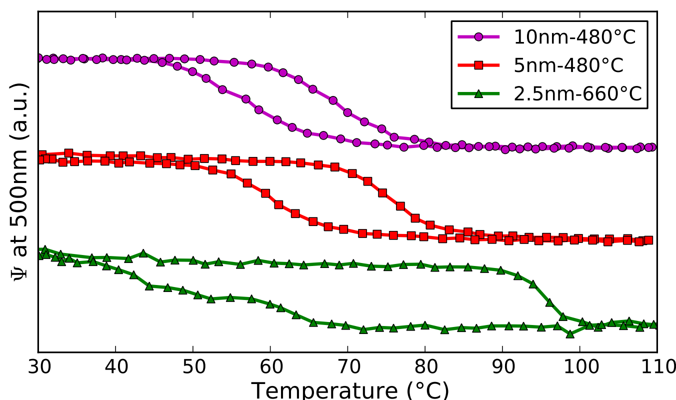

Figure 3.28. Measurements of the semiconductor-metal transition during thermal cycling between 30 °C and 110 °C: ellipsometry on thin films and nanoparticles. The films were grown by H_2O based ALD and crystallized in the H_2-O_2 gas mixture at 480 or 660 °C.

SMT in VO_2 nanoparticles: Sheet resistance measurements on thinner films were not longer applicable due to agglomeration, as explained in the previous section. With the aid of ellipsometry, the transition can however still be measured optically. Even for nanoparticles, the transition is detected, and it is observed that the hysteresis width is increased significantly, from approximately 10 °C for continuous films up to 50 °C for nanoparticles. These findings match with other publications in which hysteresis widths up to 50 °C have been reported for VO_2 nanoparticles produced via other methods.[66–68] Remark that the SMT curve represents the transition for a large collection of nanoparticles. Determination of the SMT characteristics of the individual nanoparticles would require dedicated nanoscale measurement techniques. For instance, if nanoparticles would be synthesized on an electrically conductive substrate, temperature-dependent conductive AFM (CAFM) might be applied to measure both particle size and SMT properties.

Stability: Although not studied in detail, it was observed that the crystalline VO_2 films are also not stable when exposed for long times to ambient air. First of all, XPS measurements showed a gradual shift from a V^{4+} valence towards a V^{5+} valence over time, related to surface oxidation of the VO_2 phase towards V_2O_5. In view of thermodynamics, this is expected. The V-O phase diagrams in chapter 2 (figures 2.6 and 2.7) indicated that at ambient conditions V_2O_5 is the stable phase. It are only the kinetics which limit VO_2 to spontaneously oxidize within short time frames. For very thin films however, as investigated in this work, aging can be observed in a time span of a few weeks are months. This aging has a drastic effect on the SMT characteristics, which also degraded drastically over time, certainly for the thinnest films. For applications in microelectronics this is not necessarily an issue, since the VO_2 films would be embedded inside the chip. For other kinds of applications, where normally VO_2 would be exposed to air, this is certainly a serious point of attention, and encapsulation of the VO_2 film will be a key requirement. Recently, Wang et al. showed how such encapsulation could be achieved by covering VO_2 films with thin layers of Al_2O_3, deposited by ALD.[69] Layers of 5 nm were sufficient for protecting the VO_2 films during heating in air at 350 °C for 20 hours, while 15 nm Al_2O_3 was required for maintaining the SMT properties during a damp-heating at 50 °C in an environment with relative humidity of 95% for 130 hours. As a last remark, it may be worth noting that for instance in the case where VO_2 is used for micromechanical devices (see chapter 1), the large deformations caused by the structural transition in VO_2 may be expected to degrade such Al_2O_3 coatings quite rapidly. Flexible encapsulation coatings should in those cases offer a solution.

3.3.7 Summary

The synthesis of crystalline VO_2(M1/R) is enabled by depositing amorphous VO_2 thin films by ALD from TEMAV precursor and H_2O or O_3, followed by a post-deposition annealing of these films at a minimum temperature of approximately

420 °C in a low oxygen partial pressure of 2 Pa or in a mixture of 20 Pa O_2 with 5000 Pa H_2. The process based on H_2O as reactant allows for a broader range of oxygen partial pressures for crystalline VO_2(R) formation, with respect to the O_3 based process. Continuous films with a thickness down to 10 nm were achieved. The semiconductor-metal transition was characterized by a change in resistivity of more than 3 orders of magnitude for films of 20 nm and thicker. For nanoparticles, created by annealing thinner films at higher temperatures, a wider hysteresis loop was observed up to 50 °C.

Other vanadium oxide phases were prepared as well. Crystalline V_2O_5 was obtained as deposited from plasma-enhanced ALD, or after annealing any ALD film in air at a temperature around 400 °C or higher. Monoclinic VO_2(B) was prepared from O_3 based ALD films and subsequent annealing in 20 Pa O_2 or from plasma-enhanced ALD and subsequent annealing in maximum 20 Pa O_2. The Wadsley phase V_6O_{13} was obtained as pure phase from oxidation of O_3 grown films or reduction of O_2 plasma grown films around 20 to 50 Pa O_2. The other Wadsley phases V_4O_9 and V_3O_7 were difficult to obtain as pure phases, since at the high oxygen partial pressures required for their formation, these phases easily oxidized further towards V_2O_5.

3.4 Conclusions

Deposition of VO_2 thin films has been intensively studied and reported over the last decades. Many reports show a dedicated optimization of process conditions to enable the growth of single phase, crystalline VO_2. The difficulty exists in controlling all parameters at the same time, and the fact that these may not be changed independently. For reactive sputtering, these parameters include the deposition temperature, sputter power and oxygen partial pressure. CVD growth of VO_2 requires as well the optimization of temperature and partial pressures of vanadium precursor and (optional) reactant. For obtaining a uniform deposition on large area substrates, a uniform sample temperature and precursor and reactant flux are furthermore required. Because of these reasons, reactor design and geometry can have an influence on the growth characteristics and optimized parameters for reactive sputtering and CVD may not be easily transferred from one reactor to another.

In contrast, the two approaches for thin film VO_2 deposition studied in this work are easily optimized, since in these two-step processes the process parameters are split up into deposition parameters on the one hand and annealing parameters on the other hand. In case of sputtering of vanadium films, the growth rate of a film will of course depend on the reactor geometry, but a simple calibration between sputter power and deposition rate will suffice to allow for deposition of the desired V film thickness. It should however be noted that parameters such as pressure, deposition rate and substrate will have an influence on the microstructure of the V film, which will certainly have an impact on the kinetics of oxidation and the microstructure and morphology of the oxidized film. This has been observed by the difference in VO_2 thin film morphology and grain size prepared on

SiO_2 and Al_2O_3 substrates. The growth rate and composition of a thin film during ALD is determined by the precursor chemistry, and is only slightly affected by temperature and substrate. Although reactor design will have its impact on the dosing and purge/pump times, different ALD reactors will share the same ALD growth characteristics. The same holds for the post-deposition annealing. Only three parameters are involved, i.e. oxygen partial pressure and annealing time and temperature. Certainly in the case of the balanced H_2-O_2 gas mixture, stabilization of the VO_2(R) phase was observed for both the oxidation of sputtered V films and crystallization of ALD grown amorphous VO_2 films, while allowing annealing time and temperature to vary over a relatively large window. Therefore, the thin film deposition techniques used during this work should be straightforward to transfer to other reactors and enable a large process window.

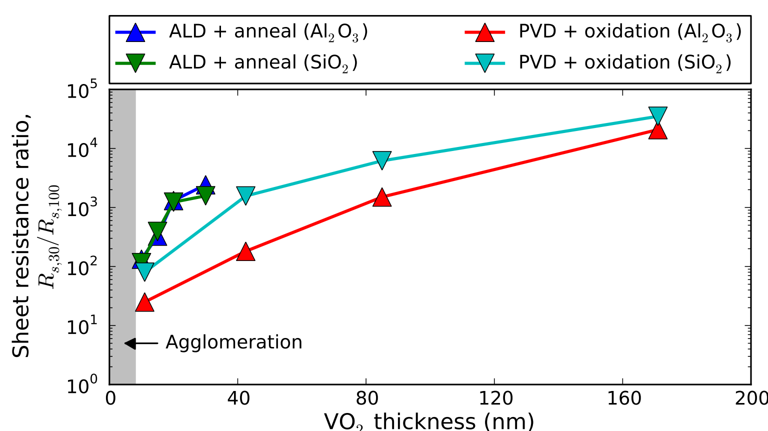

Figure 3.29. *Overview of the sheet resistance ratio $R_{s,30}/R_{s,100}$ of VO_2 thin films prepared by ALD, followed by annealing, and PVD, followed by controlled oxidation. The ALD films and the thinnest PVD film were annealed in a mixture of 5000 Pa H_2 and 20 Pa O_2 at 480 °C for 10 minutes. The thicker PVD films were oxidized in a mixture of 5000 Pa H_2 and 200 Pa O_2 at 480 °C for 15, 30 or 60 minutes for 42, 85 and 170 nm VO_2 respectively.*

The semiconductor-metal transition has been investigated by three complementary in-situ metrology techniques. Sheet resistance measurements showed over 4 orders of magnitude switching in VO_2 films (170 nm) prepared by oxidation of V, and over 3 orders of magnitude for ALD deposited VO_2 films (20-30 nm). For both approaches, the sheet resistance ratio decreases with film thickness, as visualized in figure 3.29. Both ALD and PVD films were scalable down to 10 nm, but the ALD films were significantly less sensitive to the substrate. Indeed, the VO_2 films prepared on different substrates by oxidation of sputtered V showed a significant difference in grain size, which is expected to be the cause of the difference in sheet resistance switching ratios on those substrates. In contrast, ALD deposited films were amorphous, which is independent of the substrate. This

seems to lead to similar properties of the VO_2 films after annealing, as observed by the similar switching ratios. Furthermore, ALD has the advantage of being able to deposit these VO_2 films conformally on 3D substrates.

Below 10 nm, the VO_2 films agglomerated with the formation of nanoparticles. XRD and ellipsometry allowed for the characterization of the semiconductor-metal transition in these nanoparticles. The hysteresis width was found to increase significantly, and values up to 50 °C hysteresis were observed.

Apart from the deposition of VO_2(M1/R) thin films, three other vanadium oxide phases have been synthesized by ALD and post-ALD annealing, i.e. VO_2(B), V_6O_{13} and V_2O_5. V_2O_3, V_6O_{13} and V_2O_5 have as well been prepared by gas-solid reactions with V or V_2O_5 thin films. While V_2O_3 may as well be used or investigated for applications based on the semiconductor-metal transitions, VO_2(B), V_6O_{13} and V_2O_5 can (or may) be used for other applications such as in Li-ion batteries and catalysts.

References

[1] T. J. Hanlon, R. E. Walker, J. A. Coath, and M. A. Richardson, *Thin Solid Films* **405**, 234–237 (2002).

[2] Y. Ningyi, L. Jinhua, and L. Chenglu, *Appl. Surf. Sci* **191**(1), 176–180 (2002).

[3] K. Martens, N. Aetukuri, J. Jeong, M. G. Samant, and S. S. P. Parkin, *Appl. Phys. Lett.* **104**(8), 081918 (2014).

[4] S. Lee, T. L. Meyer, S. Park, T. Egami, and H. N. Lee, *Appl. Phys. Lett.* **105**(22), 223515 (2014).

[5] M. Soltani, M. Chaker, E. Haddad, R. V. Kruzelecky, and J. Margot, *Appl. Phys. Lett.* **85**(11), 1958–1960 (2004).

[6] M. Soltani, M. Chaker, E. Haddad, R. V. Kruzelecky, and D. Nikanpour, *J. Vac. Sci. Technol. A* **22**(3), 859 (2004).

[7] J. W. Tashman, J. H. Lee, H. Paik, J. A. Moyer, R. Misra, J. A. Mundy, T. Spila, T. A. Merz, J. Schubert, D. A. Muller, and et al., *Appl. Phys. Lett.* **104**(6), 063104 (2014).

[8] J. Musil, P. Baroch, J. Vlek, K. Nam, and J. Han, *Thin Solid Films* **475**(1-2), 208–218 (2005).

[9] S. Beke, *Thin Solid Films* **519**(6), 1761–1771 (2011).

[10] J. Duchene, M. Terraillon, and M. Pailly, *Thin Solid Films* **12**(2), 231–234 (1972).

[11] C. H. Griffiths and H. K. Eastwood, *J. Appl. Phys.* **45**(5), 2201–2206 (1974).

[12] Y. Shigesato, M. Enomoto, and H. Odaka, *Jp. J. Appl. Phys.* **39**(10R), 6016 (2000).

[13] D. Brassard, S. Fourmaux, M. Jean-Jacques, J. C. Kieffer, and M. A. El Khakani, *Appl. Phys. Lett.* **87**(5), 051910 (2005).

[14] S. J. Yun, J. W. Lim, J.-S. Noh, B.-G. Chae, and H.-T. Kim, *Jpn. J. Appl. Phys.* **47**(4S), 3067 (2008).

[15] B. Sass, C. Tusche, W. Felsch, N. Quaas, A. Weismann, and M. Wenderoth, *J. Phys.: Condens. Matter* **16**, 77–87 (2004).

[16] G. Salomonsen, N. Norman, O. Lonsjo, and T. G. Finstad, *J. Less-Common Met.* **158**, 251–265 (1990).

[17] X. Xu, X. He, G. Wang, X. Yuan, X. Liu, H. Huang, S. Yao, H. Xing, X. Chen, and J. Chu, *Appl. Surf. Sci.* **257**(21), 8824–8827 (2011).

[18] J.-R. Liang, M.-J. Wu, M. Hu, J. Liu, N.-W. Zhu, X.-X. Xia, and H.-D. Chen, *Chin. Phys. B* **23**(7), 076801 (2014).

[19] C.-Y. Kim, S. H. Kim, S. J. Kim, and K.-S. An, *Appl. Surf. Sci.* **313**, 368–371 (2014).

[20] N. Bahlawane and D. Lenoble, *Chem. Vapor Depos.* **20**(7-8-9), 299–311 (2014).

[21] T. D. Manning, I. P. Parkin, R. J. H. Clark, D. Sheel, M. E. Pemble, and D. Vernadou, *J. Mater. Chem.* **12**(10), 2936–2939 (2002).

[22] M. N. Field and I. P. Parkin, *J. Mater. Chem.* **10**(8), 1863–1866 (2000).

[23] C. B. Greenberg, *Thin Solid Films* **110**(1), 73–82 (1983).

[24] Y. Takahashi, M. Kanamori, H. Hashimoto, Y. Moritani, and Y. Masuda, *J.*

Mater. Sci. **24**(1), 192–198 (1989).
[25] M. B. Sahana, G. N. Subbanna, and S. A. Shivashankar, *J. Appl. Phys.* **92**(11), 6495 (2002).
[26] M. B. Sahana, M. S. Dharmaprakash, and S. A. Shivashankar, *J. Mater. Chem.* **12**(2), 333–338 (2002).
[27] C. Piccirillo, R. Binions, and I. P. Parkin, *Chem. Vapor Depos.* **13**(4), 145–151 (2007).
[28] L. A. Ryabova, I. A. Serbinov, and A. S. Darevsky, *J. Electrochem. Soc.* **119**(4), 427–429 (1972).
[29] J. C. Badot, S. Ribes, E. B. Yousfi, V. Vivier, J. P. Pereira-Ramos, N. Baffier, and D. Lincot, *Electrochem. Solid St.* **3**(10), 485–488 (2000).
[30] R. Baddour-Hadjean, V. Golabkan, J. P. Pereira-Ramos, A. Mantoux, and D. Lincot, *J. Raman Spectrosc.* **33**(8), 631–638 (2002).
[31] J. Keränen, A. Auroux, and L. Niinistö, *Appl. Catal. A* **228**, 213–225 (2002).
[32] J. Keränen, C. Guimon, E. Iiskola, and L. Niinist, *Catal. Today* **78**, 149–157 (2003).
[33] J. Keränen, P. Carniti, A. Gervasini, E. Iiskola, A. Auroux, and L. Niinistö, *Catal. Today* **91-92**, 67–71 (2004).
[34] A. Gervasini, P. Carniti, J. Keränen, L. Niinistö, and A. Auroux, *Catal. Today* **96**(4), 187–194 (2004).
[35] K. Le Van, H. Groult, A. Mantoux, L. Perrigaud, F. Lantelme, R. Lindstrm, R. Badour-Hadjean, S. Zanna, and D. Lincot, *J. Power Sources* **160**(1), 592–601 (2006).
[36] J. Musschoot, D. Deduytsche, H. Poelman, J. Haemers, R. L. Van Meirhaeghe, S. Van den Berghe, and C. Detavernier, *J. Electrochem. Soc.* **156**(7), P122 (2009).
[37] J. Musschoot, *Advantages and challenges of plasma enhanced atomic layer deposition*, PhD thesis, Ghent University, (2011).
[38] E. Østreng, K. B. Gandrud, Y. Hu, O. Nilsen, and H. Fjellvåg, *J. Mater. Chem. A* **2**(36), 15044–15051 (2014).
[39] P. Dagur, A. U. Mane, and S. Shivashankar, *J. Cryst. Growth* **275**(1-2), e1223–e1228 (2005).
[40] I. M. Povey, M. Bardosova, F. Chalvet, M. E. Pemble, and H. M. Yates, *Surf. Coat. Tech.* **201**(22-23), 9345–9348 (2007).
[41] M.-G. Willinger, G. Neri, E. Rauwel, A. Bonavita, G. Micali, and N. Pinna, *Nano Letters* **8**(12), 4201–4204 (2008).
[42] X. Chen, E. Pomerantseva, P. Banerjee, K. Gregorczyk, R. Ghodssi, and G. Rubloff, *Chem. Mater.* **24**(7), 1255–1261 (2012).
[43] S. Boukhalfa, K. Evanoff, and G. Yushin, *Ener. Environ. Sci.* **5**(5), 6872–6879 (2012).
[44] G. Rampelberg, M. Schaekers, K. Martens, Q. Xie, D. Deduytsche, B. De Schutter, N. Blasco, J. Kittl, and C. Detavernier, *Appl. Phys. Lett.* **98**(16), 162902 (2011).
[45] P. A. Premkumar, M. Toeller, I. P. Radu, C. Adelmann, M. Schaekers, J. Meersschaut, T. Conard, and S. Van Elshocht, *ECS J. Solid State Sci. Technol.*

1(4), P169–P174 (2012).

[46] T. Blanquart, J. Niinistö, M. Gavagnin, V. Longo, M. Heikkilä, E. Puukilainen, V. R. Pallem, C. Dussarrat, M. Ritala, and M. Leskelä, *RSC Adv.* **3**(4), 1179 (2013).

[47] G. Rampelberg, D. Deduytsche, B. De Schutter, P. A. Premkumar, M. Toeller, M. Schaekers, K. Martens, I. Radu, and C. Detavernier, *Thin Solid Films* **550**, 59–64 (2014).

[48] G. Rampelberg, B. De Schutter, W. Devulder, M. Schaekers, K. Martens, C. Dussarrat, and C. Detavernier, *To be published* .

[49] P. A. Premkumar, K. Martens, G. Rampelberg, M. Toeller, J. M. Ablett, J. Meersschaut, D. Cuypers, A. Franquet, C. Detavernier, J.-P. Rueff, M. Schaekers, S. Van Elshocht, M. Jurczak, C. Adelmann, and I. P. Radu, *Adv. Funct. Mater.* **25**, 679–686 (2015).

[50] M. Tangirala, K. Zhang, D. Nminibapiel, V. Pallem, C. Dussarrat, W. Cao, T. N. Adam, C. S. Johnson, H. E. Elsayed-Ali, and H. Baumgart, *ECS J. Solid State Sci. Technol.* **3**(6), N89–N94 (2014).

[51] http://www.soxal.com/en/primary-electronics-1/aloha-advanced-precursors.html, Accessed: 2015-10-08.

[52] http://www.strem.com/catalog/d/mocvd/, Accessed: 2015-10-08.

[53] M. B. Takeyama, M. Sato, H. Sudoh, H. Machida, S. Ito, E. Aoyagi, and A. Noya, *Jpn. J. Appl. Phys.* **50**(5), 05EA06 (2011).

[54] B. E. Deal and A. S. Grove, *J. Appl. Phys.* **36**(12), 3770 (1965).

[55] A. Mukherjee and S. P. Wach, *J. Less-Common Met.* **132**, 107–113 (1987).

[56] G. Silversmit, D. Depla, H. Poelman, G. B. Marin, and R. De Gryse, *J. Electron Spectrosc.* **135**(2-3), 167–175 (2004).

[57] V. Miikkulainen, M. Leskelä, M. Ritala, and R. L. Puurunen, *J. Appl. Phys.* **113**(2), 021301 (2013).

[58] D. M. Hausmann and R. G. Gordon, *J. Cryst. Growth* **249**(1), 251–261 (2003).

[59] J. Dendooven, *Modeling and in situ characterization of the conformality of atomic layer deposition in high aspect ratio structures and nanoporous materials*, PhD thesis, Ghent University, (2012).

[60] K. Geryl, *Atomic layer deposition of vanadium oxides for lithium-ion batteries*, Master's thesis, Ghent University, (2014).

[61] M. M. Minjauw, J. Dendooven, B. Capon, M. Schaekers, and C. Detavernier, *J. Mater. Chem. C* **3**(1), 132–137 (2015).

[62] F. Théobald, R. Cabala, and J. Bernard, *J. Solid State Chem.* **17**, 431–438 (1976).

[63] C. Leroux, G. Nihoul, and G. Van Tendeloo, *Phys. Rev. B* **57**(9), 5111 (1998).

[64] D. Deduytsche, *An in-situ study of the stability of thin film Ni-silicide layers*, PhD thesis, Ghent University, (2006).

[65] D. Ruzmetov, G. Gopalakrishnan, C. Ko, V. Narayanamurti, and S. Ramanathan, *J. Appl. Phys.* **107**(11), 114516 (2010).

[66] V. A. Klimov, I. O. Timofeeva, S. D. Khanin, E. B. Shadrin, A. V. Ilinskii, and F. Silva-Andrade, *Tech. Phys.* **47**(9), 1134–1139 (2002).

[67] R. Lopez, L. A. Boatner, T. E. Haynes, L. C. Feldman, and R. F. Haglund, *J. Appl. Phys.* **92**(7), 4031 (2002).

[68] J. Y. Suh, R. Lopez, L. C. Feldman, and R. F. Haglund Jr, *J. Appl. Phys.* **96**(2), 1209–1213 (2004).

[69] X. Wang, Y. Cao, C. Yang, L. Yan, and Y. Li, *J. Vac. Sci. Technol. A* **34**(1), 01A106 (2016).

4 Synthesis and characterization of VN thin films

In this chapter, the synthesis of vanadium nitride thin films is discussed. First, a brief literature overview is presented in section 4.1. Similar as the oxidation of sputtered vanadium thin films, experimental work on the nitridation of vanadium is described in section 4.2, while the ALD work on VN is covered in section 4.3. Paper V, which is included in the appendix, describes the use of VN thin films grown by ALD as copper diffusion barriers.

4.1 Literature on thin film VN synthesis

Compared to vanadium oxides, literature on VN thin film synthesis is less comprehensive. In the following paragraphs, the most frequently applied techniques are summarized, including reactive sputtering, nitridation of V and V_2O_5 and CVD. One paragraph will deal with ALD of metal nitrides in general, including a comparison with TiN and TaN_x, as an introduction to ALD of VN.

4.1.1 Reactive sputtering

Most research on thin film vanadium nitrides has been carried out by means of reactive sputtering.[1–10] Compared to VO_2, the growth of VN thin films requires significantly less optimization, since it is the vanadium nitride phase with the highest nitrogen concentration. This was already shown in the introduction (Figure 1.18). In all cases V has been used as target material, while the sputtering ambient was

a mixture of Ar with N_2. Since both vanadium and vanadium nitrides are conductive, most sputter depositions were performed in DC mode with magnetrons. The sputter rate of VN is typically half of the value for V.[3] Mostly VN was indeed reported as the vanadium nitride phase deposited. However, in some cases V_2N was observed as well. Chu et al. were able to deposit V_2N when the partial pressure of N_2 was in the range from 0.005 to 0.01 Pa, whereas VN was obtained between 0.02 and 0.04 Pa N_2.[3] Suszko et al. found optimal values for the N_2 partial pressure between 0.1 and 0.2 Pa for the growth of V_2N, while higher N_2 pressure resulted in VN.[9] The difference in the boundary between N_2 partial pressures for V_2N and VN is related to other process parameters such as deposition temperature, sputter power and reactor configuration. In general, when the partial N_2 pressure is sufficient, VN will be deposited. The reported deposition temperatures varied from less than 300 °C to 700 °C. The VN thin films were characterized by a resistivity from 40 to 400 $\mu\Omega \cdot \mathrm{cm}$.

4.1.2 Nitridation of V and V_2O_5

Most literature on VN synthesis by nitridation concerns the high-temperature nitridation of metallic V in N_2. Alternative, the nitridation can be performed by plasma-assisted methods. Furthermore, the combination of reduction and nitridation of V_2O_5 in NH_3 has also been reported. These three different methods are discussed in the following paragraphs.

Thermal nitridation of V: Zhao et al. studied the nitridation of V foils with a thickness of 0.001 and 0.002 inch (i.e. 25.4 and 50.8 $\mu\mathrm{m}$) in molecular N_2.[1] The experiments were performed in a tube furnace which was first evacuated to a pressure of approximately 2×10^{-4} Pa, before setting the N_2 gas pressure to a value near atmospheric pressure. The samples were annealed at 1100 °C for a period of 10 to 12 h. However, small amounts of oxygen contamination were found, showing the sensitivity of V towards oxidation.

Galesic et al. did a thorough study on the impact of the temperature and heating rate on the nitridation of V thin films of 200 nm.[11;12] When using long annealing times (1 h) and slow heating rates in a tube furnace (0.4 °C/s), VO_2 was formed instead of VN. Applying higher heating rates (3 °C/s) resulted in a mixture of VN and V_2O_3. Only when a rapid thermal processing (RTP) system with very high heating rates was used (50-100 °C/s), pure vanadium nitrides were formed. Fast heating rates and short process times keep the integral reaction time of residual oxygen low and prevent oxide formation, which is favored over nitride formation in the temperature region between 400 and 800 °C. Above 800 °C the nitrogen diffusion and consequent nitridation of V occurs very fast. For processing times of 5 s, the 200 nm V film transformed to β-V_2N at temperatures between 800 and 900 °C, and to δ-VN at temperatures above 1050 °C.

Berendes et al. continued the work of Galesic et al. and studied the interface between vanadium nitride and SiO_2 and Al_2O_3 substrates.[13] At 700 and 900 °C

vanadium-oxy-nitride was formed at the interface with the SiO_2 substrate. At the higher temperature of 1100 °C, the fast nitridation prevented diffusion of oxygen from the SiO_2 into the vanadium nitride layer, and a sharp VN/SiO_2 interface was achieved. When NH_3 was used for the nitridation, hydrogen (from decomposition of NH_3) was found to attack the SiO_2 layer, and more oxygen was found to diffuse into the vanadium nitride film, leading to $V_{16}O_3$ fractions. In case of the Al_2O_3 substrate these oxygen-containing phases were not observed, since the hydrogen was not able to reduce the substrate.

Plasma-assisted nitridation of V: Chaplanov and Shcherbakova reported on the use of a $N_2{-}H_2$ plasma to transform V thin films of 100 nm into VN.[14] The total gas pressure used during experiments was 10×10^{-3} Pa. The role of H_2 was the removal of residual oxygen in the gas, which would greatly reduce the density of atomic nitrogen. Plasma exposure times varied from 5 to 30 minutes, corresponding to ion doses from 7.5×10^{18} to $5 \times 10^{19}\mathrm{cm}^{-2}$. At 400 °C a solid solution of N in V was observed. In the range from 450 °C to 750 °C, pure VN was obtained with a resistivity in between 200 and 250 $\mu\Omega \cdot \mathrm{cm}$. The grain size was found to increase with the plasma exposure time. From 800 °C on, a mixture of VN and V_2O_3 was observed, which was explained by the reactivity of residual oxygen exceeding the reactivity of the nitrogen plasma species.

Thermal reduction and nitridation of V_2O_5: Kapoor and Oyama reported on the synthesis of high-surface area VN by the simultaneous reduction and nitridation of fine V_2O_5 powder in NH_3 gas.[15] The temperature was slowly increased to values up to 800 °C and the NH_3 pressure was adjusted to 0.17 MPa. The resulting δ-VN particles had a mean particle size of 11 nm and a surface area of 90 m^2/g. Due to surface oxidation, this high surface-area VN powder was found to be pyrophoric and passivation in low pressure O_2 was required prior to exposing the powder to air. Similar experiments were performed by Zhou et al. and Glushenkov et al.[16;17] Reports on the application of this reduction/nitridation method on V_2O_5 thin films were not found.

4.1.3 Chemical vapor deposition

Deposition of VN by CVD has not been reported as often as vanadium oxides. Kieda et al. deposited δ-VN films from VCl_4, N_2 and H_2 at temperatures above 900 °C.[18] When high feeding of VCl_4 was used, minor fractions of β-V_2N were observed. Parkin and Elwin also used VCl_4, but in combination with NH_3 at much lower temperatures in the range between 350 and 650 °C.[19] However, high contents of oxygen were present in the films, which were attributed to oxygen impurities in the N_2 carrier gas. Fix et al. used TDMAV precursor, i.e. $V(NMe_2)_4$, in combination with NH_3 at 200 °C and obtained VN with a growth rate of 20 nm/min.[20] The resistivity was $10^3 \mu\Omega \cdot \mathrm{cm}$, which is relatively high compared to values obtained for reactively sputtered films. Abisset and Maury have grown δ-

VN films from bis(benzene)vanadium, $V(C_6H_6)_2$ and NH_3-H_2 gas mixtures at a temperature of 550 °C. High ratios NH_3 to $V(C_6H_6)_2$ (> 400) were required to reduce the carbon contamination to less than 5%. Watanabe and Zama granted a patent which includes the growth of VN containing diffusion barriers for copper interconnects in integrated circuits (ICs).[21] TDMAV, $V(NMe_2)_4$ and TDEAV, $V(NEt_2)_4$ were used as precursors, and (eventually) combined with NH_3, H_2 or tert-butyl-hydrazine, $C_4H_{12}N_2$ (TBH) as reactants. The films were deposited at 300 and 350 °C respectively, but were far from stoichiometric VN and contained large amounts of carbon. Oxygen contamination was rather low. The reported resistivities were very high: in the range from 1000 to 3000 $\Omega \cdot \mathrm{cm}$. Table 4.1 gives a short overview of these CVD processes.

Precursor	Reactant(s)	Temperature (°C)	Composition	Resistivity ($\mu\Omega \cdot \mathrm{cm}$)	Ref.
VCl_4	N_2-H_2	900-1100	δ-VN (+β-V_2N)	not reported	18
VCl_4	NH_3	350-650	$VN_{0.80}O_{0.18}$ - $VN_{0.56}O_{0.80}$	not reported	19
$V(C_6H_6)_2$	NH_3-H_2	550	δ-VN	not reported	22
$V(NMe_2)_4$	NH_3	200	VN	10^3	20
$V(NMe_2)_4$	-	300	$V_{0.50}N_{0.20}O_{0.06}C_{0.24}$	1000-3000 $\times 10^3$	21
	NH_3	300	$V_{0.51}N_{0.27}O_{0.08}C_{0.14}$		
	H_2	300	$V_{0.50}N_{0.21}O_{0.06}C_{0.23}$		
	TBH	300	$V_{0.49}N_{0.25}O_{0.16}C_{0.10}$		
$V(NEt_2)_4$	-	350	$V_{0.42}N_{0.13}O_{0.04}C_{0.41}$	1200-3000 $\times 10^3$	21
	NH_3	350	$V_{0.48}N_{0.19}O_{0.03}C_{0.30}$		
	H_2	350	$V_{0.43}N_{0.15}O_{0.04}C_{0.38}$		
	TBH	350	$V_{0.51}N_{0.25}O_{0.05}C_{0.19}$		

Table 4.1. *Literature overview of CVD processes for vanadium nitride.*

4.1.4 Atomic layer deposition

Takeyama et al. were the first to publish ALD of VN.[30] These researchers made use of the tetrakis(diethylamino)vanadium (TDEAV, $V(N(Et_2))_4$) precursor in combination with NH_3 gas as reactant. The deposition temperature was varied from 190 to 250 °C, resulting in a linear growth with growth rates of approximately 1Å per cycle. Detailed characteristics of the ALD process were however not reported, such as saturation behavior and temperature window. The films were amorphous as deposited and crystallized into VN upon annealing at 700 °C for 1 hour. The resistivity was as low as 120 $\mu\Omega \cdot \mathrm{cm}$, which is much lower compared to the CVD growth reported for this precursor, as described in the previous section. On the other hand, the stoichiometry, as determined by XPS, deviated significantly from VN, and a high oxygen content was observed, around 20-25%. This oxygen contamination might have been related to the oxidation of the film after exposure to air. The carbon impurity level was however drastically lower compared to the CVD films grown from TDEAV (table 4.1), i.e. around 6% in this case.

ALD of VN may show similarities with other metal nitride ALD processes, such as TiN and TaN_x. These two materials have been investigated intensively for

Table 4.2. *Literature overview of some metal nitride ALD processes. The results obtained in this thesis are included as well.*

Material	**Precursor**	**Reactant**	**Temperature ($^\circ$C)**	**Growth rate (Å/cycle)**	**Resistivity ($\mu\Omega\cdot$cm)**	**References**
TaN_x	PDMAT	H_2, N_2, H_2-N_2 plasma	200-300	0.3	350	[23]
	PDMAT	H_2, H_2-N_2, NH_3 plasma	150-250	0.5	400	[24]
	PDMAT	N_2, NH_3 plasma	50-400	0.4-0.75	not reported	[25]
TiN	$TiCl_4$	H_2-N_2 plasma	100-400	0.3-0.6	70-210	[26]
	TDMAT	NH_3 thermal	50-250	0.5-0.6	53000	[27]
		N_2, NH_3 plasma	50-250	0.5-1.5	180	[27]
	TEMAT	NH_3 thermal	150-220	4.5	210-8000	[28;29]
VN	TDEAV	NH_3 thermal	190-250	1.0	120	[30]
	TEMAV	NH_3 plasma	70-150	0.7	90-200	[31]

microelectronic applications such as copper diffusion barriers and gate electrodes, and their ALD processes are well established.[32] Compared to metal oxide ALD, the range of useful precursors for metal nitride ALD is rather limited. The reason is that metal-oxygen bonds are in general much stronger than metal-nitrogen bonds, such that it is difficult to obtain metal nitrides from oxygen-containing precursors. For instance, isopropoxide precursors are not applicable for metal nitride growth. In early reports on metal nitride ALD, metal halides, such as $TiCl_4$ and $TaCl_5$, were used in combination with NH_3.[32–34] These processes have some drawbacks: (i) they require relatively high deposition temperatures, (ii) high contamination levels of Cl are present in the films, and (iii) corrosive HCl is produced as reaction product, which can attack reactor parts. These drawbacks can be circumvented by the use of metal-organic precursor, and many of such processes have been reported during the past decade. These include both thermal and plasma-enhanced ALD processes. Although thermal ALD has the advantage of easily achieving the highest possible conformality onto complex 3D structures, plasma-enhanced ALD allows for (i) reduced processing temperatures, (ii) higher film density, and (iii) lower impurity content.[32;35] Certainly in the case of microelectronic applications, where a low resistivity is critical, the impurity level of metal nitrides should be as low as possible. Table 4.2 gives a brief, non-exhaustive literature overview of some relevant metal nitride ALD processes.

TaN_x has been investigated in much detail, and one of the crucial difficulties exists in growing low-resistive stoichiometric TaN. In many cases, the high resistive Ta_3N_5 phase is deposited, which is detrimental for use as electrode material or as diffusion barrier for Cu interconnects. This issue is not observed for TiN, which has only one possible nitride phase. Therefore it needs less optimization of the ALD process conditions. In case of VN, it is expected that only the low-resistive δ-VN phase will be deposited, since sufficient nitrogen is available in the metal-organic precursor molecules to exclude the β-V_2N phase. As a final remark, it is interesting to mention that some lower oxide phases of vanadium, such as V_2O_3, are more often observed than lower oxides of tantalum and titanium. Under similar conditions of temperature and oxygen partial pressure where V_2O_3 is thermodynamically stable, Ta_2O_5 and TiO_2 are favored phases. Since V_2O_3 is an electrical conductor (above -108 °C), and Ta_2O_5 and TiO_2 are insulators, it may be expected that the influence of oxygen contamination on the resistivity is probably significantly lower in VN films compared to TiN or TaN. Also surface or interface oxidation will potentially have reduced impact on applications where contact resistance should be kept as low as possible.

4.2 High-temperature nitridation of vanadium

In this section, the nitridation of V at high temperatures is described. This study is performed by means of in-situ XRD on the sputtered V thin films of 80 nm. Similar to the synthesis of vanadium oxides by oxidation of V in O_2-containing ambients, annealing of V in N_2 will result in vanadium nitride formation. However,

as for most metals, V is much more prone to oxidation compared to nitridation, as explained in section 4.1.2. Therefore, a very pure ambient with the lowest possible O_2 content is required. For this study, a gas mixture of 10% H_2 and 90% N_2 has been used. Compared to pure N_2, the addition of H_2 might prevent the formation of undesired vanadium oxides. Remark that the phase of interest, i.e. VN, is the vanadium nitride phase with the highest possible nitrogen content. Control of the partial pressure of N_2 to low values is therefore not required.

Influence of heating rate: As described in section 4.1.2, high temperatures and high heating rates are required to increase the chance of success for the formation of pure VN. As a first set of experiments, the effect of the heating rate on the formation of vanadium nitrides, and the possible formation of undesired vanadium oxide

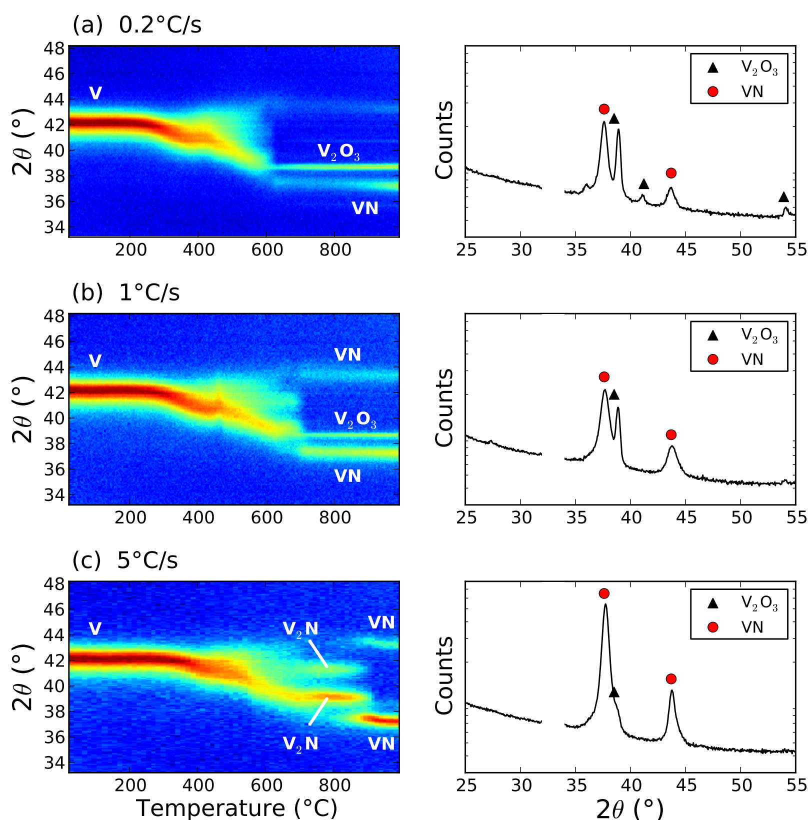

Figure 4.1. Left: in-situ XRD measurements during thermal nitridation of 80 nm vanadium layers in a 10% H_2 + 90% N_2 gas mixture at various heating rates: (a) 0.2°C/s, (b) 1°C/s, and (c) 5°C/s. Right: corresponding full XRD scans after annealing. For clarity the Si (100) substrate peak near 33 ° is removed.

phases was studied. Figure 4.1 shows the in-situ XRD measurements carried out at heating rates of 0.2, 1 and 5 °C/s, and the corresponding full XRD scans carried out after the nitridation. When looking at the lowest heating rate of 0.2 °C/s, it is observed that the first step in the nitridation process takes place in between 200 and 400 °C. The shifting of the V peak towards lower 2θ values indicates a lattice expansion caused by absorption of N_2 and formation of an undefined solid solution of V and N. The second step in the oxidation process occurs at temperatures in between 400 and 500 °C, leading to a second shift of the diffraction peak. At the lowest heating rate, this shift is abruptly ended when the formation of V_2O_3 is observed near 600 °C, with a diffraction peak near 38.5 °. This oxidation is believed to originate from the very low background of O_2 or H_2O in the reaction chamber and gas feeding, and it shows how sensitive V is towards oxidation. However, in addition to the diffraction peak related to V_2O_3, two other fainter peaks appear near 37.5 ° and 43.5 °, which correspond to δ-VN. The presence of both V_2O_3 and VN is better visualized by the full XRD scan after the anneal.

By increasing the heating rate to 1 °C/s, the formation of VN is more pronounced, whereas the V_2O_3 phase is slightly suppressed. A further increase of the

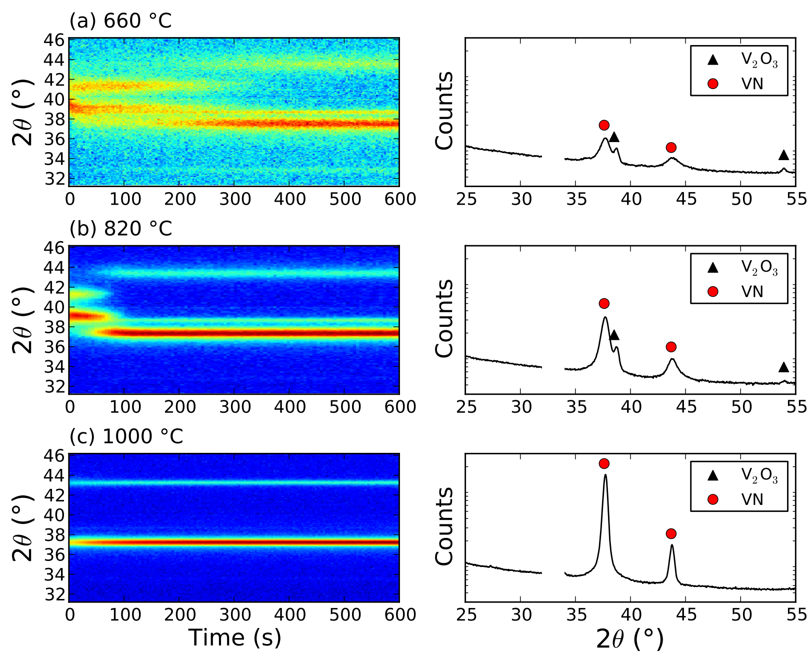

Figure 4.2. *Left: In-situ XRD measurements during isothermal nitridation of 80 nm vanadium layers in a 10% H_2 + 90% N_2 gas mixture at various temperatures: (a) 660°C, (b) 820°C, and (c) 1000°C. Right: corresponding full XRD scans after annealing. For clarity the Si (100) substrate peak near 33 ° is removed.*

heating rate to 5 °C/s results in nearly pure VN. In addition, the intermediate formation of β-V_2N is observed as well, with two diffraction peaks near 39.5 ° and 41.5 °.

Isothermal anneals: In addition to the ramp anneals, some isothermal nitridation experiments were performed. The results are shown in figure 4.2 for isothermal temperatures of 660, 820 and 1000 °C. Heating rates of 5 °C/s were applied in all cases. At all temperatures δ-VN is formed, but it is observed that pure VN is only obtained at the highest temperature. Small fractions of V_2O_3 are observed for the lower temperatures, but it can be stated that the fraction of V_2O_3 does not increase once the V film is fully transformed, as observed from the in-situ XRD measurements. This means the VN phase is stable towards oxidation under these experimental conditions.

Resistivity: Sheet resistance measurements were performed at room temperature on the annealed films. The resistivity was calculated by taking into account the thickness increase during nitridation, from 80 nm V to 102 nm VN. Figure 4.3(a) shows the resistivity as a function of the ramp rate during annealing up to 1000 °C. High heating rates are required to allow for low-resistive films. A min-

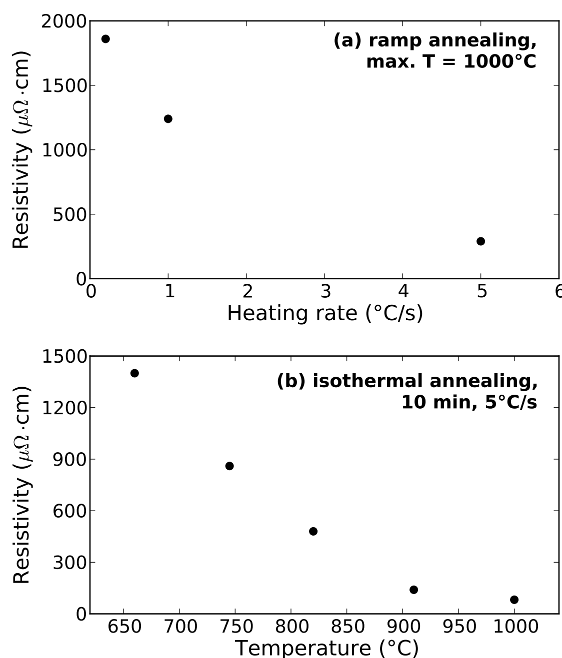

Figure 4.3. *Resistivity of the VN thin films synthesized by (a) ramp annealing to 1000 °C at different heating rates, and (b) isothermal annealing at various temperatures for 10 minutes.*

imum resistivity of 300 $\mu\Omega\cdot\mathrm{cm}$ was achieved. In figure 4.3(b), the resistivity is plotted as a function of annealing temperature, for a fixed heating rate of 5 °C/s and a dwell time of 10 minutes. A minimal value of 80 $\mu\Omega\cdot\mathrm{cm}$ is observed for the annealing temperature of 1000 °C, which is in the lower region of reported values for VN films. Isothermal anneals below 900 °C show increased resistivity values, up to 1400 $\mu\Omega\cdot\mathrm{cm}$ for an isothermal temperature of 660 °C. This is explained by the partial fractions of V_2O_3 which were observed in the XRD scans (figure 4.2). However, the resistivities are still much lower compared to the reported resistivity of V_2O_3, which is on the order of 10^4 $\mu\Omega\cdot\mathrm{cm}$.[36] In section 3.2.3 a value of 3.5×10^4 $\mu\Omega\cdot\mathrm{cm}$ was obtained for V_2O_3 films synthesized by reduction of V_2O_5. Nevertheless we should conclude that high heating rates and high temperatures are required for the synthesis of low-resistive VN films by nitridation of V.

4.3 Low-temperature atomic layer deposition of VN

As an alternative to the high-temperature nitridation of V thin films, low-temperature synthesis of VN thin films by ALD is presented in this section. As for the growth of vanadium oxides (section 3.3), the precursor used for this purpose is TEMAV. Since no oxygen is present in the precursor molecule, oxygen-free films can be grown. For the removal of the amino-groups, NH_3 was used as reactants. In the next section, it will be shown that the activation of NH_3 in a plasma is required for obtaining high-purity and low-resistive VN films.

4.3.1 ALD growth Characteristics

The growth of VN by ALD was studied in the temperature range from 70 to 150 °C. Remember that at higher temperatures uncontrolled growth is expected

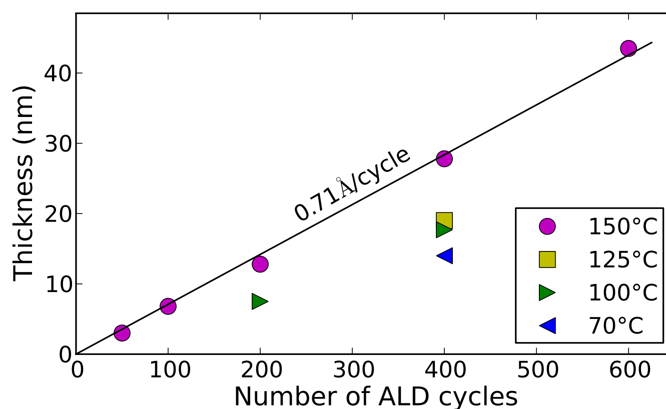

Figure 4.4. *Film thickness as a function of the number of PE-ALD cycles and deposition temperature.*

due to TEMAV decomposition, as described in section 3.3. The characterization of the process was carried out by depositions on Si wafers with a thermally grown SiO_2 layer of 100 nm. For plasma-enhanced ALD, the plasma power was initially varied from 100 to 500 W, but since no significant influence was observed within this range, 300 W was chosen for all further experiments. Figure 4.4 summarizes the ALD growth characteristics of the plasma-enhanced process. A linear growth of approximately 0.7 Å per cycle was observed at a deposition temperature of 150 °C. This is the saturated growth rate as observed during saturation experiments, i.e. by variation of the TEMAV and NH_3 plasma exposure time. The growth rate decreased to half of this value when the deposition temperature is lowered to 70 °C. For the thermal process TEMAV - NH_3, the saturated growth rate was 0.55 Å per cycle at 150 °C.

4.3.2 Film properties and influence of post-deposition annealing

Composition: By XPS measurements the composition of the thermally and plasma-enhanced grown ALD films was verified. The measurements are shown in figure 4.5, including the regions for V, O and N. Whereas the plasma-enhanced ALD process results in almost pure VN, the thermal process shows a high oxygen content. The compositions were determined by XPS peak fitting, which delivers information on atomic fractions of the different elements: $V_{0.50}N_{0.48}O_{0.02}$ and $V_{0.40}N_{0.15}O_{0.45}$ for the plasma and thermal processes respectively. The carbon impurity level was below the detection limit. The presence of high oxygen content for the thermal process has as well been observed for thermal ALD of TiN.[27] It cannot be related to the precursor nor the reactant, since both molecules do not contain oxygen. One possible explanation might be the presence of H_2O back-

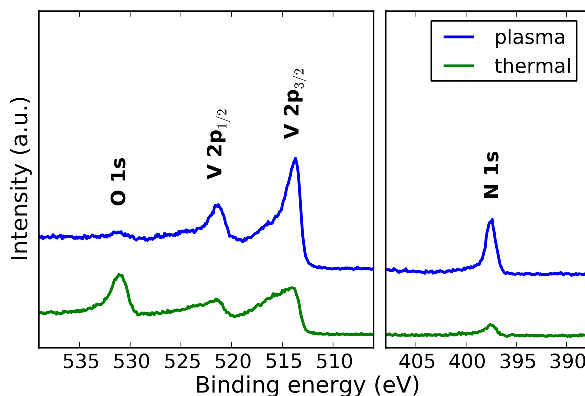

Figure 4.5. XPS measurements of films deposited at 150 °C by thermal and plasma-enhanced ALD.

ground vapor in the reactor or in the NH_3 feeding line. However, the use of the high-vacuum ALD system excludes the first one, which was confirmed in section 3.3.1 where it was shown that exposing the substrate to only TEMAV did not result in any deposition. H_2O background in the NH_3 line could however not be excluded as possible reason for oxygen contamination. An alternative explanation is a lower density of the thermally grown films, which might cause significant oxidation once the film is exposed to air. Although oxidation of VN is slow at low temperatures,[37] a low density VN layer might be more prone to oxidation.

Density: Figure 4.6 shows the V molar density of the ALD films. For the plasma-enhanced ALD process, the V molar density approaches approximately 90% of the reported value for δ-VN at a deposition temperature of 150 °C, but reduces significantly when the deposition temperature is lowered to 70 °C. In case of the thermal process, the V molar density is drastically lower, indicating a low-density film. The films deposited at 150 °C by PE-ALD could be further densified by a post-deposition annealing. Films were slowly annealed to a final temperature of approximately 800 °C in N_2 or in a gas mixture containing N_2 and H_2, as discussed in more detail in the next paragraph. The V molar density could be increased to almost 100% the value of δ-VN in the N_2-H_2 gas mixture.

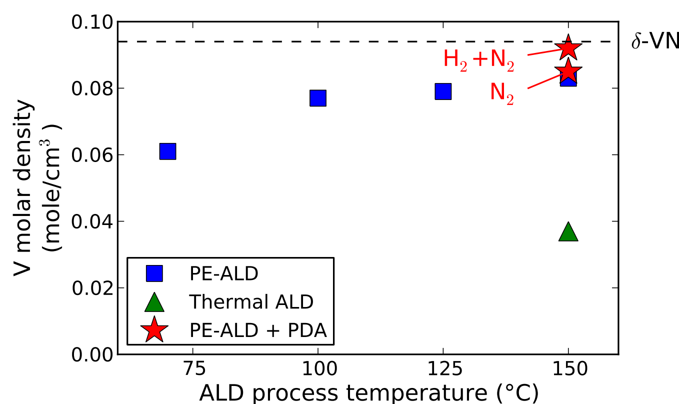

Figure 4.6. *Vanadium molar density for plasma-enhanced and thermally grown films, as a function of deposition temperature. For the plasma-enhanced ALD process, films with post-deposition annealing treatment are included as well.*

Crystallinity: As shown in figure 4.7(a), the PE-ALD process results in crystalline δ-VN films, although at least 400 cycles are required to allow for a reasonable degree of crystallinity. Post-deposition annealing in N_2 or a gas mixture of N_2 and H_2 further increases the crystallinity, while the phase is preserved. Only the orientation changes when using the N_2-H_2 mixture, to pure (111) oriented after

annealing. The in-situ XRD measurements (figure 4.7(b,c)) show that the increase of crystallinity takes place near 700 °C.

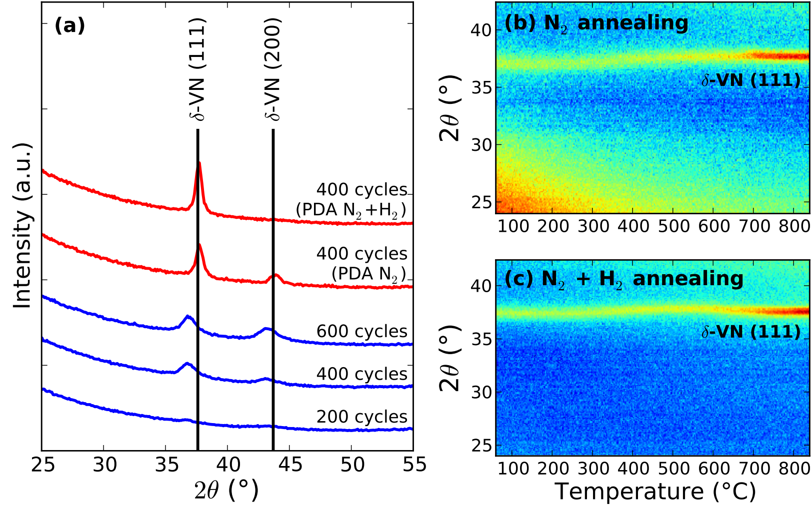

Figure 4.7. *(a) Full scan XRD measurements of plasma-enhanced ALD films, as deposited and after post-deposition annealing. (b,c) In-situ XRD measurements of PE-ALD films of 400 cycles during ramp annealing at 0.2 °C/s in N_2 and N_2-H_2 respectively.*

Resistivity: From sheet resistance measurements the resistivity of the films was determined. As shown in figure 4.8, the resistivity for films deposited at 150 °C

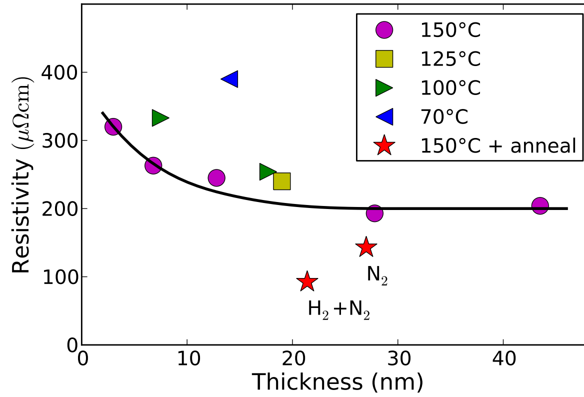

Figure 4.8. *Room temperature resistivity as a function of PE-ALD film thickness and deposition temperature. The black curve shows the trend at 150 °C. The resistivity of the annealed films is indicated as well.*

is as low at 200 $\mu\Omega\cdot\mathrm{cm}$ when the thickness is at least 20 nm. Thinner films are characterized by an increased resistivity. This phenomenon is well known for thin films, and is explained by nonspecular scattering at the surface and grain boundary scattering of conduction electrons.[38] Films deposited at decreased temperatures show an increase of the resistivity, certainly at the lowest temperature of 70 °C, which can be explained by the lower density observed for these films (figure 4.6). Post-deposition annealing of the VN films leads to a significant decrease of the resistivity, to approximately 140 and 90 $\mu\Omega\cdot\mathrm{cm}$ for anneals carried out in N_2 and N_2-H_2 respectively.

VN coating on polymer foil: Apart from ALD on Si substrates, Mylar foil was successfully coated with VN films at a low temperature of 70 °C. By depositing 400 cycles, a semi-transparent conductive coating was obtained with a low sheet resistance of 270 $\Omega/\Box$. A picture is shown in figure 4.9.

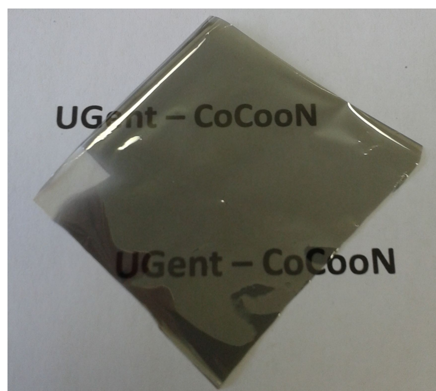

Figure 4.9. *Picture of a piece of Mylar foil, coated with a semi-transparent, electrically conductive VN coating by plasma-enhanced ALD at 70 °C.*

4.3.3 VN thin films as copper diffusion barrier

To confirm the potential of ALD VN films as copper diffusion barriers, two samples were prepared. A piece of silicon wafer was HF cleaned and coated with a 50 nm PVD copper film. However, for one of the samples a 5 nm VN layer was deposited on the silicon wafer, prior to the copper deposition. In between the ALD of VN and the PVD of Cu, the sample was not exposed to air. This was achieved by a transfer from the ALD system to the neighboring PVD system without interruption of the vacuum, as illustrated in figure 2.3.

As shown in figure 4.10, upon annealing a copper film on a silicon wafer, copper will diffuse into the silicon and form copper silicides. It is however important that the silicon wafer is HF cleaned, for avoiding native oxides to influence the diffusion behavior.

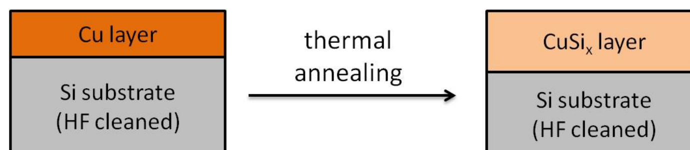

Figure 4.10. *During thermal annealing a Cu thin film on a Si substrate will react with the formation of Cu-silides.*

In-situ XRD was used to verify this diffusion of copper into silicon, with the consequent formation of copper silicides. This is shown in figure 4.11 for both the reference sample, i.e. 50 nm Cu onto HF cleaned Si, and the sample with barrier layer, i.e. 50 nm Cu / 5 nm VN / HF cleaned Si. Both samples were annealed from room temperature up to 900 °C at a heating rate of 1 °C/s. The upper plot shows the measurement of the sample with Cu directly onto Si. Initially, one diffraction peak is present near 50 °, corresponding to the (200) plane of face-centered cubic (fcc) Cu. Only one peak is visible since Cu grows epitaxially onto a (100) Si substrate. This diffraction peak vanishes near 230 °C, and simultaneously Cu_3Si is formed due to the diffusion of Cu into the Si substrate. For the sample with the VN barrier layer, two copper diffraction peaks are initially present, since the

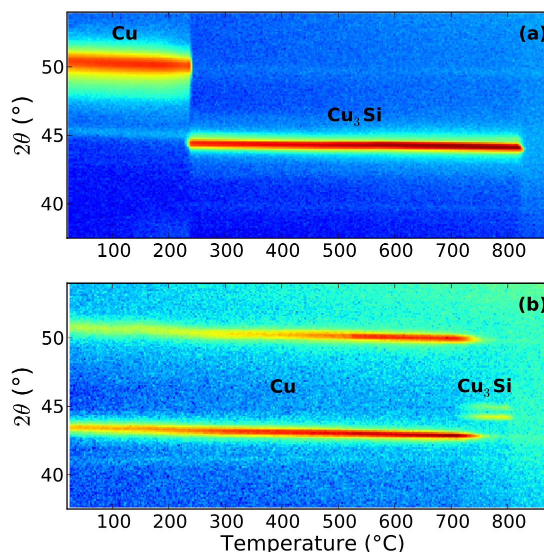

Figure 4.11. *In-situ XRD measurements during thermal annealing of a 50 nm Cu PVD film show the formation of Cu_3Si by reaction with the Si substrate: (a) without barrier layer the reaction occurs near 230 °C, (b) with a 5 nm PE-ALD VN barrier layer the reaction is delayed until a temperature of 720 °C is reached.*

VN film prevents epitaxial growth. These two diffraction peaks only vanish near a temperature of 720 °C, which indicates the stability of the VN barrier up to these high temperatures.

These in-situ XRD measurements are a fast and easy way of qualitatively investigating the potential of VN as copper diffusion barrier. More dedicated research would be required to allow for quantification of the diffusion barrier properties. This is however outside the scope of this work. A comparison with TaN_x and TiN barrier layers would be an interesting topic for further research.

4.3.4 Oxidation resistance of VN thin films

Metal-nitrides are known for their high resistance towards oxidation. In-situ XRD measurements during thermal annealing of a PE-ALD VN film of 25 nm thick-

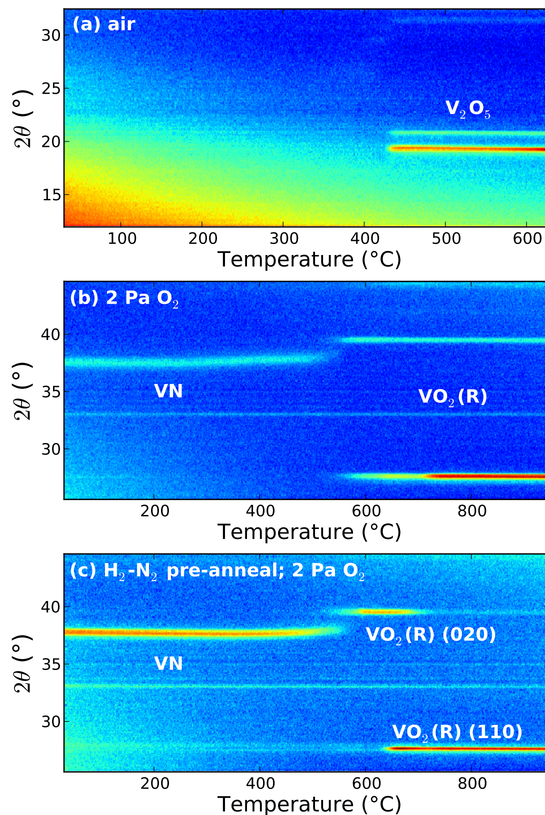

Figure 4.12. *In-situ XRD measurements during thermal annealing of a VN film of 25 nm at a heating rate of 0.2 °C/s, in (a) air, (b) 2 Pa O_2, and (c) 2 Pa O_2 after an isothermal pre-anneal in a H_2-N_2 mixture at 820 °C for 10 minutes.*

ness in air and low oxygen partial pressure (2 Pa) are shown in figure 4.12. A fixed heating rate of 0.2 °C/s has been used during these experiments. In air, a direct oxidation towards V_2O_5 is observed near 425 °C. At 2 Pa O_2, the VN diffraction peak starts to shift slightly around 400 °C. This is not necessarily an indication of oxidation, since such a shift was observed as well during the post-deposition annealing of VN films in N_2 or H_2-N_2 mixtures (figure 4.7). However, instead of intensification of the VN diffraction peak, oxidation towards VO_2(R) is observed near 550 °C. A similar experiment was performed at 2 Pa O_2, but after pre-annealing the VN film for 10 minutes at 820 °C in a H_2-N_2 gas mixture. Although the initial degree of crystallinity of the VN phase was improved significantly by the pre-treatment, also in this case the oxidation towards VO_2(R) starts near 550 °C.

Since the oxidation temperature of the VN films (≈ 550 °C) is higher than the crystallization temperature of amorphous ALD grown VO_2 films (400-450 °C), these ALD VN films might be used as bottom electrode for ALD VO_2 films. In order to investigate this, a deposition of 400 cycles VN, followed by 400 cycles of amorphous VO_2 was performed. This multilayer structure was annealed at low oxygen partial pressure (2 Pa) at a heating rate of 0.2 °C/s, as shown in figure 4.13. Although it was expected to observe crystallization of the amorphous VO_2 film around 400-450 °C, the crystallization was delayed until a temperature of 500 °C, at which the VN phase disappeared simultaneously. Even after a pre-anneal of the

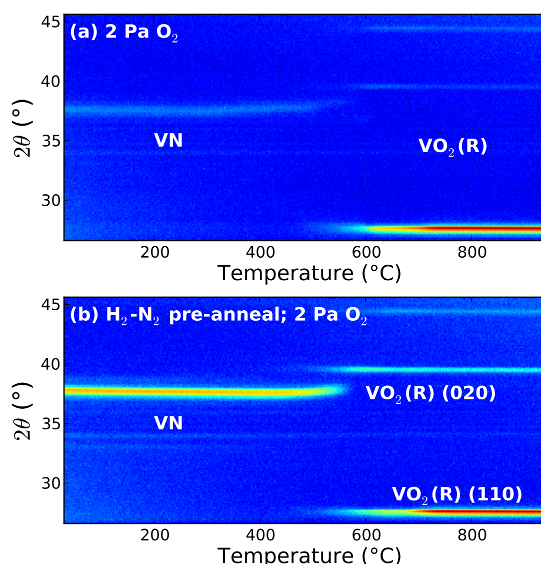

Figure 4.13. *In-situ XRD measurements during thermal annealing of a VN-VO_2 stack at a heating rate of 0.2 °C/s, in 2 Pa O_2: (a) without pre-anneal (b) after an isothermal pre-anneal in a H_2-N_2 mixture at 820 °C for 10 minutes.*

stack in a H_2-N_2 mixture at 820 °C for 10 minutes, similar results were obtained. From these few experiments it is unclear whether ALD VN is suitable as bottom electrode for ALD VO_2. More dedicated research would be required in order to find optimal conditions. For instance, the VN film may need to be annealed prior to the deposition and crystallization of VO_2.

4.4 Conclusions

The vanadium-nitrogen system is less complicated compared to the vanadium-oxygen system, since only three stable vanadium nitride phases exist. However, apart from reactive sputtering, the synthesis of pure VN thin films with a low resistivity has proven to be a challenging task due to the ease of oxidation during processing. Nitridation of metallic V has been reported by a few research groups, showing the difficulty of forming nitrides instead of the more favorable vanadium oxides. CVD coatings are often characterized by high impurity levels, leading to high resistivity values, typically one or a few orders of magnitudes higher compared to films prepared by reactive sputtering. Prior to this work, only one report had been published on ALD of VN from TDEAV precursor and NH_3, however, detailed information on the ALD growth characteristics and properties of the ALD grown films was not published.

In this work, the same techniques as those used for the deposition of VO_2 thin films (chapter 3) have been applied for the synthesis of low-resistive VN layers. The first method was a high-temperature nitridation of PVD grown metallic V films. For this method, it can be concluded that nitridation occurs already at temperatures around 600-700 °C, but higher temperatures of at least 900 °C, and high heating rates of 5 °C/s are required to prevent the formation of vanadium oxides. These results are in correspondence with available literature. Low resistivity values down to 80 $\mu\Omega \cdot \mathrm{cm}$ were obtained, close to the reported bulk value of VN.

Concerning the potential use of VN as copper diffusion barrier, it should be stated that the high-temperature nitridation process of V films is not suitable because of a few reasons. The most important one is the temperature restriction in BEOL processing, which is limited to approximately 400 to 500 °C. In addition, it is believed that for thin films on the order of a few nanometers, oxygen contamination would be much more severe, leading to an increased resistivity.

The second method involved low-temperature ALD from TEMAV and NH_3. The TEMAV precursor is perfectly suited for this purpose, since only V-N bonds are present in the molecule, without any oxygen atoms which might cause oxidation. Although both thermal and plasma-enhanced ALD processes result in film growth, only films grown from NH_3 plasma are characterized by a high purity level and a stoichiometry matching VN. Furthermore, a low resistivity of 200 $\mu\Omega \cdot \mathrm{cm}$ was achieved, which was further reduced down to 90 $\mu\Omega \cdot \mathrm{cm}$ by post-deposition annealing in a N_2-H_2 gas mixture. Apart from silicon wafers, polymer foil was successfully coated as well with low-resistive VN layers at a deposition temperature of only 70 °C.

Ultrathin VN layers, deposited by PE-ALD, show to be effective as copper diffusion barriers. By means of in-situ XRD, the thermal stability of a Cu film on Si was extended from 230 °C without barrier to 720 °C with barrier.

The high oxidation resistance of VN was studied for the ALD films, with the aim of using VN as bottom electrode for switchable VO_2 films. However, although the oxidation temperature at low oxygen partial pressures is above the crystallization temperature of ALD VO_2 films, a stack of a VN bottom electrode with crystalline VO_2(M1/R) on top was not obtained.

References

[1] B. R. Zhao, L. Chen, H. L. Luo, M. D. Jack, and D. P. Mullin, *Phys. Rev. B* **29**(11), 6198 (1984).

[2] J. Zasadzinski, R. Vaglio, G. Rubino, K. E. Gray, and M. Russo, *Phys. Rev. B* **32**(5), 2929 (1985).

[3] X. Chu, S. A. Barnett, M. S. Wong, and W. D. Sproul, *J. Vac. Sci. Technol. A* **14**(6), 3124–3129 (1996).

[4] G. Gassner, P. H. Mayrhofer, K. Kutschej, C. Mitterer, and M. Kathrein, *Tribol. Lett.* **17**(4), 751–756 (2004).

[5] M. B. Takeyama, T. Itoi, K. Satoh, M. Sakagami, and A. Noya, *J. Vac. Sci. Technol. B* **22**(5), 2542 (2004).

[6] X.-P. Qu, M. Zhou, T. Chen, Q. Xie, G.-P. Ru, and B.-Z. Li, *Microelectronic Eng.* **83**(2), 236240 (2006).

[7] N. Fateh, G. Fontalvo, G. Gassner, and C. Mitterer, *Wear* **262**(9-10), 1152–1158 (2007).

[8] Q. Sun and Z.-W. Fu, *Electrochim. Acta* **54**(2), 403–409 (2008).

[9] T. Suszko, W. Gulbiski, A. Urbanowicz, and W. Gulbiski, *Mater. Lett.* **65**(14), 2146–2148 (2011).

[10] L. Zhang, C. M. B. Holt, E. J. Luber, B. C. Olsen, H. Wang, M. Danaie, X. Cui, X. Tan, V. W. Lui, W. P. Kalisvaart, and D. Mitlin, *J. Phys. Chem. C* **115**(49), 24381–24393 (2011).

[11] I. Galesic and B. O. Kolbesen, *Thin Solid Films* **349**, 14–18 (1999).

[12] I. Galesic, U. Reusch, C. Angelkort, H. Lewalter, A. Berendes, E. Schweda, and B. O. Kolbesen, *Vacuum* **61**, 479484 (2001).

[13] A. Berendes, I. Galesic, R. Mertens, W. Bock, H. Oechsner, P. Warbichler, F. Hofer, E. Theodossiu, H. Baumann, and B. O. Kolbesen, *Z. Anorg. Allg. Chem.* **629**(10), 1769–1777 (2003).

[14] A. M. Chaplanov and E. N. Shcherbakova, *Inorg. Mater.* **37**(3), 233–236 (2001).

[15] R. Kapoor and S. T. Oyama, *J. Solid State Chem.* **99**(2), 303–312 (1992).

[16] X. Zhou, H. Chen, D. Shu, C. He, and J. Nan, *J. Phys. Chem. Solids* **70**(2), 495–500 (2009).

[17] A. M. Glushenkov, D. Hulicova-Jurcakova, D. Llewellyn, G. Q. Lu, and Y. Chen, *Chem. Mater.* **22**(3), 914–921 (2010).

[18] N. Kieda, M. N., and K. M., *Nippon Kagaku Kaishi* **1987**(11), 1934–1938 (1987).

[19] I. P. Parkin and G. S. Elwin, *J. Mater. Chem.* **11**(12), 3120–3124 (2001).

[20] R. Fix, R. G. Gordon, and D. M. Hoffman, *Chem. Mater.* **5**(5), 614–619 (1993).

[21] M. Watanabe and H. Zama, (2011), US Patent 8,034,403.

[22] S. Abisset and F. Maury, *Surf. Coat. Technol.* **108**, 200–205 (1998).

[23] H. Kim, C. Detavernier, O. van der Straten, S. M. Rossnagel, A. Kellock, and D.-G. Park, *J. Appl. Phys.* **98**, 014308 (2005).

[24] E. Langereis, H. C. M. Knoops, A. J. M. Mackus, F. Roozeboom, M. C. M.

van de Sanden, and W. M. M. Kessels, *J. Appl. Phys.* **102**(8), 083517 (2007).
[25] Q. Xie, J. Musschoot, C. Detavernier, D. Deduytsche, R. L. V. Meirhaeghe, S. V. d. Berghe, Y.-L. Jiang, G.-P. Ru, B.-Z. Li, and X.-P. Qu, *Microelectronic Eng.* **85**(10), 20592063 (2008).
[26] S. B. S. Heil, E. Langereis, F. Roozeboom, M. C. M. van de Sanden, and W. M. M. Kessels, *J. Electrochem. Soc.* **153**(11), G956 (2006).
[27] J. Musschoot, Q. Xie, D. Deduytsche, S. Van den Berghe, R. L. Van Meirhaeghe, and C. Detavernier, *Microelectronic Eng.* **86**(1), 72–77 (2009).
[28] J.-S. Min, Y.-W. Son, W.-G. Kang, S.-S. Chun, and S.-W. Kang, *Jpn. J. Appl. Phys.* **37**(9R), 4999 (1998).
[29] D.-J. Kim, Y.-B. Jung, M.-B. Lee, Y.-H. Lee, J.-H. Lee, and J.-H. Lee, *Thin Solid Films* **372**(1), 276–283 (2000).
[30] M. B. Takeyama, M. Sato, H. Sudoh, H. Machida, S. Ito, E. Aoyagi, and A. Noya, *Jpn. J. Appl. Phys.* **50**(5), 05EA06 (2011).
[31] G. Rampelberg, K. Devloo-Casier, D. Deduytsche, M. Schaekers, N. Blasco, and C. Detavernier, *Appl. Phys. Lett.* **102**(11), 111910 (2013).
[32] H. Kim, *J. Vac. Sci. Technol. B* **21**(6), 2231 (2003).
[33] R. L. Puurunen, *J. Appl. Phys.* **97**(12), 121301 (2005).
[34] V. Miikkulainen, M. Leskelä, M. Ritala, and R. L. Puurunen, *J. Appl. Phys.* **113**(2), 021301 (2013).
[35] H. B. Profijt, S. E. Potts, M. C. M. Van de Sanden, and W. M. M. Kessels, *J. Vac. Sci. Technol. A* **29**(5), 050801 (2011).
[36] F. J. Morin, *Phys. Rev. Lett.* **3**(1), 34–36 (1959).
[37] A. Glaser, S. Surnev, F. Netzer, N. Fateh, G. Fontalvo, and C. Mitterer, *Surf. Sci.* **601**(4), 1153–1159 (2007).
[38] W. Steinhögl, G. Schindler, G. Steinlesberger, and M. Engelhardt, *Phys. Rev. B* **66**(7), 075414 (2002).

5

Conclusions and suggestions for future work

5.1 Summary and conclusions

In this thesis, synthesis of VO_2 thin films by gas-solid reactions and atomic layer deposition, and the characterization of the semiconductor-metal transition in these films were the main objectives. In addition, VN thin films were prepared using the same approaches. The conclusions which can be drawn from this research are summarized below.

In-situ XRD system for the study of gas-solid reactions: A critical aspect in the study of vanadium oxides is the precise control of oxygen partial pressure, since approximately 25 different vanadium oxide phases are known to exist. For performing this research, a dedicated in-situ X-ray diffraction system was developed, allowing for oxidation and reduction reactions over a wide range of oxygen partial pressures and in reducing gases. In-situ XRD allows for the observation of crystallization and transformation from one crystalline phase into another during high-temperature reactions.

Complementary techniques for monitoring the semiconductor-metal transition: VO_2 exhibits an electronic, optical and structural transition near 68 °C. Three complementary techniques have been used in this work to characterize these features. The electronic switch was observed for continuous films by means of temperature-dependent sheet resistance measurements. The optical transition could

be monitored by spectroscopic ellipsometry, which proved to be useful as well for agglomerated films and nanoparticles. The structural transition was observed by temperature-dependent XRD measurements, showing the reversible transformation between low-temperature monoclinic VO_2(M1) and high-temperature tetragonal VO_2(R).

VO_2 thin film synthesis by gas-solid reactions: The oxidation of sputtered V thin films was investigated in detail for synthesis of VO_2. From thermodynamic considerations, the conditions of VO_2 phase stabilization were expected to be outside the experimental range of the in-situ XRD system. However, kinetics strongly limit the oxidation reactions, allowing for successful VO_2 formation under non-stable conditions. Although very low oxygen partial pressures are strongly advised, since otherwise V_2O_5 is formed, VO_2 was even obtained as transient phase during oxidation in air, resulting in a reasonable electrical switching behavior. In any case, minimum oxidation temperatures around 400-450 °C are required. A mixture of hydrogen with low pressure oxygen resulted in the highest quality VO_2 films, with electrical switching ratios up to 4 orders of magnitude. In addition, reduction of V_2O_5 towards VO_2 was achieved in the same gas mixture, leading to nearly 5 orders of magnitude electrical switching, which is close to values reported for bulk VO_2. Reducing the film thickness leads to a suppression of the electrical transition, while below 10 nm agglomeration has been observed.

VO_2 thin film synthesis by ALD and controlled posted-deposition annealing: Prior to this research, successful ALD of VO_2 was not yet reported, since most V precursors result in growth of V_2O_5, while other precursors only operate at high temperatures where CVD, rather than ALD, may be observed. The TEMAV precursor used in this work, allows for deposition of both amorphous VO_2 and crystalline V_2O_5, by using respectively H_2O or O_3, and O_2 plasma as reactant during deposition. Furthermore, a remarkable difference in density of the amorphous films was observed between the H_2O and O_3 based processes, which drastically affects the crystalline phase formation during post-deposition annealing. The high-density amorphous films grown using H_2O as reactant crystallize towards the VO_2(R) phase at low oxygen partial pressures, or oxidizes towards V_2O_5 at high oxygen partial pressures. In contrast, the low-density amorphous VO_2 films grown by using O_3 as reactant, allow for crystallization into pure VO_2(B) or oxidation towards V_6O_{13} as well, apart from VO_2(R) and V_2O_5. It was noticed that in both cases a low oxygen partial pressure of a few Pa is required to allow for VO_2(R) crystallization, and temperatures around 450 °C. The process based on H_2O as reactant allows for the broadest process window for post-deposition annealing, in terms of oxygen partial pressure. On the other hand, the crystalline V_2O_5 films grown by PE-ALD could be reduced to VO_2(B) or V_6O_{13}. High electrical switching ratios of more than 3 orders of magnitude were observed for the VO_2(R) thin films. A minimum film thickness is however required to observe the electrical switch, since agglomeration occurs during post-deposition annealing. For reduced

film thickness, nanoparticles were formed. These showed an optical transition, as measured by ellipsometry, with an increased hysteresis width up to 50 °C, compared to ≈ 10 °C in continuous films.

Discussion on VO_2 thin films, their synthesis and applications: The two methods developed during this work, have shown to enable high quality VO_2 thin film synthesis. In both cases, similar temperature ranges of 400 to 500 °C are required for obtaining the desirable crystalline phase. Both methods are also scalable down to approximately 10 nm thickness, although the oxidation of sputtered V has shown to be sensitive to the used substrate. The answer to the question about which method is the best strategy depends on a few factors. First of all, the type of application may determine if one or the other method is the most feasible. In microelectronics, where only thin films near 10 nm are required, both ALD and oxidation of sputtered V would be suitable, since ALD has matured during the last decades while sputtering is one of the most well-established technologies in this field. If however deposition is required in or onto 3D structures, ALD is favorable because of its ability of conformally coating such features. Second, if the required film thickness is on the order of several tens of nanometers up to a few hundreds of nanometers, such as in the case of thermochromic coatings on glass, ALD might be too slow, and oxidation of sputtered vanadium would be the best choice. A third parameter is the required surface morphology. In microelectronics, smooth films are certainly required. On the other hand, for thermochromic coating this is not necessarily the case. The reduction process of V_2O_5 films produced in this work may only be suitable for the latter application. Finally, process cost will as well decide which method is suitable for industrial application. Due to the high cost of ALD precursors, the process cost of many products may get to expensive.
As a final remark, the developed method for reduction of V_2O_5 might be a viable alternative. Many coating techniques are available for the deposition of V_2O_5, without the requirement of a dedicated optimization of process parameters, including reactive sputtering, CVD, ALD and sol-gel. The combination of these often well-established V_2O_5 preparation methods with the controlled reduction would lead to a broad range of strategies for VO_2 thin film deposition.

VN thin film synthesis by gas-solid reactions: In contrast to the oxidation of V thin films, high-temperature nitridation proved much more challenging. Very pure N_2 gas is critical, since V is extremely prone to oxidation. Furthermore, the nitridation time should be kept as short as possible, meaning that high temperatures (≈ 1000 °C) and high heating rates (5 °C/s or higher) are essential to obtain pure, low-resistive VN. Nitridation of metallic V is thus only suitable for production processes which tolerate very high temperatures. For microelectronics, this means that nitridation of vanadium is not suitable for back-end-of-line processing, such as copper diffusion barriers.

VN thin film synthesis by ALD: The TEMAV precursor, used for ALD of VO_2, is also useful for the deposition of VN. A low-temperature plasma-enhanced ALD process was established using NH_3 as reactant. Resistivity values down to 200 $\mu\Omega\cdot\mathrm{cm}$ were achieved for the as deposited films, which could be further reduced down to $\approx$ 90 $\mu\Omega\cdot\mathrm{cm}$ by post-deposition annealing under N_2 or N_2-H_2 gas, close to the reported value for bulk VN. Conductive films could be grown on a temperature-sensitive polymer substrate as well. These VN films were briefly evaluated as diffusion barrier for copper, by means of in-situ XRD. For Cu films deposited on Si, formation of copper silicides was strongly delayed by a thin film VN barrier of 5 nm. This shows at least similar to the well-investigated TaN and TiN. The low resistivity is however only obtained after annealing at 700 °C it seems, a temperature which is unfortunately not compatible with BEOL processing. Further investigation on the decrease of the resistivity of the as deposited films would be required, for instance by purification of the NH_3 gas. Also the performance of thinner VN barriers should be investigated, since the ITRS requires downscaling of the barrier thickness to 1 nm in 2021. It might thus be unlikely to introduce VN as a barrier layer in copper interconnect technology. In addition, VN was evaluated as bottom electrode for VO_2. However, during crystallization of the amorphous VO_2 films, the VN films oxidized as well. Although the application of VN in microelectronics might thus be questionable, other applications of this material could be investigated, such as for instance in supercapacitors. In that case, the advantage of ALD as conformal coating technology can be exploited.

5.2 Suggestions for future work

Both the methods and processes developed during this research may be employed for further research. In general, the in-situ XRD system may allow for studying gas-solid reactions in other complicated material systems, such as iron oxides or manganese oxides. On the other hand, the synthesis of VO_2 and VN by gas-solid reactions and ALD opens a wide range of future research perspectives:

Gas-solid reactions in the V-O system:

- It was noticed that a difference in VO_2 microstructure and electrical switching ratio was observed between films grown on SiO_2 and Al_2O_3. It is believed that the main reason behind this observation is related to a difference in microstructure of the sputtered V films. By optimizing the microstructure during sputtering, which may be achieved by tuning parameters such as deposition rate or pressure, improved electrical switching ratios may be achieved for thin films. Alternatively, HIPIMS may be investigated as method for deposition of V.

- Reactive sputtering may be used for the deposition of smoother V_2O_5 films, which may lead to an improved morphology of the VO_2 films after controlled reduction.

- In general, this method of controlled oxidation or reduction may be applied on vanadium oxide films prepared by other techniques.
- Moreover, this method may be applied to other metal-oxides with complex phase diagrams, such as iron oxides or manganese oxides.
- Since for many applications it is critical to tune the transition temperature, preparation of doped VO_2 might be studied. Dumortier reported on the oxidation of V films doped with Al, Ti and W which were prepared by co-sputtering.[1] In all cases it was observed that the dopants migrated to the bottom of the film, resulting in high dopant levels at the bottom and an undoped VO_2 layer on top. As a consequence, an influence of doping on the transition temperature was not observed. The oxidation process was however limited to a single temperature value of 500 °C and an oxygen partial pressure of 100 Pa. It could be a topic of further investigation if varying these two parameters could lead to uniformly doped VO_2 films with altered transition temperatures.

ALD of VO_2:

- The need for crystallization of the amorphous VO_2 films grown using the TEMAV precursor in combination with H_2O or O_3 causes morphological degradation and agglomeration when the film thickness is below 10 nm. It could be worth investigating epitaxial growth of VO_2 by ALD on templates with similar lattice parameters as VO_2(R). This has already been achieved by pulsed laser deposition (PLD) and molecular beam epitaxy (MBE) on sapphire and rutile TiO_2 single crystals.[2–5] But also other templates might enable smoother crystalline VO_2 films if the interface energy would be more favorable, leading to a reduced dewetting.
- Alternatively, other vanadium precursors can be investigated which allow for higher deposition temperatures, and in the best case result in crystalline VO_2 films as deposited. TDEAV is known to have a higher thermal stability such that it can be applied at higher deposition temperatures up to 250 °C.[6] This precursor has only very recently become commercially available. Apart from the potential of achieving smooth crystalline VO_2 films, this would be useful to reduce the maximum processing temperature to allow for crystalline VO_2 deposition on substrates which do not withstand temperatures of more than 400 °C.
- The use of a mixture of H_2 and O_2 during post-deposition annealing resulted in VO_2 phase stabilization. The question may be asked if crystalline VO_2 can be deposited by using such kind of gas mixtures during plasma-enhanced ALD. The high reactivity of plasma species may result in crystalline film growth, as in the case of O_2 plasma, while the addition of H_2 could potentially stabilize VO_2. If possible, optimization of such a process could however prove very challenging.

- Nanoscale VO_2 particles are characterized by an increased hysteresis width, while the stress present at the interface between VO_2 and the substrate is known to alter the transition temperature. ALD of VO_2 in nanoporous structures could potentially be exploited to create new insights in the possibilities of altering the transition characteristics of VO_2. Measurements of the SMT characteristics of single isolated nanoparticles would as well be useful to gain understanding of the relation between nanoparticle size and hysteresis width. A possible method could be the application of conductive AFM (CAFM) on nanoparticles deposited on a conductive substrate.

- Doping could as well be investigated for altering the SMT characteristics. As reported in literature, doping levels of only a few percent are allowed, since at higher doping levels the transition disappears. Synthesizing doped VO_2 thin films by ALD, with a uniform distribution of dopants may be challenging. The most straightforward method of depositing ternary metal-oxides by ALD makes use of combining cycles of two metal-oxide ALD processes in a certain ratio. For obtaining low dopant levels, this ratio would need to be very large, resulting in a non-homogeneous distribution of dopants throughout the film. Alternative approaches could be studied to improve the dopant distribution, including non-saturated ALD cycles for the dopant material or mixing precursors of V and the doping material. In both cases however, a drawback might be a reduced conformality onto 3D substrates. As in the case of doped VO_2 prepared by oxidation of co-sputtered doped V films, an investigation of dopant migration during post-deposition annealing will be required.

ALD of VN: As stated in the introduction, VN has many interesting applications, including diffusion barriers and electrodes for microelectronic applications, catalysts and supercapacitors. In many of these cases, deposition of very thin films in high-aspect ratio trenches, porous structures or on powders may be required. The PE-ALD process of VN, developed during this research, might thus be investigated for such kind of applications.

References

[1] J. Dumortier, *Groei en karakterisatie van gedoteerde vanadium dioxide lagen voor de nano-elektronica*, Master's thesis, Ghent University, (2012).

[2] Y. Muraoka and Z. Hiroi, *Appl. Phys. Lett.* **80**(4), 583 (2002).

[3] H. Kim, N. Charipar, M. Osofsky, S. B. Qadri, and A. Piqu, *Appl. Phys. Lett.* **104**(8), 081913 (2014).

[4] K. Martens, N. Aetukuri, J. Jeong, M. G. Samant, and S. S. P. Parkin, *Appl. Phys. Lett.* **104**(8), 081918 (2014).

[5] J. W. Tashman, J. H. Lee, H. Paik, J. A. Moyer, R. Misra, J. A. Mundy, T. Spila, T. A. Merz, J. Schubert, D. A. Muller, and et al., *Appl. Phys. Lett.* **104**(6), 063104 (2014).

[6] M. B. Takeyama, M. Sato, H. Sudoh, H. Machida, S. Ito, E. Aoyagi, and A. Noya, *Jpn. J. Appl. Phys.* **50**(5), 05EA06 (2011).

List of abbreviations

acac	Acetyl Acetonate
AFM	Atomic Force Microscopy
ALD	Atomic Layer Deposition
ALE	Atomic Layer Epitaxy
BEOL	Back End Of Line
CAFM	Conductive Atomic Force Microscopy
CVD	Chemical Vapor Deposition
DC	Direct Current
DFT	Density Functional Theory
DRAM	Dynamic Random Access Memory
EDX	Energy-Dispersive X-ray Spectroscopy
EELS	Electron Energy Loss Spectroscopy
FET	Field-Effect Transistor
HAXPES	Hard X-ray Photoelectron Spectroscopy
HIPIMS	High-Power Impulse Magnetron Sputtering
HV	High Vacuum
HRS	High-Resistive State
ILD	Interlevel Dielectric
ITRS	International Technology Roadmap for Semiconductors
LRS	Low-Resistive State
MBE	Molecular Beam Epitaxy
MIT	Metal-Insulator Transition
ML	Molecular Layering
MPU	Microprocessor Unit
MOS	Metal-Oxide-Semiconductor
MOSFET	Metal-Oxide-Semiconductor Field-Effect Transistor
PID	Proportional Integral Derivative
PLD	Pulsed Laser Deposition
PVD	Physical Vapor Deposition
RBS	Rutherford Backscattering Spectrometry
sccm	Standard cubic centimeter per minute
SDDP	Spacer-Defined Double Patterning
SE	Spectroscopic Ellipsometry
SEM	Scanning Electron Microscopy
SMT	Semiconductor-Metal Transition

slm	Standard liter per minute
TDEAV	Tetrakis(DiEthylAmino)Vanadium
TDMAV	Tetrakis(DiMethylAmino)Vanadium
TEMAV	Tetrakis(EthylMethylAmino)Vanadium
TMA	TriMethylAluminum
UHV	Ultra-High Vacuum
VTIP	Vanadyl Tri-Isopropoxide
XPS	X-Ray Photoelectron Spectroscopy
XRD	X-Ray Diffraction
XRF	X-Ray Fluorescence
XRR	X-Ray Reflectivity

List of Figures

1.1 The vanadium-oxygen phase diagram. 2
1.2 Electrical transition in single crystal VO_2. 3
1.3 Optical transition in a VO_2 thin film. 4
1.4 The VO_2(M1) and VO_2(R) crystal structures. 5
1.5 The band structure of the semiconducting and metallic VO_2 phases. 6
1.6 Effect of W-doping on the transition temperature of VO_2. 8
1.7 Effect of stress on the SMT in VO_2 thin films. 9
1.8 Increased hysteresis width in isolated VO_2 nanoparticles. 10
1.9 Hysteresis loops for VO_2 thin films with complex particle size distribution or nonuniform oxygen nonstoichiometries. 11
1.10 Operation principle of thermochromic windows. 12
1.11 Two-terminal device based on the SMT in VO_2. 13
1.12 Non-volatile memory based on NiO memory cells combined with VO_2 switches. 15
1.13 Mott-FET, example 1. 16
1.14 Mott-FET, example 2. 16
1.15 Comparison of a conventional MOSFET with a novel VO_2 based hyper-FET. 17
1.16 Electrical resistivity across the SMT in the vanadium oxide Magnéli phases. 19
1.17 Overview of SMT materials and their transition temperatures. . . . 20
1.18 The vanadium-nitrogen phase diagram. 21
1.19 Cross-section of a MPU. 22

2.1 Schematic presentation of the operation principle of magnetron sputtering. 32
2.2 Principle of ALD explained for the first cycle of Al_2O_3 growth from TMA and H_2O. 33
2.3 Schematic drawing of the ALD reactor used during this research. . 36
2.4 Examples of XRR spectra. 37
2.5 Description of XRF. 38
2.6 Ellingham diagram of the principle vanadium oxide phases. 42
2.7 Calculated phase diagram of the V-O system. 43
2.8 Schematic illustration of the Deal-Grove model. 45
2.9 Dewpoint line of water as a function of temperature. 49

2.10 Picture and drawing of a variable leak valve. 51
2.11 Variation of the oxygen partial pressure as a function of the variable leak valve position. 52
2.12 Picture and illustration of the solid electrolyte oxygen sensor. . . . 52
2.13 Drawing of the first gas panel configuration of the in-situ XRD system. 53
2.14 Calibration measurement of the oxygen pump. 54
2.15 Configuration of the mass flow controllers of the second gas mixing panel at the in-situ XRD system. 55
2.16 Principle of stepwise in-situ XRD. 57
2.17 Principle of continuous in-situ XRD. 58
2.18 Schematic illustration of the in-situ XRD annealing chamber. . . . 60
2.19 Example of in-situ XRD during oxidation of a vanadium film. . . 61
2.20 Temperature-dependent XRD measurement during the SMT in a VO_2 thin film. 62
2.21 Temperature-dependent sheet resistance measurement during the SMT in a VO_2 thin film. 63
2.22 Schematic setup of an ellipsometry measurement. 64
2.23 Temperature-dependent ellipsometry measurement during the SMT in a VO_2 thin film. 64

3.1 Growth rate of vanadium oxide grown by ALD from VTIP precursor. 73
3.2 Crystallization behavior of vanadium oxide films deposited from VTIP precursor. 74
3.3 In-situ XRD measurements during thermal oxidation of V thin films: ramp anneals. 77
3.4 In-situ XRD measurements during thermal oxidation of V thin films: isothermal anneals. 78
3.5 Schematic representation of the oxidation of a V thin film. 79
3.6 Oxidation time for VO_2 phase formation. 79
3.7 Reduction of V_2O_5 films in hydrogen. 81
3.8 VO_2 phase formation upon controlled reduction of V_2O_5 and oxidation of V in a H_2-O_2 gas mixture. 82
3.9 Temperature-dependent resistivity measurements on VO_2 films. . . 83
3.10 Sheet resistance switching ratio as a function of VO_2 film thickness. 84
3.11 Sheet resistance switching of a V_2O_3 film. 85
3.12 Overview of the oxidation and reduction processes. 86
3.13 ALD growth rate as a function of deposition temperature for different reactants. 87
3.14 V molar density of the as grown ALD films. 88
3.15 XPS measurements on the ALD vanadium oxide films. 89
3.16 Thickness increase upon air exposure for VO_2 films grown by H_2O and O_3 based ALD. 90
3.17 XRD measurements on the as deposited ALD films. 91
3.18 Model for nucleation and crystal growth during ALD. 92

3.19 Macroscopic test structure for conformality tests of the ALD process. 93
3.20 Conformality measurements of the ALD process in macroscopic test structures. 93
3.21 Conformality tests of the ALD process on micropillars. 94
3.22 In-situ XRD measurements during ramp annealing of ALD vanadium oxide films. 96
3.23 Phase formation diagrams of vanadium oxide films grown by ALD during post-deposition annealing. 98
3.24 Full scan XRD measurements of the crystalline vanadium oxide phases prepared by ALD and post-deposition annealing. 99
3.25 Indicative process window for obtaining continuous VO_2 films. . . 101
3.26 AFM measurements on VO_2 thin film and nanoparticles. 101
3.27 SMT in VO_2 ALD thin films: temperature-dependent sheet resistance measurements. 102
3.28 SMT in VO_2 ALD thin films and nanoparticles: temperature-dependent ellipsometry measurements. 102
3.29 Overview of the sheet resistance ratio $R_{s,30}/R_{s,100}$ of VO_2 thin films prepared by ALD, followed by annealing, and PVD, followed by controlled oxidation. 105

4.1 Thermal nitridation of 80 nm vanadium layers: in-situ XRD during ramp anneal and full scan XRD after anneal. 117
4.2 Thermal nitridation of 80 nm vanadium layers: in-situ XRD during isothermal anneal and full scan XRD after anneal. 118
4.3 Resistivity of the VN thin films prepared by nitridation of V. . . . 119
4.4 Film thickness as a function of the number of ALD cycles from TEMAV and NH_3 plasma and deposition temperature. 120
4.5 XPS measurements of films deposited by thermal and plasma-enhanced ALD from TEMAV and NH_3. 121
4.6 Vanadium molar density for plasma-enhanced and thermally grown ALD films. 122
4.7 XRD measurements of films grown by PE-ALD from TEMAV and NH_3. 123
4.8 Room temperature resistivity as a function of VN thickness and deposition temperature. 123
4.9 Picture of Mylar foil, coated with ALD VN. 124
4.10 Illustration of copper silicide formation during thermal annealing. 125
4.11 In-situ XRD measurements for testing the copper barrier performance of a thin VN layer. 125
4.12 In-situ XRD measurements during thermal oxidation of a VN ALD film. 126
4.13 In-situ XRD measurements during thermal annealing of a VN-VO_2 stack. 127

List of Tables

2.1 Properties of some crystalline vanadium and vanadium oxide phases. 39

3.1 Literature overview of CVD processes for vanadium oxides. . . . 72
3.2 Literature overview of ALD processes for vanadium oxides. . . . 75
3.3 Overview of synthesis parameters for vanadium oxide phases prepared by ALD and post-ALD annealing. 99

4.1 Literature overview of CVD processes for vanadium nitride. . . . 114
4.2 Literature overview of some metal nitride ALD processes. 115

List of publications and conference contributions

Publications related to this work

- ***In-situ* X-ray diffraction study of the controlled oxidation and reduction in the V-O system for the synthesis of VO_2 and V_2O_3 thin films**
  G. Rampelberg, B. De Schutter, W. Devulder, K. Martens, I. Radu and C. Detavernier
  J. Mater. Chem. C **3**, 11357 (2015)
- **Semiconductor-metal transition in thin VO_2 films grown by ozone based atomic layer deposition**
  G. Rampelberg, M. Schaekers, K. Martens, Q. Xie, D. Deduytsche, B. De Schutter, N. Blasco, J. Kittl, and C. Detavernier
  Appl. Phys. Lett. **98**, 162902 (2011)
- **Crystallization and semiconductor-metal switching behavior of thin VO_2 layers grown by atomic layer deposition**
  G. Rampelberg, D. Deduytsche, B. De Schutter, P. A. Premkumar, M. Toeller, M. Schaekers, K. Martens, I. Radu, and C. Detavernier
  Thin Solid Films **550**, 59-64 (2014)
- **Vanadium oxide thin films and nanoparticles prepared by atomic layer deposition and controlled post-deposition annealing**
  G. Rampelberg, B. De Schutter, W. Devulder, M. Schaekers, K. Martens, C. Dussarrat, and C. Detavernier
  To be published
- **VO_2, a metal-insulator transition material for nanoelectronic applications**
  K. M. Martens, I. P. Radu, G. Rampelberg, J. Verbruggen, S. Cosemans, S. Mertens, X. Shi, M. Schaekers, C. Huyghebaert, S. De Gendt, C. Detavernier, M. Heyns, and J. A. Kittl
  ECS Trans. **45**, 151-158 (2012)

- **Metal-insulator transition in ALD VO_2 ultrathin films and nanoparticles: morphological control**
  P. A. Premkumar, K. Martens, G. Rampelberg, M. Toeller, J. M. Ablett, J. Meersschaut, D. Cuypers, A. Franquet, C. Detavernier, J.-P. Rueff, M. Schaekers, S. Van Elshocht, M. Jurczak, C. Adelmann, and I. P. Radu
  Adv. Func. Mater. **25**, 679-686 (2015)

- **Low temperature plasma-enhanced atomic layer deposition of thin vanadium nitride layers for copper diffusion barriers**
  G. Rampelberg, K. Devloo-Casier, D. Deduytsche, M. Schaekers, N. Blasco, and C. Detavernier
  Appl. Phys. Lett. **102**, 111910 (2013)

Other publications

- **Low-Temperature atomic layer deposition of platinum using (methylcyclopentadienyl)trimethylplatinum and ozone**
  J. Dendooven, R. K. Ramanchandran, K. Devloo-Casier, G. Rampelberg, M. Filez, H. Poelman, G. B. Marin, E. Fonda, and C. Detavernier
  J. Phys. Chem. C **117**, 20557-20561 (2013)

- **Plasma enhanced atomic layer deposition on powders**
  G. Rampelberg, D. Longrie, D. Deduytsche, and C. Detavernier
  ECS Trans. **64**, 51-62 (2014)

- **Composition influence on the physical and electrical properties of $Sr_xTi_{1-x}O_y$-based metal-insulator-metal capacitors prepared by atomic layer deposition using TiN bottom electrodes**
  N. Menou, M. Popovici, S. Clima, K. Opsomer, W. Polspoel, B. Kaczer, G. Rampelberg , M. A. Pawlak, C. Detavernier, D. Pierreux, J. Swerts, J. W. Maes, D. Manger, M. Badylevich, V. V. Afanas'ev, T. Conard, P. Favia, H. Bender, B. Brijs, W. Vandervorst, S. Van Elshocht, G. Pourtois, D. J. Wouters, S. Biesemans, and J. A. Kittl
  J. Appl. Phys. **106**, 094101 (2009)

- **Structural and kinetic study of the reduction of $CuOCeO_2/Al_2O_3$ by time-resolved X-ray diffraction**
  V. Galvita, H. Poelman, G. Rampelberg, B. De Schutter, C. Detavernier, and G. B. Marin
  Catal. Lett. **142**, 959968 (2012)

- **Partially fluorinated MIL-47 and Al-MIL-53 frameworks: influence of functionalization on sorption and breathing properties**
  S. Biswas, T. Rémy, S. Couck, D. Denysenko, G. Rampelberg, J. F. M. Denayer, D. Volkmer, C. Detavernier, and P. Van Der Voort
  Phys. Chem. Chem. Phys. **15**, 3552 (2013)

- **Interfacial reactions of Gd- and Nb-oxide based high-k layers deposited by aqueous chemical solution deposition**
  D. Dewulf, N. Peys, S. Van Elshocht, G. Rampelberg, C. Detavernier, S. De Gendt, A. Hardy, and M. K. Van Bael
  Microelectronic Eng. **88**, 1338-1341 (2011)

- **Optimization of electrodeposited p-doped Sb_2Te_3 thermoelectric films by millisecond potentiostatic pulses**
  C. Schumacher, K. G. Reinsberg, L. Akinsinde, S. Zastrow, S. Heiderich, W. Toellner, G. Rampelberg, C. Detavernier, J. A. C. Broekaert, and K. Nielsch
  Adv. Energy Mater. **2**, 345-352 (2012)

- **Optimizations of pulsed plated p and n-type Bi_2Te_3-based ternary compounds by annealing in different ambient atmospheres**
  C. Schumacher, K. G. Reinsberg, R. Rostek, L. Akinsinde, S. Baessler, S. Zastrow, G. Rampelberg, P. Woias, C. Detavernier, J. A. C. Broekaert, J. Bachmann, and K. Nielsch
  Adv. Energy Mater. **3**, 95-104 (2013)

- **Improved thermal stability and retention properties of Cu-Te based CBRAM by Ge alloying**
  W. Devulder, K. Opsomer, G. Rampelberg, B. De Schutter, Bob K. Devloo-Casier, M. Jurczak, L. Goux, and C. Detavernier
  J. Mater. Chem. C **3**, 12469-12476 (2015)

Conference contributions

- **Semiconductor-metal transition in thin VO_2 films grown by ozone based atomic layer deposition**
  G. Rampelberg, M. Schaekers, K. Martens, Q. Xie, D. Deduytsche, B. De Schutter, N. Blasco, J. A. Kittl, and C. Detavernier
  AVS-ALD 2011, Cambridge, Massachusetts, USA, June 26-29, 2011 (oral presentation)

- **Semiconductor-metal transition in thin VO_2 films grown by ozone based atomic layer deposition**
  G. Rampelberg, M. Schaekers, K. Martens, Q. Xie, D. Deduytsche, B. De Schutter, N. Blasco, J. A. Kittl, and C. Detavernier
  RRAM Workshop, Leuven, Belgium, October 20-21, 2011 (poster)

- **Semiconductor-metal transition in thin VO_2 films grown by ozone based atomic layer deposition**
  G. Rampelberg, M. Schaekers, K. Martens, Q. Xie, D. Deduytsche, B. De Schutter, N. Blasco, J. A. Kittl, and C. Detavernier
  MAM 2012, Grenoble, France, March 11-12, 2012 (oral presentation)

- **Optimization of the annealing conditions for thin VO_2 ALD films**
  G. Rampelberg, M. Schaekers, K. Martens, D. Deduytsche, B. De Schutter, J. A. Kittl, and C. Detavernier
  AVS-ALD 2012, Dresden, Germany, June 17-20, 2012 (oral presentation)

- **Atomic layer deposition of VO_2 thin films: growth, crystallization and semiconductor-metal transition**
  G. Rampelberg, M. Schaekers, K. Martens, D. Deduytsche, B. De Schutter, N. Blasco, and C. Detavernier
  Enhance Winter School 2013, Eindhoven, The Netherlands, January 14-17, 2013 (poster)

- **Plasma-enhanced atomic layer deposition of thin vanadium nitride layers as a copper diffusion barrier**
  G. Rampelberg, K. Devloo-Casier, D. Deduytsche, M. Schaekers, N. Blasco, and C. Detavernier
  MAM 2013, Leuven, Belgium, March 10-13, 2013 (oral presentation)

- **Plasma-enhanced atomic layer deposition of thin vanadium nitride layers as a copper diffusion barrier**
  G. Rampelberg, K. Devloo-Casier, D. Deduytsche, M. Schaekers, N. Blasco, and C. Detavernier
  AVS-ALD 2013, San Diego, California, USA, July 28-31, 2013 (oral presentation)

- **Atomic layer deposition: a 3D surface engineering technique for nanomaterials**
  G. Rampelberg, J. Dendooven, D. Deduytsche, and C. Detavernier
  ICACC 2014, Daytona Beach, Florida, USA, January 26-31, 2014 (invited talk)

- **Conformal nanocoatings for surface engineering of particles by thermal and plasma-enhanced atomic layer deposition using a rotary reactor**
  G. Rampelberg, D. Longrie, D. Deduytsche, J. Haemers, K. Driesen, and C. Detavernier
  ICACC 2014, Daytona Beach, Florida, USA, January 26-31, 2014 (poster)

- **Plasma enhanced atomic layer deposition on powders**
  G. Rampelberg, and C. Detavernier
  ECS 2014, Cancun, Mexico, October 5-9, 2014 (invited talk)

- **Thermal and plasma enhanced atomic layer deposition on powders**
  G. Rampelberg, D. Longrie, D. Deduytsche, and C. Detavernier
  Workshop - ALD for Batteries, Ghent, Belgium, September 15-16, 2015 (oral presentation)

Appendix: Papers I-V

Paper I
In-situ X-ray diffraction study of the controlled oxidation and reduction in the V-O system for the synthesis of VO_2 and V_2O_3 thin films *

Abstract

VO_2 and V_2O_3 thin films have been prepared by controlled oxidation and reduction reactions in the vanadium-oxygen system. During these reactions, crystalline phase formation and stability were characterized by means of *in-situ* X-ray diffraction. Oxidation of vanadium thin films was carried out over a wide range of oxygen partial pressures between 20 and 20000 Pa and temperatures between 430 °C and 615 °C. Depending on the oxygen partial pressures and temperatures, VO_2, V_6O_{13} and V_2O_5 could be obtained as pure or mixed phases. Reduction of V_2O_5 in 5000 Pa H_2 resulted in a continuous reduction towards V_2O_3. Stabilization of the VO_2 phase was obtained by adding low O_2 concentrations in the range from 20 to 200 Pa to the H_2 gas, a method which proved to be successful as well for the controlled oxidation of vanadium towards VO_2. The semiconductor-metal transition was observed by means of temperature dependent sheet resistance measurements. VO_2 films prepared by oxidation of vanadium in low oxygen partial pressures were characterized by a 3 order of magnitude decrease in resistance during transition. Annealing in air only yielded comparable switching ratios when the annealing time was carefully optimized. Both the VO_2 films prepared by oxidation of vanadium or reduction of V_2O_5 in the mixture of H_2 and O_2 showed 4 to 5 orders of magnitude switching, which is close to the best reported values for bulk, single-crystal VO_2. This excellent switching performance is believed to originate from a decreased level of defects at grain boundaries and in the bulk. In addition, the V_2O_3 films prepared by reduction of V_2O_5 showed 3 orders of magnitude increase in resistance near -100 °C. Our results provide methods for transforming vanadium oxide phases into VO_2 and V_2O_3 with high resistance switching ratios.

*Published as: G. Rampelberg, B. De Schutter, W. Devulder, K. Martens, I. Radu, and C. Detavernier, *J. Mater. Chem. C*, 3, 11357 (2015).

Introduction

Vanadium dioxide (VO_2) is well-known for its semiconductor-metal transition near 67 °C.[1] This reversible transition is characterized by a change in crystal structure from a low temperature monoclinic phase (M1) to a high temperature tetragonal phase (R) while being accompanied with an electronic transition, altering the optical properties and resistivity up to five orders of magnitude.[2] Applications are found in e.g. optical shutters and thermochromic windows and recently VO_2 attracted interest for optoelectronic and microelectronic applications, including switching devices and memories.[3–10] Vanadium sesquioxide (V_2O_3) shows a similar transition at a temperature near -110 °C, with an even higher change in resistivity up to seven orders of magnitude, although this high switching ratio is difficult to achieve in thin films.[1;11;12]

The vanadium-oxygen system is known to exhibit a broad range of compositions, in which subtle variations of the oxygen content lead to drastic changes in crystal structure and electronic properties. Apart from the pure vanadium valences of 0, +2, +3, +4 and +5, related to the phases V, VO, V_2O_3, VO_2 and V_2O_5 respectively, two series of mixed valences are known as stable phases. These are the series V_nO_{2n-1} and V_nO_{2n+1}, known as the Magnéli and Wadsley phases respectively, and they connect the three most common phases, being V_2O_3, VO_2 and V_2O_5.[13–16]

Synthesis of the several phases in their pure stoichiometric form is a challenging task for material scientists. In thin film research many techniques are being used for this purpose, including sol-gel,[17;18] reactive sputtering,[19–22] molecular beam epitaxy (MBE),[23] pulsed laser deposition (PLD),[24;25] chemical vapor deposition (CVD)[26–29] and atomic layer deposition (ALD).[30–36] An alternative approach is thermal oxidation or reduction in the vanadium-oxygen system to transform one phase into another.[9;37–39] In this way, phases which are easily synthesized such as V and V_2O_5, can be transformed to VO_2 or V_2O_3. During these thermal oxidation and reduction reactions, thermodynamics determine the favorable phases under certain conditions of temperature and oxygen partial pressure.[15] On the other hand, the rate at which oxidation and reduction occur is determined by kinetics and quite often this is observed as the limiting step. Early studies on kinetics of the thermal oxidation of vanadium were often performed by means of vacuum microbalances, indicating the mass gain of a vanadium foil due to oxygen uptake.[40–45] It was observed that the linear-parabolic rate law dominates the oxidation of vanadium, meaning that the oxidation rate is limited by diffusion. Kirkendall marker experiments furthermore showed that the diffusing atom during vanadium oxidation is oxygen.[46]

In this work we take advantage of *in-situ* X-ray diffraction (XRD), a technique enabling the characterization of crystalline phases during thermal annealing, to study thermal oxidation and reduction in the vanadium-oxygen system.

Experimental details

To study the oxidation of vanadium, layers of 20, 40 and 80 nm vanadium were deposited on silicon (100) wafers by DC magnetron sputtering. In order to prevent reaction between vanadium and the silicon substrate prior to oxidation, which could lead to vanadium silicide formation, the silicon wafers were first thermally oxidized with a resulting SiO_2 thickness of 100 nm, or covered with a 20 nm Al_2O_3 layer grown by atomic layer deposition using trimethylaluminum (TMA) and water at 300 °C and annealed in nitrogen for 1 minute at 1000 °C. Both SiO_2 and Al_2O_3 cannot be reduced by vanadium, since these oxides are thermodynamically more stable compared to all vanadium oxides. Thus, oxidation of vanadium will only occur due to gas-solid reactions. By subsequent annealing of these vanadium layers in air for 30 minutes at 480 °C, V_2O_5 thin films were obtained, which were used for the reduction studies.

Oxidation and reduction studies were carried out by means of *in-situ* X-ray diffraction (XRD). The system consisted of a commercial Bruker D8 Discover XRD system with an integrated experimental annealing chamber. The XRD system was equipped with a copper X-ray source ($\lambda = 0.154$ nm) and a linear X-ray detector. By making use of a linear detector, source and detector could be kept at fixed positions, while collecting snapshots of the diffracted X-rays every few seconds in a 2θ window of approximately 17 °. This configuration can be used very efficient for polycrystalline materials or powder samples.[47;48] The annealing chamber can operate at both inert, reducing and oxidizing ambient at a total absolute pressure slightly above atmospheric pressure. The system was first pumped down to a pressure below 5 Pa, was then filled with the desired gas after which the flow of gas was set to a constant value around 1 standard liter per minute. In order to achieve a reliable control of the oxidation process of metallic vanadium, oxygen partial pressures in the range between 20 and 20000 Pa were used, by mixing helium and oxygen with mass flow controllers. In addition, anneals in air were carried out with an open chamber. For the reduction of V_2O_5 a mixture of 5% hydrogen in helium was used. Low concentrations of oxygen were added to this mixture to stabilize the VO_2 phase. The temperature of the sample can be varied between room temperature and 1000 °C, and was measured using a K-type thermocouple and calibrated using Au-Si, Al-Si and Ag-Si eutectic systems. Ramp anneals were carried out from room temperature up to 615 °C at heating rates of 0.25 °C/s, while isothermal anneals were carried out in the range from 430 °C up to 615 °C with a fixed heating rate of 5 °C/s from room temperature up to the desired setpoint temperature.

After annealing the samples were characterized by XRD measurements at room temperature in the same system, but operated in $\theta - \theta$ scan mode, covering a 2θ range from 12 ° to 60 °. This enabled the detection of additional diffraction peaks in order to get a more thorough identification of the crystalline phases.

The semiconductor-metal transition was characterized by means of temperature dependent sheet resistance measurements using a Keithley 2601A source measure unit in combination with 4 probes in a square configuration. Thermal

cycling experiments were performed between room temperature and 110 °C for VO_2 and between room temperature and -150 °C for V_2O_3. In addition, scanning electron microscopy (SEM) was carried out on the oxidized and reduced films for characterization of the morphology.

Results and discussion

Oxidation of vanadium thin films

Fast survey of the P_{O_2}-T parameter space

Temperature ramp profiles were carried out in various oxygen partial pressures on the sputtered V layers of 80 nm on Al_2O_3, while performing *in-situ* XRD. The most prominent diffraction peaks of the vanadium oxides observed during this work are found in the 2θ range between 15 ° and 45 °. To cover this 30 ° range, identical anneals were performed on two identical samples at complementary 2θ windows of [15-32] ° and [30-47] °. Figure 1 shows the combined *in-situ* XRD results for ramp anneals carried out in 20000, 2000, 200 and 20 Pa of oxygen at a heating rate of 0.25 °C/s.

In all cases the vanadium diffraction peak at 42 °, corresponding to the (110) plane of the body-centered cubic (bcc) structure (JCPDS 22-1058), does not change in position nor intensity below 300 °C. Between 300 °C and 400 °C a shift is observed, related to oxygen dissolution in the vanadium layer. Uptake of oxygen results in an expansion of the lattice, and consequently in a decrease of the diffraction angle. The peak broadens and finally disappears, indicating that sufficient oxygen is incorporated to destroy the lattice. At higher temperatures, oxidation to several crystalline vanadium oxide phases occurs, with a clear difference between the anneals at 20000 and 2000 Pa and those at 2 and 20 Pa of oxygen.

At the high oxygen partial pressures, two minor signals related to tetragonal VO_2(R) are visible near 37 ° and 40 °, related to the (011) and (020) planes respectively (JCPDS 44-0253). These only occur for a short period, starting around a temperature of 475 °C. When temperature is further increased to approximately 500 °C, various peaks suddenly show up, explained by the nucleation of a mixture containing V_2O_5, V_6O_{13} and V_3O_7. The peaks near 20 °, 40 ° and 41 ° are assigned to the (001), (311) and (002) planes of orthorhombic V_2O_5 (JCPDS 41-1426), the peaks at 18 °, 26.5 ° and 45 ° to the (002), (003) and (005) planes of base-centered monoclinic V_6O_{13} (JCPDS 27-1318), while the peak at 25 ° corresponds to the (101) plane of body-centered V_3O_7 (JCPDS 71-1591). At 20000 Pa O_2 the film fully oxidizes towards V_2O_5, while at 2000 Pa O_2 the lower oxide phase V_6O_{13} gains importance upon increase of the temperature towards 550 °C and higher. This can be explained by thermodynamical reasons, i.e. the lower oxide phase being more stable at increased temperatures and decreased oxygen partial pressures.

The situation at 200 and 20 Pa O_2 is very different. Above 500 °C oxidation towards single phase VO_2 occurs with a strong (020) texturing, which maintains

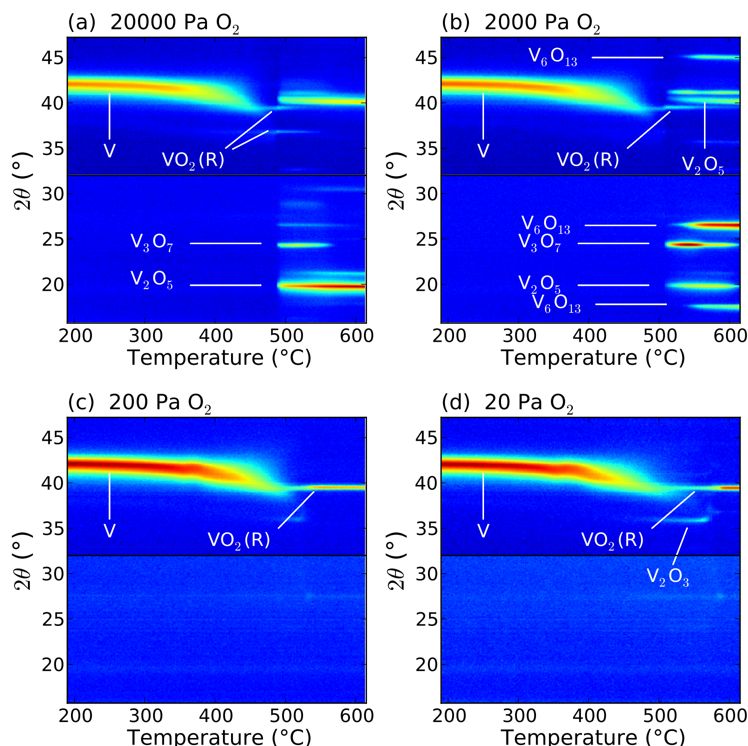

Figure 1. *Combined in-situ XRD measurements during thermal oxidation of 80 nm vanadium layers on the Al_2O_3 template in various oxygen partial pressures: (a) 20000 Pa, (b) 2000 Pa, (c) 200 Pa and (d) 20 Pa O_2. The temperature was increased at a fixed rate of 0.25 °C/s.*

its stability upon further increase of the temperature. During the oxidation at the lowest oxygen partial pressure, a faint indication of V_2O_3 is present as intermediate phase. The observed peak at 36 ° between 500 and 550 °C corresponds to the (110) plane of rhombohedral V_2O_3 (JCPDS 34-0187).

From this limited set of experiments it is clear that to obtain VO_2 by means of oxidation temperatures around 500 °C are sufficient, while the oxygen partial pressure is preferably limited to values in the range between 200 and 20 Pa. In the next section, isothermal annealing experiments are discussed, which allow for obtaining more detailed insight on the formation and stability of the several vanadium oxide phases, while in addition the influence on film thickness and template will be highlighted.

Isothermal oxidation of vanadium

Although ramp annealing delivers fast insight of the oxidation process, it is not the preferred way of forming VO_2 for practical applications. These usually involve isothermal oxidation. Moreover, during ramp annealing the heating rate greatly affects the temperature of phase formations, while certain phases might even be overlooked. Figure 2 shows how the oxygen partial pressure affects the oxidation process of 80 nm V during isothermal annealing at 480 °C. *In-situ* XRD measurements were performed for one hour in air and mixtures of He with 2000, 200 and 20 Pa of O_2, followed by full XRD scans.

In all cases VO_2 is formed, but it is only at the lowest oxygen partial pressures obtained as a stable vanadium oxide phase. At 20 Pa it is stable, while at 200 Pa a small fraction of V_2O_5 is observed after one hour of annealing. In contrast, in air and at 2000 Pa O_2, the formation of VO_2 is followed quickly by a further oxidation towards V_2O_5. Similar experiments were carried out to study the phase formation over a wide temperature range from 430 °C to 615 °C. From the full XRD scans acquired after one hour of annealing, the fractions of crystalline VO_2, V_6O_{13} and V_2O_5 were estimated, and summarized in figure 3. Only at 20 Pa O_2, VO_2 is stabilized in a large temperature range from 480 °C to 570 °C. On the other hand, V_2O_5 is easy to stabilize in air starting from 480 °C, while the Wadsley phase V_6O_{13} can be formed at relatively high purity at 200 Pa O_2 and a temperature of 615 °C. These findings are in strong contrast with the V-O phase diagram, from which it is expected to obtain only V_2O_5 in this range of temperatures and oxygen partial pressures.[15] Due to the relatively low temperatures used in our experiments, kinetics can however act as strong limiting factor for the oxidation reactions towards the thermodynamically favored phases.

An interesting observation is the fact that the V diffraction peak has almost disappeared completely prior to the temperature setpoint was reached. This means a simple assumption of VO_2 growing on top of a metallic V layer does not hold. Instead, a vanadium oxide phase with a lower oxygen concentration forms very fast, without a strongly defined crystalline structure. Due to the lack of crystal structure, it is unclear from XRD measurements which composition should be assigned to this vanadium oxide. It is even not unlikely that a vanadium oxide layer exists with a graded oxygen concentration. However, in case of the lowest oxygen partial pressure, the small diffraction signal near 36 ° suggests V_2O_3 has at least a small contribution in the initial stages of oxidation. The fast oxidation of the complete V layer could have a drawback for the potential purpose of synthesizing a structure with VO_2 on top of V where VO_2 acts as the SMT material and V would be used as bottom electrode. The low resistivity of the V metal layer may be deteriorated due to the incorporation of oxygen. However, from the sheet resistance measurements in the following paragraphs it will get clear that the increase of resistivity is limited to less than one order of magnitude.

The results discussed so far relate to oxidation of V layers on the crystalline Al_2O_3 template which was deposited on the Si wafer. Another template involved in this oxidation study was a thermally oxidized Si wafer with a SiO_2 layer thickness

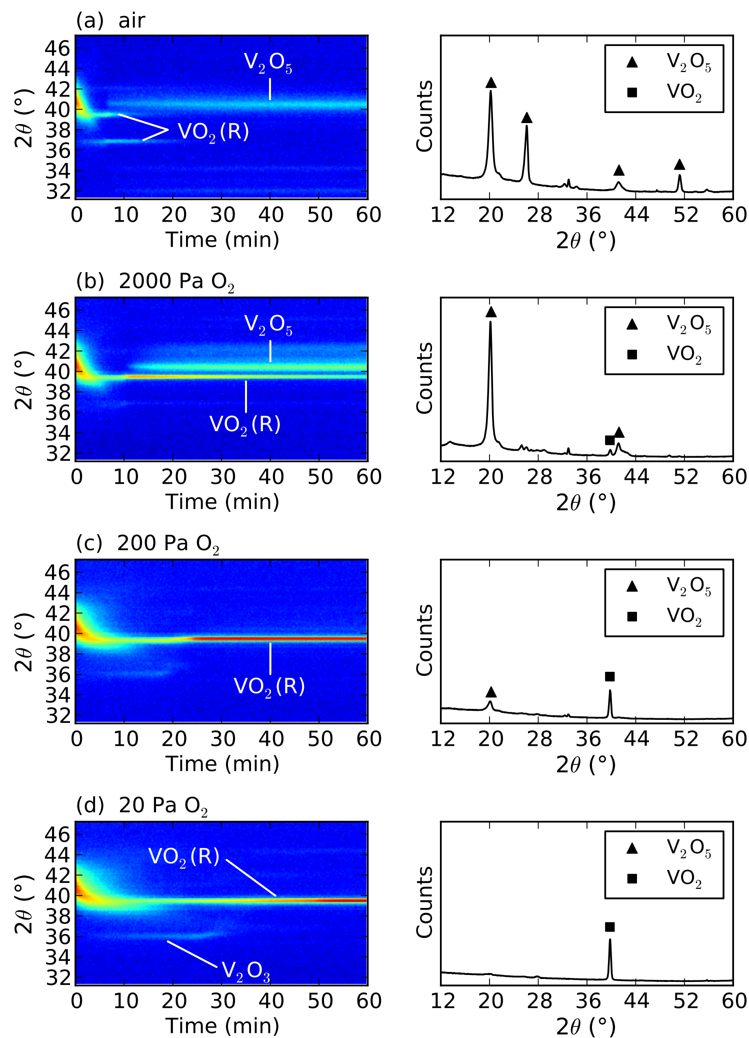

Figure 2. *Left: in-situ XRD measurements during isothermal oxidation at 480 °C of 80 nm vanadium layers on the Al_2O_3 template in various oxygen partial pressures: (a) air, (b) 2000 Pa, (c) 200 Pa and (d) 20 Pa O_2. Right: the corresponding full XRD scans measured after 1 hour of annealing.*

of 100 nm. For the same optimized conditions for VO_2 phase stabilization on the Al_2O_3 template, i.e. 1 hour of annealing at 480 °C in an oxygen partial pressure of 20 Pa, VO_2 is as well observed as the only vanadium oxide phase (supplementary information).

As for the 80 nm V layers, oxidation experiments have as well been performed

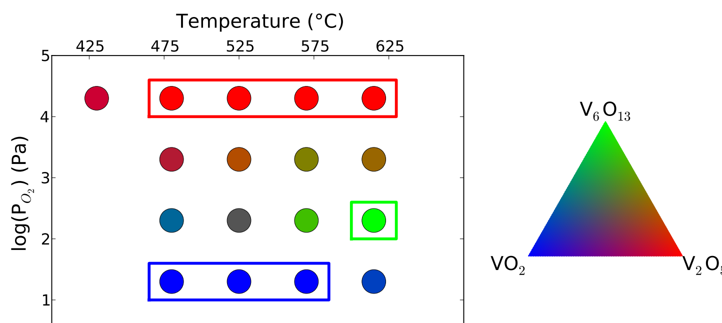

Figure 3. *Overview of the observed vanadium oxide phases after one hour of annealing as a function of temperature and oxygen partial pressure. As indicated in the colored triangle, blue, red and green correspond with VO_2, V_2O_5 and V_6O_{13} respectively. Intermediate colors are attributed to mixtures of these three phases.*

on thinner layers, i.e. 20 nm and 40 nm. The *in-situ* XRD measurements (supplementary information) showed that for all thicknesses VO_2 is formed on both the Al_2O_3 and SiO_2 templates when 20 Pa O_2 is used as oxygen partial pressure. The required oxidation time does not relate in a proportional way to the thickness: 200 s for 20 nm, 600 s for 40 nm and 3000 s for 80 nm starting thickness of vanadium. The oxidation thus seems not to behave linearly, and it may be supposed that for the thicker layers oxygen diffusion plays a critical role in limiting the oxidation rate, as explained by Deal and Grove for the thermal oxidation of Si.[49] This corresponds to the report of Mukherjee and Wach, who observed a linear-parabolic growth rate.[45]

Figures 4 (a) and (b) show some temperature dependent sheet resistance measurements carried out on the 80 nm V layers on the Al_2O_3 template oxidized at 480 °C in 20 Pa O_2 and at 430 °C in air respectively. For both cases, the sheet resistance of the as deposited vanadium is shown as a reference. For short oxidation times, e.g. 1200 s at 20 Pa O_2, an overall low-resistive film is observed with a small switching ratio. This can be explained by a partially oxidized vanadium film, with a low-resistive bottom layer and a VO_2 layer on top. The sheet resistance measurement should thus be treated as the measurement of two resistors in parallel: a sub-oxide with a low resistance and VO_2 with a temperature dependent resistance. The low resistance sub-oxide suppresses the observation of a high switching ratio in VO_2. After 2400 to 3600 s of oxidation the switching curve stabilizes, which is in accordance with the phase formation observed by *in-situ* XRD. Indeed, Figure 2(d) showed how the VO_2 peak settles to a maximum after approximately 50 minutes. Between 2 and 3 orders of magnitude change in resistance is obtained for these oxidation conditions.

In contrast, annealing in air at 430 °C does not show this stabilization of the sheet resistance and switching ratio. Around 30 minutes of annealing a 3 orders of magnitude switch is observed, but this switching ratio is not conserved upon

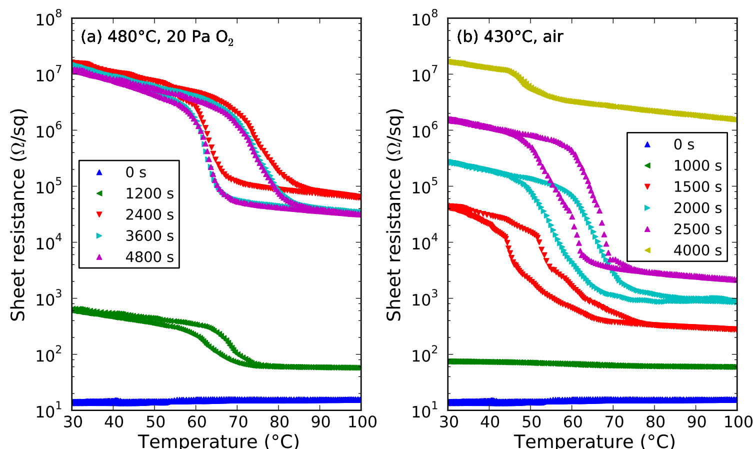

Figure 4. *Sheet resistance as a function of temperature for 80 nm V on Al_2O_3 oxidized for various annealing times: (a) at 480 °C in 20 Pa O_2, (b) at 430 °C in air.*

longer annealing. *In-situ* XRD confirmed that after 30 minutes of oxidation in air at 430 °C VO_2 reached a maximum fraction and V_2O_5 started to nucleate. Since V_2O_5 is a semiconducting material which does not show a semiconductor-metal transition, the high sheet resistance at both 30 °C and 100 °C after longer oxidation times is explained by full oxidation of the VO_2 layer towards V_2O_5.

It should be noted that although the term semiconductor-metal transition is used, the high temperature phase does not show a typical metallic behavior. Indeed, for metals it is expected that resistivity increases with temperature, whereas in our observations a negative temperature coefficient is present. This behavior is however most times observed in polycrystalline VO_2 thin films, and may be explained by grain boundary resistance.[9;50]

Figure 5 summarizes the sheet resistance ratio $R_{s,30}/R_{s,100}$, as a function of the oxidation time, where $R_{s,30}$ and $R_{s,100}$ are the sheet resistance at 30 °C and 100 °C respectively. Both the results for oxidation in air at 430 °C and under 20 Pa O_2 at 480 °C are shown, on both the Al_2O_3 and SiO_2 template. It is clear that oxidation at low oxygen partial pressures enables stable high switching ratios of approximately three orders of magnitude on both templates. More data is provided in the supplementary information, showing the temperature dependent sheet resistance measurements of thinner films as well. Oxidation in air however requires a precise control of the annealing time to obtain an optimum switching. It is furthermore obvious that changing parameters as vanadium film thickness and temperature will have a large impact on the optimum annealing time. In addition, a difference between the Al_2O_3 and SiO_2 templates is observed. Whereas on Al_2O_3 three orders of magnitude switching was achieved, on the SiO_2 template the maximum was only two orders of magnitude. It may thus be concluded that

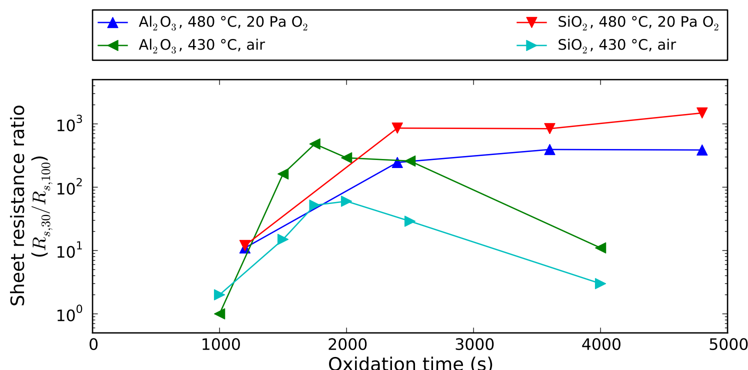

Figure 5. *Influence of the oxidation time on the sheet resistance ratio ($R_{s,30}/R_{s,100}$) for anneals carried out in air and 20 Pa O_2 on 80 nm vanadium. Both the Al_2O_3 and SiO_2 as templates are shown.*

low oxygen partial pressures are advantageous for reliable oxidation of vanadium towards VO_2.

Reduction of V_2O_5 thin films

As a counterpart of the oxidation of vanadium, the reduction of V_2O_5 has been studied as well. For this purpose, V_2O_5 thin films were prepared from sputtered V layers by oxidation in air, as discussed in the previous section. Anneals were carried out at 480 °C for 30 minutes.

Attempts to reduce V_2O_5 under inert gas did not lead to any significant reduction. After more than one hour of annealing at temperatures in the range from 480 °C to 525 °C, V_2O_5 was still the main phase detected with XRD, whereas only a minor fraction of V_6O_{13} appeared. A reducing gas is thus required. For this purpose gas bottle with a mixture of 5% H_2 in He was used with a purity level of 99.999%. From figure 6(a) it is clear that a fast continuous reduction process occurs. The diffraction peaks related to V_2O_5 at 20 ° and 26 ° dissappear in a first step in favor of V_6O_{13}, with peaks close to 18 °, 25.5 ° and 26.5 °. Second, a peak near 27.5 ° appears, which is believed to correspond to VO_2(R). Next, a peak at 29 ° shows up which is expected to be related to one of the many Magnéli phases. The exact identification is however not possible from this single peak. Finally, a peak at 24 ° is formed, showing the presence of V_2O_3. The full scan XRD confirms that the reduction of V_2O_5 proceeded towards single phase V_2O_3 (figure 6(b)).

As in the case of the oxidation of vanadium layers in air, the question rises if it is possible to maximize the VO_2 fraction by quenching the sample during the reduction process. In order to provide an answer, figure 6(c) shows the summed peak intensities related to V_2O_5, V_6O_{13}, VO_2, the unidentified phase (denoted as VO_x) and V_2O_3 as a function of the reducing time. The plot reveals that the

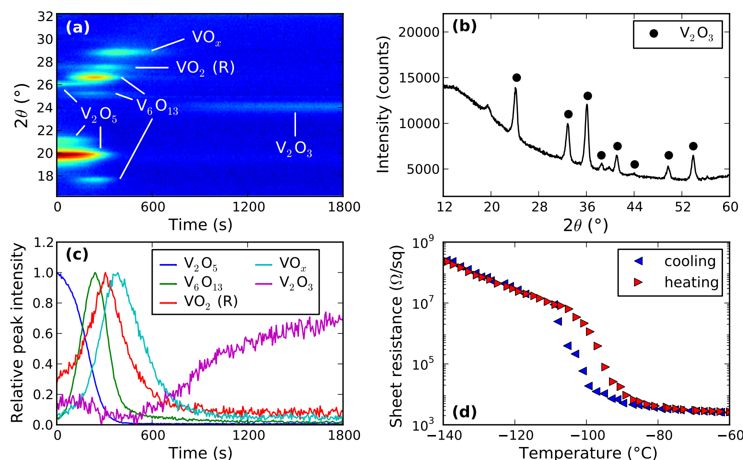

Figure 6. *(a) In-situ XRD during the reduction of V_2O_5 at 480 °C in 5000 Pa H_2. (b) The corresponding full XRD scan after one hour of annealing. (c) Evolution of the diffraction peak intensities corresponding to V_2O_5, V_6O_{13}, VO_2, VO_x and V_2O_3. (d) Temperature dependent sheet resistance measurement of the V_2O_3 thin film.*

reduction involves a path through a continuously evolving mixture of these phases. For instance after 300 s, except for V_2O_3, the four other phases coexist. The maximum VO_2 intensity does not at all correspond to pure VO_2.

The other alternative is decreasing the hydrogen partial pressure to fully stabilize the VO_2 phase, this method being the counterpart of the controlled oxidation of vanadium. This route is however not expected to lead to success since the vanadium oxide phase formation would probably depend on the oxygen impurity level in the annealing chamber. Instead, a controlled mixture of H_2 and O_2 was studied, with the aim of stabilizing the reduction once the VO_2 phase has been reached, as explained in the next section.

Similar as VO_2, V_2O_3 is characterized by a semiconductor-metal transition. The transition temperature is however much lower, near -110 °C. A liquid nitrogen cooled system allowed for temperature dependent sheet resistance measurement, as shown in figure 6(d). Around -100 °C the sheet resistance changes with approximately 3 orders of magnitude.

Balanced gas mixture for VO_2 phase stabilization

The fact that reduction of V_2O_5 in H_2 (5000 Pa) reduces towards V_2O_3 instead of the desired VO_2 phase is an indication that the oxygen partial pressure is too low, which seems reasonable since no oxygen was intentionally added into the gas flow. Adding O_2 to the diluted H_2 gas mixture would definitely increase this value. Reaction between both components would result in the formation of water,

as described by the reaction

$$2H_2 + O_2 \rightleftharpoons 2H_2O. \qquad (1)$$

By forming water, oxygen will be consumed, lowering the oxygen partial pressure to a value fixed by thermodynamics. The use of such gas buffer, often applied in metallurgic high temperature applications, requires sufficiently high temperatures to allow for a gas dynamic equilibrium.[51] The temperatures involved during our experiments are too low to cause this reaction to occur in a reasonable timeframe. It may thus be expected that the partial pressure of oxygen will be nearly equal to the ratio of oxygen flow to the total gas flow.

Based on this assumption and the observations concerning the oxidation of vanadium (section 5.2), adding oxygen to a level of 20 to 200 Pa would likely result in stabilization of the VO_2 phase. Of course, in such cases a competition between reduction and oxidation will take place in the vanadium oxide layer. Figures 7 (a) and (b) show the *in-situ* XRD measurement obtained during reduction of V_2O_5 at 480 °C in a mixture containing 200 Pa O_2 and 5000 Pa H_2, as well as the corresponding full XRD scan performed after the reduction process. As was desired, single phase VO_2 is observed after less than 10 minutes of annealing and remained stable, as being clear from 7(c), which shows the intensity of the VO_2 diffraction peak over time. Figure 7(d) shows the temperature dependent sheet resistance measurement for the VO_2 film prepared by reduction of V_2O_5. A remarkable switching ratio of nearly 5 orders of magnitude is achieved, close to the highest reported values for single crystal bulk VO_2.

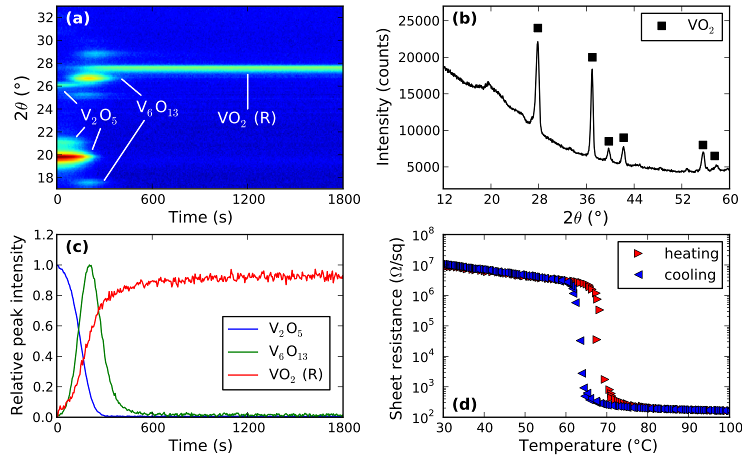

Figure 7. *(a) In-situ XRD during the reduction of V_2O_5 at 480 °C in a mixture 200 Pa O_2 with 5000 Pa H_2 in He. (b) The corresponding full XRD scan after one hour of annealing. (c) Evolution of the diffraction peak intensities corresponding to V_2O_5, V_6O_{13} and VO_2. (d) Temperature dependent sheet resistance measurement of the VO_2 thin film.*

Since these mixtures of H_2 with O_2 result in stabilization of VO_2 upon reduction from V_2O_5, it is not unlikely that such mixtures can as well serve for the controlled oxidation of vanadium. Figures 8 (a) and (b) show the *in-situ* XRD measurements performed during oxidation at 480 °C in a mixture of 5000 Pa H_2 and 200 Pa O_2, as well as the full XRD scans performed after annealing. The gas mixture indeed results in formation of VO_2 as stable phase. When using a lower oxygen partial pressure of 20 Pa O_2 (not shown), oxidation proceeded much slower, and a long period of coexistence of VO_2 and V_2O_3 was observed. In that case, the vanadium layer was not yet fully transformed to VO_2 after one hour of annealing. Thus, compared with the oxidation without hydrogen, the oxidation proceeds much slower, as could be expected due to the competition between the reduction by hydrogen and the oxidation by oxygen.

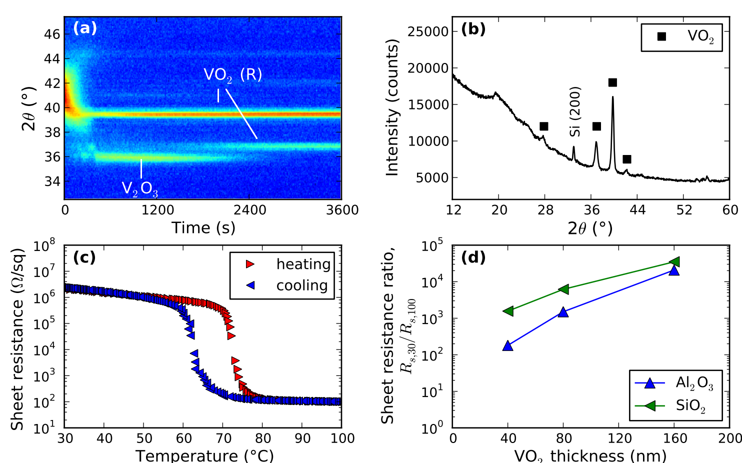

Figure 8. *(a) In-situ XRD measurement during the oxidation of 80 nm V at 480 °C in a mixture of 200 Pa O_2 and 5000 Pa H_2. (b) The corresponding full XRD scan after one hour of annealing. The peak at* 33 ° *is related to the silicon substrate. (c) Temperature dependent sheet resistance measurement of the resulting VO_2 thin film. (d) Dependency of VO_2 film thickness and template on the sheet resistance switching ratio.*

The temperature dependent sheet resistance measurement (figure 8(c)) reveals a 4 orders of magnitude change in resistance across the SMT, which is an improvement of one order of magnitude compared to the oxidized vanadium layers in low oxygen partial pressures without hydrogen. Figure 8 (d) summarizes the switching ratios observed as a function of VO_2 film thickness and template for vanadium layers oxidized at 480 °C under the same gas conditions. The corresponding temperature dependent sheet resistance measurements are available in the supplementary information. Although the switching ratio is suppressed for the thinnest films, we were able to prepare VO_2 layers as thin as 40 nm using this approach, which still showed several orders of magnitude change in sheet resistance.

Comparison of thin film VO_2 synthesis methods

The question rises what explains the large difference in sheet resistance of the several prepared VO_2 thin films. It is commonly observed that thin films have suppressed switching behavior compared to bulk VO_2. Brassard et al. showed the influence of grain size on both the magnitude and sharpness of the transition.[20] Smaller grains involve a high density of grain boundaries, affecting the sheet resistance of a thin film. The authors stated that defects at the grain boundaries decrease the sheet resistance of the low-temperature high-resistive state, whereas they increase the sheet resistance of the high-temperature low-resistive state.

The SEM images in figure 9 show the morphology of VO_2 thin films prepared under various conditions on both the Al_2O_3 (top) and SiO_2 template (middle), as well as their respective temperature dependent sheet resistance measurements (bottom). Additional data are provided in the supplementary information. Annealing in air (first column) results in a rather irregular morphology, which seemed to be strongly dependent on the oxidation time (not shown). Annealing for 1 hour in 20 Pa O_2 at 480 °C leads to a columnar microstructure (second column). The grain size however strongly depends on the template, more precisely the mean lateral

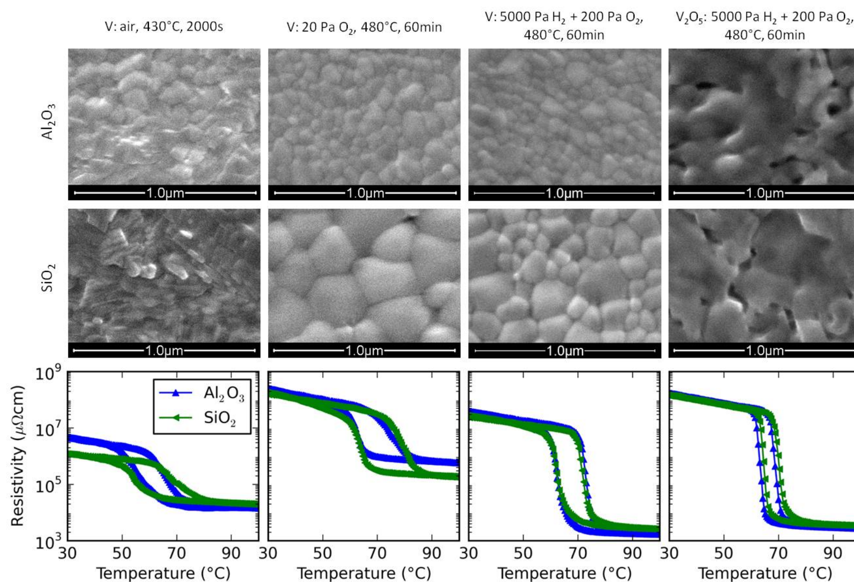

Figure 9. *SEM images of VO_2 thin films prepared under different conditions. First row: Al_2O_3 template. Second row: SiO_2 template. Third row: corresponding temperature dependent resistivity. Left to right: Oxidation of V in air at 430 °C for 2000 seconds; oxidation of V in 20 Pa O_2 at 480 °C for 60 minutes; oxidation of V in a mixture of 5000 Pa H_2 with 200 Pa O_2 at 480 °C for 60 minutes; reduction of V_2O_5 in a mixture of 5000 Pa H_2 with 200 Pa O_2 at 480 °C for 60 minutes.*

grain size is approximately 90 nm on Al_2O_3 and 180 nm on SiO_2, as determined from SEM. Similar to the observations of Brassard et al., the larger grain size on SiO_2 results in an increased resistance switching ratio.

Oxidations carried out in a mixture of 5000 Pa H_2 and 200 Pa O_2 show as well larger grains on SiO_2 compared to Al_2O_3 (third column), although especially on SiO_2 the grain size is smaller compared to the anneals in low pressure oxygen. Grain sizes are approximately 75 nm and 130 nm on the Al_2O_3 and SiO_2 templates respectively. The larger resistance switching ratios observed for these films, around 4 orders of magnitude, indicate that sheet resistance cannot solely be explained by the grain size. Instead, it is expected that the level of defects at the grain boundaries is strongly suppressed by the interplay of oxidation by O_2 and reduction by H_2, minimizing their effect on the sheet resistance, such that the VO_2 thin film behaves more like bulk material. On the other hand, it may not be excluded that the bulk stoichiometry is further optimized when using the H_2-O_2 gas mixture. Griffiths, for instance, showed how an excess or deficiency of oxygen in the VO_2 lattice suppresses the transition.[19] Excess of oxygen would result in a drastically increased resistivity of the high temperature phase. Such high resistivity is observed in our case of oxidation in 20 Pa O_2. It may thus be expected that the VO_2 films prepared under this condition contain a considerable amount of defects, whereas the films prepared in the H_2-O_2 mixture have a much purer stoichiometry.

Finally the fourth column in figure 9 shows SEM images of the reduced V_2O_5 films. A more complex morphology is observed in these cases, i.e. a non-closed but still continuous layer. This morphology originates from the morphology of the V_2O_5 layers which were prepared by oxidation of vanadium (supplementary information). Grains and grain boundaries are however vague. This relates to the high switching ratio of nearly 5 orders of magnitude observed for these films. This microstructure results in resistivity values and switching behavior as reported for bulk single-crystal VO_2.

In the supplementary information SEM images are provided for the V_6O_{13} and V_2O_3 thin films prepared in this work. These phases formed as well continuous layers.

Apart from the resistance switching ratio, the sharpness and hysteresis width of the transition are clearly improving when the H_2-O_2 gas mixture is used during oxidation of V, and certainly in the case of the controlled reduction of V_2O_5. Klimov et al. discussed the shape of the hysteresis loop in terms of grain size distribution and oxygen nonstoichiometry.[52] Whereas VO_2 single crystals show a hysteresis width of 2 °C, in thin films this can easily broaden up to 15 °C or more. Klimov et al. explained this by the grain size distribution in thin films. Each grain has its own hysteresis loop with characteristic transition temperatures for transition from metallic to semiconductive state and vice versa. It is observed that the internal hysteresis loop broadens when grain size decreases. Certainly in the case of a fine grained thin film with a broad grain size distribution, the hysteresis will be wide and the transition less sharp. In case of grain size ditribution with various maxima, multistep transitions in the resistance switching curve are

even observed. Furthermore, if oxygen nonstoichiometry is present, the shape of the hysteresis curve can be asymmetric. This was explained by the tendence of the smaller grains to have a higher degree of nonstoichiometry.

In case of the oxidation of V in 20 Pa O_2, an asymmetric curve with wide hysteresis was observed, indicating the presence of a grain size distribution with a non-uniform oxygen nonstoichiometry. When the H_2-O_2 gas mixture was used during oxidation the asymmetry disappears, which confirms our statement of the improved stoichiometry in the film. In the case of the reduction of V_2O_5 the transition was observed to be symmetric and sharp with a small hysteresis width, showing the presence of a highly stroichiometric film with larger grains.

Conclusions

In this work, *in-situ* XRD was used to investigate thermal oxidation and reduction reactions in the V-O system. Starting from V and V_2O_5 thin films, VO_2 and V_2O_3 have been prepared which show a semiconductor-metal transition.

During oxidation of V thin films in air, VO_2 forms as an intermediate phase prior to the full oxidation towards V_2O_5. By careful optimization of the annealing time and temperature, resistance changes up to 3 orders of magnitude were obtained. A more reliable way of oxidation was obtained by lowering the oxygen partial pressure to a level of 20 Pa. Under this condition, single phase VO_2 appeared, which did not further oxidize. A stable resistance switching ratio of 3 orders of magnitude was observed for these films. However, the asymmetric shape of the resistance switching curve suggests oxygen nonstoichiometry is present.

Oxidation of V in a mixture of 5000 Pa H_2 and 20 to 200 Pa O_2 showed stabilization of the VO_2 phase as well, enlarging the range of applicable oxygen partial pressures. Remarkable was the increased switching ratio of more than 4 orders of magnitude observed for these VO_2 thin films, whereas the transition is sharper and more symmetric. This suggests that less defects are present at the grain boundaries and in the bulk, minimizing their influence on the sheet resistance and switching ratio of the film.

Alternatively, VO_2 was prepared by the reduction of V_2O_5. However, a continuous reduction was observed when using 5000 Pa H_2, through V_2O_5, V_6O_{13} and VO_2, finally ending up as V_2O_3. This phase showed an electrical switch of 3 orders of magnitude near -100 °C. The balanced gas mixture of 5000 Pa H_2 and 200 Pa O_2 proved to be useful as well for the stabilized reduction of V_2O_5 thin films towards VO_2, leading to even higher resistance switching ratios, close to the 5 orders of magnitude as reported for bulk, single-crystal VO_2.

Acknowledgments

This research was supported by the Special Research Fund BOF of Ghent University (GOA 01G01513) and the Flemish Research Foundation FWO.

References

[1] F. J. Morin, *Phys. Rev. Lett.* **3**(1), 34–36 (1959).

[2] A. Zylbersztejn and N. F. Mott, *Phys. Rev. B* **11**(11), 4383–4395 (1975).

[3] T. D. Manning, I. P. Parkin, R. J. H. Clark, D. Sheel, M. E. Pemble, and D. Vernadou, *J. Mater. Chem.* **12**(10), 2936–2939 (2002).

[4] I. P. Parkin and T. D. Manning, *J. Chem. Educ.* **83**(3), 393 (2006).

[5] C. E. Lee, R. A. Atkins, W. N. Gibler, and H. F. Taylor, *Appl. Opt* **28**(21), 4511–4512 (1989).

[6] M. Soltani, M. Chaker, E. Haddad, R. V. Kruzelecky, and J. Margot, *Appl. Phys. Lett.* **85**(11), 1958–1960 (2004).

[7] M.-J. Lee, Y. Park, D.-S. Suh, E.-H. Lee, S. Seo, D.-C. Kim, R. Jung, B.-S. Kang, S.-E. Ahn, C. B. Lee, D. H. Seo, Y.-K. Cha, I.-K. Yoo, J.-S. Kim, and B. H. Park, *Adv. Mater.* **19**(22), 3919–3923 (2007).

[8] H.-T. Kim, B.-G. Chae, D.-H. Youn, S.-L. Maeng, G. Kim, K.-Y. Kang, and Y.-S. Lim, *New J. Phys.* **6**, 52 (2004).

[9] I. P. Radu, K. Martens, S. Mertens, C. Adelmann, X. Shi, H. Tielens, M. Schaekers, G. Pourtois, S. Van Elshocht, S. De Gendt, M. Heyns, and J. A. Kittl, *ECS Trans.* , 233–243 (2011).

[10] K. Martens, I. P. Radu, S. Mertens, X. Shi, L. Nyns, S. Cosemans, P. Favia, H. Bender, T. Conard, M. Schaekers, and et al., *J. Appl. Phys.* **112**(12), 124501 (2012).

[11] D. B. McWhan, A. Menth, J. P. Remeika, W. F. Brinkman, and T. M. Rice, *Phys. Rev. B* **7**(5), 1920–1932 (1973).

[12] S. Yonezawa, Y. Muraoka, Y. Ueda, and Z. Hiroi, *Solid State Commun.* **129**(4), 245–248 (2004).

[13] H. A. Wriedt, *Bulletin of Alloy Phase Diagrams* **10**(3), 271–277 (1989).

[14] U. Schwingenschlögl and V. Eyert, *Ann. Phys.* **13**(9), 475–510 (2004).

[15] Y.-B. Kang, *J. Eur. Ceram. Soc.* **32**(12), 3187–3198 (2012).

[16] N. Bahlawane and D. Lenoble, *Chem. Vapor Depos.* **20**(7-8-9), 299–311 (2014).

[17] T. J. Hanlon, R. E. Walker, J. A. Coath, and M. A. Richardson, *Thin Solid Films* **405**, 234–237 (2002).

[18] Y. Ningyi, L. Jinhua, and L. Chenglu, *Appl. Surf. Sci* **191**(1), 176–180 (2002).

[19] C. H. Griffiths and H. K. Eastwood, *J. Appl. Phys.* **45**(5), 2201–2206 (1974).

[20] D. Brassard, S. Fourmaux, M. Jean-Jacques, J. C. Kieffer, and M. A. El Khakani, *Appl. Phys. Lett.* **87**(5), 051910 (2005).

[21] S. J. Yun, J. W. Lim, J.-S. Noh, B.-G. Chae, and H.-T. Kim, *Jpn. J. Appl. Phys.* **47**(4S), 3067 (2008).

[22] Y.-K. Dou, J.-B. Li, M.-S. Cao, D.-Z. Su, F. Rehman, J.-S. Zhang, and H.-B. Jin, *Appl. Surf. Sci.* **345**, 232–237 (2015).

[23] J. W. Tashman, J. H. Lee, H. Paik, J. A. Moyer, R. Misra, J. A. Mundy, T. Spila, T. A. Merz, J. Schubert, D. A. Muller, and et al., *Appl. Phys. Lett.* **104**(6), 063104 (2014).

[24] K. Martens, N. Aetukuri, J. Jeong, M. G. Samant, and S. S. P. Parkin, *Appl.*

Phys. Lett. **104**(8), 081918 (2014).
[25] S. Lee, T. L. Meyer, S. Park, T. Egami, and H. N. Lee, *Appl. Phys. Lett.* **105**(22), 223515 (2014).
[26] M. B. Sahana, M. S. Dharmaprakash, and S. A. Shivashankar, *J. Mater. Chem.* **12**(2), 333–338 (2002).
[27] M. B. Sahana, G. N. Subbanna, and S. A. Shivashankar, *J. Appl. Phys.* **92**(11), 6495 (2002).
[28] D. Vernardou, M. Pemble, and D. Sheel, *Thin Solid Films* **516**(14), 4502–4507 (2008).
[29] C. Piccirillo, R. Binions, and I. P. Parkin, *Chem. Vapor Depos.* **13**(4), 145–151 (2007).
[30] J. C. Badot, S. Ribes, E. B. Yousfi, V. Vivier, J. P. Pereira-Ramos, N. Baffier, and D. Lincot, *Electrochem. Solid St.* **3**(10), 485–488 (2000).
[31] J. Musschoot, D. Deduytsche, H. Poelman, J. Haemers, R. L. Van Meirhaeghe, S. Van den Berghe, and C. Detavernier, *J. Electrochem. Soc.* **156**(7), P122 (2009).
[32] G. Rampelberg, M. Schaekers, K. Martens, Q. Xie, D. Deduytsche, B. De Schutter, N. Blasco, J. Kittl, and C. Detavernier, *Appl. Phys. Lett.* **98**(16), 162902 (2011).
[33] G. Rampelberg, D. Deduytsche, B. De Schutter, P. A. Premkumar, M. Toeller, M. Schaekers, K. Martens, I. Radu, and C. Detavernier, *Thin Solid Films* **550**, 59–64 (2014).
[34] P. A. Premkumar, M. Toeller, I. P. Radu, C. Adelmann, M. Schaekers, J. Meersschaut, T. Conard, and S. Van Elshocht, *ECS J. Solid State Sci. Technol.* **1**(4), P169–P174 (2012).
[35] T. Blanquart, J. Niinistö, M. Gavagnin, V. Longo, M. Heikkilä, E. Puukilainen, V. R. Pallem, C. Dussarrat, M. Ritala, and M. Leskelä, *RSC Adv.* **3**(4), 1179 (2013).
[36] P. A. Premkumar, K. Martens, G. Rampelberg, M. Toeller, J. M. Ablett, J. Meersschaut, D. Cuypers, A. Franquet, C. Detavernier, J.-P. Rueff, M. Schaekers, S. Van Elshocht, M. Jurczak, C. Adelmann, and I. P. Radu, *Adv. Funct. Mater.* **25**, 679–686 (2015).
[37] L. A. Beresneva, S. F. Devyatova, and L. L. Vasilyeva, *Thin Solid Films* **75**(1), 47–51 (1981).
[38] J. Qi, G. Ning, and Y. Lin, *Mater. Res. Bull.* **43**(8-9), 2300–2307 (2008).
[39] F. Théobald, R. Cabala, and J. Bernard, *J. Solid State Chem.* **17**, 431–438 (1976).
[40] E. A. Gulbransen and K. F. Andrew, *J. Electrochem. Soc.* **97**(11), 396–404 (1950).
[41] W. R. Price and J. Stringer, *J. Less-Common Met.* **8**, 165–185 (1965).
[42] W. R. Price, S. J. Kennett, and J. Stringer, *J. Less-Common Met.* **12**, 318–325 (1967).
[43] A. Mukherjee and S. P. Wach, *J. Less-Common Met.* **92**, 289–300 (1983).
[44] A. Mukherjee, *J. Less-Common Met.* **107**, 89–97 (1985).
[45] A. Mukherjee and S. P. Wach, *J. Less-Common Met.* **132**, 107–113 (1987).

[46] G. Salomonsen, N. Norman, O. Lonsjo, and T. G. Finstad, *J. Less-Common Met.* **158**, 251–265 (1990).

[47] W. Knaepen, C. Detavernier, R. Van Meirhaeghe, J. Jordan Sweet, and C. Lavoie, *Thin Solid Films* **516**(15), 4946–4952 (2008).

[48] W. Knaepen, S. Gaudet, C. Detavernier, R. L. Van Meirhaeghe, J. J. Sweet, and C. Lavoie, *J. Appl. Phys.* **105**(8), 083532 (2009).

[49] B. E. Deal and A. S. Grove, *J. Appl. Phys.* **36**(12), 3770 (1965).

[50] G. Reiss, J. Vancea, and H. Hoffmann, *Phys. Rev. Lett.* **56**(19), 2100–2103 (1986).

[51] A. Bolind, *Control of oxygen partial pressure of the cover gas in a molten lead-bismuth eutectic system*, PhD thesis, University of Illinois at Urbana-Champaign, (2006).

[52] V. A. Klimov, I. O. Timofeeva, S. D. Khanin, E. B. Shadrin, A. V. Ilinskii, and F. Silva-Andrade, *Tech. Phys.* **47**(9), 1134–1139 (2002).

Paper I - supplementary information

In-situ X-ray diffraction study of the controlled oxidation and reduction in the V-O system for the synthesis of VO_2 and V_2O_3 thin films *

*Published as: G. Rampelberg, B. De Schutter, W. Devulder, K. Martens, I. Radu, and C. Detavernier, *J. Mater. Chem.*, 3, 11357 (2015).

Oxidation in 20 Pa O_2

Figure 1 shows the *in-situ* XRD measurements of the oxidation of V films with thicknesses 20 nm, 40 nm and 80 nm on Al_2O_3 and SiO_2 in 20 Pa O_2 at 480 °C. In all cases VO_2(R) is formed, characterized by a diffraction peak near 40 °, which corresponds with the (020) plane. Temperature dependent sheet resistance measurements for these oxidized films are shown in figure 2. The change in sheet resistance during transition varies between 2 and 3 orders of magnitude. All films show more or less the same absolute values, except from the thinnest film on SiO_2 which has an overall higher sheet resistance of approximately 2 orders of magnitude. Figure 3 shows SEM images of these VO_2 films. The morphology is clearly much different on the Al_2O_3 and SiO_2 templates. The grain sizes are much larger on SiO_2 and the thinnest film has even agglomerated, which explains the drastically increased sheet resistance. In the other cases, grain sizes are smaller when film thickness decreases.

Oxidation in a mixture of 5000 Pa H_2 and 200 Pa O_2

Figure 4 shows the temperature dependent sheet resistance of the V films oxidized at 480 °C in a mixture of 5000 Pa H_2 and 200 Pa O_2. The change in sheet resistance during transition varies from approximately 2 orders of magnitude for the thinnest film to more than 4 orders of magnitude for the thickest film. Figure 5 shows the SEM images for these films. All films show a fine grained structure, with smaller grains compared to the films oxidized in 20 Pa O_2. The same trends are visible, i.e. grain size increases with film thickness and grains are larger on the SiO_2 template.

V_2O_5, V_6O_{13} and V_2O_3

Apart from VO_2, three other vanadium oxide phases were prepared during this work. V_2O_5 was prepared by oxidation of 80 nm V in air at 480 °C for 30 minutes. V_6O_{13} was prepared by oxidation of 80 nm V in 200 Pa O_2 at 480 °C for 60 minutes. V_2O_3 was prepared from the V_2O_5 film, by a subsequent reduction in 5000 Pa H_2 at 480 °C for 60 minutes. Figure 6 shows SEM images for these phases. All of these phases formed as continuous layers.

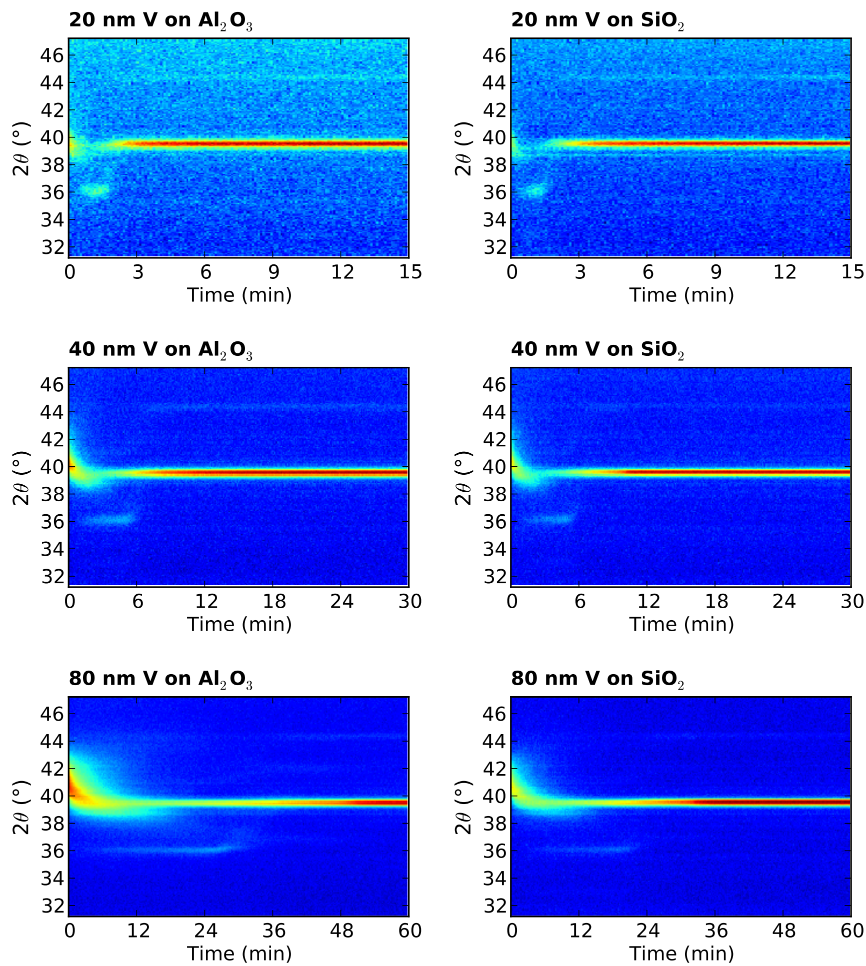

Figure 1. *In-situ XRD measurements during isothermal oxidation of 20 nm, 40 nm and 80 nm vanadium layers on the Al_2O_3 and SiO_2 templates at 480 °C in an oxygen partial pressures of 20 Pa.*

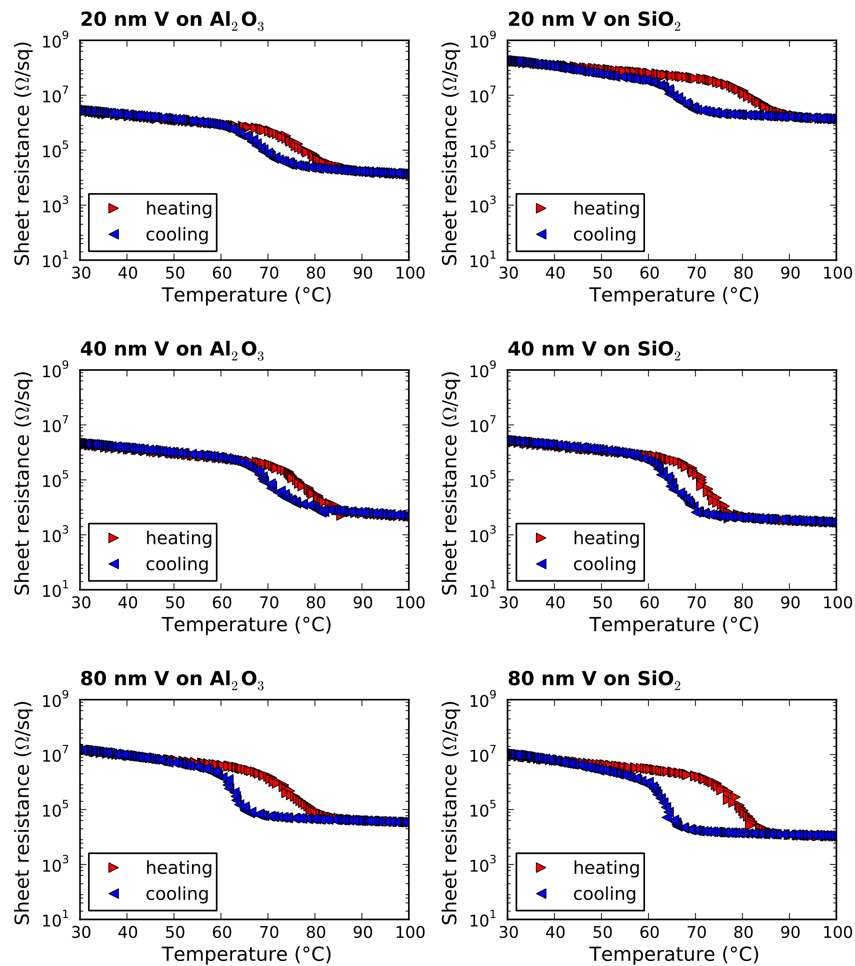

Figure 2. *Temperature dependent sheet resistance measurements after isothermal oxidation of 20 nm, 40 nm and 80 nm vanadium layers on the Al_2O_3 and SiO_2 templates at 480 °C in an oxygen partial pressures of 20 Pa.*

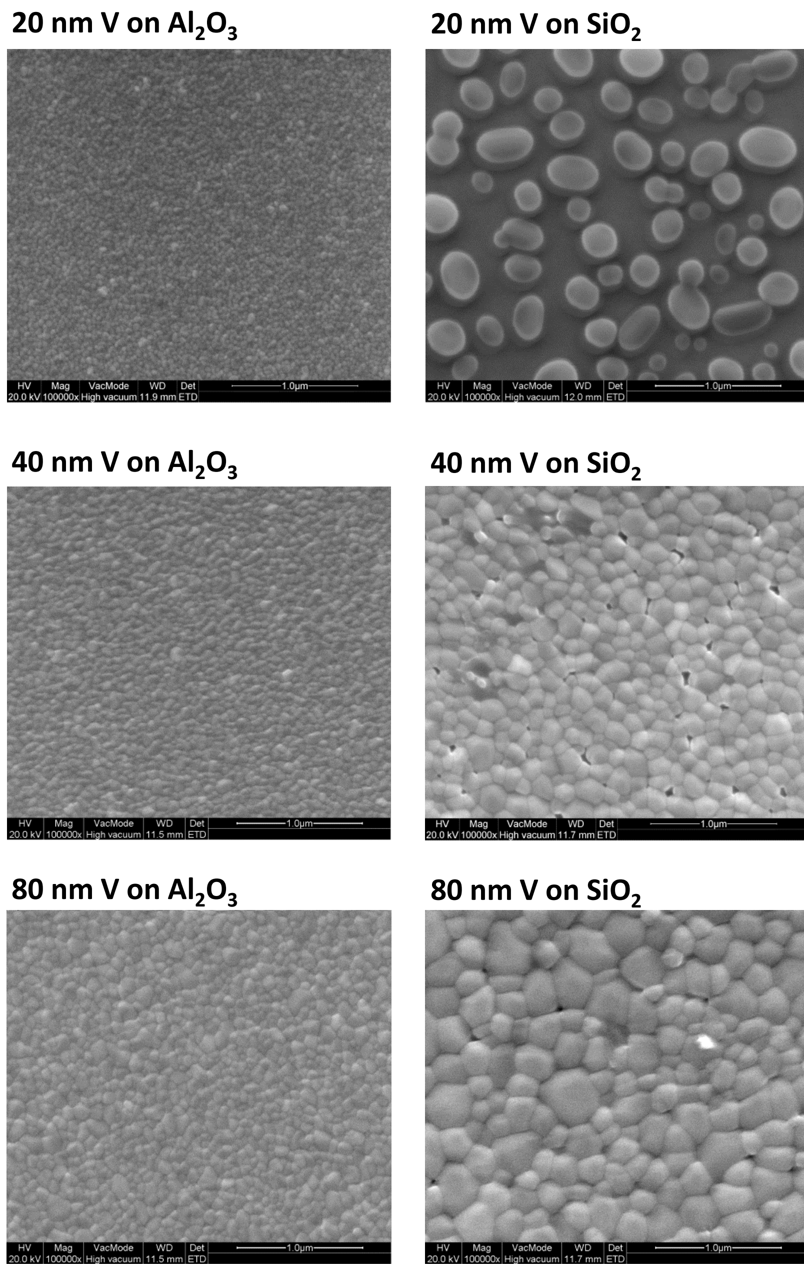

Figure 3. *SEM images of the films annealed at 480 °C in 20 Pa* O_2.

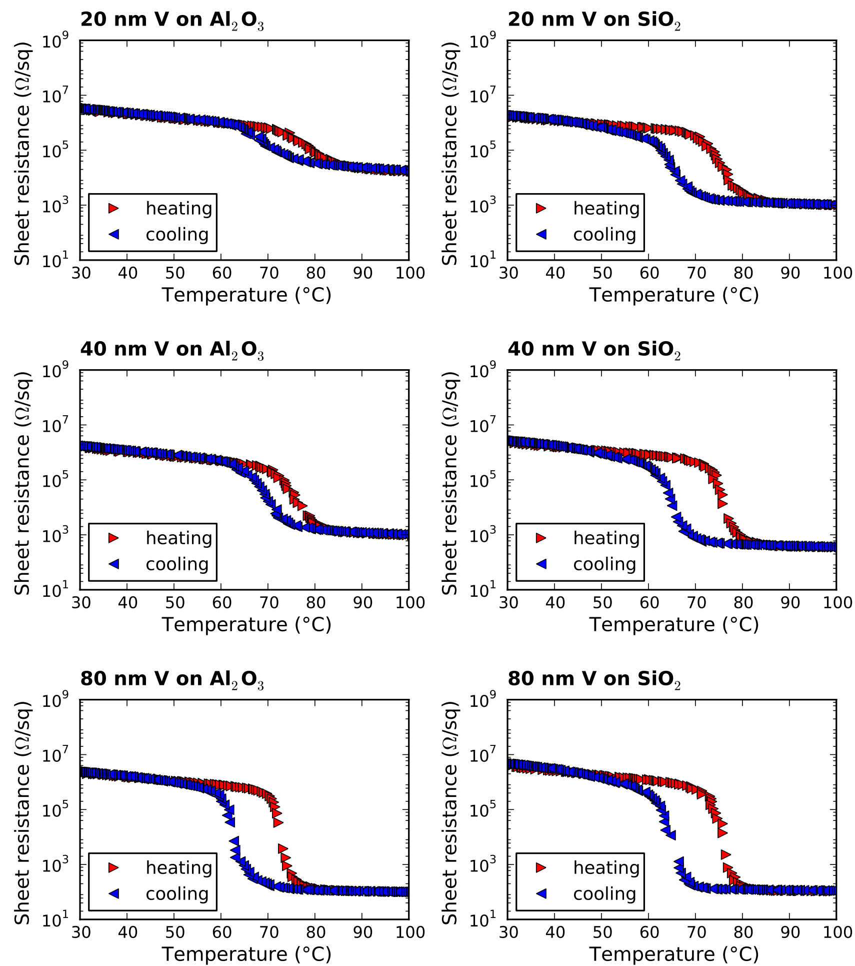

Figure 4. *Temperature dependent sheet resistance measurements after isothermal oxidation of 20 nm, 40 nm and 80 nm vanadium layers on the Al_2O_3 and SiO_2 templates at 480 °C in a mixture of 5000 Pa H_2 and 200 Pa O_2.*

20 nm V on Al_2O_3

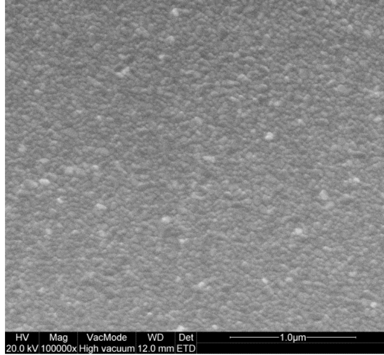

20 nm V on SiO_2

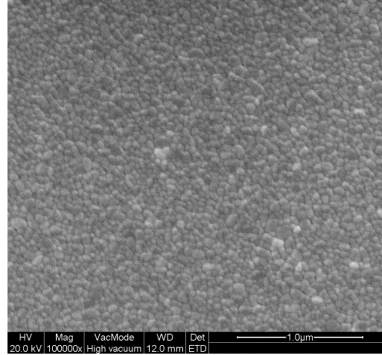

40 nm V on Al_2O_3

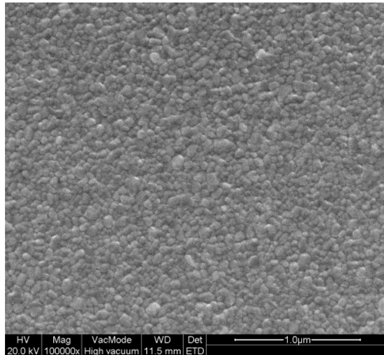

40 nm V on SiO_2

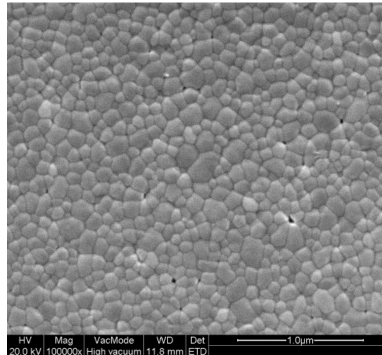

80 nm V on Al_2O_3

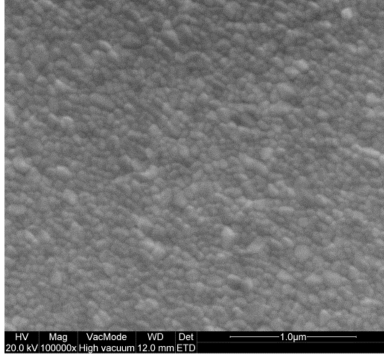

80 nm V on SiO_2

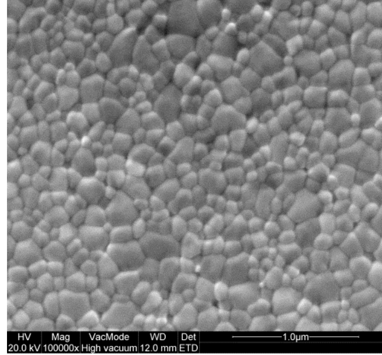

Figure 5. *SEM images of the films annealed at 480 °C in a mixture of 5000 Pa H_2 and 200 Pa O_2.*

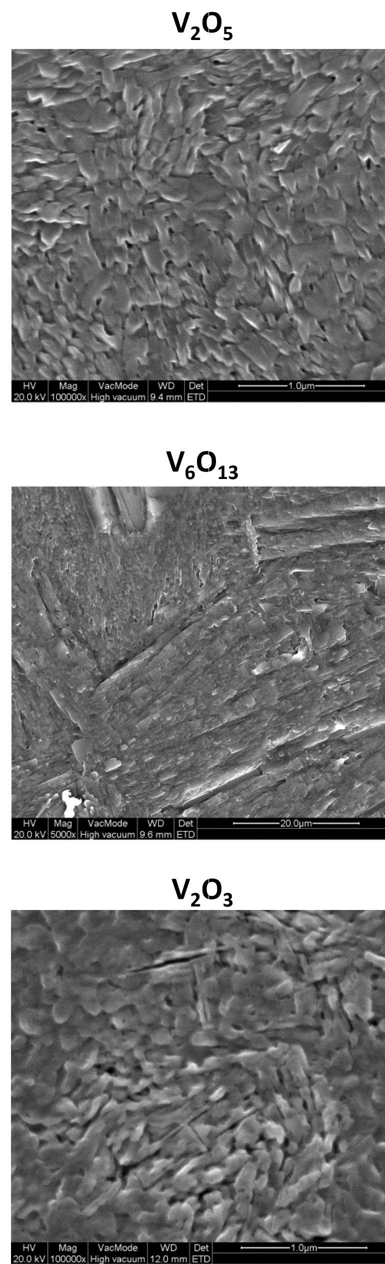

Figure 6. *SEM images of the V_2O_5, V_6O_{13} and V_2O_3 thin films.*

Paper II
Semiconductor-metal transition in thin VO_2 films grown by ozone based atomic layer deposition *

Abstract

Thin films of vanadium dioxide (VO_2) have been grown by a low temperature atomic layer deposition process at 150 °C using Tetrakis [EthylMethylAmino] Vanadium as a vanadium source and ozone as reactant gas. Films deposited on SiO_2 were amorphous, but during a thermal treatment at 450 °C tetragonal VO_2(R) was formed. During in-situ X-ray diffraction measurements, the semiconductor-metal transition was observed as a reversible transition between VO_2(M1) and VO_2(R) near 67 °C. Correlated to this phase change, a reversible change in resistivity was observed of more than 2 orders of magnitude for a film of 42 nm thickness.

*Published as: G. Rampelberg, M. Schaekers, K. Martens, Q. Xie, D. Deduytsche, B. De Schutter, N. Blasco, J. Kittl, and C. Detavernier, *Appl. Phys. Lett.*, 98, 162902 (2011).

In the large group of vanadium oxides, VO_2 has the interesting feature that a large reversible change in resistivity occurs near a temperature of 68 °C,[1] which is referred to as a metal-insulator transition (MIT) or semiconductor-metal transition (SMT). The transition is known to be accompanied with a transformation in crystallographic structure, from monoclinic VO_2(M1) below the transition temperature to tetragonal VO_2(R) above.[2] For single crystals the resistivity change can be as high as 5 orders of magnitude and occurs in a very narrow temperature range of only a few degrees Celsius.[3] This property makes VO_2 an interesting candidate for applications in resistive memories and switches in microelectronics. In that case one is interested in inducing the resistive switch electrically rather than thermally and several groups succeeded already in making such test devices.[4;5].

A lot of results are reported in literature on thin film growth of VO_2, typically using pulsed laser deposition,[6] reactive sputtering[7;8] or chemical vapor deposition[9–11] as deposition techniques. For applications in microelectronic devices, however, atomic layer deposition (ALD) is gaining importance for depositing oxide films, due to aggressive scaling of device dimensions and increasing integration complexity, requiring in many cases conformal depositions in 3D structures. The key feature for this technique is the self-limiting character of the surface reactions, making layer by layer growth possible.[12;13] The main advantages are the excellent control of thickness and stoichiometry and a very good uniformity and conformality on complex structures. Also the typical deposition temperatures are rather low compared to other deposition techniques. However, ALD processes for vanadium oxides mostly result in V_2O_5 growth.[14]

In this work, it is shown that amorphous VO_2 films can be deposited with an ALD process at only 150 °C. During an additional thermal treatment at 450 °C in inert gas VO_2(R) is observed as the first and only crystalline phase, which on cooling down transforms to VO_2(M1). A SMT is observed with a resistivity change of more than 2 orders of magnitude for a film with a thickness of 42 nm.

Thin vanadium oxide films were grown in an experimental low-pressure ALD reactor[15;16] on Si substrates with 100 nm thermally grown SiO_2. TEMAV, i.e. $V(NEtMe)_4$, (Air Liquide) was used as metal-organic vanadium precursor, which has an oxidation state of 4+ for the vanadium, in contrast to other vanadium precursors like $VO[O(C_3H_7)i]_3$ where it is 5+. This could possibly facilitate the formation of VO_2 instead of V_2O_5, since 4+ is also the oxidation state of vanadium in VO_2. As reactant gases, both H_2O (thermal), O_2 (plasma enhanced) and O_3 were tested. Although it seemed possible to obtain similar results with all three reactants, the process with O_3 behaved as the most reliable. Therefore, only results of the ozone based ALD process will be discussed in detail in this letter. The ozone was produced from a pure flow of O_2 with an OzoneLabTM OL100, resulting in an O_3 concentration of 175 μg/ml. The base pressure in the reactor was 10^{-4} Pa, whereas the partial pressures for TEMAV and ozone were 10^{-2} Pa and 50 Pa respectively. Ar was used as a carrier gas for the TEMAV.

Since the main characteristic of ALD is the self-limiting nature of the surface reactions, it is important to verify in which temperature range this behavior is

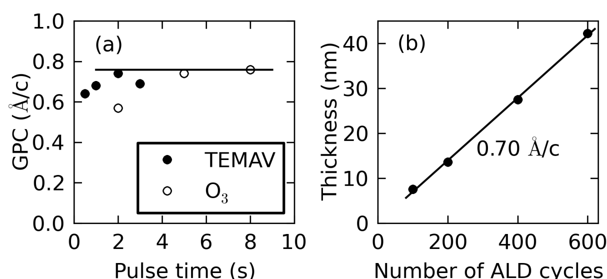

Figure 1. *ALD characteristics for the process TEMAV O_3 at 150 °C: (a) Growth per cycle versus exposure times for TEMAV with a fixed O_3 exposure of 5 s (filled symbols) and for O_3 with a fixed TEMAV exposure of 2 s (open symbols); (b) Thickness of the deposited films as a function of the number of ALD cycles.*

observed. Therefore, a process was performed at several substrate temperatures, consisting of 200 times 2 s exposure with TEMAV while no reactant gas was used. At 200 °C, a film was grown with a growth rate of 0.3 Å per second of TEMAV exposure as derived from an X-ray reflectivity (XRR) measurement, corresponding to thermal decomposition of the precursor. While no clearly detectable layer was observed with XRR when the temperature was lowered to 175 °C, X-ray fluorescence (XRF) revealed that there was still some vanadium deposited. The XRF signal ratio V/Si was 10 times lower than the deposition at 200 °C. Although very low, this signal was again lowered 5 times at 150 °C substrate temperature. These results suggest that the maximum ALD temperature for TEMAV is 150 °C, although at 175 °C the decomposition of TEMAV is actually very small. Saturation experiments for the ALD process were performed at 150 °C and it was concluded that 2 s TEMAV and 5 s ozone resulted in a saturated ALD growth (figure 1(a)). Pump times were respectively 25 s and 15 s after the TEMAV and ozone pulse. The corresponding growth per cycle (GPC), which is derived from dividing the measured thickness of the film by the number of ALD cycles (100 cycles in these cases), is 0.76 Å/c. Although a slight decrease in GPC is observed for 3 s TEMAV with respect to 2 s TEMAV exposure, it is within the error range of the XRR measurements. The uniformity of the saturated process at 150 °C was excellent, with a deviation in thickness of less than 2% on a sample of 30 cm^2. Also the linearity of the ALD process was good, as shown in figure 1(b). From the slope of a linear fit a GPC of 0.7 Å/c was extracted.

In order to determine the stoichiometry of the films, X-ray photoelectron spectroscopy (XPS) measurements were performed on (i) a film grown with the O_3-based ALD process and (ii) a film grown with an O_2-plasma enhanced ALD process, having a long plasma exposure (figure 2). For the latter it seemed that, as long as the plasma exposure was sufficient, crystalline V_2O_5 could be observed with X-ray diffraction (XRD), as shown in figure 3. The O1s peak (V-O bond) was used as a reference for the binding energy (530.0 eV). For the O_2 plasma grown film, the binding energy of the $V2p_{3/2}$ peak was fitted as 517.2 eV, while for the

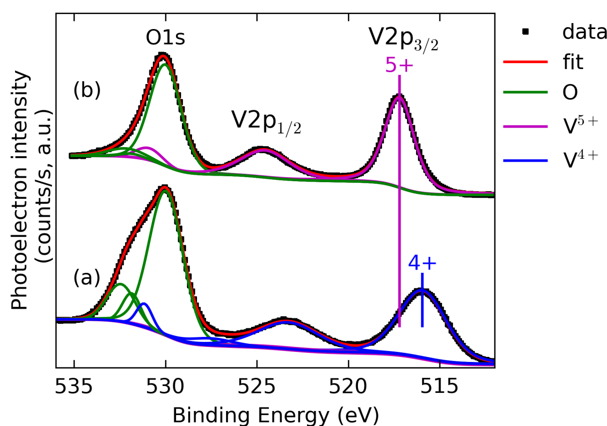

Figure 2. *XPS of (a) an as deposited O_3-grown ALD film, and (b) a film grown by an O_2-plasma enhanced ALD process with long plasma exposure.*

ozone-based ALD film this value was 515.95 eV. According to Silversmit et al.[17] these values are related to the V^{5+} and V^{4+} oxidation states respectively, i.e. to V_2O_5 and VO_2 respectively. Thus, it can be concluded that the O_3-based ALD films were VO_2 as deposited. Additionally, no detectable amount of impurities like C and N were observed in the as grown films.

From XRD (λ=0.154nm) of the as deposited films it was concluded that O_3-grown films, independent of the thickness, showed no sign of crystallinity (figure 3). Therefore, on some films isothermal anneals were performed at different temperatures and for varying times in an inert atmosphere (He). These thermal treatments were performed in an experimental heating chamber which was placed

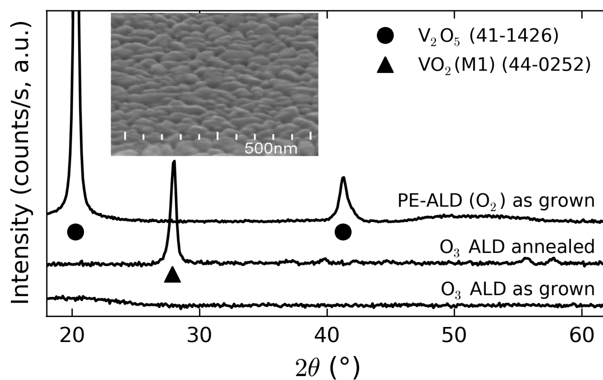

Figure 3. *XRD spectra of an O_3-grown ALD films, the same film annealed for 30 minutes in He at 450 °C and a film grown by an O_2-plasma enhanced ALD process with long plasma exposure. In the inset a SEM picture is shown for the annealed O_3-grown ALD film.*

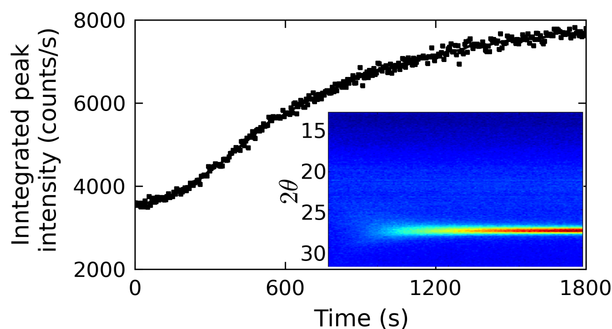

Figure 4. *Integrated intensity for the diffraction peak of the VO_2(R) 110 plane during an isothermal anneal of 30 minutes at 450 °C in He for a film of 42 nm. The inset shows the in-situ XRD measurement from which the peak intensity was integrated.*

in a Bruker D8 Discover XRD system.[18] The XRD pattern was captured every 5 s with a linear Vantec detector, having a range in 2θ of 20°. For the 42 nm film it was observed that at 450 °C in He the crystallization started within less than 10 minutes, while the integrated peak intensity slowly increased during the first 30 minutes (figure 4). Although there are many possible crystalline phases of VO_2, the position of the peak (27.65° ± 0.05° as 2θ value) suggests that it corresponded with the 110 plane of tetragonal VO_2(R) (JCPDS 44-0253), while no signs of other vanadium oxide phases were observed. Scanning electron microscopy (SEM) of the annealed film of 42 nm (inset of figure 3) revealed a continuous polycrystalline film, while from atomic force microscopy (AFM) the root mean square value for the surface roughness was derived as 4.5 nm. For thinner films the roughness increased substantially when the same heating procedure was performed. More evidence for the assumption of VO_2(R) is provided by the observation that the diffracted peak position shifted between 27.85° and 27.65° when the sample temperature was varied between 30 and 100 °C (figure 5(a)). This corresponded with the reversible transformation between VO_2(M1) (JCPDS 44-0252) at low temperature and VO_2(R) at high temperature. In addition, figure 3 also shows the XRD pattern for the annealed film, measured at room temperature. The transition temperature was approximately 73 °C during heating and 61 °C during cooling. Thus, the mean transition temperature was 67 °C and the hysteresis 12 °C.

In the same heating stage as used for the in-situ XRD measurements 2 point resistivity measurements were performed with a Keithley 2000 Multimeter in order to correlate the crystallographic phase transformation with a change in resistivity. Since the measured resistivities were in the range of $k\Omega$ or higher, the contact resistance was negligible and the use of a 2 probe setup was justified. In addition, 4 point resistivity measurements were performed at room temperature in order to obtain absolute resistivity values. Figure 5(b) shows the resistivity as a function of temperature for the 42 nm film crystallized by annealing 3 times 10 minutes at 450 °C in He. A semiconductor-metal transition is clearly observed with a tran-

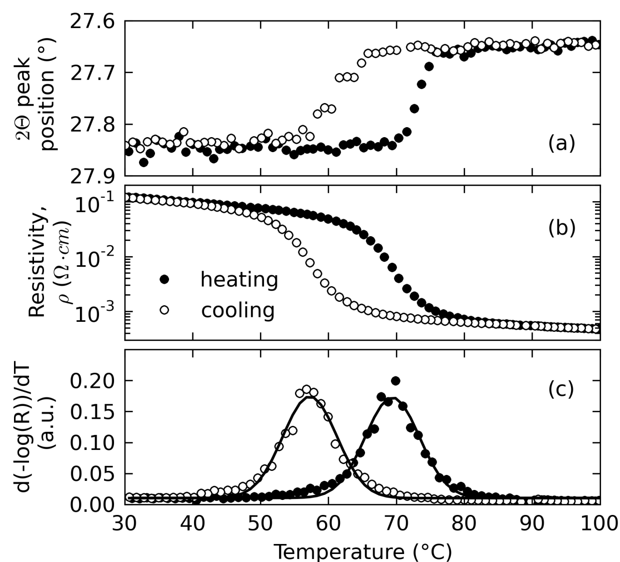

Figure 5. *Semiconductor-metal transition as observed during a thermal cycle between 30 and 100 °C, with fixed heating and cooling rate of 0.1 °C/s: (a) in-situ XRD, showing the change in crystal structure, (b) the correlated change in resistivity, and (c) a Gaussian curve fit to d(-log(R))/dT for the analysis of the resistivity.*

sition temperature a few °C lower than the crystallographic phase transformation and a resistivity ratio of approximately 200 in the range 30-100 °C. Transition temperatures were derived by fitting a Gaussian curve to d(-log(R))/dT for both heating and cooling (figure 5(c)). This resulted in a mean transition temperature of 63 °C, which is 4 °C lower than derived from in-situ XRD, and a hysteresis of 12 °C.

In conclusion, ozone based ALD was used to deposit thin films of vanadium oxide, with TEMAV as a vanadium precursor. XPS revealed that the stoichiometry was VO_2. Since all films were amorphous, isothermal anneals were applied in an inert atmosphere, resulting in tetragonal VO_2(R). In-situ XRD measurements also showed a reversible transformation between VO_2(M1) and VO_2(R) near 67 °C with a hysteresis of approximately 12 °C. This crystallographic phase transformation was correlated with a semiconductor-metal transition (SMT) as observed during resistivity measurements. The mean transition temperature in this case has been derived as 63 °C, with a hysteresis of 12 °C. The resistivity dropped by a factor of 200 in the range 30-100 °C for a 42 nm film.

Acknowledgments

The authors acknowledge Nico De Roo for XPS, Christa Vrancken for SEM and Marco Cirillo for AFM measurements. C.D. acknowledges the ERC for a starting grant.

References

[1] F. J. Morin, *Phys. Rev. Lett.* **3**(1), 34–36 (1959).

[2] A. Zylbersztejn and N. F. Mott, *Phys. Rev. B* **11**(11), 4383–4395 (1975).

[3] D. Kucharczyk and T. Niklewski, *J. Appl. Cryst.* **12**(4), 370–373 (1979).

[4] M.-J. Lee, Y. Park, D.-S. Suh, E.-H. Lee, S. Seo, D.-C. Kim, R. Jung, B.-S. Kang, S.-E. Ahn, C. B. Lee, D. H. Seo, Y.-K. Cha, I.-K. Yoo, J.-S. Kim, and B. H. Park, *Adv. Mater.* **19**(22), 3919–3923 (2007).

[5] H.-T. Kim, B.-G. Chae, D.-H. Youn, S.-L. Maeng, G. Kim, K.-Y. Kang, and Y.-S. Lim, *New J. Phys.* **6**, 52 (2004).

[6] K. Nagashima, T. Yanagida, H. Tanaka, and T. Kawai, *J. Appl. Phys.* **100**(6), 063714 (2006).

[7] D. Brassard, S. Fourmaux, M. Jean-Jacques, J. C. Kieffer, and M. A. El Khakani, *Appl. Phys. Lett.* **87**(5), 051910 (2005).

[8] S. J. Yun, J. W. Lim, J.-S. Noh, B.-G. Chae, and H.-T. Kim, *Jpn. J. Appl. Phys.* **47**(4S), 3067 (2008).

[9] M. B. Sahana, M. S. Dharmaprakash, and S. A. Shivashankar, *J. Mater. Chem.* **12**(2), 333–338 (2002).

[10] M. B. Sahana, G. N. Subbanna, and S. A. Shivashankar, *J. Appl. Phys.* **92**(11), 6495 (2002).

[11] D. Vernardou, M. Pemble, and D. Sheel, *Thin Solid Films* **516**(14), 4502–4507 (2008).

[12] T. Suntola and J. Antson, (1977), US Patent 4,058,430.

[13] R. L. Puurunen, *J. Appl. Phys.* **97**(12), 121301 (2005).

[14] J. Musschoot, D. Deduytsche, H. Poelman, J. Haemers, R. L. Van Meirhaeghe, S. Van den Berghe, and C. Detavernier, *J. Electrochem. Soc.* **156**(7), P122 (2009).

[15] Q. Xie, Y.-L. Jiang, C. Detavernier, D. Deduytsche, R. L. Van Meirhaeghe, G.-P. Ru, B.-Z. Li, and X.-P. Qu, *J. Appl. Phys.* **102**(8), 083521 (2007).

[16] Q. Xie, J. Musschoot, D. Deduytsche, R. L. Van Meirhaeghe, C. Detavernier, S. Van den Berghe, Y.-L. Jiang, G.-P. Ru, B.-Z. Li, and X.-P. Qu, *J. Electrochem. Soc.* **155**(9), H688 (2008).

[17] G. Silversmit, D. Depla, H. Poelman, G. B. Marin, and R. De Gryse, *J. Electron Spectrosc.* **135**(2-3), 167–175 (2004).

[18] W. Knaepen, C. Detavernier, R. Van Meirhaeghe, J. Jordan Sweet, and C. Lavoie, *Thin Solid Films* **516**(15), 4946–4952 (2008).

Paper III
Crystallization and semiconductor-metal switching behavior of thin VO_2 layers grown by atomic layer deposition *

Abstract

Crystalline vanadium dioxide (VO_2) thin films were prepared by annealing amorphous VO_2 films which were deposited by atomic layer deposition on a SiO_2 substrate. A large influence of the oxygen partial pressure in the annealing ambient was observed by means of in-situ X-ray diffraction. In the range between 1 and 10 Pa of oxygen the interesting VO_2(R) phase crystallized near 450 °C. Between 2 and 10 Pa of oxygen, the metastable VO_2(B) was observed as an intermediate crystalline phase before it transformed to VO_2(R). Anneals in inert gas did not show any crystallization, while oxygen partial pressures above 10 Pa resulted in oxidation into the higher oxide phase V_6O_{13}. Film thickness did not have much effect on the crystallization behavior, but thinner films suffered more from agglomeration during the high-temperature crystallization on the SiO_2 substrate. Nevertheless, continuous polycrystalline VO_2(R) films were obtained with thicknesses down to 11 nm. In the case where VO_2(R) was formed, the semiconductor-metal transition was observed by three complementary techniques. This transition near 68 °C was characterized by X-ray diffraction, showing the transformation of the crystal structure, by spectroscopic ellipsometry, mapping optical changes, and by sheet resistance measurements, showing resistance changes larger than 2 orders of magnitude between the low-temperature semiconducting state and the high-temperature metallic state.

*Published as: G. Rampelberg, D. Deduytsche, B. De Schutter, P. A. Premkumar, M. Toeller, M. Schaekers, K. Martens, I. Radu, and C. Detavernier, *Thin Solid Films*, 550, 59-64 (2014).

Introduction

Vanadium dioxide (VO_2) has been attracting a lot of interest since Morin published his paper about the metal-insulator transition (MIT) in metal-oxides.[1] Below 68 °C it behaves like a semiconductor with a band gap of 0.7 eV,[2] while heating above 68 °C transforms VO_2 in a metallic state. Therefore we refer to it as a semiconductor-metal transition (SMT). The resistivity can change up to 5 orders of magnitude during the transition and also the optical parameters change drastically, affecting transmission and reflection. The electronic transition is accompanied by a structural transition, from monoclinic VO_2(M1) to tetragonal VO_2(R),[3] which implies a local displacement of atoms.

One of the most investigated applications of VO_2 is its use as a thermochromic coating on windows,[4;5] while other possible applications include optoelectronic devices and as a memory or switch element in microelectronics.[6–9] Several deposition techniques were reported for the growth of VO_2 thin films, including reactive sputtering (PVD),[10;11] pulsed laser deposition (PLD),[12] chemical vapor deposition (CVD),[13–16] and sol-gel.[17;18] However, some of these techniques are not useful for application in microelectronics which are highly demanding due to the aggressive scaling of the electronic components dimensions, increasing complexity of structures and the need for uniform deposition over large wafers. Atomic layer deposition (ALD) has proven to fulfill these demands.[19–22] The main difference with other deposition techniques lies in its self-limiting nature, i.e. films are grown layer by layer by dividing the deposition in a series of cycles. In that way films are deposited with high uniformity on large areas and good conformality in high aspect ratios.[23;24] However, in contrast to traditional ALD-grown metal oxides such as Al_2O_3, HfO_2 and TiO_2, ALD of VO_2 is challenging since the vanadium-oxygen system consists of a large variety of phases with different vanadium oxidation states. Apart from the phases with the single oxidation states of +2, +3, +4 and +5 for the vanadium atom, i.e. VO, V_2O_3, VO_2 and V_2O_5 respectively, two series of vanadium oxide phases exist with mixed oxidation states. These are called the Magnéli series with chemical formula V_nO_{2n-1} ($3 \leq n \leq 9$) and the Wadsley series with chemical formula V_nO_{2n+1} ($n = 3, 4, 6$).[25] For V_2O_5, the most stable vanadium oxide in air, several ALD processes have been reported.[26;27] Literature on ALD of VO_2 is scarce. One paper has been published on the use of $VO(acac)_2$ in combination with O_2.[28] Although at the relative high deposition temperatures in the range 400-475 °C crystalline VO_2 was grown, details on ALD characteristics were not reported and only results of 200 nm thick films were discussed. Another result was published on the use of $VOCl_3$ and H_2O, but these experiments did not lead to pure VO_2.[29]

In our recent work we demonstrated ALD of VO_2 on SiO_2 at 150 °C by using tetrakis(ethylmethylamino)vanadium (TEMAV) and ozone.[30] X-ray photoelectron spectroscopy (XPS) confirmed the 4+ oxidation state of vanadium, indicating growth of VO_2. However, all films were amorphous and a post-deposition anneal was indispensable to obtain the interesting monoclinic VO_2(M1) phase which exhibits the semiconductor-metal transition by transforming to tetragonal VO_2(R) above

68 °C. In this work a detailed investigation of the crystallization behavior is reported. It will be shown that a low oxygen partial pressure is necessary to crystallize tetragonal VO_2(R) during annealing. Additionally, a systematic study is reported on the agglomeration of thin VO_2 layers on SiO_2.

Experimental details

ALD of VO_2 was performed in an experimental high-vacuum reactor,[31;32] using TEMAV as metal-organic precursor and ozone as reactant gas.[30] During the deposition, which was carried out at 150 °C substrate temperature, each ALD cycle consisted of a 2 s TEMAV pulse at 10^{-2} Pa partial pressure, with Ar as a carrier gas, 20 s pumping, 5 s O_3 pulse at 50 Pa and 15 s pumping. Films of varying thickness have been grown on thermally oxidized silicon wafers (100 nm SiO_2). Film thicknesses were determined by X-ray reflectivity (XRR) in a Bruker D8 Discover equipped with a copper source (wavelength 0.154 nm). In order to study the crystallization of the ALD grown films, which are amorphous as deposited, annealing processes were performed in an experimental heating chamber, also mounted in a Bruker D8 Discover, dedicated for in-situ X-ray diffraction (XRD).[33;34] Cu Kα radiation was used as an X-ray source, while a linear detector monitored the crystallinity of the thin films. More specifically, the diffraction pattern over a range of 20° in 2θ was captured every 5 seconds during the annealing process, while the temperature was increased at a rate of 0.2 °C/s. Low partial pressures of oxygen were obtained in the heating chamber by adding oxygen into a helium flow using a leak valve, before entering the chamber, while the total pressure in the chamber was slightly above atmospheric pressure. A Rapidox 2100 oxygen sensor from Cambridge Sensotec, calibrated for use in He gas, was used to measure the oxygen partial pressure at the outlet of the chamber. After the tetragonal phase had crystallized, the structural transition was monitored with the same setup. In another heating chamber the change in sheet resistance was measured with a Keithley 2000 multimeter in a 2 probe setup, while the optical transition was monitored simultaneously by means of spectroscopic ellipsometry (Woollam M-2000). In principle, fitting of the ellipsometric data allows for determining both thickness and optical parameters of the material. However, since errors can arise from modeling these thin film properties, only raw data will be reported here to demonstrate the transition.[35] More precisely, the parameter ψ, which covers the amplitude of the complex reflectance ratio will be plotted versus temperature. Although spectroscopic ellipsometry has been used, only the values of ψ at the wavelength of 1000 nm will be shown to simplify plotting.

Results and discussion

Crystallization of VO_2

Figure 1 shows the phase formation of a 15 nm thick film during thermal an-

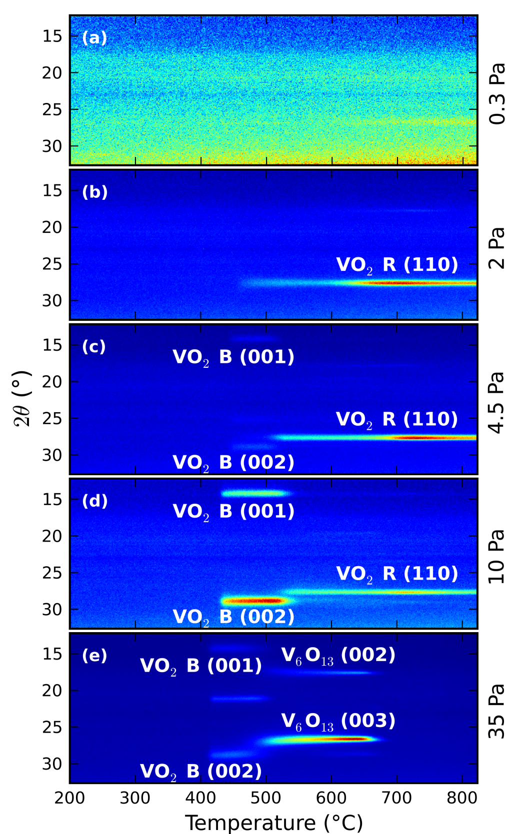

Figure 1. *In-situ XRD of a 15 nm VO_2 ALD film during a ramp anneal with ramp rate 0.2 °C/s in various oxygen partial pressures. The blue color indicates the lowest intensities (i.e. background), red shows the highest intensities (i.e. diffraction peaks).*

nealing in varying oxygen partial pressures at a fixed heating rate of 0.2 °C/s. The plot corresponds to a two-dimensional representation of three variables, with temperature on the x-axis, diffraction angle (2θ values) on the y-axis and the diffracted intensities indicated by a color scale. On all 5 graphs it can be seen that at the start of the annealing process intensities were low, corresponding to amorphous material. From these plots it cannot be concluded that we are dealing with amorphous VO_2. However, as discussed in our previous work, X-ray photo-electron spectroscopy (XPS) confirmed the 4+ oxidation state of the vanadium in these amorphous films, related to VO_2.[30]

During annealing at the lowest obtained oxygen partial pressure, i.e. when no oxygen was intentionally added to the helium (99.996% pure) flow (figure 1(a)), no crystalline phase was observed. At 2 Pa oxygen partial pressure (figure 1(b)) a single diffraction peak appeared slightly above 450 °C near 27.7°, which closely

corresponds to the (110) peak of VO_2(R).[36] For oxygen partial pressures of 4.5 and 10 Pa (figures 1(c,d)) the VO_2(R) phase was also obtained during annealing, however an intermediate phase appeared with two diffraction peaks near 14.4° and 29° respectively. These could be identified as the (001) and (002) planes of VO_2(B), which has been typically observed as a metastable phase in the formation of VO_2(R) during reduction of V_2O_5 below 500 °C.[37;38] Its structure is monoclinic and closely related to that of V_6O_{13}. Finally, at a partial oxygen pressure of 35 Pa (figure 1(e)), the VO_2(B) phase was again the first crystalline phase, but an additional peak near 21° could be observed, which probably can be attributed to V_4O_9.[18] Instead of transforming to VO_2(R), V_6O_{13} was the final phase, with (002) and (003) peaks near 17.8° and 26.8° respectively. Further increase of the temperature to approximately 670 °C lead to melting of this phase, as expected since bulk V_6O_{13} melts near this temperature.[25]

The identification of the VO_2(R) phase for the samples annealed at 2, 4.5 and 10 Pa oxygen partial pressure is confirmed in Figure 2. Figure 2(a) shows an in-situ XRD measurement during heating from 30 °C to 110 °C with a heating rate of 0.2 °C/s of the film annealed to 820 °C in 4.5 Pa of oxygen. A small shift of approximately 0.15° of the diffraction peak is observed near 75 °C. The peak below that temperature is related to the (011) plane of VO_2(M1),[36] while at the higher temperatures the shifted peak indicates the (110) plane of VO_2(R) as was already observed in figure 1(c). Figure 2 (b), (c) and (d) show cross sections of the in-situ XRD plots at the temperatures of 40 and 90 °C, for both the anneals in 2, 4.5 and 10 Pa of oxygen. All three samples show the shift in peak position corresponding to the semiconductor-metal transition.

A plot of the oxygen potential $\mu_{O_2} = RTln(p_{O_2})$ versus temperature is shown in figure 3. Although this graph could be interpreted as an Ellingham diagram,[39] one should be careful doing so. Ellingham diagrams are typically constructed for thermodynamic equilibria, while in this case the reactions are limited by kinetics, as will be discussed further in this section. Nevertheless it is a clear way to visualize the experiments from figure 1 in one single graph. Since the oxygen potential is proportional to the temperature a straight line is followed during each of the anneals presented in figure 1. The slope of such a line is determined by the oxygen partial pressure during the corresponding anneal. On these lines, symbols show at which temperature the observed crystalline phases start to nucleate. It is observed that the temperature for VO_2(B) crystallization increased by lowering the oxygen partial pressure, while it decreased for the crystallization of VO_2(R). Although only 3 data points are available for both phases, a linear trend can be observed. Extrapolation of those 2 lines shows that VO_2(B) will not crystallize anymore below 2 Pa of oxygen. Three interesting regions are being marked on the plot. The first region (C1) indicates where the metastable VO_2(B) phase will be crystallized. To obtain this phase, a minimum oxygen partial pressure of 2 Pa is required, while temperature should be limited within a small window. Higher values of the oxygen partial pressure enlarge the temperature window for this phase as was already clear from figures 1 (c) and (d). The maximum oxygen partial pressure is limited to a few tens of Pa, but a clear border cannot be drawn from this limited set of ex-

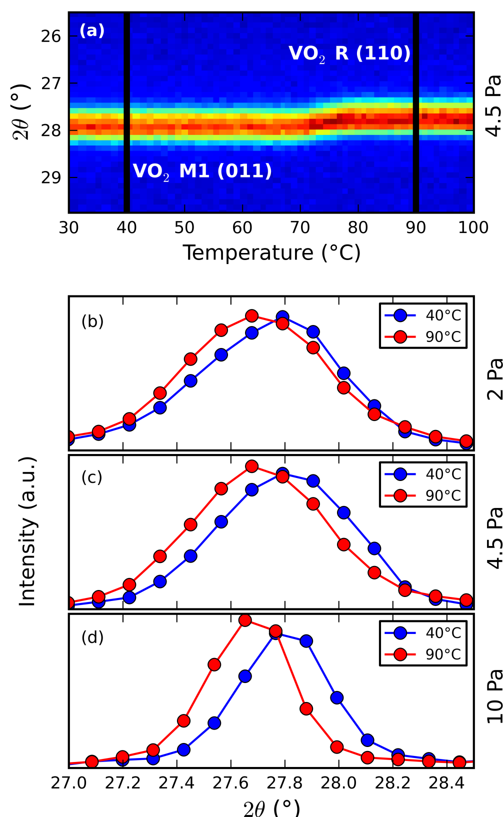

Figure 2. *Observation of the transformation in crystal structure between the low temperature VO_2(M1) phase and high temperature VO_2(R) for a 15 nm VO_2 film annealed up to 820 °C in various oxygen partial pressures. (a) In-situ XRD as a function of temperature for the film annealed in 4.5 Pa oxygen partial pressure indicating a transformation near 75 °C. (b), (c), (d) XRD scans (cross-section of (a)) at 40 and 90 °C for the anneals in 2, 4.5 and 10 Pa oxygen partial pressure.*

periments. When temperature is increased, one ends up in the second region (C2) where crystalline VO_2(R) is obtained. This phase is stable up to at least 820 °C, but again it is not possible to extract the upper boundary of this region in terms of oxygen partial pressure. In the third region (C3) VO_2(R) crystallizes as the first and only phase, i.e. without intermediate formation of metastable VO_2(B). This region is the most favorable, since the crystallization temperature is lower. The lower boundary of this region could also not be extracted from the limited amount of experiments, but at least some addition of oxygen to the He gas is required. A boundary has been drawn at an oxygen partial pressure of 1 Pa, although the real value could be somewhat lower. For the following annealing experiments, 1 Pa

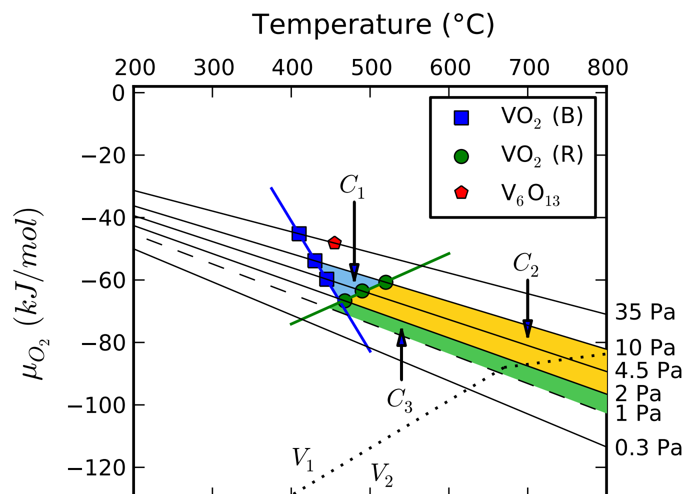

Figure 3. *Oxygen potential $\mu_{O_2} = RTln(p_{O_2})$ as a function of temperature for the ramp anneals from Figure 1. Crystallization temperatures of the VO_2(B), VO_2(R) and V_6O_{13} phases are indicated by markers.*

of oxygen has been chosen as a safe condition which should lead to crystalline VO_2(R).

Our observations on the effect of oxygen partial pressure on the crystallization of the VO_2(R) phase are quite similar to recently published work by Premkumar et al. on an ALD process study of VO_2, also using TEMAV and O_3 as precursor and reactant respectively.[40] Their results of post-ALD annealing of VO_2 on a Si substrate with native oxide show that for oxygen partial pressures between 1.6 and 11 Pa, VO_2(R) could be obtained at 500 °C, while no crystalline phases were observed in pure N_2 and higher oxide phases were observed such as V_6O_{13}, V_3O_7 and V_2O_5 above 30 Pa oxygen partial pressure. Also when Si wafers covered with SiO_2 or crystalline Al_2O_3 were used as substrates, the VO_2(R) phase was obtained under similar annealing conditions.

It is important to mention that although VO_2 is observed, this is not expected from thermodynamics. In figure 3 the regions where bulk V_2O_5 and VO_2 are thermodynamically stable are separated by a dotted line and marked as region (V1) and (V2) respectively. The equilibrium line between those to vanadium oxide phases was calculated by means of the free energy of the reaction $4VO_2 + O_2 \longrightarrow 2V_2O_5$. Thermochemical data were collected from the NIST Chemistry WebBook and Yamaguchi et al.[41;42] Clearly all experimental conditions where nucleation is observed lie in the V_2O_5 region, indicating that kinetics, rather than thermodynamics, are limiting the phase formations in these thin films.

Agglomeration and thickness dependence

Figure 4 (left) shows the in-situ XRD results for 4 samples with varying thickness during annealing in He with 1 Pa oxygen partial pressure. All the films started to crystallize into the VO_2(R) phase near a temperature of 450 °C, even for a film of 5 nm. The 11 nm film is a peculiar case in that sense that a strong increase in peak intensity occurred near 700 °C, indicating grain growth and strong texturing of the (110) plane. However, the VO_2(R) does not seem to be stable since the diffraction peak lost its intensity again above 800 °C. This behavior is not observed for the other thicknesses. In figure 4 (right) scanning electron microscope (SEM) graphs are shown for these 4 samples, after they were quenched. It is clear that the films are morphologically unstable at those high temperatures since strong agglomeration is observed. Instead of a smooth layer, the SiO_2 substrate is covered by VO_2 islands.

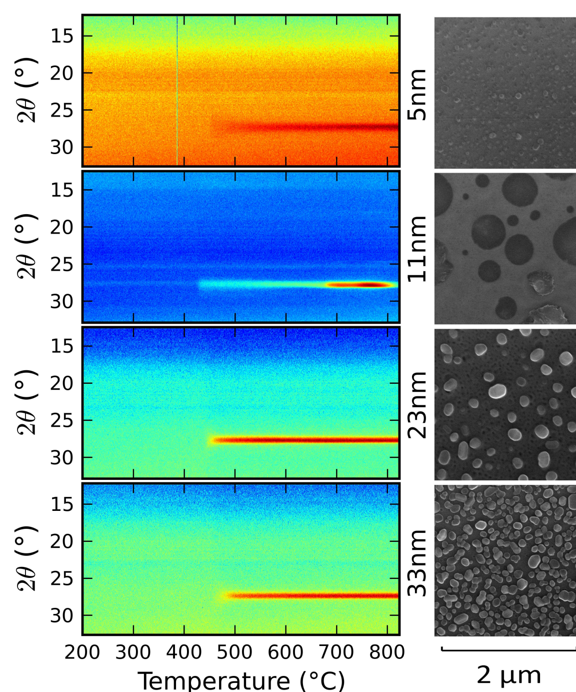

Figure 4. *(Left) In-situ XRD during a ramp anneal (0.2 °C/s) in 1 Pa oxygen partial pressure for 4 different film thicknesses, showing crystallization of the VO_2(R) phase. (Right) Corresponding SEM pictures taken after the quenching of the 4 samples at 820 °C.*

To study the optimum annealing temperatures and the agglomeration on the SiO_2 substrate, isothermal anneals were carried out on the samples with film thicknesses 11, 23 and 33 nm. These anneals were performed in 1 Pa of oxygen partial pressure at temperatures of 450, 500, 550 and 600 °C, each for 30 minutes. Figure

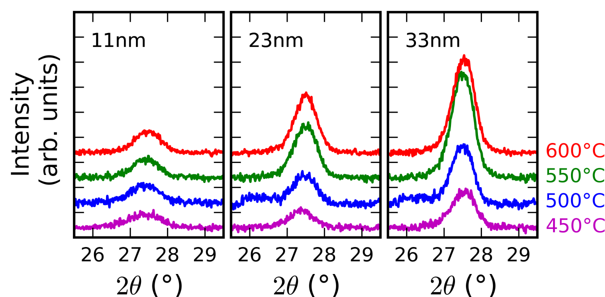

Figure 5. *XRD of samples with initial film thickness of 11, 23 and 33 nm after isothermal annealing for 30 minutes in 1 Pa oxygen partial pressure at 450, 500, 550 and 600 °C. All peaks indicate the presence of the VO_2(M1) phase.*

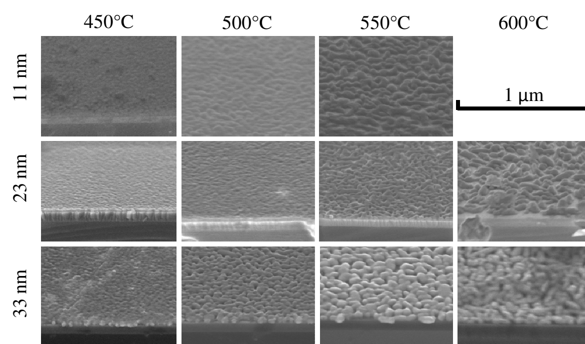

Figure 6. *SEM pictures of the samples with film thickness of 11, 23 and 33 nm after isothermal annealing for 30 minutes in 1 Pa oxygen partial pressure at 450, 500, 550 and 600 °C.*

5 shows the increase of the VO_2(M1) peak as a function of the annealing temperature for the 3 thicknesses. Annealing at 450 °C lead to crystallization of all films, while higher temperatures caused intensification of the diffraction peak, corresponding to an increasing volume fraction of crystals because the width at half height of the diffraction peaks looks unchanged. Figure 6 shows the SEM images for those samples. Especially the thinner samples and the samples annealed to higher temperatures show again the morphological instability. However, at 450 °C all layers are relatively smooth and are at least continuous, as will be confirmed in the next section by sheet resistance measurements. Figure 7 illustrates the effect of film thickness and annealing temperature on the crystallization and agglomeration. As indicated, film thickness does not have much influence on the crystallization temperature, which is around 450 °C, while the onset of agglomeration depends both on film thickness and annealing temperature.

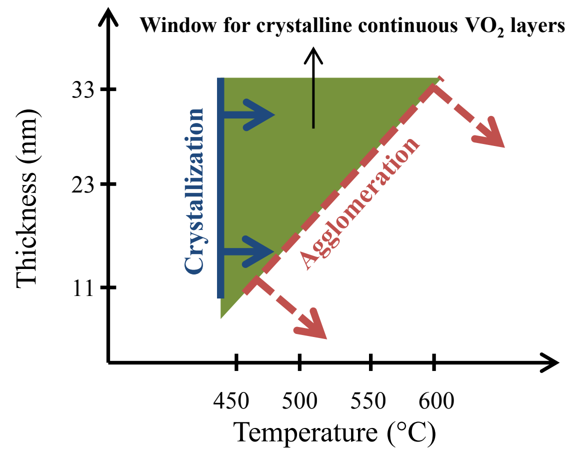

Figure 7. *Process window as a function of film thickness and annealing temperature to obtain continuous crystalline VO_2 layers (green). The blue arrows indicate where crystallization starts, the red (dashed) arrows indicate where agglomeration is observed.*

Characterization of the semiconductor-metal transition

Semiconductor-metal transition measurements were performed on the systematic matrix of samples with varying film thickness (11, 23 and 33 nm), isothermally annealed for 30 minutes at 4 different temperatures (450, 500, 550 and 600 °C) in 1 Pa of oxygen partial pressure. Three different techniques were used to analyze this transition. While XRD and ellipsometry can be used on all samples, 2-probe sheet resistance measurements require continuous films. If a film starts to agglomerate, sheet resistance will increase significantly until finally it cannot be measured any more for separate islands. Figure 8 gives an overview of the SMT characteristics for the samples with thickness of 11, 23 and 33 nm after a 30 minutes anneal at 450 °C in 1 Pa of oxygen.

Figures 8 (a), (b) and (c) show the fitted 2θ values of the XRD peak as a function of temperature during a thermal cycle between 30 and 110 °C with a heating and cooling rate of 0.2 °C/s and a collection time of 5 s. Red symbols are used for heating, while blue symbols show the behavior during cooling. Some smoothing has been applied before plotting to improve the signal-to-noise ratio, by binning over 4 measurements before fitting the peak position. A non-linear least square method was performed to fit a combination of a Gaussian function with a linear background to the measured data. Only for the thinnest film, the intensities were too low to perform a good fit so that the structural transition is difficult to observe. For the samples with film thickness of 23 and 33 nm the structural transition between monoclinic VO_2(M1) and tetragonal VO_2(R) is clearly visible.

Figures 8 (d), (e) and (f) show the optical transition measured by spectroscopic

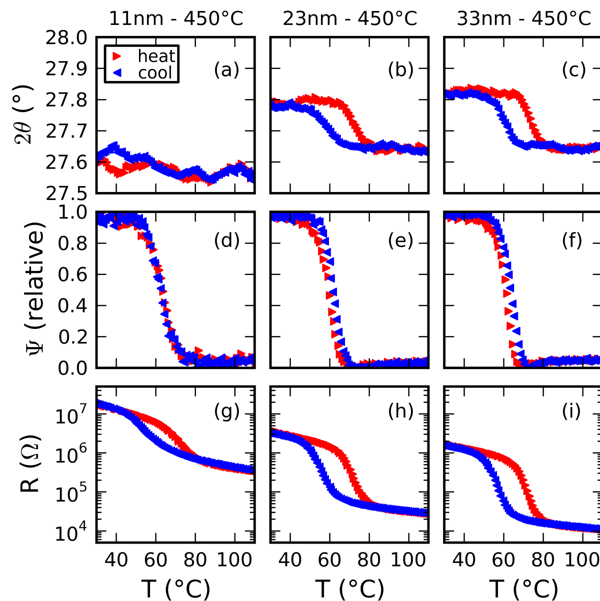

Figure 8. *Observation of the semiconductor-metal transition by thermal cycling between 30 and 110 °C of samples with varying thickness which were annealed for 30 minutes at 450 °C in 1 Pa oxygen partial pressure. The first row shows the change in diffracted peak position as fitted from in-situ XRD measurements, indicating a transformation between the low temperature monoclinic phase and the high temperature tetragonal phase. The second row shows the optical changes observed by ellipsometry at a wavelength of 1000 nm. The third row shows the change in sheet resistance between the semiconducting and metallic state at low and high temperature respectively.*

ellipsometry. The same thermal cycle had been performed with a measurement each 5 s (i.e. each 1 °C). The raw ψ data at a wavelength of 1000 nm is first normalized between its minimum and maximum value and then plotted against temperature. This technique shows for all three samples a clear optical transition. Compared to XRD, which needed some smoothing and peak fitting before plotting, the noise level for the ellipsometry data is very low due to its high sensitivity. Therefore, ellipsometry serves as a helpful tool to observe the semiconductor-metal transition. One peculiar observation is a reduction of the hysteresis width for ellipsometry. No suitable explanation is immediately apparent, but one possible explanation is the important role of the interface between the SiO_2 substrate and the VO_2 layer in ellipsometry. In the case of XRD the bulk needs to transform to observe a transition. Further investigation is required to get a better understanding of this observation.

Finally, figures 8 (g), (h) and (i) show the sheet resistance measurements during the same thermal cycle. In this case there is again a hysteresis of which the width corresponds with the hysteresis observed by XRD. Since these measurements were

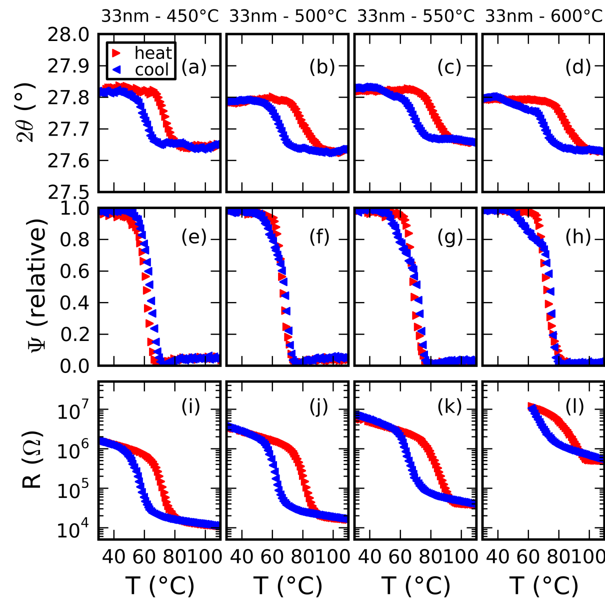

Figure 9. *Observation of the semiconductor-metal transition by thermal cycling between 30 and 110 °C of samples of 33 nm thickness which were annealed for 30 minutes in 1 Pa oxygen partial pressure at various temperatures.*

performed simultaneously with the ellipsometry measurements, it can be excluded that the strange behavior observed by ellipsometry is related to a poor temperature calibration. For all samples a change in sheet resistance of approximately two orders of magnitude is observed and indicates that at an annealing temperature of 450 °C all films were still continuous. Similar results are summarized in figure 9 for the film of 33 nm annealed for 30 minutes at 4 different temperatures in the range 450-600 °C. Again the SMT is observed by all three techniques. The sheet resistance gradually increased for higher annealing temperatures, but only for 600 °C the measured curve is influenced by agglomeration. Figure 10 summarizes the sheet resistance measurements on the whole sample matrix. The top of each bar represents the highly resistive, semiconducting state at low temperature (40 °C), while the bottom of such a bar indicates the low resistive, metallic state at high temperature (90 °C). Only measurements are shown of which the sheet resistance was within the measuring range of the multimeter. It is clear that thinner films and higher annealing temperatures result in severe agglomeration, as was already discussed in the previous section and illustrated in figure 7. Nevertheless, at 450 °C all films stayed continuous and a general change in resistance of roughly two orders of magnitude is observed.

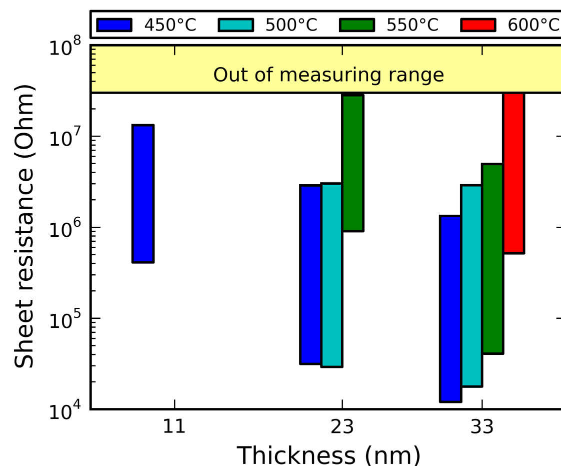

Figure 10. *Sheet resistance of samples with varying thickness which were annealed to various temperatures. The top of each bar represents the sheet resistance at 30 °C (i.e. the semiconducting state), the bottom indicates the sheet resistance at 100 °C (i.e. the metallic state).*

Conclusions

Crystallization of amorphous VO_2 films which are deposited by ALD is very sensitive to the oxygen partial pressure of the annealing ambient. An inert atmosphere does not lead to crystalline films. Addition of a low oxygen partial pressure in the range between 1 and 10 Pa is indispensable to form the desired VO_2(R) phase. The lowest crystallization temperature of 450 °C was observed at 1 Pa oxygen partial pressure. However, above 2 Pa metastable VO_2(B) appeared as an intermediate phase and the subsequent formation of VO_2(R) required slightly higher annealing temperatures. At an oxygen partial pressure of 35 Pa VO_2(B) transformed into V_6O_{13} instead of VO_2(R). The VO_2 films agglomerated easily on the SiO_2 substrate. However, at 450 °C it is possible to obtain continuous crystalline VO_2 layers, even for films as thin as 11 nm. The semiconductor-metal transition was characterized by three complementary techniques. In-situ XRD served as a tool to observe the structural transition between the low-temperature monoclinic phase (M1) and the high-temperature tetragonal phase (R). The correlated electronic transition has been investigated by means of optical and electrical measurements. In-situ spectroscopic ellipsometry has proven to be a suitable technique to monitor the optical changes during the SMT. However, a decreased hysteresis width was observed, which needs further investigation. As a third technique, sheet resistance measurements were performed and indicated a typical 2 order of magnitude change in sheet resistance between the low-temperature semiconducting and the high-temperature metallic state.

Acknowledgments

The research leading to these results has received funding from the European Research Council under the European Union's Seventh Framework Programme (FP7/2007-2013) / ERC grant agreement n° 239865.

References

[1] F. J. Morin, *Phys. Rev. Lett.* **3**(1), 34–36 (1959).
[2] S. Shin, S. Suga, M. Taniguchi, M. Fujisawa, H. Kanzaki, A. Fujimori, H. Daimon, Y. Ueda, K. Kosuge, and S. Kachi, *Phys. Rev. B* **41**(8), 4993 (1990).
[3] A. Zylbersztejn and N. F. Mott, *Phys. Rev. B* **11**(11), 4383–4395 (1975).
[4] T. D. Manning, I. P. Parkin, R. J. H. Clark, D. Sheel, M. E. Pemble, and D. Vernadou, *J. Mater. Chem.* **12**(10), 2936–2939 (2002).
[5] I. P. Parkin and T. D. Manning, *J. Chem. Educ.* **83**(3), 393 (2006).
[6] C. E. Lee, R. A. Atkins, W. N. Gibler, and H. F. Taylor, *Appl. Opt* **28**(21), 4511–4512 (1989).
[7] M. Soltani, M. Chaker, E. Haddad, R. V. Kruzelecky, and D. Nikanpour, *J. Vac. Sci. Technol. A* **22**(3), 859 (2004).
[8] M.-J. Lee, Y. Park, D.-S. Suh, E.-H. Lee, S. Seo, D.-C. Kim, R. Jung, B.-S. Kang, S.-E. Ahn, C. B. Lee, D. H. Seo, Y.-K. Cha, I.-K. Yoo, J.-S. Kim, and B. H. Park, *Adv. Mater.* **19**(22), 3919–3923 (2007).
[9] H.-T. Kim, B.-G. Chae, D.-H. Youn, S.-L. Maeng, G. Kim, K.-Y. Kang, and Y.-S. Lim, *New J. Phys.* **6**, 52 (2004).
[10] D. Brassard, S. Fourmaux, M. Jean-Jacques, J. C. Kieffer, and M. A. El Khakani, *Appl. Phys. Lett.* **87**(5), 051910 (2005).
[11] S. J. Yun, J. W. Lim, J.-S. Noh, B.-G. Chae, and H.-T. Kim, *Jpn. J. Appl. Phys.* **47**(4S), 3067 (2008).
[12] K. Nagashima, T. Yanagida, H. Tanaka, and T. Kawai, *J. Appl. Phys.* **100**(6), 063714 (2006).
[13] M. B. Sahana, M. S. Dharmaprakash, and S. A. Shivashankar, *J. Mater. Chem.* **12**(2), 333–338 (2002).
[14] M. B. Sahana, G. N. Subbanna, and S. A. Shivashankar, *J. Appl. Phys.* **92**(11), 6495 (2002).
[15] D. Vernardou, M. Pemble, and D. Sheel, *Thin Solid Films* **516**(14), 4502–4507 (2008).
[16] C. Piccirillo, R. Binions, and I. P. Parkin, *Chem. Vapor Depos.* **13**(4), 145–151 (2007).
[17] T. J. Hanlon, R. E. Walker, J. A. Coath, and M. A. Richardson, *Thin Solid Films* **405**, 234–237 (2002).
[18] Y. Ningyi, L. Jinhua, and L. Chenglu, *Appl. Surf. Sci* **191**(1), 176–180 (2002).
[19] T. Suntola, *Mater. Sci. Rep.* **4**(5), 261–312 (1989).
[20] R. L. Puurunen, *J. Appl. Phys.* **97**(12), 121301 (2005).
[21] S. M. George, *Chem. Rev.* **110**(1), 111–131 (2010).
[22] N. Pinna and M. Knez, *Atomic layer deposition of nanostructured materials*, John Wiley & Sons, (2012).
[23] J. Dendooven, D. Deduytsche, J. Musschoot, R. L. Vanmeirhaeghe, and C. Detavernier, *J. Electrochem. Soc.* **156**(4), P63 (2009).
[24] J. Dendooven, D. Deduytsche, J. Musschoot, R. L. Vanmeirhaeghe, and C. Detavernier, *J. Electrochem. Soc.* **157**(4), G111 (2010).
[25] H. A. Wriedt, *Bulletin of Alloy Phase Diagrams* **10**(3), 271–277 (1989).

[26] J. Musschoot, D. Deduytsche, H. Poelman, J. Haemers, R. L. Van Meirhaeghe, S. Van den Berghe, and C. Detavernier, *J. Electrochem. Soc.* **156**(7), P122 (2009).

[27] J. C. Badot, A. Mantoux, N. Baffier, O. Dubrunfaut, and D. Lincot, *J. Mater. Chem.* **14**(23), 3411 (2004).

[28] P. Dagur, A. U. Mane, and S. Shivashankar, *J. Cryst. Growth* **275**(1-2), e1223–e1228 (2005).

[29] I. M. Povey, M. Bardosova, F. Chalvet, M. E. Pemble, and H. M. Yates, *Surf. Coat. Tech.* **201**(22-23), 9345–9348 (2007).

[30] G. Rampelberg, M. Schaekers, K. Martens, Q. Xie, D. Deduytsche, B. De Schutter, N. Blasco, J. Kittl, and C. Detavernier, *Appl. Phys. Lett.* **98**(16), 162902 (2011).

[31] Q. Xie, Y.-L. Jiang, C. Detavernier, D. Deduytsche, R. L. Van Meirhaeghe, G.-P. Ru, B.-Z. Li, and X.-P. Qu, *J. Appl. Phys.* **102**(8), 083521 (2007).

[32] Q. Xie, J. Musschoot, D. Deduytsche, R. L. Van Meirhaeghe, C. Detavernier, S. Van den Berghe, Y.-L. Jiang, G.-P. Ru, B.-Z. Li, and X.-P. Qu, *J. Electrochem. Soc.* **155**(9), H688 (2008).

[33] W. Knaepen, C. Detavernier, R. Van Meirhaeghe, J. Jordan Sweet, and C. Lavoie, *Thin Solid Films* **516**(15), 4946–4952 (2008).

[34] W. Knaepen, S. Gaudet, C. Detavernier, R. L. Van Meirhaeghe, J. J. Sweet, and C. Lavoie, *J. Appl. Phys.* **105**(8), 083532 (2009).

[35] A. Dejneka, I. Aulika, V. Trepakov, J. Krepelka, L. Jastrabik, Z. Hubicka, and A. Lynnyk, *Opt. Express* **17**(16), 14322 (2009).

[36] K. D. Rogers, *Powder Diffr.* **8**, 240 (1993).

[37] F. Théobald, R. Cabala, and J. Bernard, *J. Solid State Chem.* **17**, 431–438 (1976).

[38] C. Leroux, G. Nihoul, and G. Van Tendeloo, *Phys. Rev. B* **57**(9), 5111 (1998).

[39] H. J. T. Ellingham, *J. Soc. Chem. Ind.* **63**, 125 (1944).

[40] P. A. Premkumar, M. Toeller, I. P. Radu, C. Adelmann, M. Schaekers, J. Meersschaut, T. Conard, and S. Van Elshocht, *ECS J. Solid State Sci. Technol.* **1**(4), P169–P174 (2012).

[41] P. J. Linstrom and W. G. Mallard, http://webbook.nist.gov, Retrieved: 2013-03-25.

[42] J. Qi, G. Ning, and Y. Lin, *Mater. Res. Bull.* **43**(8-9), 2300–2307 (2008).

Paper III - corrigendum
Crystallization and semiconductor-metal switching behavior of thin VO_2 layers grown by atomic layer deposition *

In the original version of the article, a peculiar behavior was observed in figures 8 and 9. More precisely, the hysteresis width as observed by temperature-dependent ellipsometry seemed to be very small, or in some cases even slightly negative. After careful analysis of the data, a synchronization error has been found, leading to a mismatch in temperature. The data has been corrected and the original figures 8 and 9 are here updated as figures 1 and 2.

*Published as: G. Rampelberg, D. Deduytsche, B. De Schutter, P. A. Premkumar, M. Toeller, M. Schaekers, K. Martens, I. Radu, and C. Detavernier, *Thin Solid Films*, 550, 59-64 (2014).

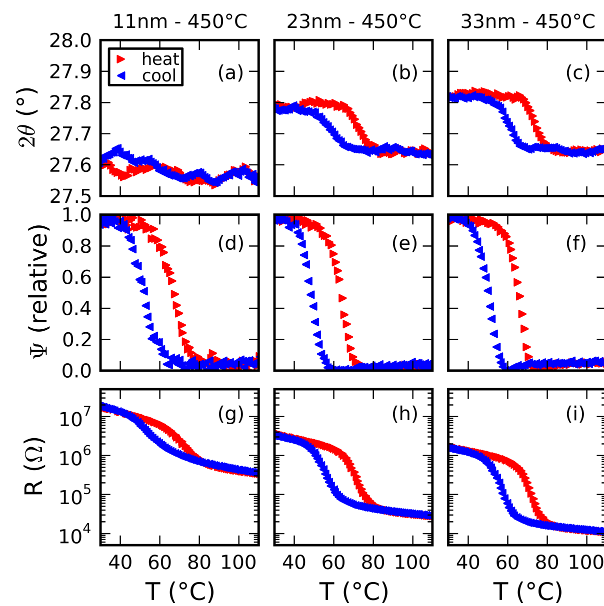

Figure 1. *Observation of the semiconductor-metal transition by thermal cycling between 30 and 110 °C of samples with varying thickness which were annealed for 30 minutes at 450 °C in 1 Pa oxygen partial pressure. The first row shows the change in diffracted peak position as fitted from in-situ XRD measurements, indicating a transformation between the low temperature monoclinic phase and the high temperature tetragonal phase. The second row shows the optical changes observed by ellipsometry at a wavelength of 1000 nm. The third row shows the change in sheet resistance between the semiconducting and metallic state at low and high temperature respectively.*

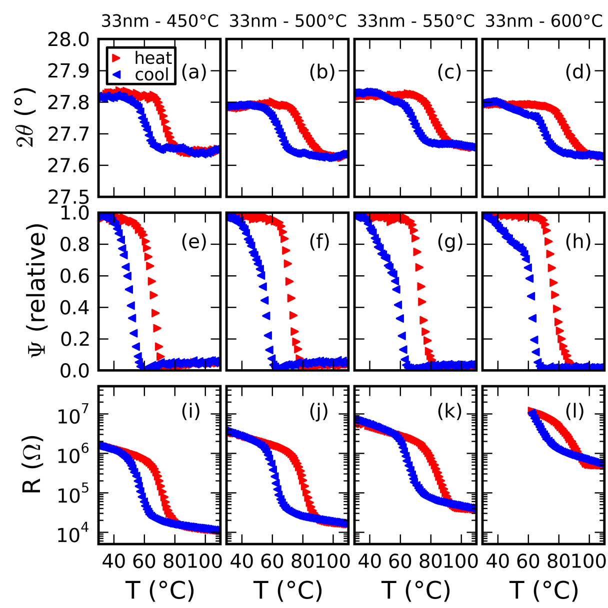

Figure 2. *Observation of the semiconductor-metal transition by thermal cycling between 30 and 110 °C of samples of 33 nm thickness which were annealed for 30 minutes in 1 Pa oxygen partial pressure at various temperatures.*

Paper IV
Vanadium oxide thin films and nanoparticles prepared by atomic layer deposition and controlled post-deposition annealing *

Abstract

Atomic layer deposition of vanadium oxides from tetrakis(ethylmethylamino)-vanadium as metal-organic precursor was studied, with a comparison between H_2O, O_3 and O_2 plasma as reactants. Depending on the deposition conditions, amorphous VO_2 or crystalline V_2O_5 were grown. The amorphous films slowly oxidize when exposed to air, leading to a parabolic increase of film thickness over time and a gradual transformation from a V^{4+} to a V^{5+} valence. The crystalline phase formation, as well as the oxidation and reduction of these amorphous VO_2 and crystalline V_2O_5 films upon annealing in various O_2 partial pressures was studied by means of *in-situ* X-ray diffraction. Depending on the reactant used during deposition and gas conditions used during annealing, single phase VO_2(R), VO_2(B), V_6O_{13} and V_2O_5 were obtained. The tetragonal VO_2(R) films showed a reversible semiconductor-metal transition to monoclinic VO_2(M1) during cooling below 68 °C, often referred to as a metal-insulator transition. Accompanied with this structural transition, changes in sheet resistance of more than three orders of magnitude were observed in films with a thickness from 10 to 30 nm. In addition, VO_2 nanoparticles were synthesized by agglomeration of thinner films upon crystallization. These nanoparticles showed an optical semiconductor-metal transition with a hysteresis as large as 50 °C.

*__To be published:__ G. Rampelberg, B. De Schutter, W. Devulder, M. Schaekers, K. Martens, C. Dussarrat, and C. Detavernier, ***JOURNAL*****, VOL, PAGES (YEAR).**

Introduction

The vanadium-oxygen system consists of an intriguing series of solid phases with a wide variation in properties and applications. Five main vanadium valence states exist, from 0 up to +5, related to the phases V, VO, V_2O_3, VO_2 and V_2O_5. In addition two series connect V_2O_3 with VO_2 and VO_2 with V_2O_5, i.e. the Magnéli and Wadsley phases respectively, with chemical formulas of the form V_nO_{2n-1} and V_nO_{2n+1}.[1–3]

Characteristic for most phases in the Magnéli series is a semiconductor-metal transition (SMT), more often called a metal-insulator transition (MIT).[4;5] Amongst them, vanadium dioxide (VO_2) has attracted most interest from technological point of view. Near 68 °C a reversible structural transition occurs from low temperature monoclinic VO_2(M1) to high temperature tetragonal VO_2(R).[6] This structural transition is accompanied with an electronic transition resulting in a drastic change in optical properties and a drop in resistivity of up to 5 orders of magnitude. Due to the reduced infrared transmittance above the transition temperature, VO_2 is considered as a coating material for thermochromic windows, which may play an important role in the energy efficiency of buildings.[7;8] For this purpose, reduction of the transition temperature down to 25 °C has been achieved by doping the VO_2 thin film with elements like tungsten. In optoelectronics and microelectronics, VO_2 has been considered for the fabrication of ultrafast switches, selectors and memory cells.[9–16]

Other applications of vanadium oxides are found for instance in energy and catalysis. VO_2(B), a metastable polymorph of VO_2(M1/R), as well as V_2O_5 and the Wadsley vanadium oxide phases have been studied for their use as cathode materials for Li-ion batteries.[17] V_2O_5 is furthermore often reported for its high catalytic activity.[18–20]

Due to the complexity of the vanadium-oxygen system, apart from V_2O_5, the synthesis of VO_2 and other vanadium oxide thin films is challenging. Many techniques proved successful, including sol-gel,[21] pulsed laser deposition (PLD),[22] reactive sputtering (PVD)[23–25] and chemical vapor deposition (CVD).[26–28] Alternative methods exist, e.g. controlled oxidation of vanadium or reduction of V_2O_5 thin films.[13;29? ;30]

Industrial processes rely on scalable, highly reproducible depositions with a high degree of uniformity on large area substrates, limiting the applicability of some of these techniques. Furthermore, downscaling of feature sizes in microelectronics and the requirement of conformally coating 3-dimensional structures raised the interest for atomic layer deposition (ALD) as key enabling technology.[31–36] ALD of vanadium oxides has been reported several times. Vanadium oxytriisopropoxide ($VO(O^iPr)_3$) is the most widely used precursor, resulting in the deposition of V_2O_5, which might be related to the transfer of the +5 oxidation state of the vanadium atom within the precursor molecule to the growing film.[18;37] Also $VO(thd)_2$ has been reported for the growth of V_2O_5.[19] For the deposition of VO_2, V^{4+} precursors have been used, including $VO(acac)_2$, $VOCl_3$ and $VO(O^nPr)_3$.[38–40] However, details on ALD characteristics were not reported, and high deposition

temperatures were used, typically above 400 °C. More recently several reports appeared in which tetrakis(ethylmethylamino)vanadium (TEMAV) was used as V^{4+} precursor for the ALD growth of VO_2. Both H_2O and O_3 have been used as oxygen sources to obtain amorphous vanadium oxide thin films.[41–46]

In this work, we compared three oxygen sources, i.e. H_2O, O_3 and O_2 plasma, for the ALD growth of both VO_2 and V_2O_5 thin films from the TEMAV precursor. Upon post-deposition annealing, pure crystalline VO_2(M1/R), VO_2(B), V_6O_{13} and V_2O_5 were obtained, depending on the reactant used during growth and the post-deposition annealing conditions. VO_2(M1/R) films showed up to three orders of magnitude change in resistivity across the semiconductor-metal transition. In addition to VO_2 thin films, nanoparticles were synthesized by annealing the thinnest films at high temperatures. These nanoparticles were characterized by a metal-insulator transition with an extended hysteresis width up to 50 °C.

Experimental details

Vanadium oxide depositions were carried out in an experimental high-vacuum ALD reactor with a base pressure below 1×10^{-4} Pa.[47;48] Tetrakis(ethylmethylamino)vanadium, denoted as TEMAV, was used as metal-organic precursor. The precursor was stored in a stainless steel bottle at a temperature of 70 °C. During a TEMAV pulse, the partial pressure of TEMAV in the reactor was at least 1×10^{-2} Pa, while Ar was used as carrier gas. For this ALD study, H_2O, O_3 and O_2 plasma were used as reactants. H_2O was stored in a glass bottle at room temperature, with the partial pressure adjusted to 3×10^{-1} Pa during exposure. O_3 was generated from pure O_2 using an OzoneLab OL100 ozone generator, delivering concentrations up to 175 μg/ml. Ozone pulses were carried out in static exposure mode, at a pressure of 50 Pa. A remote inductively coupled plasma (ICP) source was used to generate the O_2 plasma. The pressure was adjusted to 5×10^{-1} Pa, and the plasma power was set to 300 W. As a substrate, thermally oxidized Si wafers were used during this study, with a SiO_2 thickness of 100 nm.

After deposition, the film thickness was measured by X-ray reflectivity (XRR). These measurements were carried out in a Bruker D8 Discover, equipped with a Cu source. By means of X-ray fluorescence (XRF), the amount of deposited V atoms in the film was characterized. A Mo source and energy-dispersive detector served for this purpose. Quantitative analysis was enabled by a calibration with Rutherford backscattering spectroscopy (RBS), allowing to correlate the XRF peak area with the V areal density. X-ray photoelectron spectroscopy (XPS) was used to analyze the V valence, and thus to distinguish between VO_2 and V_2O_5. X-ray diffraction (XRD) measurements were performed in a similar Bruker D8 Discover XRD system as used for XRR, equipped with a linear detector. $\theta - 2\theta$ measurements were performed in a 2θ range from 12 ° to 60 °.

Crystallization studies were carried out by means of *in-situ* X-ray diffraction (XRD).[49] For this purpose, an experimental annealing chamber was installed in the XRD system. By making use of a linear detector, source and detector could be kept

at fixed positions, while collecting snapshots of the diffracted X-rays every few seconds. The 2θ window was limited to approximately 20 °. This configuration can be used very efficiently for polycrystalline materials or powder samples.[50;51] The annealing chamber can operate under both inert, reducing and oxidizing ambient at a total absolute pressure slightly above atmospheric pressure. The system was first pumped down to a pressure below 5 Pa, was then filled with the desired gas after which the flow of gas was set to a constant value around 1 standard liter per minute. Helium was mixed with diluted O_2 (3%) by means of mass flow controllers, allowing O_2 partial pressures as low as 2 Pa. The temperature of the sample could be varied between room temperature and 1000 °C. Temperature was measured using a K-type thermocouple and calibrated using Au-Si, Al-Si and Ag-Si eutectic systems. Ramp anneals were carried out from room temperature up to 750 °C at a heating rate of 0.25 °C/s, while during isothermal anneals a fixed heating rate of 5 °C/s was applied from room temperature up to the desired setpoint temperature.

The semiconductor-metal transition was characterized by means of thermal cycling experiments between room temperature and 110 °C. Sheet resistance measurements were performed using a Keithley 2601A source measure unit in combination with 4 probes in a square configuration. *In-situ* spectroscopic ellipsometry revealed the optical transition, as described in our earlier work.[44] Due to its high sensitivity, this technique is highly suitable for probing very thin films. In contrast to sheet resistance measurements, it does not require continuous film. Agglomerated films and nanoparticles can be measured as well.

In addition, atomic force microscopy (AFM) was carried out on the crystallized films for characterization of the morphology and to determine nanoparticle sizes.

Results and discussion

ALD growth characteristics

The self-terminating surface reactions during ALD allow for deposition of the same amount of material each cycle. It is often observed that the growth per cycle varies with the deposition temperature, although this temperature effect is rather low. Figure 1 shows the growth rate, in Å per cycle, as a function of deposition temperature for H_2O, O_3 and O_2 plasma. A slight increase in growth rate with temperature is observed for all three reactants up to 150 °C. From 175 °C on, the increase is more pronounced. However, Figure 1 also shows deposition at 175 °C and higher, even if no reactant is used. This means the TEMAV precursor starts to decompose at temperatures of 175 °C and higher. No decomposition is observed at temperatures of 150 °C or lower. Therefore, 150 °C is the highest possible temperature for performing ALD. At all temperatures, the plasma enhanced process with O_2 shows the highest growth rate. The growth rate varies from about 0.5 to 0.8 Å/cycle for the O_3 and H_2O processes, up to 1.5 Å/cycle for the plasma process.

Figure 2 summarizes the saturation behavior of the three ALD processes at

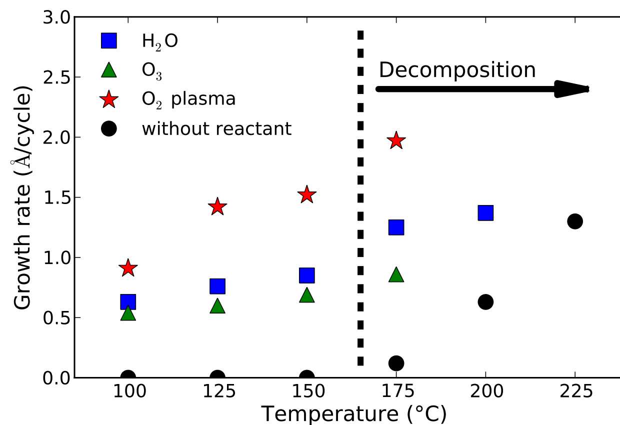

Figure 1. *Growth rate as a function of deposition temperature for different reactants.*

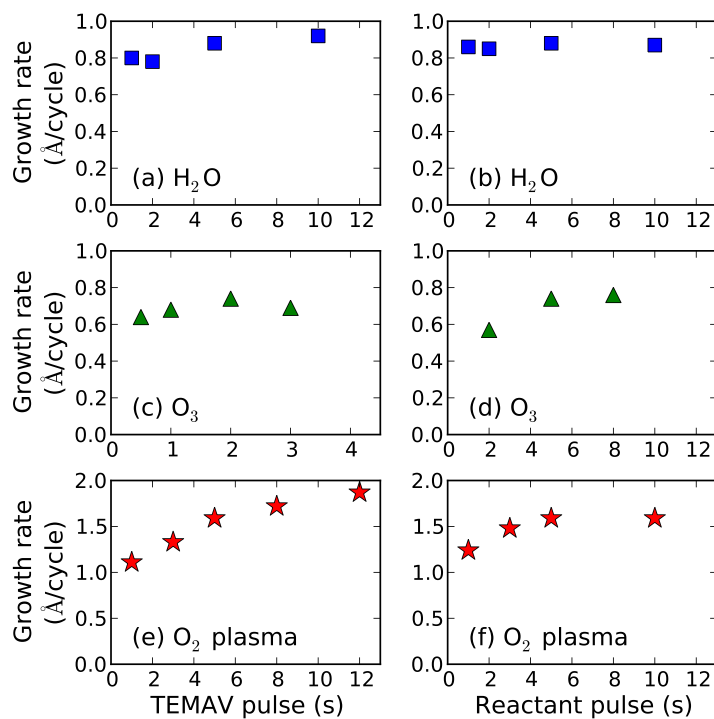

Figure 2. *Saturation of the TEMAV (left) and reactant exposures (right) for the three ALD processes at 150 °C deposition temperature.*

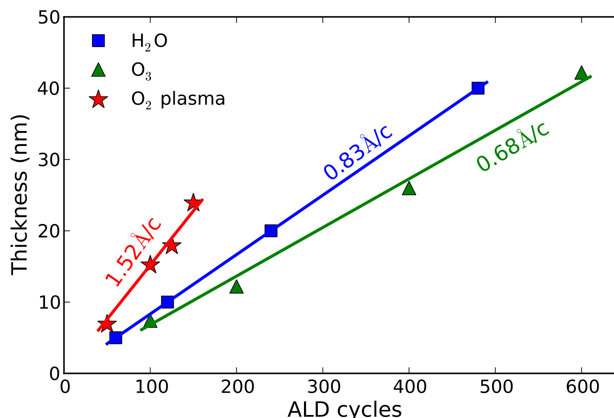

Figure 3. *Thickness as a function of the number of ALD cycles for the three ALD processes.*

a deposition temperature of 150 °C. The left column shows the growth rate as a function of TEMAV pulse time for fixed reactant exposure times, whereas the second column shows the growth rate for a fixed TEMAV pulse and varying reactant pulse times. For the H_2O process, the observed growth rate at 150 °C corresponds well with the reported values of Blanquart et al.[43] The growth rate for the O_3 based process is however almost doubled compared to their values. On the other hand, Premkumar et al. reported much higher deposition rates for the O_3 process, up to a few Angstrom per cycle, which was explained by the use of high feeding rates of TEMAV through liquid injection.[42]

The thickness increase as a function of the number of ALD cycles is plotted in Figure 3. Again, results are shown for the three processes at 150 °C deposition temperature. All three processes show a linear growth, and growth rates of 0.83, 0.68 and 1.52 Å/cycle are extracted for the H_2O, O_3 and O_2 plasma process respectively, in agreement with the results shown in Figures 1 and 2.

As deposited ALD layers: properties and stability

Apart from the film thickness, the V density was determined as well by combining XRR and XRF measurements. In order to get quantitative data, the peak intensities measured by XRF were calibrated for one sample by means of an RBS measurement. Figure 4 shows the as deposited V molar density, expressed in mole/cm^3, for the three ALD processes and for varying deposition temperatures. The horizontal dotted lines indicate the reported densities for the crystalline phases VO_2(M1), VO_2(B) and orthorhombic V_2O_5. From the graph it is first of all clear that the H_2O process results in the highest V density. The fact that the density lies in between these of the high density VO_2(M1) phase and the lower density VO_2(B) phase, is a first indication that the deposited layer is VO_2. The density of the films deposited by the O_3 process are characterized by a lower V density. However, the data do

not allow for determination of the vanadium oxide phase. Either low density VO_2 is deposited, or the film consists of a mixed V^{4+} and V^{5+} valence. In case of the films deposited by the O_2 plasma process, the V density is close to the reported value of orthorhombic V_2O_5.

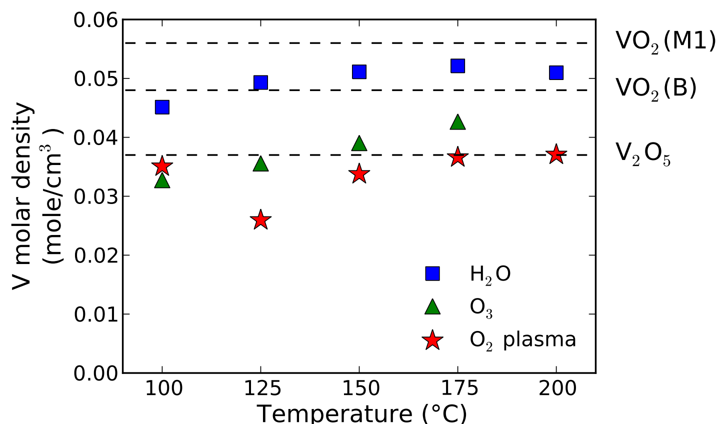

Figure 4. *As deposited molar V density as a function of deposition temperature for the three ALD processes. The densities of crystalline VO_2(M1), VO_2(B) and V_2O_5 are indicated by the horizontal lines.*

Figure 5 shows five XPS measurements. As explained by Silversmit et al.,[52] the difference in binding energy between the O1s level and the V2p levels is a direct indication for the V valence. Following the procedure of these authors, the O1s level was used as a reference at 530.0 eV, while for the $V2p_{3/2}$ peak, the binding energy levels corresponding to the V^{5+} and V^{4+} valences are indicated by the red and blue vertical lines. The top three measurements were performed on H_2O, O_3 and O_2 plasma processed films, shortly after the deposition. Whereas the H_2O and O_3 process show a V^{4+} valence, corresponding to VO_2, the O_2 plasma process results in V^{5+}, i.e. V_2O_5.

Two additional XPS measurements are plotted. These correspond to films deposited by the H_2O process, but exposed to air for approximately two weeks and one year respectively. For these samples the $V2p_{3/2}$ has shifted from a V^{4+} to a V^{5+} valence, indicating oxidation due to air exposure. After two weeks, a mixed valence still exists, but after one year pure V^{5+} is observed. Similar observations were made for the films grown by the O_3 process. We thus can conclude that aging takes place in VO_2 films and that interpretation of XPS measurements is only valid when the air exposure time of such samples is limited to a minimum. Our findings also explain the mixed V^{4+}/V^{5+} valences observed by other researchers.[43;46]

Furthermore, the aging effect in these amorphous films was characterized by XRR measurement of the thickness as a function of the air exposure time. These results are shown in Figure 6. A parabolic increase of the film thickness was observed, as visualized by the indicative lines drawn in the plot. Such behavior is

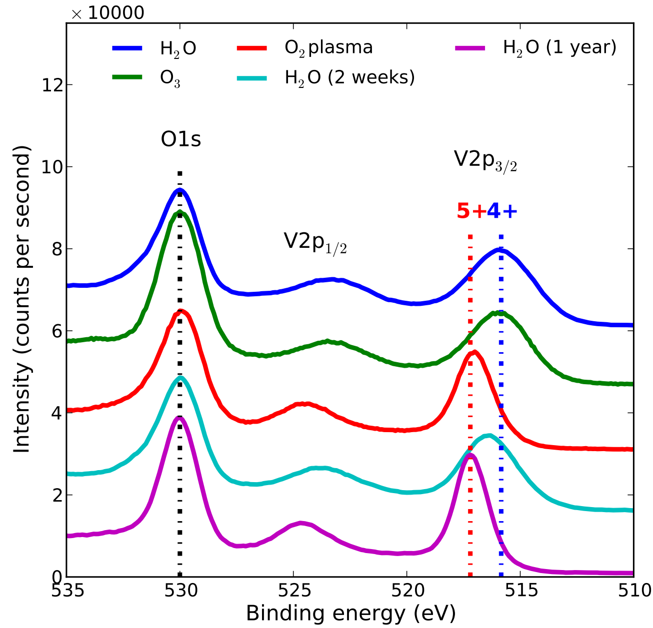

Figure 5. *XPS measurements on vanadium oxide layers deposited by the three ALD processes, shortly after deposition, as well as films grown with H_2O, but exposed to air for two weeks and one year.*

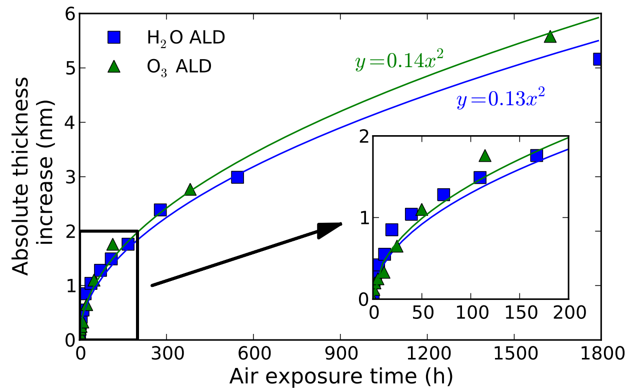

Figure 6. *Absolute thickness increase, measured by XRR, of the ALD films grown with the H_2O and O_3 process as a function of exposure time to air. The lines are drawn as an indication for parabolic growth. The initial film thickness was 10 nm.*

often observed during oxidation processes. According to Deal and Grove, this

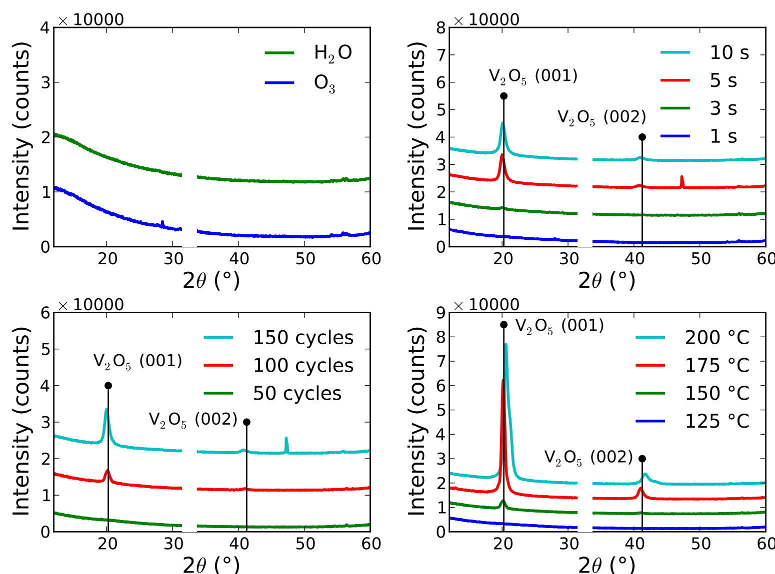

Figure 7. *XRD spectra for the as deposited ALD films: (a) H_2O and O_3 process, (b)-(c)-(d) O_2 plasma process for varying plasma exposure, amount of ALD cycles and deposition temperature. For clarity the different spectra were shifted vertically and the Si(100) substrate peak near 33 ° was removed.*

parabolic behavior can be explained by the limited diffusion of oxygen (or water) in the growing oxide layer.[53] We found that the absolute increase in thickness is independent of the initial film thickness and the deposition temperature, and similar rates of oxidation were observed for the H_2O and O_3 processes. After one day of air exposure the thickness increase is between 0.5 and 1 nm, while after one week it is almost 2 nm (see inset of Figure 6). Considering the limited information depth of XPS, which is on the order of a few nanometers, a mixed V valence will be observed even after a few hours due to surface oxidation. On the other hand, Premkumar et al. used hard X-ray photoelectron spectroscopy (HAXPES), which has a considerable larger information depth compared to conventional XPS, typically on the order of 10 nm. These authors observed a V^{4+} for the H_2O processed films, which can be explained by the limited impact of the surface oxidation on the HAXPES measurement.[45]

Figure 7 shows XRD measurements performed on the as deposited films. The H_2O and O_3 processes result in amorphous films, whereas crystalline V_2O_5 is observed for the O_2 plasma process. There are however some minimal requirements in order to obtain this crystalline structure. These include a minimum plasma exposure of 5 s, a minimum amount of 100 ALD cycles and a minimum deposition temperature of 150 °C. Increasing the deposition temperature to 175 °C further increases the degree of crystallinity, but such temperatures may involve some un-

controlled growth, as explained in the previous section. The observations of crystalline V_2O_5 support the V^{5+} valence derived from XPS, and the V molar density, which closely corresponded with crystalline V_2O_5.

Crystalline phase formation

A detailed study on the crystalline phase formation during post-ALD annealing was performed by means of in-situ XRD measurements as a function of the O_2 partial pressure. Figure 8 shows the in-situ XRD measurements performed under various annealing ambients for films of 20 nm thickness deposited by the three ALD processes.

Figure 8. *In-situ XRD measurements during ramp annealing of 20 nm ALD films in various ambients. Row 1 to 3: H_2O, O_3 and O_2 plasma ALD processes. Column 1 to 4: annealing in 2 Pa O_2, 20 Pa O_2, 5000 Pa H_2 + 20 Pa O_2 and air.*

Annealing in pure inert gas does not result in reliable crystalline phase formation (not shown). A minimum amount of oxygen is thus required. At a low O_2 partial pressure of 2 Pa, the amorphous VO_2 films deposited by the H_2O and O_3 based ALD processes crystallize into VO_2(R) near a temperature of 400 °C, which remains as a single phase to the maximum annealing temperature of 750 °C. No significant influence of the reactant used during ALD is observed on the phase formation.

In contrast, when the O_2 partial pressure is increased to 20 Pa, a difference in crystallization behavior is observed between the H_2O and O_3 grown ALD films. Whereas the H_2O grown film crystallizes immediately into VO_2(R), the O_3 based film first crystallizes into VO_2(B), prior to transforming to VO_2(R). VO_2(B) is

a monoclinic metastable polymorph of VO_2 which is often observed during reduction of V_2O_5, and is known to transform towards the stable VO_2(R) phase at temperatures around 400-450 °C.[54;55] This difference in initial crystallization between H_2O and O_3 based ALD films is believed to originate from the difference in density of the as deposited films, as was illustrated in figure 4. A plausible explanation is that the low-density films deposited by the O_3 based ALD process are more prone to oxidation at elevated temperatures, such that oxygen interstitials are easily incorporated in the lattice. These interstitials would allow for the formation of metastable, low-density VO_2(B), instead of forming the more stable, high-density VO_2(R) phase. Only when the temperature is further increased, the transformation towards VO_2(R) occurs.

Apart from the difference in initial crystalline phase formation, the films annealed at 20 Pa O_2 furthermore show a subsequent oxidation of the VO_2 phase towards the Wadsley phase V_6O_{13}. This is in contrast to the findings of our recent work on the oxidation of sputtered V films, where we found 20 Pa to be a suitable O_2 partial pressure for VO_2 phase formation.[49] In that case, oxidation towards V_6O_{13} was only observed at 200 Pa O_2. We assume the lower film thickness of the ALD films compared to the sputtered films, i.e. 20 nm ALD films versus 170 nm oxidized V films, could explain the faster oxidation of the ALD films at 20 Pa O_2.

Annealing in air results in oxidation of the amorphous VO_2 films towards V_2O_5 near 350 °C. The oxidation is however preceded by formation of V_4O_9. Small traces of V_3O_7 were observed as well. By varying the oxygen partial pressure over a wide range between 2 Pa and 20000 Pa, six different crystalline vanadium oxide phases were observed: VO_2(R), VO_2(B), V_6O_{13}, V_4O_9, V_3O_7 and V_2O_5. A detailed overview of all the in-situ XRD measurements is presented in the phase formation diagram in Figure 9. This plot indicates the phase formation temperatures as a function of O_2 partial pressure for H_2O and O_3 based ALD films of 20 nm during ramp annealing at 0.25 °C/s. The dotted lines indicate all the O_2 partial pressures used during the experiments: 2, 5, 10, 20, 50, 100, 200, 500, 1000, 2000, 5000, 10000 and 20000 Pa. In Figure 8 only a small part of this dataset was shown. Based on the appearance and disappearance of the several crystalline vanadium oxide phases during the anneals, the phase formation diagram has been constructed. A horizontal line at 1 Pa indicates that a minimal partial O_2 pressure is required for crystallization. However, the exact value is not known. It should be noted that such phase formation diagram cannot be considered as a true thermodynamic phase diagram, since the oxidation reactions might be limited by kinetics. Nevertheless, the diagram clearly illustrates under which conditions the several crystalline vanadium oxides can be obtained as pure or mixed phases. It also shows the strikingly different phase formation between the films deposited using H_2O and O_3 as reactants. The lower density of the O_3 based ALD films are characterized by a much more complex phase formation diagram, allowing for the formation of the crystalline VO_2(B) and V_6O_{13} phases. In total, four different phases could be prepared in their pure form, i.e. VO_2(R), VO_2(B), V_6O_{13} and V_2O_5, using the following annealing conditions: 2 Pa O_2 and 480 °C for VO_2(M1/R), 20 Pa O_2 and 400 °C for VO_2(B), 50 Pa O_2 and 570 °C for V_6O_{13}, and 400 °C in air for V_2O_5. Figure 10

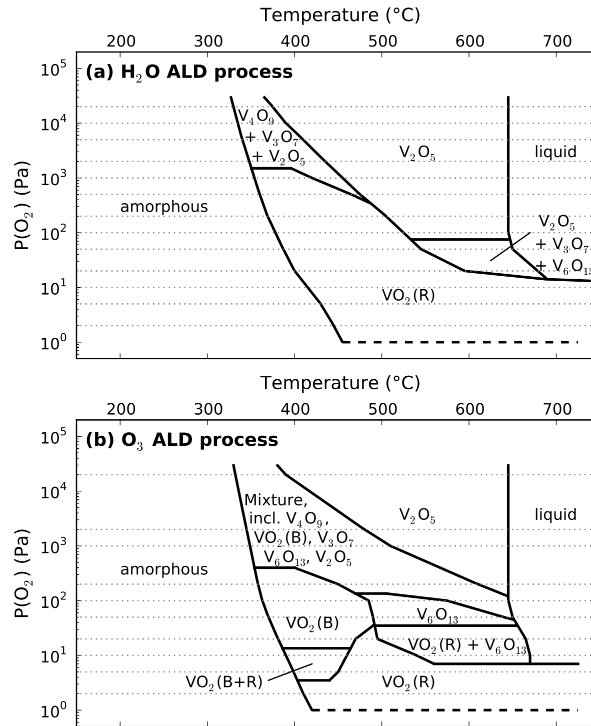

Figure 9. *Phase formation diagrams, based on the ramp annealing experiments in various oxygen partial pressures at 0.25 °C/s, for 20 nm films grown by H_2O and O_3 based ALD.*

shows full scan XRD measurements of the various phases prepared in this work.

In our previous report on the controlled oxidation of sputter deposited V towards VO_2 we showed that a mixture of 5000 Pa H_2 and 20 Pa O_2 yielded a an improved quality of the VO_2 films. Here we observe that such gas mixture is equally well useful for the formation of pure, crystalline VO_2 ALD films and prevention of oxidation towards higher oxide phases (Figure 8(c,g)). In that sense, this H_2-O_2 mixture behaves similar as the lower O_2 partial pressure of 2 Pa. The main difference is found in the ability of forming metastable VO_2(B) in the case of the O_3 based ALD film. The full XRD scans of VO_2 prepared using this gas mixture are also shown in Figure 10.

The 20 nm ALD film grown using O_2 plasma reduces from V_2O_5 towards VO_2(B), independent of the use of the three low pressure O_2 annealing ambients. However, as for the other ALD films, at 20 Pa O_2 without H_2, the formation of VO_2 is followed by oxidation towards V_6O_{13}. A remarkable high-temperature VO_2(B) phase stability is found in the other cases. Upon annealing in air, the as deposited crystalline V_2O_5 phase increases in crystallinity starting from 300 °C. Room temperature full scan XRD measurements of pure vanadium oxide phases,

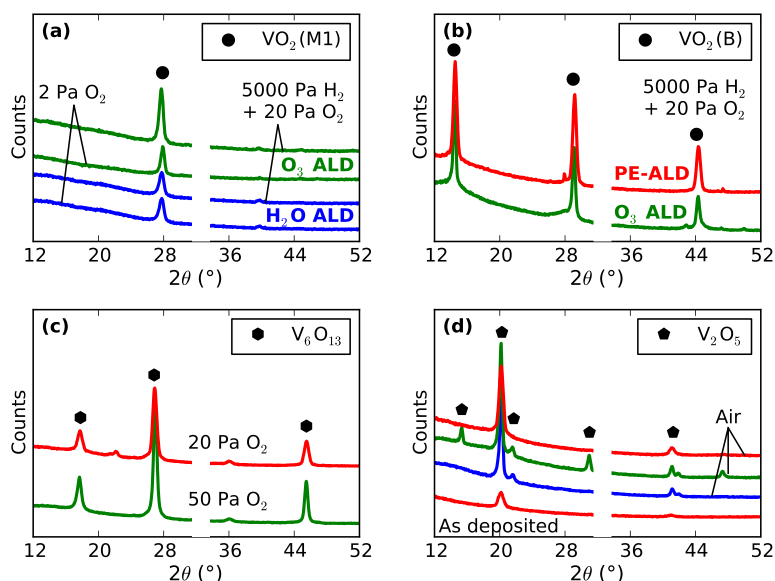

Figure 10. *Room temperature full scan XRD measurements of 20 nm vanadium oxide ALD films prepared using H_2O (blue), O_3 (green) and O_2 plasma (red) as reactants, and annealed under various conditions: (a) VO_2(M1), (b) VO_2(B), (c) V_6O_{13}, and (d) V_2O_5. For clarity the different spectra were shifted vertically and the peak near 33 °, related to the Si(100) substrate, was removed.*

prepared by post-deposition annealing of the PE-ALD films, are also shown in Figure 10. The annealing conditions were 2 Pa O_2 or 5000 Pa H_2 + 20 Pa O_2 at 480 °C for VO_2(B) formation, 20 Pa O_2 at 570 °C for V_6O_{13}, and 400 °C in air for V_2O_5.

Thus, four crystalline vanadium oxide phases have been prepared in this work: VO_2(M1/R) from the H_2O and O_3 process, VO_2(B) and V_6O_{13} from the O_3 and O_2 plasma process, and V_2O_5 from all three processes. The preparation of pure V_4O_9 and V_3O_7 was however not achieved. The formation of single-phase VO_2(M1/R) can be exploited for applications based on its characteristic semiconductor-metal transition. This is investigated in the next section.

Semiconductor-metal transition in VO_2(R) films and nanoparticles

Amorphous VO_2 films of various thickness have been deposited and crystallized towards the VO_2(M1/R) phase by isothermal annealing at 480 °C for 10 minutes. Figure 11 shows the temperature dependent sheet resistance measurements performed on such samples. Films of 20 nm or thicker are characterized by a change

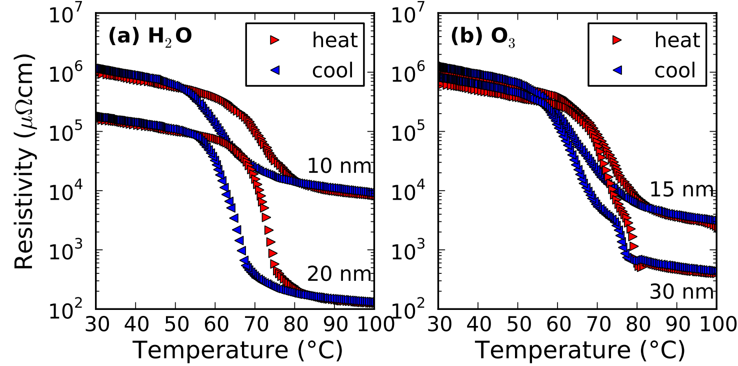

Figure 11. Temperature dependent sheet resistance measurements of VO_2 films prepared by H_2O based ALD (left) and O_3 based ALD (right), and post-deposition annealing at 480 °C in 5000 Pa H_2 and 20 Pa O_2.

in resistivity of approximately 3 orders of magnitude, independent of the deposition process. For thinner films the transition is suppressed, down to 2 orders of magnitude for a film thickness of 10 nm. Such reduced magnitudes of resistance switching are commonly observed in thin films. Brassard et al. related the suppression of the resistance switching to the decrease of grain size when film thickness is reduced.[25] It was hypothesized that decreased grain sizes imply a higher density of grain boundaries, which influence the sheet resistance. More precisely, these grain boundaries decrease the low-temperature sheet resistance of the VO_2 film through the present of defect levels in the gap, while increasing the high-temperature sheet resistance by grain boundary scattering of electrons. Nevertheless, the magnitudes of transition observed for our films of 10 to 20 nm are still high compared to results achieved by other techniques. In most cases, VO_2 films cannot be scaled down to a few tens of nanometers.[25]

Figure 12 shows the sheet resistance switching ratio as a function of the film thickness. The films were crystallized by post-deposition annealing in the mixture of 5000 Pa H_2 with 20 Pa O_2, at 480 °C for 10 minutes. No difference is observed between the switching ratios of films prepared on SiO_2 or Al_2O_3 templates. Below 10 nm, films were agglomerated. For comparison, VO_2 films prepared by controlled oxidation of sputtered V films, as reported in our previous work, are included in the plot.[49] For these films, a similar decreasing trend is observed, and agglomeration occurred as well below 10 nm. The electrical switching ratios in these oxidized PVD films were however strongly influenced by the template, which is believed to be originated from the difference in microstructure of the sputtered V films. In that sense, ALD has the advantage of being independent of the type of substrate, although it could be expected that in cases of crystalline substrates with lattice parameters similar to those of VO_2(R) might have a significant influence on the crystalline phase formation and morphology, and consequently on the electrical switching characteristics. This would be an interesting topic for further research.

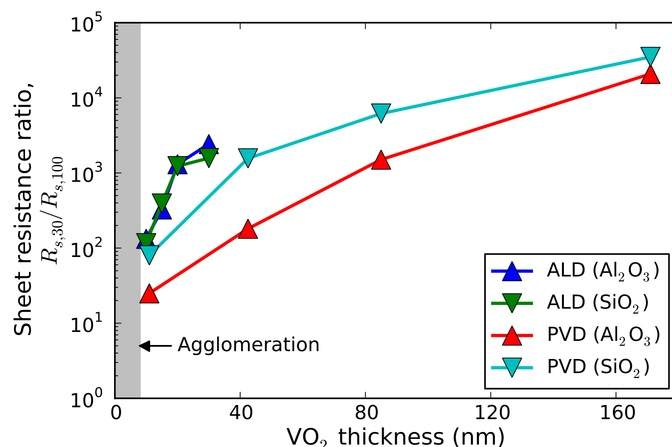

Figure 12. *Overview of the sheet resistance ratio $R_{s,30}/R_{s,100}$ of VO_2 thin films prepared by ALD, followed by annealing, and PVD, followed by controlled oxidation.[49] The ALD films and the thinnest PVD film were annealed in a mixture of 5000 Pa H_2 and 20 Pa O_2 at 480 °C for 10 minutes. The thicker PVD films were oxidized in a mixture of 5000 Pa H_2 and 200 Pa O_2 at 480 °C for 15 to 60 minutes depending on the film thickness.*

Films of 5 nm or less were not measurable since agglomeration occurred during annealing. Certainly when the post-deposition annealing temperature was increased, the formation of nanoparticles was observed. AFM measurements revealed that after crystallization of a 10 nm ALD film at 480 °C a continuous layer was present with a RMS roughness of 1.6 nm (Figure 13(a)), while for a 2.5 nm film annealed at 660 °C the film was broken up into nanoparticles (Figure 13(b,c)). These nanoparticles had approximate diameters of 50 to 100 nm, and heights up to 25 nm.

Although the nanoparticles could not be characterized electrically, temperature

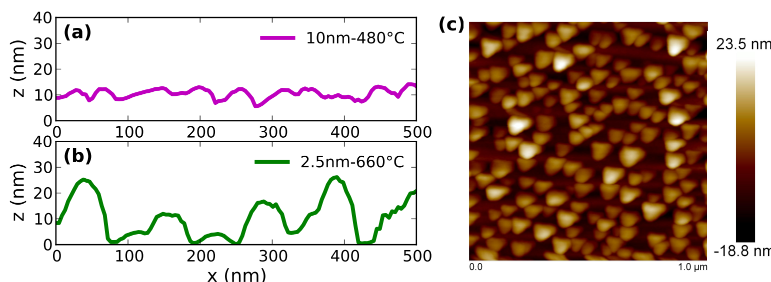

Figure 13. *(a) AFM line scans on a VO_2(M1/R) thin film of 10 nm. (b-c) AFM line scan and 2D scan on VO_2(M1/R) nanoparticles synthesized by annealing a 2.5 nm ALD film at 660 °C. All films were annealed in a mixture of 5000 Pa H_2 and 200 Pa O_2.*

dependent ellipsometry revealed optical changes across the transition. In Figure 14 the relative changes of the ellipsometric parameter Ψ are plotted as a function of temperature. Also the samples with the thinnest annealed layers show a clear transition. The hysteresis width however increased significantly, from approximately 10 °C for continuous films, up to 50 °C for nanoparticles. Several publications have been reported on VO_2 nanoparticles, synthesized by implantation or pulsed laser deposition, with broader hysteresis loops compared to thin films or bulk material.[56–60] A typical hysteresis loop in bulk VO_2 has a width of 2 °C, while for thin films the typical values are around 15 °C. In case of nanoparticles, similar hysteresis widths up to 50 °C have been reported for particle sizes down to 40 nm.

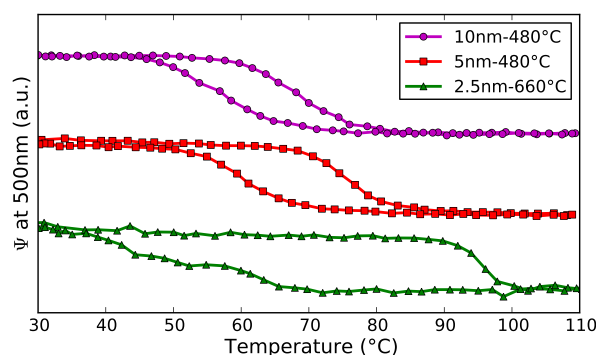

Figure 14. *Optical changes of VO_2 films and nanoparticles across the semiconductor-metal transition.*

Conclusions

In this work we reported on the synthesis of vanadium oxide thin films and nanoparticles by atomic layer deposition and post-deposition annealing in controlled gas ambients. TEMAV precursor allows for deposition of both amorphous VO_2 and crystalline V_2O_5, by using respectively H_2O or O_3, and O_2 plasma as reactant during deposition. The amorphous films are however prone to oxidation when exposed to air, gradually transforming V^{4+} into V^{5+}. Furthermore, a remarkable difference in density of the amorphous films was observed between the H_2O and O_3 based processes, which drastically affects the crystalline phase formation during post-deposition annealing. The high-density amorphous films grown using H_2O as reactant crystallize towards the VO_2(R) phase at low oxygen partial pressures, or oxidizes towards V_2O_5 at high oxygen partial pressures. In contrast, the low-density amorphous VO_2 films grown by using O_3 as reactant, allow for crystallization or oxidation into pure VO_2(B) and V_6O_{13} as well, apart from VO_2(R) and V_2O_5. It was noticed that in both cases a low oxygen partial pressure of a few Pa

is required to allow for VO_2(R) crystallization, and temperatures around 450 °C. On the other hand, the crystalline V_2O_5 films grown by PE-ALD could be reduced to VO_2(B) or V_6O_{13}. High electrical switching ratios of more than 3 orders of magnitude were observed for the VO_2(R) thin films. A minimum film thickness is however required to observe the electrical switch, since agglomeration occurs during post-deposition annealing. For reduced film thickness, nanoparticles were formed. These showed an optical transition, as measured by ellipsometry, with an increased hysteresis width up to 50 °C, compared to $\approx$ 10 °C in continuous films.

Acknowledgments

This research was supported by the Special Research Fund BOF of Ghent University (GOA 01G01513) and the Flemish Research Foundation FWO. CD furthermore acknowledges the Hercules Foundation for funding SPINAL (AUGE/09/014). Tareq Ahmad and Kilian Devloo-Casier are acknowledged for AFM and XPS measurements.

References

[1] H. A. Wriedt, *Bulletin of Alloy Phase Diagrams* **10**(3), 271–277 (1989).
[2] Y.-B. Kang, *J. Eur. Ceram. Soc.* **32**(12), 3187–3198 (2012).
[3] N. Bahlawane and D. Lenoble, *Chem. Vapor Depos.* **20**(7-8-9), 299–311 (2014).
[4] F. J. Morin, *Phys. Rev. Lett.* **3**(1), 34–36 (1959).
[5] U. Schwingenschlögl and V. Eyert, *Ann. Phys.* **13**(9), 475–510 (2004).
[6] A. Zylbersztejn and N. F. Mott, *Phys. Rev. B* **11**(11), 4383–4395 (1975).
[7] T. D. Manning, I. P. Parkin, R. J. H. Clark, D. Sheel, M. E. Pemble, and D. Vernadou, *J. Mater. Chem.* **12**(10), 2936–2939 (2002).
[8] I. P. Parkin and T. D. Manning, *J. Chem. Educ.* **83**(3), 393 (2006).
[9] C. E. Lee, R. A. Atkins, W. N. Gibler, and H. F. Taylor, *Appl. Opt* **28**(21), 4511–4512 (1989).
[10] M. Soltani, M. Chaker, E. Haddad, R. V. Kruzelecky, and J. Margot, *Appl. Phys. Lett.* **85**(11), 1958–1960 (2004).
[11] M.-J. Lee, Y. Park, D.-S. Suh, E.-H. Lee, S. Seo, D.-C. Kim, R. Jung, B.-S. Kang, S.-E. Ahn, C. B. Lee, D. H. Seo, Y.-K. Cha, I.-K. Yoo, J.-S. Kim, and B. H. Park, *Adv. Mater.* **19**(22), 3919–3923 (2007).
[12] H.-T. Kim, B.-G. Chae, D.-H. Youn, S.-L. Maeng, G. Kim, K.-Y. Kang, and Y.-S. Lim, *New J. Phys.* **6**, 52 (2004).
[13] I. P. Radu, K. Martens, S. Mertens, C. Adelmann, X. Shi, H. Tielens, M. Schaekers, G. Pourtois, S. Van Elshocht, S. De Gendt, M. Heyns, and J. A. Kittl, *ECS Trans.* , 233–243 (2011).
[14] K. Martens, I. P. Radu, S. Mertens, X. Shi, L. Nyns, S. Cosemans, P. Favia, H. Bender, T. Conard, M. Schaekers, and et al., *J. Appl. Phys.* **112**(12), 124501 (2012).
[15] K. M. Martens, I. P. Radu, G. Rampelberg, J. Verbruggen, S. Cosemans, S. Mertens, X. Shi, M. Schaekers, C. Huyghebaert, S. De Gendt, C. Detavernier, M. Heyns, and J. A. Kittl, *ECS Trans.* **45**(4), 151–158 (2012).
[16] I. P. Radu, B. Govoreanu, S. Mertens, X. Shi, M. Cantoro, M. Schaekers, M. Jurczak, S. De Gendt, A. Stesmans, J. A. Kittl, M. Heyns, and K. Martens, *Nanotechnology* **26**(16), 165202 (2015).
[17] N. Ganganagappa and A. Siddaramanna, *Mater. Charact.* **68**, 58–62 (2012).
[18] J. C. Badot, S. Ribes, E. B. Yousfi, V. Vivier, J. P. Pereira-Ramos, N. Baffier, and D. Lincot, *Electrochem. Solid St.* **3**(10), 485–488 (2000).
[19] E. Østreng, K. B. Gandrud, Y. Hu, O. Nilsen, and H. Fjellvåg, *J. Mater. Chem. A* **2**(36), 15044–15051 (2014).
[20] S. Beke, *Thin Solid Films* **519**(6), 1761–1771 (2011).
[21] T. J. Hanlon, R. E. Walker, J. A. Coath, and M. A. Richardson, *Thin Solid Films* **405**, 234–237 (2002).
[22] K. Nagashima, T. Yanagida, H. Tanaka, and T. Kawai, *J. Appl. Phys.* **100**(6), 063714 (2006).
[23] C. H. Griffiths and H. K. Eastwood, *J. Appl. Phys.* **45**(5), 2201–2206 (1974).
[24] S. J. Yun, J. W. Lim, J.-S. Noh, B.-G. Chae, and H.-T. Kim, *Jpn. J. Appl.*

Phys. **47**(4S), 3067 (2008).

[25] D. Brassard, S. Fourmaux, M. Jean-Jacques, J. C. Kieffer, and M. A. El Khakani, *Appl. Phys. Lett.* **87**(5), 051910 (2005).

[26] M. B. Sahana, G. N. Subbanna, and S. A. Shivashankar, *J. Appl. Phys.* **92**(11), 6495 (2002).

[27] D. Vernardou, M. Pemble, and D. Sheel, *Thin Solid Films* **516**(14), 4502–4507 (2008).

[28] C. Piccirillo, R. Binions, and I. P. Parkin, *Chem. Vapor Depos.* **13**(4), 145–151 (2007).

[29] L. A. Beresneva, S. F. Devyatova, and L. L. Vasilyeva, *Thin Solid Films* **75**(1), 47–51 (1981).

[30] J. Qi, G. Ning, and Y. Lin, *Mater. Res. Bull.* **43**(8-9), 2300–2307 (2008).

[31] T. Suntola and J. Antson, (1977), US Patent 4,058,430.

[32] R. L. Puurunen, *J. Appl. Phys.* **97**(12), 121301 (2005).

[33] S. M. George, *Chem. Rev.* **110**(1), 111–131 (2010).

[34] C. Detavernier, J. Dendooven, S. P. Sree, K. F. Ludwig, and J. A. Martens, *Chem. Soc. Rev.* **40**(11), 5242–5253 (2011).

[35] J. Dendooven, D. Deduytsche, J. Musschoot, R. L. Vanmeirhaeghe, and C. Detavernier, *J. Electrochem. Soc.* **156**(4), P63 (2009).

[36] J. Dendooven, D. Deduytsche, J. Musschoot, R. L. Vanmeirhaeghe, and C. Detavernier, *J. Electrochem. Soc.* **157**(4), G111 (2010).

[37] J. Musschoot, D. Deduytsche, H. Poelman, J. Haemers, R. L. Van Meirhaeghe, S. Van den Berghe, and C. Detavernier, *J. Electrochem. Soc.* **156**(7), P122 (2009).

[38] P. Dagur, A. U. Mane, and S. Shivashankar, *J. Cryst. Growth* **275**(1-2), e1223–e1228 (2005).

[39] I. M. Povey, M. Bardosova, F. Chalvet, M. E. Pemble, and H. M. Yates, *Surf. Coat. Tech.* **201**(22-23), 9345–9348 (2007).

[40] M.-G. Willinger, G. Neri, E. Rauwel, A. Bonavita, G. Micali, and N. Pinna, *Nano Letters* **8**(12), 4201–4204 (2008).

[41] G. Rampelberg, M. Schaekers, K. Martens, Q. Xie, D. Deduytsche, B. De Schutter, N. Blasco, J. Kittl, and C. Detavernier, *Appl. Phys. Lett.* **98**(16), 162902 (2011).

[42] P. A. Premkumar, M. Toeller, I. P. Radu, C. Adelmann, M. Schaekers, J. Meersschaut, T. Conard, and S. Van Elshocht, *ECS J. Solid State Sci. Technol.* **1**(4), P169–P174 (2012).

[43] T. Blanquart, J. Niinistö, M. Gavagnin, V. Longo, M. Heikkilä, E. Puukilainen, V. R. Pallem, C. Dussarrat, M. Ritala, and M. Leskelä, *RSC Adv.* **3**(4), 1179 (2013).

[44] G. Rampelberg, D. Deduytsche, B. De Schutter, P. A. Premkumar, M. Toeller, M. Schaekers, K. Martens, I. Radu, and C. Detavernier, *Thin Solid Films* **550**, 59–64 (2014).

[45] P. A. Premkumar, K. Martens, G. Rampelberg, M. Toeller, J. M. Ablett, J. Meersschaut, D. Cuypers, A. Franquet, C. Detavernier, J.-P. Rueff, M. Schaekers, S. Van Elshocht, M. Jurczak, C. Adelmann, and I. P. Radu, *Adv.*

Funct. Mater. **25**, 679–686 (2015).

[46] M. Tangirala, K. Zhang, D. Nminibapiel, V. Pallem, C. Dussarrat, W. Cao, T. N. Adam, C. S. Johnson, H. E. Elsayed-Ali, and H. Baumgart, *ECS J. Solid State Sci. Technol.* **3**(6), N89–N94 (2014).

[47] Q. Xie, Y.-L. Jiang, C. Detavernier, D. Deduytsche, R. L. Van Meirhaeghe, G.-P. Ru, B.-Z. Li, and X.-P. Qu, *J. Appl. Phys.* **102**(8), 083521 (2007).

[48] Q. Xie, J. Musschoot, D. Deduytsche, R. L. Van Meirhaeghe, C. Detavernier, S. Van den Berghe, Y.-L. Jiang, G.-P. Ru, B.-Z. Li, and X.-P. Qu, *J. Electrochem. Soc.* **155**(9), H688 (2008).

[49] G. Rampelberg, B. De Schutter, W. Devulder, K. Martens, I. Radu, and C. Detavernier, *J. Mater. Chem. C* , 11357–11365 (2015).

[50] W. Knaepen, C. Detavernier, R. Van Meirhaeghe, J. Jordan Sweet, and C. Lavoie, *Thin Solid Films* **516**(15), 4946–4952 (2008).

[51] W. Knaepen, S. Gaudet, C. Detavernier, R. L. Van Meirhaeghe, J. J. Sweet, and C. Lavoie, *J. Appl. Phys.* **105**(8), 083532 (2009).

[52] G. Silversmit, D. Depla, H. Poelman, G. B. Marin, and R. De Gryse, *J. Electron Spectrosc.* **135**(2-3), 167–175 (2004).

[53] B. E. Deal and A. S. Grove, *J. Appl. Phys.* **36**(12), 3770 (1965).

[54] F. Théobald, R. Cabala, and J. Bernard, *J. Solid State Chem.* **17**, 431–438 (1976).

[55] C. Leroux, G. Nihoul, and G. Van Tendeloo, *Phys. Rev. B* **57**(9), 5111 (1998).

[56] V. A. Klimov, I. O. Timofeeva, S. D. Khanin, E. B. Shadrin, A. V. Ilinskii, and F. Silva-Andrade, *Tech. Phys.* **47**(9), 1134–1139 (2002).

[57] R. Lopez, L. A. Boatner, T. E. Haynes, L. C. Feldman, and R. F. Haglund, *J. Appl. Phys.* **92**(7), 4031 (2002).

[58] J. Y. Suh, R. Lopez, L. C. Feldman, and R. F. Haglund Jr, *J. Appl. Phys.* **96**(2), 1209–1213 (2004).

[59] E. U. Donev, *Metal-semiconductor transition in nanoscale VO_2 thin films, subwavelength holes and nanoparticles*, PhD thesis, Vanderbilt University, (2008).

[60] K. Appavoo, D. Y. Lei, Y. Sonnefraud, B. Wang, S. T. Pantelides, S. A. Maier, and R. F. Haglund, *Nano Lett.* **12**(2), 780–786 (2012).

Paper V
Low temperature plasma-enhanced atomic layer deposition of thin vanadium nitride layers for copper diffusion barriers *

Abstract

Thin vanadium nitride (VN) layers were grown by atomic layer deposition using tetrakis(ethylmethylamino)vanadium and NH_3 plasma at deposition temperatures between 70 °C and 150 °C on silicon substrates and polymer foil. X-ray photoelectron spectroscopy revealed a composition close to stoichiometric VN, while x-ray diffraction showed the δ-VN crystal structure. The resistivity was as low as 200 $\mu\Omega$cm for the as deposited films, and further reduced to 143 $\mu\Omega$cm and 93 $\mu\Omega$cm by annealing in N_2 and H_2/He/N_2 respectively. A 5 nm VN layer proved to be effective as a diffusion barrier for copper up to a temperature of 720 °C.

*Published as: G. Rampelberg, K. Devloo-Casier, D. Deduytsche, M. Schaekers, N. Blasco, and C. Detavernier, *Appl. Phys. Lett.*, 102, 111910 (2013).

Transition metal nitrides are characterized by a variety of interesting properties, including high melting point and thermal stability, hardness, corrosion resistance and low resistivity. In microelectronics many of these nitrides, such as TiN and TaN, have been extensively investigated for their use as copper diffusion barriers for interconnects.[1–3] More recently VN gained interest for this type of application because of its room-temperature resistivity of 40 to 100 $\mu\Omega$cm.[4–6] Other potential applications were reported, such as high-temperature self-lubricant coatings and for use as a supercapacitor material, for which it showed superior characteristics compared to ruthenium oxide.[7;8] Thin films of VN are mainly deposited by reactive sputtering and high temperature nitridation of metallic vanadium.[4;5;9–12] However, for deposition in high aspect ratios, as required in microelectronics, atomic layer deposition (ALD) is the most suitable technique to grow conformal thin films.[13–15] Recently ALD of VN has been reported using tetrakis(diethylamido)vanadium (TDEAV) as precursor and NH_3 as reactant with a temperature window in the range from 190 to 250 °C.[16]

In this work we report on the plasma-enhanced atomic layer deposition (PE-ALD) of vanadium nitride in the low-temperature range from 150 °C down to 70 °C on both Si substrates and polymer foil. The ultimate resistivity of the as-deposited films was as low as 200 $\mu\Omega$cm, while post-ALD annealing reduced this value to 93 $\mu\Omega$cm. Finally a thin VN layer was tested as a diffusion barrier for copper.

The VN thin films were deposited in an experimental pump-type high vacuum ALD reactor with a base pressure below 10^{-4} Pa.[17;18] Tetrakis(ethylmethylamino)vanadium (TEMAV), recently reported for the growth of VO_2,[19] was used as a metal-organic precursor with argon as a carrier gas. Both NH_3 gas and NH_3 plasma, generated in a remote RF-plasma tube above the sample, were used as reactants. For the characterization of the ALD process, Si substrates with a thermally grown 100 nm SiO_2 layer were used.

From our experience with VO_2 ALD 150 °C was chosen as a standard deposition temperature, since above 175 °C the TEMAV precursor decomposes, resulting in uncontrolled growth. At this temperature of 150 °C, the conditions of saturation were examined by changing the precursor and reactant exposure, which was obtained by varying the pulse times. Figure 1(a) shows the saturation behavior for the plasma-enhanced process, at a plasma power of 300 W. The closed symbols indicate the thickness obtained by x-ray reflectivity (XRR) for 200 ALD cycles with a fixed NH_3 plasma pulse of 10 s and a varying TEMAV pulse time. The open symbols indicate the thickness for the case where the TEMAV pulse was kept fixed for 5 s and the NH_3 plasma pulse time was varied. For both cases only a minor variation in thickness was observed, which proves that a saturated ALD process was obtained. For all further experiments 5 s TEMAV and 10 s NH_3 plasma pulses were being used. In addition, experiments were carried out to investigate the influence of plasma power on the film growth. As observed in figure 1(b), varying the plasma power in the range 100 to 500 W did not influence film thickness and vanadium areal density, the latter one being determined by x-ray fluorescence

(XRF). On the other hand, the thermal process (i.e. 0 W power) had a slightly lower thickness but a much lower vanadium areal density. This indicates that the thermal process results in a lower density or leads to a different composition compared to the plasma-enhanced process. Figure 1(c) shows the evolution of the film thickness as a function of the number of PE-ALD cycles. A linear increase with a growth rate of 0.71 Å per ALD cycle is observed. Some data points are shown for lower deposition temperatures. Although these indicate a decreased growth rate, the PE-ALD process still results in film growth at the low temperature of 70 °C, which is lower than other reported processes for metal nitride ALD.[15]

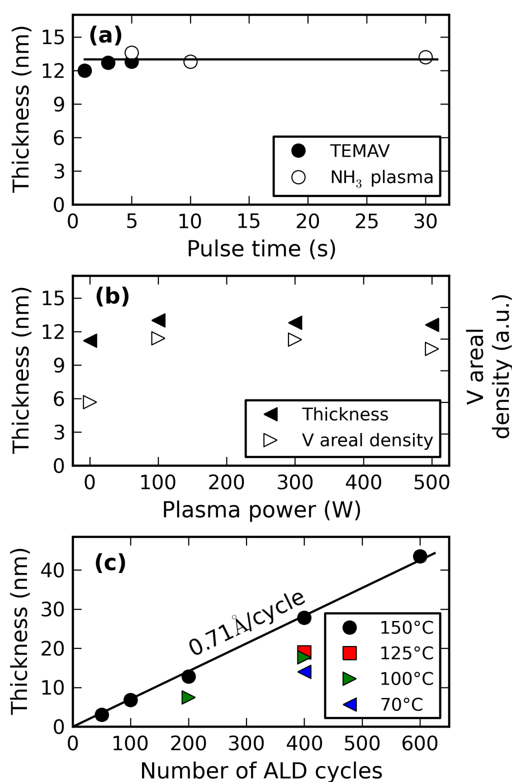

Figure 1. Characteristics of the PE-ALD process: (a) saturation behavior for variation of the TEMAV and NH_3 plasma pulse times for 200 ALD cycles at 150 °C, (b) influence of plasma power on the film thickness and areal density of vanadium for 200 ALD cycles at 150 °C with the thermal process included as 0W, and (c) film thickness as a function of the number of PE-ALD cycles for various deposition temperatures.

X-ray photoelectron spectroscopy (XPS) was performed on both a thermal and a plasma-enhanced processed sample, both deposited at 150 °C (figure 2). The C 1s level from absorbed surface species was used as a reference (284.8 eV) for the binding energies. To exclude contributions of these surface contaminants for

film analysis, the surface had been pre-sputtered in the XPS chamber using an Ar ion beam. For the plasma-grown film the binding energy of the V $2p_{3/2}$ was determined as 513.7 eV, with a shoulder on the higher binding energy side. These observation are in accordance with reported XPS data for VN, where the shoulder was interpreted as shake-up satellites which originate from poorly screened core-hole states in VN.[20] The observation of the N 1s peak at 397.4 eV further confirms the presence of the V-N bonding. Since the O 1s peak is only very small, the oxygen impurity level in the film is quite low. In addition, no C impurities were detected. From the areas under the peaks a composition close to stoichiometric VN was derived (50% V, 48% N) with an oxygen concentration less than 3%. In the case of the thermal ALD process, the O 1s peak was increased drastically, indicating an oxygen-rich composition (40% V, 15% N, 45% O), while again no carbon was detected. Although no oxygen atoms were intentionally introduced in the ALD reactor, neither by the TEMAV precursor, neither by the reactant, the film was oxidized. Two possible reasons can be suggested: (i) oxygen is being built-in in the film during growth due to background gases like water vapor in the reactor and/or impurities in the Ar carrier gas and NH_3 gas, or (ii) a lower density film is being deposited, which easily oxidizes when exposed to air.

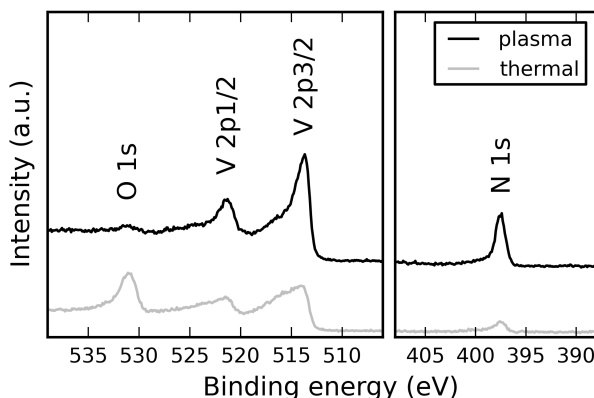

Figure 2. *XPS for both the plasma-enhanced and thermal ALD process, including the peaks of O 1s, V 2p and N 1s. The displayed spectra were collected after pre-sputtering the surface.*

X-ray diffraction (XRD) patterns for the plasma-enhanced grown films are shown in figure 3 ($\lambda = 0.154nm$). A polycrystalline structure can clearly be observed for the as deposited films of 400 and 600 cycles, but even a small hint of crystallinity is present for the case of 200 cycles. The two peaks almost match the signature of the desirable δ-VN phase, but are shifted to slightly lower 2θ values. This could possibly be explained by the small amount of oxygen impurities or nitrogen vacancies within the crystal lattice. Furthermore, the width of the diffraction peaks indicates that the crystallite size is small.

Post-ALD annealing has been performed on samples with 400 PE-ALD cycles

in both N_2 and a mixture H_2/He/N_2 (5/90/5%) by heating the samples from room temperature up to 820 °C with a constant heating rate of 0.2 °C/s, immediately followed by a quench. After cooling down to room-temperature the XRD spectra show that the diffraction peaks shifted to the desirable δ-VN XRD signature, which indicates that the stoichiometry further improved. The peak widths also decreased due to grain growth. In the case of the H_2-N_2 mixture this grain growth is preferential for the (111) orientation, since the (111) peak increased in intensity, while the (200) peak disappeared.

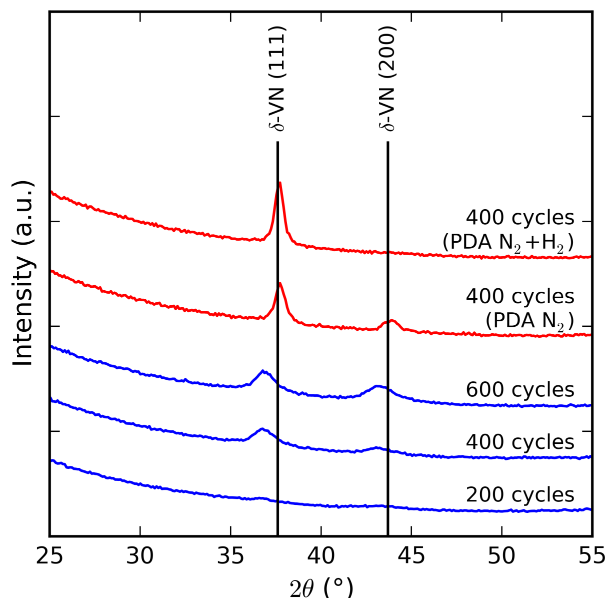

Figure 3. *XRD spectra for the as deposited samples of 200, 400 and 600 PE-ALD cycles and annealed samples of 400 PE-ALD cycles. In addition the XRD signature of the δ-VN phase is indicated.*

The resistivity of the VN layers was determined at room-temperature by four-point probe measurements, as shown in figure 4 for the PE-ALD films. A minimum value near 200 $\mu\Omega$cm was achieved for films of more than 20 nm, deposited at 150 °C, while for a 3 nm layer the resistivity only increased to 320 $\mu\Omega$cm. Also for lower deposition temperatures a slightly increased resistivity has been observed. It is worth noting that the resistivity of the VN films deposited using a thermal NH_3 ALD process was at least a factor of 50 higher. In addition, the room-temperature resistivities of the post-ALD annealed samples with 400 PE-ALD cycles are also plotted. The value of 200 $\mu\Omega$cm for the as-deposited film dropped to 143 $\mu\Omega$cm for the film annealed in N_2 and to 93 $\mu\Omega$cm when the N_2-H_2 mixture was used. As already stated, we expect from the XRD results that the stoichiometry of the VN films improved during the anneals. The decreased resistivity further supports

this explanation. XRR revealed a slight reduction in thickness of respectively 3 and 13% for pure N_2 and for the H_2N_2 mixture and only a minor increase of the roughness, which was still less than 2 nm for both cases.

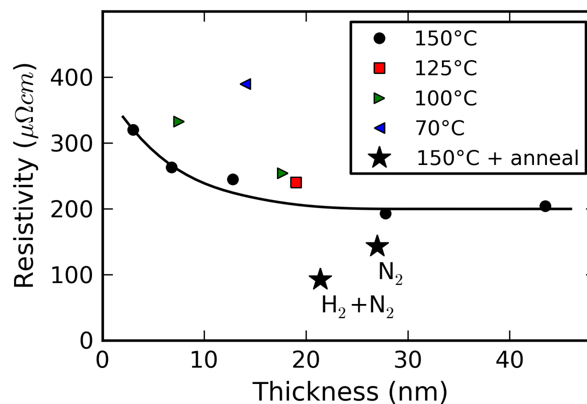

Figure 4. *Room-temperature resistivity as a function of thickness and deposition temperature of the PE-ALD process. The black curve shows the trend with respect to thickness for the samples with 150 °C deposition temperature. In addition the room-temperature resistivity of the annealed samples in N_2 and a mixture containing H_2 and N_2 are displayed.*

In addition to depositions on oxidized Si substrates, a plasma-enhanced deposition of 400 cycles was performed on polymer foil (Mylar, i.e. biaxially-oriented polyethylene terephthalate) at a temperature of 70 °C. A semi-transparent conductive film was grown with a transmission of 35 to 42% in the visual spectrum (390-700 nm) and a sheet resistance of $270\Omega/\Box$.

For testing the diffusion barrier properties, a thin layer of 5 nm VN was grown on a HF-cleaned Si substrate using the PE-ALD process. Without interrupting the vacuum, the sample was transferred to a neighboring high-vacuum chamber, where a 50 nm Cu layer was deposited by DC magnetron sputtering. Also a reference sample was prepared, with 50 nm Cu on a HF-cleaned Si substrate. In-situ XRD during thermal annealing was performed on both samples.[21–23] The film was heated at a linear rate of 1 °C/s to 900 °C, while simultaneously XRD snapshots were collected every 2 s in a 2θ range of 20°. Figure 5(a) shows how for the reference sample the Cu diffraction peaks disappear near a temperature of 230 °C. A reaction with the Si substrate takes place and Cu_3Si is formed, which stays stable up to a temperature of 800 °C. In contrast, figure 5(b) shows how for the sample with the VN layer in between the Cu and the Si substrate, the reaction between the Cu and Si is delayed to a temperature of approximately 720 °C, before the Cu_3Si is formed. Thus, the thin PE-ALD VN layer proved to be effective as a diffusion barrier for Cu.

In conclusion, VN thin films have been grown by ALD using TEMAV as metal-organic precursor and NH_3-plasma as reactant. Depositions were carried out in the

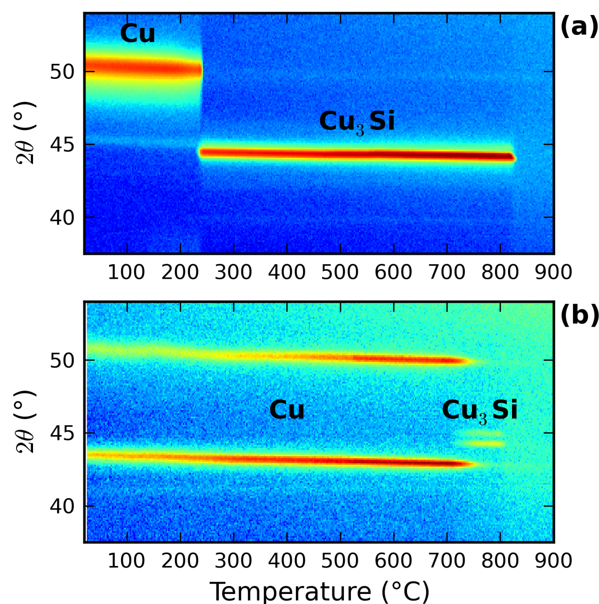

Figure 5. *In-situ XRD plots of the Cu diffusion barrier tests. Blue colors indicate low intensities (i.e. background), red is related to high intensities (i.e. diffraction peaks). (a) Cu on HF-cleaned Si reacts at 230 °C to form Cu_3Si, while (b) a 5 nm PE-ALD VN layer in between the Cu and HF-cleaned Si delays the reaction up to a temperature of 720 °C.*

low-temperature range from 150 °C down to 70 °C, which is lower than other reported metal nitride ALD processes and enables deposition of metallic conducting films on temperature sensitive materials such as polymers. The highest growth rate of 0.71 Å/c was achieved at 150 °C. XPS revealed a composition close to stoichiometric VN, while XRD indicated a crystalline phase which closely corresponds to δ-VN. The optimal resistivity was 200 $\mu\Omega$cm for the as-deposited films. Post-ALD annealing in N_2 or a H_2-N_2 mixture lead to a closer match of the XRD spectra to the desired δ-VN crystal structure, while a decrease in resistivity to respectively 143 $\mu\Omega$cm and 93 $\mu\Omega$cm was obtained. A 5 nm PE-ALD VN layer proved to be effective as a diffusion barrier for Cu up to a temperature of 720 °C.

Acknowledgments

C. D. Acknowledges UGent-BOF, GOA and ERC grant agreement No. 239865 for funding.

References

[1] H. C. M. Knoops, L. Baggetto, E. Langereis, M. C. M. van de Sanden, J. H. Klootwijk, F. Roozeboom, R. A. H. Niessen, P. H. L. Notten, and W. M. M. Kessels, *J. Electrochem. Soc.* **155**(12), G287 (2008).

[2] Q. Xie, J. Musschoot, C. Detavernier, D. Deduytsche, R. L. V. Meirhaeghe, S. V. d. Berghe, Y.-L. Jiang, G.-P. Ru, B.-Z. Li, and X.-P. Qu, *Microelectronic Eng.* **85**(10), 20592063 (2008).

[3] J. Musschoot, Q. Xie, D. Deduytsche, S. Van den Berghe, R. L. Van Meirhaeghe, and C. Detavernier, *Microelectronic Eng.* **86**(1), 72–77 (2009).

[4] M. B. Takeyama, T. Itoi, K. Satoh, M. Sakagami, and A. Noya, *J. Vac. Sci. Technol. B* **22**(5), 2542 (2004).

[5] X.-P. Qu, M. Zhou, T. Chen, Q. Xie, G.-P. Ru, and B.-Z. Li, *Microelectronic Eng.* **83**(2), 236240 (2006).

[6] J. Zasadzinski, R. Vaglio, G. Rubino, K. E. Gray, and M. Russo, *Phys. Rev. B* **32**(5), 2929 (1985).

[7] G. Gassner, P. H. Mayrhofer, K. Kutschej, C. Mitterer, and M. Kathrein, *Tribol. Lett.* **17**(4), 751–756 (2004).

[8] D. Choi, G. E. Blomgren, and P. N. Kumta, *Adv. Mater.* **18**(9), 1178–1182 (2006).

[9] X. Chu, S. A. Barnett, M. S. Wong, and W. D. Sproul, *J. Vac. Sci. Technol. A* **14**(6), 3124–3129 (1996).

[10] I. Galesic and B. O. Kolbesen, *Thin Solid Films* **349**, 14–18 (1999).

[11] I. Galesic, U. Reusch, C. Angelkort, H. Lewalter, A. Berendes, E. Schweda, and B. O. Kolbesen, *Vacuum* **61**, 479484 (2001).

[12] A. Berendes, I. Galesic, R. Mertens, W. Bock, H. Oechsner, P. Warbichler, F. Hofer, E. Theodossiu, H. Baumann, and B. O. Kolbesen, *Z. Anorg. Allg. Chem.* **629**(10), 1769–1777 (2003).

[13] T. Suntola and J. Antson, (1977), US Patent 4,058,430.

[14] R. L. Puurunen, *J. Appl. Phys.* **97**(12), 121301 (2005).

[15] V. Miikkulainen, M. Leskelä, M. Ritala, and R. L. Puurunen, *J. Appl. Phys.* **113**(2), 021301 (2013).

[16] M. B. Takeyama, M. Sato, H. Sudoh, H. Machida, S. Ito, E. Aoyagi, and A. Noya, *Jpn. J. Appl. Phys.* **50**(5), 05EA06 (2011).

[17] Q. Xie, Y.-L. Jiang, C. Detavernier, D. Deduytsche, R. L. Van Meirhaeghe, G.-P. Ru, B.-Z. Li, and X.-P. Qu, *J. Appl. Phys.* **102**(8), 083521 (2007).

[18] Q. Xie, J. Musschoot, D. Deduytsche, R. L. Van Meirhaeghe, C. Detavernier, S. Van den Berghe, Y.-L. Jiang, G.-P. Ru, B.-Z. Li, and X.-P. Qu, *J. Electrochem. Soc.* **155**(9), H688 (2008).

[19] G. Rampelberg, M. Schaekers, K. Martens, Q. Xie, D. Deduytsche, B. De Schutter, N. Blasco, J. Kittl, and C. Detavernier, *Appl. Phys. Lett.* **98**(16), 162902 (2011).

[20] A. Glaser, S. Surnev, F. Netzer, N. Fateh, G. Fontalvo, and C. Mitterer, *Surf. Sci.* **601**(4), 1153–1159 (2007).

[21] H. Kim, C. Detavernier, O. van der Straten, S. M. Rossnagel, A. Kellock, and D.-G. Park, *J. Appl. Phys.* **98**, 014308 (2005).

[22] W. Knaepen, C. Detavernier, R. Van Meirhaeghe, J. Jordan Sweet, and C. Lavoie, *Thin Solid Films* **516**(15), 4946–4952 (2008).

[23] W. Knaepen, S. Gaudet, C. Detavernier, R. L. Van Meirhaeghe, J. J. Sweet, and C. Lavoie, *J. Appl. Phys.* **105**(8), 083532 (2009).

Dankwoord

Bij het einde van dit doctoraatsonderzoek gekomen, is de tijd aangebroken om alles eens op een rijtje te zetten. Alvorens een heleboel mensen te bedanken, wil ik even schetsen wat ik al die tijd heb uitgespookt in "S1". Vaak kreeg ik die vraag van mensen uit mijn omgeving, en in de meeste gevallen was "atoomlaag per atoomlaag groeien" mijn nogal vage antwoord. Daarom wou ik er toch even wat cijfers bij halen. In de zes jaren die gepasseerd zijn heb ik ongeveer 100000 ALD cycli uitgevoerd (gelukkig gaat dat grotendeels automatisch), wat neer komt op ongeveer 10 µm totale dikte van de gedeponeerde coatings. Dat lijkt bedroevend weinig, zeker als je bedenkt dat in die tijd de Mount Everest ongeveer 25 mm in hoogte is toegenomen.[†] Maar we leven dan ook in een nano-tijdperk, wat mijn werk toch weer rechtvaardigt! Naast die honderden deposities heb ik uiteraard nog vele andere experimenten uitgevoerd, en de samenvatting heb je zonet gelezen in dit doctoraat... waarvoor dank!

En daarmee ben ik gekomen aan het echte doel van dit dankwoord: mensen in de bloemetjes zetten. Uiteraard mag mijn promotor, professor Christophe Detavernier als eerste aanschuiven in de rij om zijn trofee in ontvangst te nemen. Bedankt om mij deze kans te bieden dit onderzoek uit te voeren en mij een rol van betekenis te laten spelen binnen uw onderzoeksgroep CoCooN. Het was me een waar genoegen en ik kijk met veel plezier terug naar de voorbije jaren. Bedankt om me steeds van het nodige advies en kritische opmerkingen te voorzien, wat bijzonder nuttig was om dit onderzoek tot een hoger niveau te tillen.

Experimenteel onderzoek vereist uiteraard de nodige apparatuur. En aangezien in de CoCooN onderzoeksgroep het eerder regel dan uitzondering is dat apparatuur zelf gebouwd moet worden, kan ik niet anders dan een heleboel mensen te bedanken voor hun bijdrage. In de eerste plaats heb ik vele woorden van lof voor Jo Haemers. Ondanks zijn gezegende leeftijd was hij nagenoeg elke dag trouw op post om zich met hart en ziel in te zetten om de jonge garde bij te staan bij de ontwikkeling van experimentele apparatuur. Jo, ik heb ontzettend veel van jou geleerd, en ik hoop je dan ook in de komende jaren nog terug te zien in S1. In de tweede plaats wil ik Davy Deduytsche bedanken. Voor de mensen die hem niet kennen, Davy is de man die ervoor zorgde dat technische problemen met o.a. de ALD-reactoren in een handomdraai werden opgelost.

[†] Bron: http://www.nationalgeographic.com/

Verder wil ik alle CoCooN'ers bedanken die de afgelopen jaren een belangrijke rol van betekenis gespeeld hebben: Davy, Werner, Koen, Charlotte, Jan Musschoot, Jolien, Delphine, Boris, Kilian, Bob, Liesje, Wouter, Jan Dumortier, Felix, Filip, Kevin, Thomas, Matthias en Véronique. Uiteraard hebben jullie op wetenschappelijk vlak veel bijgedragen, maar er zijn nog zo veel andere redenen om jullie te bedanken: omdat ik soms meer dan twee handen nodig had om iets te monteren, omwille van de meestal veel te late birthday cakes (of whatever-reason-is-fine-muffins in het geval van Delphine), de gezellige babbels tijdens jullie koffiepauzes / mijn Cola-pauzes, het bekijken van hilarische youtube filmpjes (zoals het legendarische ClF_3-doet-echt-alles-branden of I-survived-lake-Peigneur)[‡,§], of het bedenken van de vele Friday-afternoon-experimenten die meestal toch niet uitgevoerd werden wegens totaal onrealistisch, veel te veel veronderstellingen of veel meer dan een halve dag werk. Kortom, het was een leuke en inspirerende tijd.
Specifiek wil ik het software-team Bob, Wouter, Kevin en Filip bedanken, alsook Thomas voor zijn electronica-know-how en het weer werkend krijgen van het plasma!
And of course, many thanks to my English- and other language-speaking colleagues: Qi, Shaoren, Ranjith, Amit, Eduardo and Jacob. It was (and still is) a pleasure of working together with you, guys! (Since I don't really trust Google Translate, I won't try to write this in Chinese, Indian, Spanish or German.)

Verder wil ik ook de ATP'ers bedanken voor hun waardevolle bijdragen wat betreft de technische kant van de zaak: Olivier, Gilbert, Jo Seys, Lode, Stefaan en Nico. En niet te vergeten: Elly, Kristof en Wouter Leroy voor het in orde brengen van administratie, bestellingen en recepties.

During my research on VO_2 and VN, I had a lot of interesting discussions with other people in the field. I want to thank the team at IMEC, Marc Schaekers, Karl Opsomer, Koen Martens, Iuliana Radu, Peter Anthony Premkumar, Michael Toeller, Malgorzata Jurczak and Jorge Kittl, for sharing their expertise on VO_2 and thin film research in general. Furthermore I would like to thank Nicolas Blasco and Christian Dussarrat (Air Liquide Electronics) for some valuable suggestions and for supplying the TEMAV precursor, which proved to be quite critical for this research topic. I should also thank the members of the jury, for thoroughly reviewing my thesis and for their interesting suggestions which certainly increased the scientific level of this work.

Ook de masterthesisstudenten Jeroen, Jan en Kobe wil ik bedanken voor hun enthousiasme (en gedeelde frustraties) tijdens hun werk op vanadium oxides. Het was me een genoegen om samen met jullie dat VO_2 beestje te temmen. Uiteraard heb ik ook beroep gedaan op andere personen binnen en buiten de vakgroep voor het analyseren van samples (SEM, EDX, XPS, AFM, RBS,...). Bedankt aan Nico, Jan, Kilian, Olivier, Wouter, Tareq en Koen Vanstiphout.

[‡] https://www.youtube.com/watch?v=M4l56AfUTnQ
[§] https://www.youtube.com/watch?v=3cXnxGIDhOA

Meer toekomstgericht wil ik alvast Danaë en nogmaals Christophe bedanken voor de steun, het vertrouwen en de motivatie om aan een nieuw avontuur te beginnen. Ik ben alvast benieuwd wat de toekomst te bieden heeft.

Naast de collega's wil ik ook de familie en vrienden bedanken voor de mooie jaren. Merci aan mijn ma, Jeannine, mijn broer en zussen Bart, Veerle, Katleen en Sigrid, en de schoonbroers Jeroen, Jonathan en Kris. Jammer dat onze pa, Augustin, dit niet meer kan meemaken. Ook bedankt aan de toffe schoonfamilie, Lieve, Roland, Evelien, Jeroen en Wendy, voor de steeds weer hartelijke ontvangst.
Ook merci aan de vele vrienden, voor de vele gezelschapsspelletjesavonden, de leuke weekends, de oudejaarsfeestjes, de frietjesavonden,... Merci Paul en Liesbeth, Brecht en Christine, Lesley en Kris, Tim en Sarah, Luc aka Frederik (of omgekeerd) en Bea, Ward en Hanne, Kim en Evi.

Tot slot wil ik mijn vrouw Charlotte bedanken voor de 11 voorbije jaren, voor alle steun toen we samen zaten te blokken, of op tijd in de les statistiek probeerden te geraken, voor het eindeloos lang wachten op het einde van dit doctoraat, voor de vele toffe reizen, voor alle dingen die ik hier niet moet vermelden,... en voor de ongetwijfeld even mooie toekomst die ons nog te wachten staat.

Geert
Gent, maart 2016